The Dissertation Committee for Christopher Glenn Cameron
certifies that this is the approved version of the following dissertation:

Comprehensive Aeromechanical Measurements of a Model-Scale, Coaxial, Counter-Rotating Rotor System

Committee:

Jayant Sirohi, Supervisor

David G. Bogard

David B. Goldstein

K. Ravi-Chandar

Rajneesh Singh

Comprehensive Aeromechanical Measurements of a Model-Scale, Coaxial, Counter-Rotating Rotor System

by

Christopher Glenn Cameron, B.E.; M.S.E.

DISSERTATION

Presented to the Faculty of the Graduate School of

The University of Texas at Austin

in Partial Fulfillment

of the Requirements

for the Degree of

DOCTOR OF PHILOSOPHY

THE UNIVERSITY OF TEXAS AT AUSTIN

December 2016

Acknowledgments

No large undertaking is truly accomplished alone, and this work is no exception. I would like to take this opportunity to thank those who, either directly or indirectly, have contributed to my success.

First I owe a deep debt of gratitude to my advisor Dr. Jayant Sirohi. From our first meeting, when he pitched this project to me, until the day of my defense, he has been instrumental in the success of my work and my growth as a researcher. His incisive intellect has been a joy, whether participating in class lectures, debating design decisions, or going out for lab happy hour. Most of all I am grateful for his commitment to the success of his students, whether it means staying up late fixing a broken sensor in the wind tunnel, or making introductions at conferences. I am truly lucky to count him as a mentor and friend.

I would like to thank my dissertation committee members: Dr. David Bogard, Dr. David Goldstein, Dr. K. Ravi-Chandar and Dr. Rajneesh Singh. I have benefited from their wisdom, both in the classroom and in discussions about my work. I was challenged to consider the broader implications of my work, placing it into a larger context. In doing so I gained a fresh perspective and was able to discover connections between seemingly disparate parts of my work.

The success of my project hinged on the contributions of many of the aerospace engineering staff. In particular I want to thank the machinists who brought my designs into reality, Joe Pokluda, Travis Crooks, David Gray, and Ricardo Palacios, Pablo Cortez for his electronics fabrication and Jeremy Jagodzinsky for his help with the test facility at Pickle Research Campus. Several undergraduates also contributed directly to the construction of the test stand, particularly, Jesse, Fernando, Karsten, and Alexis.

My project offered the opportunity for collaboration with researchers at The University of Maryland. I am especially grateful for Joseph Schmaus, whose collaboration was instrumental in shaping the design and execution of the wind tunnel tests. I also want to acknowledge Dr. Inderjit Chopra, Dr. V.T. Nagaraj, Dr. Anand Saxena, and the Glenn L. Martin wind tunnel staff for their support of our forward flight experiments.

Whether studying for class, prepping for qualifying exams, or taking mid-day coffee breaks, the scholarship and friendship of my fellow graduate students has propelled me forward. I would like to thank the students, past and current, in the aeroelasticity research group: Jerome, Brent, George, Anand, Daiju, Jason, and Young-Joon. From long days of wind tunnel testing, to traveling to conferences, I have been lucky to have them at my side.

My girlfriend, Kristina, has been by my side, whether near or far, for the last eight years. She is my best friend and confidant, always ready to laugh at a bad joke, listen to my worries, or provide encouragement and guidance. Her own dedication and scholarship have been an inspiration, and I am excited

for the next chapter of our lives together.

Finally I must acknowledge my family. My sister Elizabeth for her irrepressible joyous energy, which she spreads and shares so graciously. And my parents, who, since before my earliest memory have supported me with love and encouragement, opening opportunities at every turn. To them, most of all, I say thank you.

Comprehensive Aeromechanical Measurements of a Model-Scale, Coaxial, Counter-Rotating Rotor System

Publication No. _____

Christopher Glenn Cameron, Ph.D.
The University of Texas at Austin, 2016

Supervisor: Jayant Sirohi

With the renewed interest in rigid, counter-rotating coaxial rotor designs, and the increased fidelity of fully coupled CFD/CSD simulations, there exists a lack of comprehensive experimental data for a rotor system with which to validate analyses. The goal of this dissertation is to generate a new set of measurements on a model-scale rigid coaxial rotor systems in hover and high speed forward flight. A counter-rotating transmission was built, incorporating 6-component upper and lower rotor load cells for individual hub load measurements. Upper and lower rotor control systems, as well as complementary instrumentation including pushrod load cells, root pitch measurement and blade tip clearance sensors were developed. Two sets of rotor blades were fabricated and characterized using stereoscopic digital image correlation in combination with static and dynamic loads. A novel rotating-frame operational modal analysis successfully identified the first blade flap frequency and aerodynamic damping.

Hover testing focused on quantifying the effects of upper and lower coaxial rotor interference when compared to isolated rotors. Statistical analysis of the measured data revealed clear trends with a known confidence level. Due to mutual interference, the upper and lower rotors of the coaxial configuration consumed 18% and 49% more induced power than that of an isolated two-bladed rotor. The coaxial counter-rotating configuration was found to consume 6% less induced power than an isolated, four-bladed single rotor of equal solidity. While torque balanced, the upper rotor was found to produce 54% of the total system thrust regardless of blade loading. Significant four-per-revolution vibratory thrust was observed in the lower rotor, with primary and secondary peaks corresponding to bound vortex and blade thickness interactions respectively.

Wind tunnel testing examined the effects of lift offset and rotor phasing at high forward flight speeds. Rotor effective lift-to-drag ratio was found to increase with increasing advance ratio and lift offset, resulting in a 50% peak efficiency gain. The lower coaxial rotor was found to operate at higher lift-to-drag ratio than the upper rotor, due to the reversal of differential upper and lower rotor thrust compared to hover. Lift offset resulted in a decrease in blade tip clearance with a corresponding rise in rotor side force. Vibratory loads increased with advance ratio, with the largest occurring at two and four-per-revolution harmonics. Lift offset decreased vibratory forces while increasing vibratory in-plane moments. The coaxial system experienced reduced vibratory in-plane forces and torque compared to the isolated rotors due to

cancellation between upper and lower rotor loads. Adjusting the inter-rotor index angle modified vibratory forces and moments transmitted to the fixed frame, increasing some components while decreasing others.

Table of Contents

Acknowledgments iv

Abstract vii

List of Tables xiv

List of Figures xvi

Nomenclature xxiv

Chapter 1. Introduction 1

1.1 Problem Statement 1
1.2 State of the Art 5
1.2.1 Coaxial Rotorcraft 6
1.2.1.1 Experimental Investigations 6
1.2.1.2 Analytical and Computational Studies 9
1.2.2 Blade Deformation Measurement 13
1.2.3 Operational Modal Analysis 16
1.3 Present Approach 19
1.3.1 Contributions of the Present Research 20
1.3.2 Organization of the Dissertation 22

Chapter 2. Analytical Tools 25

2.1 Aerodynamic Models 26
2.1.1 Momentum Theory 26
2.1.1.1 Nondimensionalization 29
2.1.1.2 Momentum Theory for Coaxial Rotors 31
2.1.2 Blade Element Momentum Theory 33
2.1.2.1 Derivation of BEMT Model 33

2.1.2.2 Coaxial Interference Implementation 39
2.1.3 Free Vortex Wake Model 39
2.1.4 Airfoil Tables 43
2.2 Structural Models 43
2.2.1 Linear Beam Model 45
2.2.2 Nonlinear Beam Model 52
2.2.3 Cross Section Analysis 54
2.2.3.1 Composite Materials 56
2.2.3.2 Midplane Calculations 57
2.3 Uncertainty and Statistical Analysis 59
2.3.1 Precision and Bias Uncertainties 60
2.3.2 Propagation of Error 62
2.3.2.1 Sequential Perturbation 65
2.3.2.2 Covariance and Numerical Jacobian 66
2.3.2.3 Example Calculations 67
2.3.3 Model Fits and Regressions 69

Chapter 3. Experimental Design **72**
3.1 Test Stand Hardware 72
3.1.1 Drive System 72
3.1.2 Hub Design 74
3.1.3 Pitch Control System 77
3.1.3.1 Fixed Pitch 77
3.1.3.2 Swashplates and Linkages 78
3.1.3.3 Servo Controller and Calculations 85
3.1.3.4 Linear Servo Design 87
3.2 Instrumentation 91
3.2.1 Fixed Frame Instrumentation 91
3.2.2 Main Load Cells 93
3.2.2.1 Calibration and Drift Corrections 93
3.2.3 Pitch Link Load Cells 97
3.2.4 Root Pitch Angle Sensors 106

3.2.5 Blade Tip Clearance Sensor . . . 109
3.3 Data Acquisition . . . 112
3.3.1 LabView Virtual Instrument . . . 114

Chapter 4. Blade Construction and Characterization 118
4.1 Blade Construction . . . 118
4.1.1 Materials . . . 119
4.1.2 Reference Blades . . . 122
4.1.2.1 Core and Insert Preparation . . . 123
4.1.2.2 Composite Layup and Curing . . . 124
4.1.2.3 Finish Machining . . . 126
4.1.3 Reinforced Blades . . . 126
4.1.3.1 Root Reinforcement Cuff . . . 131
4.2 Static Characterization . . . 133
4.2.1 Uniform Beam . . . 134
4.2.2 Non-Uniform Beam . . . 139
4.2.2.1 Digital Image Correlation . . . 139
4.2.2.2 Linear Beam Model Fit . . . 145
4.3 Dynamic Characterization . . . 150
4.3.1 Modal Analysis Techniques . . . 150
4.3.1.1 Ibrahim Time Domain . . . 152
4.3.1.2 Eigensystem Realization Algorithm . . . 153
4.3.1.3 Natural Excitation Technique . . . 155
4.3.1.4 Eliminating Noise Modes . . . 156
4.3.2 Dynamic DIC Shaker Test . . . 157
4.3.3 Rotating Frame Modal Extraction . . . 163

Chapter 5. Hover Testing 174
5.1 Experimental Procedure . . . 176
5.2 Performance and Steady Loads . . . 180
5.2.1 Tip speed effect . . . 181
5.2.2 Different test setups . . . 182
5.2.3 Effect of torque balance . . . 184

5.2.4 Coaxial and Isolated Rotor System Performance 186
5.2.5 Upper and Lower Coaxial Rotor Performance 193
5.2.6 Collective Response 199
5.3 Vibratory Loads 203

Bibliography **211**

Chapter 6. Wind Tunnel Testing **228**
6.1 Experimental Procedure 228
6.1.1 Test Matrix 228
6.1.2 Trimming 230
6.1.3 Data Processing and Error Analysis 233
6.1.4 Wind Tunnel Wall Corrections 235
6.2 Steady Loads and Performance 238
6.2.1 Trimmed Forward Flight 238
6.2.2 Lift Offset and Steady Loads 241
6.2.3 Control Angles and Blade Tip Clearance 251
6.3 Vibratory Loads 256
6.3.1 Isolated Rotor Hub Loads 258
6.3.2 Coaxial Rotor Hub Loads 265
6.3.3 Pushrod Loads 271

Chapter 7. Summary and Future Work **274**
7.1 Summary 274
7.1.1 Hover Results 276
7.1.2 Forward Flight Results 278
7.2 Future Work 280

Appendix **283**

Appendix 1. Circuit Design **284**
1.1 Load Cell Amplifier 284
1.2 Digital Tip Clearance Sensor 284

Bibliography **290**

List of Tables

2.1 Coaxial rotor induced power interference factors 32
2.2 Ordering scheme for nonlinear beam model 53
2.3 Nonlinear beam model elastic cross-sectional constants 54
2.4 Nonlinear beam model inertial cross-sectional constants 54
2.5 Example uncertainty propagation parameters 68

3.1 Design Loads for Hub 75
3.2 Upper and lower rotor pitch dynamics 84
3.3 Geartrain stages and reductions 90
3.4 Servo actuator characteristics 91
3.5 Omega-160 load cell factory calibration 95
3.6 In-plane moment-force coupling correction factors 96
3.7 Pushrod loadcell calibrations 106
3.8 Data acquisition card specifications 114

4.1 3501-6 and 8552 epoxy comparison 120
4.2 IM7/8552 unidirectional tape properties 121
4.3 AS4/8552 plain weave properties 121
4.4 AS4/8552 plain weave elastic properties, $\pm 45^\circ$ orientation . . . 122
4.5 Additional blade construction materials 122
4.6 reference and reinforced blade composition 131
4.7 Dimensions for tip bending slope experiments 138
4.8 Mean blade properties for reference blades 139
4.9 Cuff and blade stiffness scaling factors 148
4.10 Shaker test identified modal frequencies and damping ratios . 163
4.11 Rotating ITD and predicted natural frequencies and damping ratios 171

5.1 Hover test matrix 207

5.2 Summary of rotor properties (hover testing) 208
5.3 Comparison between tests: momentum theory fits to measured rotor system performance, including 95% confidence intervals . 209
5.4 Reference blade rotor systems: momentum theory fits to measured rotor system performance, with 95% confidence intervals 209
5.5 Reinforced blade rotor systems: momentum theory fits to measured rotor system performance, with 95% confidence intervals 209
5.6 Rotor thrust collective sensitivity for isolated and coaxial rotors 210

6.1 Summary of rotor properties (wind tunnel) 229
6.2 Forward Flight Test Matrix 232
6.3 Wall correction factor and parameters 236

A.1 Load cell amplifier bill of materials 286
A.2 Tip clearance sensor bill of materials 289

List of Figures

1.1 Blade tangential velocity in forward flight 3

1.2 Thrust distribution of trimmed conventional and ABC rotor systems, (a) Conventional, (b) ABC, from Ref. [8] 4

2.1 Cross section of control volume used for derivation of momentum theory results 27

2.2 Rotor disk and cross sectional view of annulus used for BEMT calculations 34

2.3 Blade sectional geometry at rotor radius x with inflow from axial and induced velocities 35

2.4 Blade element momentum theory predictions for three rotors at $C_T = 0.010$: untwisted and un-tapered, $-10°$ linear twist, $-10°$ linear twist with 2:1 root-tip taper 38

2.5 Coaxial rotor wake geometry showing contracted upper rotor wake interference with lower rotor 40

2.6 Coaxial rotor wake geometry showing contracted upper rotor wake interference with lower rotor 42

2.7 Coaxial rotor wake geometry showing contracted upper rotor wake interference with lower rotor 44

2.8 Coaxial rotor wake geometry showing contracted upper rotor wake interference with lower rotor 45

2.9 Diagram of the linear beam model with coordinate system and displacements, external forcing, and root torsional spring . . . 46

2.10 Detail view of the differential beam element including the kinematic foreshortening, du 48

2.11 Blade cross section with labeled components 56

2.12 Example of degenerate geometry produced during blade offset 58

2.13 Level set offset method, (a) Contours of initial scalar function ϕ with zero-level in white, (b) Offsets of 0.3mm from the initial contour 60

2.14 Student's-t probability distribution function for various degrees of freedom 63

2.15 Graphical illustration of the propagation of uncertainty in μ_x, σ_x to uncertainty in $\mu_y = f(X)$, σ_y, from Ref. [6] 65

3.1 Belt driven coaxial transmission with hydraulic motor 73
3.2 Coaxial transmission cross sectional view 74
3.3 Modular, rigid rotor hub design (a) Central hub with bearing carriers (b) Cross-sectional view of bearing carrier and bladegrip 76
3.4 Manually adjusted pitch control system for hover experiments 79
3.5 Lower rotor pushrod support with full-bridge strain gauge instrumented arms 80
3.6 Lower rotor swashplate and linkage assembly 81
3.7 Upper rotor swashplate and linkage assembly 83
3.8 Pitch horn geometry, (a) Upper rotor, (b) Lower rotor 84
3.9 Diagram of the servo control system, red arrows are power, black arrows are control and feeback signals 86
3.10 Hitec angular servo actuator with custom arm 88
3.11 Characterization of pitch angle error due to servo resolution, (a) Error in θ_0, (b) Error in θ_{1S}, (c) Error in θ_{1C}, (d) Variation of maximum error with servo resolution 89
3.12 Upper rotor linear servo-actuator CAD views (a) Isometric (b) Cross-sectional view 90
3.13 Finished linear servo actuator components before assembly . . 91
3.14 Fixed frame instrumentation, (a) MEMS accelerometer with rapid prototyped mount, (b) Optical incremental encoder . . . 92
3.15 ATI Omega-160 6-component load cell 94
3.16 Lower rotor load cell in-plane moment-force couplings with linear fits and confidence bounds, (a) F_x-M_y coupling, (b) F_y-M_x coupling 96
3.17 Raw and drift corrected upper rotor F_z with no applied rotor loads 98
3.18 Free body diagram of pushrods, hub and load cell 99
3.19 Raw and drift corrected upper rotor F_z with no applied rotor loads 101
3.20 Strain gauge hoop (a) Dimensioned drawing (in) (b) Assembly with amplifier board 102
3.21 FEA calculated strain under $220N$ tension loading (a) Tangential strain (b) Transverse strain 103

3.22 Pitch link load cell strain gauge arrangement, (a) Gauge location on hoop, (b) Electrical arrangement in Wheatstone bridge 103
3.23 Diagram of upper rotor root pitch angle sensor and magnets . 107
3.24 Variation of Hall effect output with variation in axial separation distance (radial separation = 6.2 mm) 108
3.25 Installed sensor calibration, (a) Raw data with first and third order polynomial fits, (b) Fit residuals for first and third order polynomials 109
3.26 Jigs for pitch angle sensor construction (a) Rapid prototyped fixture for Hall effect mount (b) Laser cut magnet locating jig with bladegrips 110
3.27 Blade clearance sensor operational diagram 111
3.28 Embedded blade clearance sensors (a) Digital sensor (b) Discrete analog sensor 112
3.29 Blade clearance sensor calibration curve 113
3.30 Diagram of LabView VIs, red dashed lines indicate asynchronous queue communication 115
3.31 Diagram of LabView VI trimming and safety panel 117

4.1 Comparison of VR12 airfoil baseline with 5% trailing edge tab (a) Complete airfoil (b) Trailing edge detail 119
4.2 Blade cross section with labeled components 123
4.3 Foam core and insert machining, (a) Milling leading edge slots for tungsten inserts, (b) Cutting tungsten leading edge masses to length using diamond cutting wheel 124
4.4 Foam core with bonded root insert and tungsten leading edge masses 125
4.5 Blade construction, (a) Completed D-spar joined to aft foam core, (b) Blade wrapped with outer skin and release film in mold 126
4.6 Closed mold in autoclave oven 127
4.7 Blade finish machining, (a) Trimming blade tip with diamond cutoff wheel, (b) Drilling holes for bladegrip bolts 127
4.8 Finished blade dimensions, numbers indicate order of finish machining 128
4.9 Maximum lift offset capability vs. Lock number and flap frequency, reference and reinforced blades marked 130
4.10 Diagram of blade root reinforcement cuff with cross sectional views 132

4.11 Blade cuff construction, (a) Female and male cuff molds, (b) Unfinished blade cuff post-curing 133
4.12 Diagram of blade tip slope experimental setup, pictured are the flap-bending slope w' and associated tip load 136
4.13 Picture of the jig for applying tip loads, combined flap-bending torsion load shown 137
4.14 Results from flap-bending stiffness tests for four blades, (a) Tip slope vs. applied force, (b) Derived flap-beding stiffness vs. applied force 138
4.15 Blade prepared for DIC with stochastic speckle pattern 140
4.16 Overhead view of DIC imaging setup for bench-top structural property validation 142
4.17 DIC Camera arrangement, (a) MIRO M310 camera mounted sideways to maximize blade resolution, (b) Reference image with split-plane calibration plate 143
4.18 DIC measured blade flap-bending deflections at several tip loadings with computational model fits and uncertainty bounds . . 147
4.19 DIC measured blade lag-bending deflections at several tip loadings with computational model fits and uncertainty bounds . . 147
4.20 DIC measured blade torsional deflections at several tip loadings with computational model fits and uncertainty bounds 148
4.21 Reinforced blade distributed structural properties after model fitting 149
4.22 Stabilization diagram for out-of-plane displacements overlaid on Markov parameter power spectrum, x's are accepted modes . . 158
4.23 Diagram of shaker test setup showing synchronization between NI and LaVision hardware 159
4.24 Electrodynamic shaker with sting attachment to load cell and blade 160
4.25 Natural Excitation Technique signals, (a) Raw blade displacements, (b) Output Markov parameters from cross-correlations 161
4.26 ERA extracted mode shapes projected to quarter chord, (a)Raw 1st flap, (b)Projected 1st flap, (c)Raw 1st torsion, (d)Projected 1st torsion 162
4.27 Fanplot of nonlinear beam code natural frequencies with non-rotating frequencies measured using NExT ERA 164
4.28 Mode shapes extracted using NExT ERA of DIC images with nonlinear beam code predictions 165

4.29 Calibration setup for rotating DIC testing 166
4.30 Air excitation DIC experiment, (a) Diagram of excitation, cameras and ITD Markov parameters, (b) Photograph of excitation implementation 168
4.31 Raw flap displacements with uniform interpolation grids . . . 169
4.32 Measured and theoretical 1st flap frequency and damping ratio vs. RPM 172
4.33 Measured and theoretical 1st flap mode shapes, (a) 300 RPM, (b) 600 RPM 173

5.1 Dimensions (m) of rotor system on hover tower 175
5.2 Phase averaged data over one rotor revolution (Tip speed = 190 m/s and $C_T/\sigma = 0.089$) (a) Lower rotor thrust (F_{ZL}), (b) push rod force (F_{PR}) 177
5.3 Coaxial rotor thrust vs. torque balance τ with linear fits for estimating thrust at exactly torque balanced condition 178
5.4 Measured push rod load vs rotor thrust including polynomial fits with 95% confidence intervals 179
5.5 Rotating frame load cell coordinate system (red) and fixed frame coordinate system (blue) 181
5.6 Comparison of coaxial rotor performance data between 153 and 190 m/s tip speeds 183
5.7 Comparison of coaxial rotor performance data from Test 1 and Test 2 conducted six months apart 184
5.8 Effect of torque balance on coaxial rotor hover performance . . 185
5.9 Mean thrust vs. power, measurements with FVM and BEMT predictions of single rotor configurations 187
5.10 Mean thrust vs. power, measurement and FVM and BEMT prediction of the two-bladed coaxial rotor system 188
5.11 Comparison of 2-bladed coaxial rotor performance to, (a) 2-bladed single rotor, (b) 4-bladed single rotor 190
5.12 Power breakdown of 2-bladed coaxial, 2-bladed single, and 4-bladed single rotor systems calculated using the FVM 192
5.13 Performance comparison of two-bladed isolated rotor to upper and lower coaxial rotors with FVM predictions 194
5.14 Performance comparison of two-bladed isolated rotor to upper and lower coaxial rotors with BEMT predictions 195

5.15 Performance comparison of two-bladed isolated rotor to upper and lower coaxial rotors with analytical fit 196
5.16 Thrust sharing between upper and lower coaxial rotors, (a) Torque balanced upper and lower rotor thrust vs. total thrust, (b) Ratio of upper to total thrust vs. torqe balance 198
5.17 Radial variation of coaxial rotor performance, comparison between BEMT and FVM ($C_T/\sigma = 0.084$), (a) Inflow ratio, (b) Thrust 200
5.18 Radial variation of rotor performance, four-bladed isolated and two-bladed coaxial rotors ($C_T/\sigma = 0.084$), (a) Inflow ratio, (b) Thrust 201
5.19 Hover performance vs. collective angle (a) Blade loading (b) Power 204
5.20 Isolated and coaxial upper and lower rotor vibratory hub load amplitudes in hover, ($\theta_0 = 8°$) 205
5.21 Azimuthal variation of isolated and coaxial rotor thrust in hover, blade crossings indicated by dashed lines at $20° + n \times 90°$ . . . 206

6.1 Rotor stand installed in the Glenn L. Martin Wind Tunnel . . 229
6.2 Inter-rotor index angle, ϕ, definition, (upper rotor: red, lower rotor: blue) 231
6.3 Diagram of coaxial rotor trimming procedure 234
6.4 Dimensions (m) of rotor system in the Glenn L. Martin wind tunnel 237
6.5 Variation of shaft tilt angle correction factor with advance ratio and rotor thrust coefficient 237
6.6 Isolated lower rotor performance variation with advance ratio, $LO = 0$ 239
6.7 Coaxial system performance variation with advance ratio, $LO = 0$ 242
6.8 Isolated upper and lower rotor hub loads vs. LO, $\theta_0 = 8°$ . . . 243
6.9 Coaxial upper and lower rotor hub loads vs. LO, $\theta_0 = 8°$ . . . 246
6.10 Coaxial rotor blade loading vs. collective pitch angle at three LO levels ($\mu = 0.5$) 247
6.11 Contour plot of coaxial rotor collective sensitivity vs. LO and μ 247
6.12 (a) Isolated rotors L/D_e variation with Lift Offset (b) Coaxial upper and lower rotor L/D_e variation with lift offset 248
6.13 Ratio of upper to lower rotor thrust vs. advance ratio at three lift offset values ($\theta_0 = 8°$) 250

6.14 Side-view of upper and lower coaxial rotor wake slipstreams at $\mu = 0.2$ and $\mu = 0.3$ 251
6.15 (a) Coaxial system L/D_e variation with lift offset (b) Interpolated contour plot of coaxial system L/D_e variation with lift offset and μ 252
6.16 Coaxial rotor system effective lift-to-drag ratio vs lift offset at 900 and 1200 RPM, $\theta_0 = 6°$ 252
6.17 Azimuthal variation of upper rotor pitch angle colored by advance ratio, μ 254
6.18 Isolated rotors root pitch harmonics normalized by corresponding 1/rev cyclic pitching amplitude (θ^1), $\theta_0 = 8°$, LO=0 (a) Upper rotor (b) Lower rotor 254
6.19 Lower rotor cyclic controls vs. advance ratio and lift offset $\theta_0 = 8°$, (a) θ_{1C} (b) θ_{1S} 255
6.20 Blade clearance vs. LO (a) Raw azimuthal signal($\theta_0 = 8°$, $\mu = 0.53$), (b) Variation of minimum clearance with μ ($\theta_0 = 8°$), (c) Variation of minimum clearance with collective($\theta_0 = 8°$, $\mu = 0.53$), (d) Variation of minimum clearance with tip speed ($\theta_0 = 6°$,$\mu = 0.32$) 257
6.21 Isolated lower rotor vibratory hub load amplitudes, vs. advance ratio ($LO = 0$, $\theta_0 = 8°$) 260
6.22 Isolated lower rotor azimuthal thrust variation (normalized by mean thrust) vs. advance ratio ($LO = 0$, $\theta_0 = 8°$) 261
6.23 Isolated lower rotor vibratory hub load amplitudes vs. LO ($\mu = 0.53$, $\theta_0 = 8°$) 262
6.24 Isolated lower rotor azimuthal thrust variation (normalized by mean thrust) vs. lift offset ($\mu = 0.53$, $\theta_0 = 8°$) 263
6.25 Isolated upper and lower rotor vibratory hub load amplitudes vs. summed coaxial rotor hub loads ($LO = 0$, $\theta_0 = 8°$, $\mu = 0.53$) 264
6.26 C_{MX} azimuthal variation ($LO = 20\%$, $\theta_0 = 6°$, $\mu = 0.32$) (a)Summation of upper and lower rotor C_{MX} ($\phi = 0°$), (b) Coaxial system summed C_{MX} vs. index angle ϕ 266
6.27 Rotor system vibratory hub load amplitudes vs. inter-rotor index angle ($\mu = 0.31$, $\theta_0 = 6°$, $LO = 20\%$) 267
6.28 Variation of two-per-revolution in-plane forces (normalized by C_T^0) with lift offset and index angle ($\mu = 0.31$, $\theta_0 = 6°$), (a) C_X^4, (b) C_Y^4 268

6.29 Variation of four-per-revolution in-plane forces (normalized by C_T^0) with lift offset and index angle ($\mu = 0.31$, $\theta_0 = 6°$), (a) C_X^4, (b) C_Y^4 269
6.30 Variation of two-per-revolution thrust force (normalized by C_T^0) with lift offset and index angle ($\mu = 0.31$, $\theta_0 = 6°$) 269
6.31 Variation of two-per-revolution in plane moments (normalized by $C_T^0 R$) with lift offset and index angle ($\mu = 0.31$, $\theta_0 = 6°$), (a) C_{MX}^2, (b) C_{MY}^2 270
6.32 Azimuthal variation of upper rotor pushrod force colored by advance ratio, μ 270
6.33 1st harmonic pitch link load amplitude variation with lift offset ($\mu = 0.53$, $\theta_0 = 8°$) 271
6.34 Higher harmonic pitch link load variation with lift offset ($\mu = 0.53$, $\theta_0 = 8°$) 273

A.1 Load cell amplifier circuit diagram 284
A.2 Load cell amplifier board layout, (a) Upper, (b) Lower 285
A.3 Digital tip clearance sensor circuit diagram 287
A.4 Digital tip clearance sensor board layout, (a) Upper, (b) Lower 288

Nomenclature

Roman Symbols

A	Disk area, πR^2
a	Lift curve slope
c	Rotor blade chord
c_d	Sectional drag coefficient
C_l	Wing lift coefficient
c_l	Sectional lift coefficient
c_m	Sectional moment coefficient
C_P	Rotor Power Coefficient
C_Q	Rotor Torque Coefficient
C_T	Rotor Thrust Coefficient
C_X	Rotor Drag Force Coefficient
C_Y	Rotor Side Force Coefficient
C_{MX}	Rotor Rolling Moment Coefficient
C_{MY}	Rotor Pitching Moment Coefficient
D_e	Rotor effective drag

E Young's modulus

F_{pr} Pushrod force, positive in tension

G Shear modulus

I Blade flap inertia

I_η, I_ξ Area moments of inertia about η and ξ axes

J Polar moment of inertia

L Rotor lift

LO Lift Offset

m Blade mass per unit length

N_b Number of blades

R Rotor radius

r Nondimensional blade span

U_T Tangential velocity

v Lag bending deflection

V_∞ Free stream velocity

w Flap bending deflection

Greek Symbols

α Blade angle of attack

β Blade flapping angle

χ	Wake skew angle
γ	Lock Number
λ	Inflow ratio
μ	Advance ratio
ν	Poisson's ratio
ν_β	First blade flap frequency nondimensionalized by Ω
Ω	Rotor angular velocity
ω	Excitation frequency
ω_n	Blade natural frequency
ϕ	Inter-rotor index angle
Ψ	Matrix of eigenvectors
ψ	Rotor azimuth angle
ρ	Air density
σ	Rotor solidity $N_b c/(\pi R)$
τ	Rotor torque balance
θ_0	Collective Pitch
θ_{1C}	Longitudinal Cyclic Pitch
θ_{1S}	Lateral Cyclic Pitch
ζ	Damping ratio

$\{\zeta, \eta, \xi\}$ Blade fixed coordinate system

$\{X, Y, Z\}$ Fixed reference frame coordinate system

$\{x, y, z\}$ Rotating hub fixed coordinate system

Superscripts

$()'$ Spatial derivative

$(\overset{*}{\ })$ $(1/\Omega)\partial/\partial t$

$(\dot{\ })$ Time derivative

n n/rev, frequency normalized by Ω

Subscripts

L Lower rotor in coaxial configuration

U Upper rotor in coaxial configuration

Chapter 1

Introduction

1.1 Problem Statement

Coaxial counter-rotating (CCR) rotor systems trace their history back as far as the mid 18th century, to the design of simple elastic and spring powered toys. As progress towards a fully functional rotorcraft continued into the early 1900s, many prototypes continued to use the CCR rotor arrangement as a means of managing rotor torque reactions, as well as for dealing with lift asymmetry in forward flight. The advent of the familiar single main rotor and tail rotor design with cyclic pitch control led to the near wholesale abandonment of the CCR. With the exception of designs by the Russian Kamov Design Bureau, no modern, manned CCR helicopters have seen mass production.

However, in the last decade, there has been a renewed interest in the CCR rotor system paired with auxiliary propulsion as a serious candidate for next-generation helicopter designs. The key driving requirements for these new rotorcraft are high-speed forward flight, increased range, and greater cruise efficiency. Conventional, single main rotor designs are unable to meet the performance targets due largely to the inherent asymmetry of the flow conditions around the rotor disk in forward flight. This asymmetry is most apparent in

the tangential velocity seen by a blade section as it rotates around the rotor disk. Equation 1.1 shows the dependence of tangential velocity, U_T, on blade azimuth angle that increases with forward flight speed. The resulting blade operating conditions are shown in figure 1.1 for a forward flight speed equal to one half the rotor tip speed. On the advancing side of the rotor, with azimuthal angle $\psi < 180°$, the forward flight velocity adds to the rotor angular velocity creating a region of high dynamic pressure. At high speeds this can lead to adverse compressibility effects at the blade tip as the drag divergence Mach number is reached. On the retreating side, $\psi > 180°$, the forward flight speed subtracts from the rotor angular velocity resulting in a large region of reversed flow near the blade root. Outboard of the reversed flow region the retreating blade operates at a low dynamic pressure, reducing the capacity for producing lift on the retreating blade.

$$U_T = \Omega R + V \sin(\psi) \tag{1.1}$$

These inflow conditions result in large vibratory loads and power consumption as well as place hard limits on the ability to trim the helicopter in high-speed forward flight. As flight speeds increase, rotor rolling moments are trimmed by reducing the advancing blade pitch while simultaneously increasing the retreating blade pitch to compensate for the dynamic pressure mismatch. As the reverse flow region grows, the retreating blade angle of attack becomes so large as to induce dynamic stall. The blade undergoing dynamic stall experiences a gross flow separation, resulting in the migration

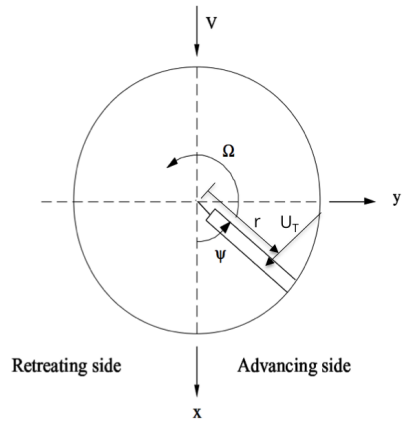

(a) Rotor blade coordinates in forward flight

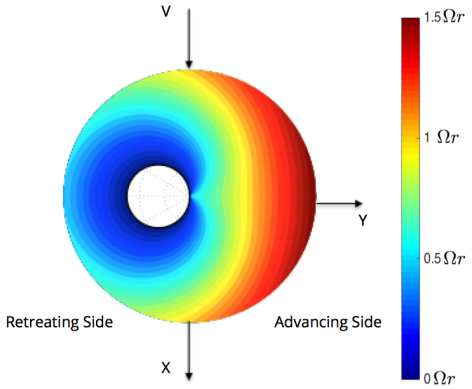

(b) Countours of U_t normalized by tip velocity at $V_\infty/(\Omega R) = 0.5$

Figure 1.1: Blade tangential velocity in forward flight

of the aerodynamic center to the mid-chord, generating large vibratory lift and blade pitching moments. Additionally, the reversed flow region, with the flow traversing from the airfoil trailing to leading edge, produces a large drag penalty. At a high enough advance ratio the retreating blade will no longer produce sufficient lift to balance the advancing blade rolling moment placing a hard limit on the flight speed. These retreating blade effects may be mitigated by increasing rotor speed, Ω, however as the advancing blade tip approaches transonic speeds vibratory loads and high drag once again limit forward flight speed.

In order to overcome the limitations of flow asymmetry in single rotors Sikorsky Aircraft has proposed a closely spaced CCR rotor system with auxiliary propulsion. This design was first introduced as the Advancing Blade Concept (ABC) in the 1970s. It was recently redeveloped as a modern proto-

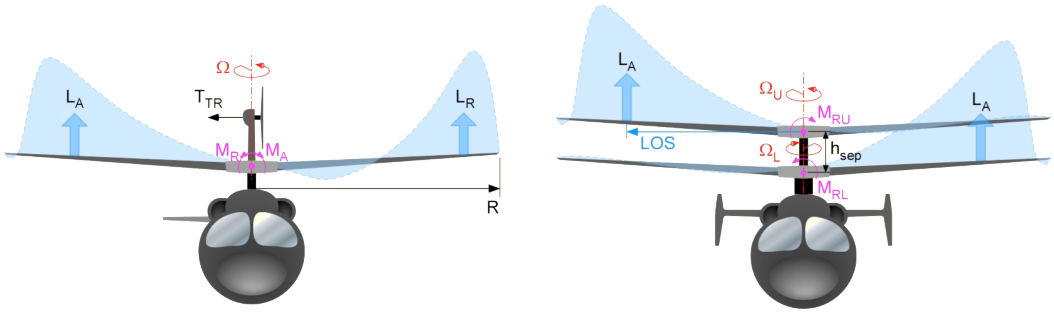

(a) (b)

Figure 1.2: Thrust distribution of trimmed conventional and ABC rotor systems, (a) Conventional, (b) ABC, from Ref. [8]

type, the Sikorsky X2 Technology Demonstrator (X2TD), which achieved 250 knot level flight in 2010 [8]. This exceeds the cruise speed modern, conventional helicopters by 80-100 knots. Key to the success of the ABC helicopter is the close spacing between rotors to reduce hub drag, and the very stiff rotor blades which support significant unbalanced rolling moments on each rotor. As shown in figure 1.2 trimming the upper and lower rotors to opposite rolling moments more fully harnesses the high dynamic pressure environment of the advancing blades while minimizing the drag penalty from the retreating blades operating in significant reversed flow at high forward flight speeds. The untrimmed rolling moments, M_X are described in terms of a non-dimensional lift-offset (LO), which is the rolling moment divided by the product of the mean upper and lower rotor thrust and radius, shown in equation 1.2.

$$LO \equiv \frac{2M_X}{(T_U + T_L)\,R} \tag{1.2}$$

While overcoming inherent limitations of single rotor systems, the CCR design introduces complicated interactional aerodynamics between upper and lower rotors as well as significant vibratory loads which may be affected by the location of rotor blade crossings. The design of these advanced helicopters requires reliable and proven analytical tools of varying fidelities, which must be validated with experimental data. In contrast to the data available for single rotors, there is a noticeable absence of detailed experimental data for rigid, coaxial, counter-rotating rotors.

This dissertation encompasses the design and testing of a model-scaledCCR rotor system in both hover and forward flight. The design of a test stand with instrumentation for measuring individual upper and lower rotor steady and vibratory loads is described along with the data acquisition tools for real time system trimming and safety monitoring. A unique rotor blade and hub design for achieving high flap-bending stiffness is presented. Blade static and dynamic structural properties are measured using operational modal analysis techniques in combination with optical deformation measurements using digital image correlation. The results of hover and wind tunnel tests are presented with a focus on upper-lower rotor interactional aerodynamics, efficiency and vibrational loads.

1.2 State of the Art

The literature review begins with an overview of coaxial rotor system research. Experimental studies and their results are described in §1.2.1.1, with

analytical and computational modeling following in §1.2.1.2. Studies describing non-contact blade deformation measurement techniques are presented in §1.2.2. Finally §1.2.3 describes a variety of operational modal analysis techniques for output-only identification of linear systems.

1.2.1 Coaxial Rotorcraft

1.2.1.1 Experimental Investigations

The comprehensive review of 20$^{\text{th}}$ century coaxial rotor research by Coleman [25] indicated a limited number of experimental data sets on coaxial rotors. Several studies have been performed on CCR systems which lack the rigid hub design and close rotor spacing of the ABC. Harrington [36] performed hover tests on two full-scale coaxial rotors, as well as isolated upper and lower rotors in 1951. Measurement of total system performance was performed at tip speeds between 350 and 500 feet per second at thrust coefficients up to $C_T = 0.0055$. Harrington concluded that differences in coaxial and isolated system performance were attributable solely to solidity effects and that equivalent solidity single rotor blade element theory was adequate for characterizing the performance of the coaxial rotor. Subsequently, Dingeldein [30] performed measurements on the first of the Harrington rotors in hover and in forward flight. The results were compared the performance of a smaller diameter, but equivalent solidity tandem rotor. The forward flight testing revealed the coaxial system consuming up to 14% more power than a theoretical equivalent single rotor in forward flight. The author ascribes the difference to interference

effects between the upper and lower rotors although no mechanism for the efficiency loss is given.

Coleman [25] reports several experimental studies performed by Russian scientists, although details are scarce. Of note are tests investigating the effect of upper-lower rotor blade crossing location on vibrations. Tests were performed on a Kamov Ka-25 coaxial helicopter with widely-spaced, articulated, three-bladed rotors and vertical three-per-revolution vibrations were found to be minimized when upper-lower rotor blade crossing occurred 15° off the aircraft nose. This result did not agree with predictions and Burtsev [19] notes that no explanation for the discrepancy is given. It was also noted that the reduction in vertical vibration was accompanied by a corresponding increase in in-plane vibratory loads.

In 1977 Nagashima [75] carried out experiments on a 0.76 m diameter rotor system. Individual upper and lower rotor loads were acquired over a range of rotor spacings at a tip speed of 120 m/s. Experiments run at combinations of upper and lower rotor collectives demonstrated interference effects between upper and lower rotors, although most of these experiments were not torque balanced. An interesting observation was that the lower rotor had a significant effect on the upper rotor, a phenomenon that had been considered negligible. The authors found an optimum pitch angle separation of $\theta_l = \theta_u + 1.3°$ which maximized system figure of merit. The same rotor system was tested in low speed forward flight ($\mu \leq 0.2$). These tests in the transition between hover and forward flight demonstrated a reduction in the interference

effect as the free stream velocity convects the rotor wakes downstream [102].

The only set of studies focusing on the closely-spaced CCR rotor system which is of interest to this dissertation were performed during the development and testing of the Sikorsky XH-59A demonstrator (Advancing Blade Concept) helicopter in the late 1960's [24]. Reduced-scale (2 ft diameter) rotor tests [24] were performed in hover on both three-bladed isolated rotors and a six-bladed coaxial rotor system (three upper and three lower blades). Total system thrust and power was measured and the six-bladed coaxial rotor was found to outperform theoretical predictions for a six-bladed isolated rotor, although no direct experimental comparison was performed. This system, with Froude-scaled four foot diameter blades, was tested in forward flight, but the lack of cyclic controls limited the operational envelope. Froude-scaled aircraft tests [85] were performed, focusing on complete aircraft control aspects including control surface sizing and aerodynamic derivatives. Full-scale aircraft hover [5] as well as forward-flight tests [33] were also performed. The XH-59A data, while detailed, suffers several drawbacks. Tests were performed on four different systems making direct comparisons to a single computational model difficult. The full-scale forward flight and hover tests focused mainly on integrated aircraft performance and control, not rotor loads, with measurement of 6-axis forces on the aircraft and estimates of rotor power from engine hydraulics, necessitating significant data treatment for comparison with isolated rotor codes. Additionally, these tests do not provide data on the effect of lift offset variation on performance and loads, one of the key characteristics of the

ABC rotor system.

More recently, McAlister and Tung performed hover testing on the 48.9 inch diameter, 1/7 scale AFDD coaxial rotor system [71]. Tests were performed with isolated and coaxial rotors at various spacings and heights above ground. Results included steady thrust and torque measurements as well as flow characterization through PIV. Later work by Ramasamy [89] on the same system included comparisons of coaxial, tandem and equivalent isolated rotor performance. However, these studies were limited to a tip Mach number of 0.23 and low blade loadings for the equivalent isolated rotor performance. Due to the drive system design the upper and lower rotors cannot maintain a fixed phase relationship during operation and, without cyclic controls, no forward flight testing can be performed on the system.

1.2.1.2 Analytical and Computational Studies

A variety of analyses have been performed on rotors operating in the coaxial, counter-rotating configuration, with much of the work occurring quite recently. In general these studies may be divided into three groups based on the level of complexity and the dynamics which appear to be resolved. The first uses simple, actuator disc based momentum theory or combined blade element momentum theory with prescribed wakes and simple structural models to rapidly analyze rotor systems in hover. The next set combines reduced order aerodynamic models, generally vortex filament techniques or similar, with nonlinear beam models for more accurate predictions, especially in forward

flight. Finally, the most detailed studies combine high order computational fluid dynamics flow solvers with either geometrically exact beam structural models or full three-dimensional finite element models to capture high resolution vibratory loads.

Early simulation of coaxial rotor systems was done by employing single rotor blade element models [51] with an equivalent number of blades to the coaxial rotors. While this approach neglects interactional aerodynamic effects Harrington [36] found it sufficient for total system performance prediction in hover. Dingledein [30] however noted that this single rotor theory underpredicted power requirements in forward flight. An attempt to capture the effect of the upper rotor wake impinging on the lower rotor was made during the development of the Sikorsky XH59 in work by Paglino [80]. A blade element model was implemented with the upper rotor experiencing induced inflow equivalent to half the total thrust, while the lower experiences this induced inflow plus the downwash from the upper rotor undeveloped wake (equivalent to operating the rotor with zero separation distance). Paglino reports that modeling this interaction significantly improves correlation with scale model test data.

More recently, Leishman and Syal [65] used momentum theory to develop theoretical ideal performance criteria for thrust and torque balanced coaxial rotors with both zero separation distance, and with the lower rotor operating in the fully developed slipstream of the upper rotor. By comparing these results with the isolated rotors interference factors, describing the

ratio of coaxial to isolated rotor induced power, of 1.26 to 1.42 were derived. Leishman and Ananthan [63,64] developed a coaxial blade element momentum theory with the lower rotor operating in the fully developed slipstream of the upper rotor for axial flight performance prediction. The code was compared to the Harrington rotor experiments [36] as well as a free vortex wake based model and found to satisfactorily predict total system performance. Bagai [8] notes that the initial development of the modern X2 Technology Demonstrator was performed assuming a single coplanar rotor of equivalent solidity to the coaxial system, reflecting the suggestion of Harrington over 50 years earlier. Later work by Xin et al. [108] used a free vortex wake analysis to calculate coefficients for a Pitt and Peters three-state dynamic inflow model [84] allowing for accurate prediction of forward flight performance and steady loads for realtime simulation.

The previous analyses either neglect upper-lower rotor interactions, or model only the interference of the upper rotor on the lower rotor, ignoring the reverse. More realistic performance and load predictions including full interactional effects are achieved using what are commonly referred to in the rotorcraft community as comprehensive analysis codes. One of these codes, CAMRAD-II developed by Johnson [48], has been used extensively for both validation of experiments, as well as preliminary design. Lim et al. [67] correlated the hover performance (mean thrust and torque) measured in the Harrington rotor, the full-scale XH-59A, and the model-scale AFDD rotor tests with further validation performed by Ho et al. [40]. Johnson [49] used CAMRAD-II to investigate

the effect of lift offset on forward flight performance concluding that lift offset ratios of up to 0.30 provide substantial gains in rotor lift to drag ratio at high flight speeds, although the author notes that wind tunnel data is needed to confirm the accuracy of the modeling. Further forward flight investigations with CAMRAD-II include work by Yeo and Johnson [109] investigating the maximum thrust capability of a lift offset rotorcraft, as well as a notional design for a lift offset compounded rotorcraft by Johnson et al. [50]. The second of these publications contains the notable result that, in contrast to hover performance, at high flight speeds the the lower rotor produces more lift than the upper rotor.

Full computational fluid dynamics (CFD) simulations of helicopter rotors have only recently become feasible. The main difficulty lies in designing schemes which capture the highly vortical wake structure without excessive numerical dissipation. A traditional approach involves an unsteady Reynolds Averaged Navier Stokes (RANS) simulation implemented with blade-fixed, structured grids overset on a structured far wake grid. The structured grids allow for high order flux scheme implementation to minimize diffusivity. Lakshminarayan and Baeder [60] used this technique implemented in a code, OVERTURNS, to predict the performance and unsteady loading of a CCR rotor system; the performance data from the Harrington experiments was used for validation. In addition to steady loads, this high resolution CFD analysis was able to predict transient loading due to upper-lower rotor wake interference at the blade passage frequency; although there was no available experimental

data for comparison.

Other high resolution schemes involve solving the vorticity formulation of the Navier Stokes equations directly. Brown et al. [18] coupled unsteady lifting line blade aerodynamics with a semi-Lagrangian grid based CFD solution of the inviscid vorticity-velocity equations, calling it the Vorticity Transport Method. This code was correlated with the Harrington rotor measurements and used to predict individual rotor performance in hover including examining the thrust sharing ratio between rotors [54, 55]. While the use of lifting line theory for blade aerodynamics and neglect of viscous forces makes this VTM treatment more closely related to the previously described vortex-filament methods, the authors note that coupling to a near-field full CFD solution is possible. Indeed, a later study by Rajmohan et al. [87] couples a near-field CFD solver for blade aerodynamics with a Lagrangian vortex particle method for solving the vorticity equation in the far-field wake. Compared to a lifting-line theory coupled solution the authors found an improvement in correlation with the AFDD rotor simulations.

1.2.2 Blade Deformation Measurement

Measuring blade deformations in helicopter rotors is challenging. Traditionally estimates of blade deformation have been obtained by integrating measurements from strain gauges bonded along the rotor blade. There are several limitations to this technique. The first, and most fundamental drawback is the inherently low spatial resolution of the discrete strain gauges creating large

regions of uncertainty in the integrated displacement. In the full scale UH-60 airloads program, a blade was instrumented with flap and chord-wise gauges at nine span-wise stations, with torsion gauges at only three stations [59]. This limitation in full scale tests is exacerbated at the model scale, where gauge sizes are larger relative to the blades under test. For scaled rotor testing the gauge installation and wiring also introduces non-negligible changes to blade structural and aerodynamic characteristics causing harmful blade-to-blade variations between instrumented and uninstrumented blades. Finally these sensors are susceptible to noise as they pass through electrical sliprings, damage during installation and operation, as well as slipring channel count limitations.

Non-invasive techniques for measuring blade deformations with high spatial and temporal resolution are therefore highly desirable. With the advent of digital cameras and powerful computers, several optical deformation measurement methods have been developed since the 1980s. Of these, only three types have seen application to rotor blade deformation measurements.

The first class of techniques involve measurements performed with uniform grids projected onto blades using lasers. During the Higher Harmonic Control Aeroacoustic Rotor Tests, (HART) the pure grid method [101] was used to measure blade deformations at four azimuthal locations [58]. The method compares images of the projected grids on undeformed blade with deformed grids to calculate displacements using registration and tracking. Flap-bending and torsional displacements were captured at 25 points along

the blade span and compared to integrated strain gauge signals. A variation on this projected grid technique, projection moiré interferometry [86], was performed by Fleming and Gorton on a four-bladed, Mach-scaled rotor in the NASA-Langley 14-by 22 foot Subsonic Wind Tunnel [34]. This technique evaluates fringe interference patterns between the deformed projected grid and a computer generated phase shifted grid to calculate full-field out-of-plane displacements. Vertical displacements were calculated with approximately 0.1% rotor radius resolution and 3% uncertainty with spacing in the chord-wise and span-wise directions of 0.25% rotor radius. Later tests were performed on active twist rotor blades by Fleming et al. [35] and on a hovering rotor at several heights in ground effect by Sekula [100]. These projected grid techniques require low ambient light, a single camera, a grid light source and blade surfaces painted matte white for displaying the projected grid.

The second optical method utilizes stereo photogrammetry to track reflective targets placed on the blade. The technique was used during the HART-II tests, a successor to the previously mentioned HART tests. Results reported by Schneider [99] include three dimensional deformations measured at 25 mm diameter targets distributed at 18 spanwise locations along the leading and trailing edge for 36 total measurement stations. Flap, lag and torsion deformations were extracted at 24 azimuthal locations around the rotor disc with estimated accuracy of 0.4mm and 0.5° respectively. The technique was next used for rotor blades during testing of the Smart Material Active Rotor in work reported by Olson et al. and Abrego et al. [4, 76]. Using three chordwise

targets per spanwise station, blade twist angles were measured with accuracy of less than 0.1°. In comparison with the projected grid based techniques, reflective target stereo photogrammetry has the advantage of measuring displacement in all three dimensions instead of out-of-plane motion only, however the reflective targets limit the spatial resolution of the measurements along the blade.

Finally, Sirohi and Lawson [107] used stereoscopic digital image correlation (DIC) to measure the flap-bending and twist of spinning micro-helicopter blades. Stereoscopic DIC uses a pair of cameras to capture undeformed reference images and deformed images of a specimen with a stochastic speckle pattern. Displacements of groups of pixels are calculated for each image pair using cross correlations followed by stereo photogrammetry. The technique combines the full three dimensional displacements of the target based techniques with high spatial resolution of the projection moiré' interferometry. The initial study was later extended to record the operational deflections of very flexible micro-helicopter blades by Sicard and Sirohi with validation performed using laser displacement sensor measurements. [104].

1.2.3 Operational Modal Analysis

The characterization of rotor blade structural dynamic properties is important for ensuring safe operation, as well as for enabling accurate simulations of loads transmitted to the rotorcraft. These dynamic properties vary with rotational speed, as rotor blades experience strong centrifugal, as

well as aerodynamic forces. Traditional experimental modal analysis (EMA) techniques, which identify structural natural frequencies, mode shapes, and damping ratios, require the knowledge of input forcing, as well as structural response. With the previously mentioned optical measurement techniques, the structural response of a rotating blade may be measured, however measurements of the input forcing remain impractical. Operational Modal Analysis (OMA) techniques were created for situations where measuring or applying input forcing is difficult, for example: bridges [83], automobiles and aircraft [37], and wind turbines. With certain assumptions about the characteristics of the unknown input excitation, reliable estimates of the modal characteristics are possible.

Over time a large number of techniques have been formulated, with new techniques extending or combining older techniques, as the framework for their understanding has matured. These techniques are divided into frequency domain (FD) and time domain (TD) based identification schemes, and further divided into two-step methods, which first compute pseudo impulse or frequency response function before modal analysis, and one step methods which work directly with the measured response data. While many OMA techniques exist, only a handful have seen application to rotating structures including wind turbines and helicopters.

The Natural Excitation Technique (NExT), a method for deriving pseudo-impulse response functions from output only data, was first applied to modal identification of a Vertical Axis Wind Turbine [23]. NExT was used with two

time domain modal analysis techniques, Polyreference Time Domain [112] and Eigensystem Realization Algorithm [52], to extract natural frequencies, damping ratios and mode shapes [45,46]. Later work by Ozbek et al. [78] combined target-based stereo photogrammetry with NExT and the Least Squares Complex Exponential method to extract operating modal properties. In later papers the author explores the difficulties associated with wind turbine modal analysis, especially in identifying certain highly damped modes and suggests a modified NExT algorithm for their identification. [77,79].

To date there have been two studies to collect spatially resolved operational data from helicopter rotor blades. The first study, reported by Lundstrom et al. [68], used target stereo photogrammetry to measure deflections of Robinson R44 rotor blades in hover. Operational deflection shape information was extracted using LMS Test.Lab commercial software. These operational deflection shapes represent the response to the rotor forcing and do not necessarily reflect fundamental modal properties. In a later study, Rizo-Patron and Sirohi successfully extracted natural mode shapes, and frequencies from a reference beam as well as a Mach-scaled rotor blade [93]. The Ibrahim Time Domain (ITD) technique [44,81] was used along with DIC displacement measurements to calculate modal properties of the spinning beam and rotor blade. Two interesting features of the study were the excitation, a periodic gust from a compressed air source, as well as a field of view limited to only 30° azimuth. Despite the discontinuous nature of the measurements, and the excitation which was not consistent with the impulse excitation assumed in the

derivation of the ITD, the first three flap-bending mode shapes and natural frequencies were successfully identified.

1.3 Present Approach

The goal of the present research is to perform detailed measurements on a scaled rigid CCR rotor system in hover and forward flight. Specifically the study seeks to fill in noticeable gaps in experimental data available for correlation with high fidelity computational studies. To this end a model-scale, closely spaced rigid CCR rotor system with the capability of measuring individual upper and lower rotor loads is built. A unique hub and blade arrangement, necessary to support the large flap-bending moments encountered in forward flight with lift offset, is developed, characterized using operational modal analysis techniques, and correlated with a numerical structural model. Data from a series of hover and wind tunnel tests is presented. Hover testing focuses on the interference effects between upper and lower rotors, and compares the measurements to results derived from analytical models, as well as from a free vortex wake computational model. Additionally the effect of upper-lower rotor blade passage on vibratory loads, previously only predicted by CFD studies is examined. In forward flight the influence of lift offset on rotor system efficiency as well as vibratory loads is examined. Blade tip clearance data is measured using a custom optical sensor. The reversal of the upper-lower rotor interference effect is explored, while tests conducted at various inter-rotor index angles demonstrate the ability of the designer to tailor

the vibratory loads transmitted to the fixed frame.

1.3.1 Contributions of the Present Research

1. A model-scale, closely spaced, rigid CCR rotor test stand capable of high speed, high lift offset forward flight was designed and constructed. A complete upper and lower rotor control system was designed, including linear servos for high force, precise positioning. Custom instrumentation for measuring individual rotor loads, control loads, control angles and blade tip clearance were built and characterized.

2. Two sets of model-scale rotor blades were constructed. The second set featured a root reinforcement cuff, increasing the flap stiffness from that of a conventional rotor to allow for high lift offset in forward flight. Blade structural properties were estimated using cross-sectional analysis. The stiffness properties were then verified and updated by using non-contact, digital image correlation deflection measurements in response to tip loads. A framework for adjusting the calculated cross-sectional properties using the measured deflections and a linear beam FEM model was created.

3. Blade dynamics, including natural frequencies and mode shapes, were measured using DIC in combination with operational modal analysis techniques. Full-field non-rotating mode shapes and natural frequencies were extracted using the NExT in conjunction with ERA analysis. A modified ITD analysis, with a revised sampling technique, was used to

identify the rotating first flap frequency, damping ratio and mode shape. The results from both stationary and rotational analyses were found to correlate well with a nonlinear beam model.

4. Hover testing revealed the effects of upper and lower rotor interactions in hover. Comparisons were performed with single rotors, using analytical model fits, along with statistical significance tests to compare rotor induced powers. Vibratory hub loads were found to increase in the coaxial rotor system, with the lower rotor exhibiting a strong four-per-revolution thrust load. Primary and secondary peaks in the thrust indicate multiple modes of interaction between the rotors.

5. Forward flight testing demonstrated the beneficial effects of lift offset on rotor system performance, increasing effective lift to drag ratio by up to 50%. A previously unmeasured reversal of the upper lower rotor interference effect from hover to forward flight was observed and found to diminish with lift offset. Trends in coaxial rotor blade tip clearance, important for safety and maneuvering flight, were successfully captured at all four blade crossing locations.

6. Vibratory loads, especially two-per-revolution thrust and four-per-revolution in-plane forces were found to increase with flight speed. The thrust vibratory load was attributed to lift concentration at the rotor leading and trailing edges, using the rotor dynamic properties from rotating modal analysis. Lift offset tended to decrease vibratory loads, except for the

two-per-revolution pitching and rolling moments. Variation of coaxial rotor index angle was used to modify the vibratory loads transmitted to the fixed frame through cancellation of upper and lower rotor loads.

7. Uncertainty analysis and propagation of error techniques, including the allowance for measurement covariance, were employed throughout the testing. Results are presented with 95% confidence intervals.

1.3.2 Organization of the Dissertation

Chapter 1 describes the limitations of the conventional helicopter in high-speed forward flight and the ability of the closely spaced CCR rotor with lift offset to overcome these limitations. The history of coaxial rotor experimental and computational research is presented, highlighting the gap in fidelity between numerical simulations and the available experimental data. Additionally experimental techniques for non-contact measurement of blade deformations, and operational modal analysis as applied to rotorcraft research are explored. The scope and approach of the current study is presented along with the major contributions to the study of CCR rotorcraft.

Chapter 2 contains details of analytical and numerical models used for both design and validation of experiments. The derivation of an actuator disk model is presented and results relating to coaxial rotors are discussed. A higher fidelity blade element model is coupled to the momentum theory and adapted for simulating coaxial rotors. Next a free vortex wake model designed for simulating CCR rotors is introduced. The derivation of a finite

element linear beam model for use with rotating beams is presented and a cross-sectional analysis tool for use with a nonlinear beam structural model is described. Finally statistical and uncertainty analysis tools used throughout the dissertation are introduced.

Chapter 3 presents the design and fabrication of the model-scale CCR rotor test stand with individual upper and lower rotor load cells. The control systems and actuators necessary for forward flight are described, along with a variety of custom instrumentation for measuring loads, control angles, and blade tip clearance.

Chapter 4 details the design and structural validation of the rotor blades. The construction techniques and material properties for both reference and reinforced sets of blades is presented. Static and dynamic deformation measurements, in both the fixed and rotating frames are presented. Modal analysis techniques, including NExT ERA and ITD with modified sampling, are used to extract blade natural frequencies, damping ratios and mode shapes. These results are used to validate the structural properties derived from material properties and blade cross-sectional models.

Chapter 5 describes hover testing of the rotor system. Results include the characterization of upper and lower coaxial rotor interference. Coaxial and isolated rotor systems are compared using momentum theory model fits for extracting the rotor induced and profile power. Additional results include an examination of the rotor pitch angles and an examination of vibratory loads due to aerodynamic interactions.

Chapter 6 describes the wind tunnel testing of the rotor system. The testing focuses on the effects of lift offset on rotor system performance at high advance ratio. Isolated and coaxial rotors are compared and interference effects quantified. The variation of rotor controls and blade tip clearance with lift offset are also reported. Vibratory loads are examined, with an emphasis on the effect of varying the inter-rotor index angle.

Chapter 7 summarizes the primary conclusions of the research and presents recommendations for future avenues of study.

Chapter 2

Analytical Tools

A variety of analytical and computational models and tools were used during the preliminary design of the experiments, as well as for evaluating results. This chapter is broken into three major sections. §2.1 details the three aerodynamic models used for prediction and evaluation of rotor performance in hover, as well as the process used for generating the two-dimensional airfoil tables necessary for these analyses. In §2.2 a linear Euler-Bernoulli beam model with centrifugal stiffening is derived, and a finite element method for solving the model for non-uniform structural properties introduced. Next, an overview is given of a nonlinear beam model, used for more accurate blade modal characterization. The cross-sectional properties required for the nonlinear beam model are defined and a tool for evaluating the integrals over a two-cell, composite beam is described, including a method for robust calculation of laminate mid-plane locations. Finally, §2.3 describes the uncertainty analysis techniques used for characterizing uncertainty in experimental results, as well as for evaluating model fits via linear regression.

2.1 Aerodynamic Models

Three aerodynamic models are presented in order of increasing complexity. First an idealized actuator disk model of a rotor is derived in §2.1.1 resulting in a relationship between rotor thrust and power. This model is used for fitting and comparing experimental data between rotor configurations. The results of an extension of this theory to coaxial rotors are examined. A higher fidelity model, blade element momentum theory (BEMT), which includes two-dimensional airfoil theory with lookup tables is presented in §2.1.2. The model is derived with arbitrary radial free stream inflow velocity and then adapted for estimating the impact of upper-lower coaxial rotor interference effects. The third aerodynamic model, described in §2.1.3, is a free vortex wake model (FVM), which models the inflow due to wake vorticity using discrete trailed and shed vortex filaments. §2.1.4 describes the computational fluid dynamics (CFD) model used for calculation of the two-dimensional airfoil lookup tables used for the BEMT and FVM analyses.

2.1.1 Momentum Theory

The derivation of a momentum theory model establishes an ideal upper bound for rotor efficiency in hover, and provides an opportunity to define non-dimensional quantities used throughout the dissertation. Following the derivation by Leishman [62], consider an actuator disk of radius R which induces a finite velocity v_i on the surrounding air producing thrust, T. Drawing a control volume along the rotor slipstream boundaries define four cross sections

as shown in figure 2.1: A_0-far upstream, A_1-immediately above rotor plane, A_2-immediately below rotor plane and A_3-far downstream. Flow is assumed to be one-dimensional (uniform across the disk), inviscid, incompressible and irrational. Next formulate conservation laws for mass, momentum and energy:

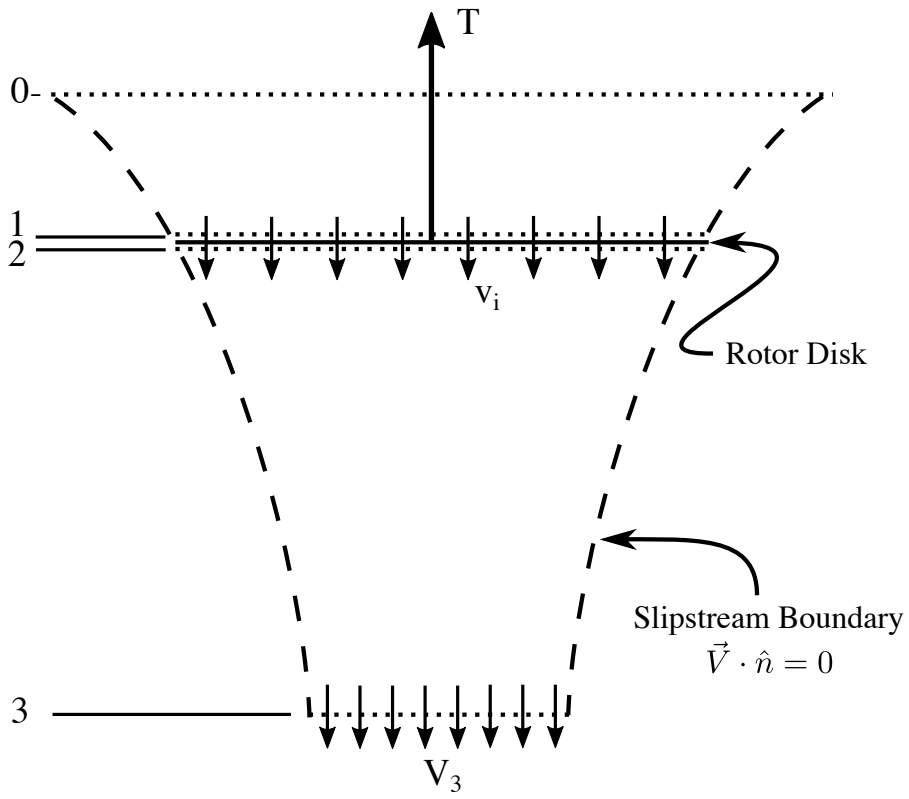

Figure 2.1: Cross section of control volume used for derivation of momentum theory results

$$A_0 V_0 = A_1 V_1 = A_2 V_2 = A_3 V_3 \tag{2.1}$$

$$T = \rho \left(A_3 V_3^2 - A_0 V_0^2 \right) \tag{2.2}$$

$$V_2 T = \rho \left(\frac{A_3 V_3^3}{2} - \frac{A_0 V_0^3}{2} \right) \tag{2.3}$$

With the assumption that far from the rotor, $A_0 \to \infty$ and $V_0 \to 0$ equations 2.1 2.2 and 2.3 may be combined to solve for the slipstream velocity and converged slipstream area:

$$V_2 \left(A_3 V_3^2 \right) = \frac{A_3 V_3^3}{2} \tag{2.4}$$

$$V_3 = 2V_2 \tag{2.5}$$

$$A_3 = \frac{A_2}{2} \tag{2.6}$$

The velocity in the far-wake is twice the velocity at the rotor disk and the ideal slipstream contracts to 1/2 the disk area. Defining the rotor disk area as $A = A_1 = A_2$, the induced velocity ($v_i = V_1 = V_2$) is related to thrust by:

$$v_i = \sqrt{\frac{T}{2\rho A}} \tag{2.7}$$

For a given thrust level the ideal induced power is then:

$$P_i = Tv_i \tag{2.8}$$

$$= \frac{T^{3/2}}{\sqrt{2\rho A}} \tag{2.9}$$

Given the assumptions used in the derivation of this momentum theory the induced power in 2.8 does not include factors such as wake swirl, blade drag, tip-losses and non-uniform inflow. A multiplicative induced power factor κ and a constant profile power P_0, are simple corrections that may be added to account for these terms:

$$P = \kappa \frac{T^{3/2}}{\sqrt{2\rho A}} + P_0 \tag{2.10}$$

κ and P_0 may be estimated analytically, however in this work they are fit to experimental data using linear regressions on measured thrust and power.

2.1.1.1 Nondimensionalization

For ease of comparison between various rotors the above relationships between thrust, power and induced velocity are most often reported in non-dimensional forms defined as follows:

$$\lambda = \frac{v_i}{\Omega R} \tag{2.11}$$

$$C_T = \frac{T}{\rho A \left(\Omega R\right)^2} \tag{2.12}$$

$$C_P = \frac{P}{\rho A \left(\Omega R\right)^3} \tag{2.13}$$

With these definitions of thrust and power coefficients, equation 2.10 relating power to thrust may be rewritten as:

$$C_P = \kappa \frac{C_T^{3/2}}{\sqrt{2}} + C_{P0} \tag{2.14}$$

The above quantities are normalized by rotor disk area, however, it is often more appropriate when comparing two dissimilar rotor systems to normalize by rotor blade area. To this end the rotor solidity, σ, is defined in terms of the number of blades, N_b, and blade chord length, c as:

$$\begin{aligned} \sigma &= \frac{A_{blades}}{A} \\ &= \frac{N_b R c}{\pi R^2} \\ &= \frac{N_b c}{\pi R} \end{aligned} \tag{2.15}$$

Dividing the thrust and power coefficients defined in 2.11 by solidity results in terms C_T/σ and C_P/σ, thrust and power normalized by blade area instead of disk area. C_T/σ is commonly referred to as blade loading while

there is no widely accepted nomenclature for C_P/σ. The equation relating power to thrust may once again be rewritten in terms of these new quantities as:

$$\frac{C_P}{\sigma} = \kappa\sqrt{\sigma}\left(\frac{\left(\frac{C_T}{\sigma}\right)^{3/2}}{\sqrt{2}}\right) + \frac{C_{PO}}{\sigma} \tag{2.16}$$

In 2.16 an additional factor of $\sqrt{\sigma}$ appears in the rotor induced power. Thus when two rotors of differing solidity are operated at equal blade loadings, the rotor with higher solidity incurs higher induced power. This becomes important when making comparisons between coaxial and isolated single rotor systems. Misleading conclusions may be drawn if the effect of rotor solidity is not taken into account.

2.1.1.2 Momentum Theory for Coaxial Rotors

Momentum theory results for coaxial rotors, with the lower rotor operating in the slipstream of the upper rotor, were derived by Leishman and Syal [65] for two different operating configurations. In the first, the upper and lower rotors are separated by an infinitesimal distance and there is no slipstream contraction between rotors. The second condition considers the case where the upper rotor slipstream has fully developed to one-half the rotor disk area before impinging on the lower rotor. For each case the derivation was performed for equal upper and lower rotor thrusts, as well as for equal rotor torques. They defined an induced power factor κ_{int} as the ratio of coaxial system induced power to that of the two rotors operating independently. Their

results are summarized in the the fourth column of table 2.1.

Table 2.1: Coaxial rotor induced power interference factors

Case	Configuration	Trim	$\kappa_{int}(\sigma = 0.5\sigma_{coax})$	$\kappa_{int}(\sigma = \sigma_{coax})$
1	Co-Planar	Equal Thrust	1.414	1.0
2	Co-Planar	Equal Torque	1.414	1.0
3	Fully Developed	Equal Thrust	1.2808	0.906
4	Fully Developed	Equal Torque	1.2810	0.906

Depending on the configuration and trim state, Leishman and Syal report that coaxial rotors consume between 28 and 40% more induced power than the two rotors operating separately. While this seems to imply superiority of the isolated rotors it is important to note that the chosen comparison, with both rotors operating independently, is between rotors of unequal solidity. The isolated rotors have twice the projected disk area as the coaxial rotor, but the same number of blades, and therefore half the solidity per equation 2.15. Considering the leading factor of $\sqrt{\sigma}$ for blade-normalized induced power in equation 2.16, it is clear that at a given blade loading the difference in solidity causes a $\sqrt{2}$ increase in the coaxial rotor system induced power as $\sigma_{coax}/\sigma_{iso} = 2$. If the coaxial rotor is instead compared to an isolated rotor of equivalent solidity and blade loading the induced power interference factor is quite different. As shown in the last column of table 2.1 the induced power for the co-planar configurations is equal to the equivalent solidity isolated rotor while the cases with fully developed wake show a 10% decrease in induced power.

2.1.2 Blade Element Momentum Theory

While momentum theory provides insights into the theoretical or ideal behavior of rotor systems, more advanced tools are needed to generate realistic performance predictions given non-ideal effects such as blade drag and non-uniform inflow. BEMT combines results from two-dimensional blade aerodynamics with momentum theory to solve for the non-uniform inflow distribution across the rotor disk. BEMT codes may achieve good correlation with single rotor performance in hover when the basic model is extended to include airfoil lookup tables and tip loss effects. For this study a BEMT model with provisions for radially varying inflow was derived and extended to model the coaxial system with the upper rotor wake impinging on the lower rotor.

2.1.2.1 Derivation of BEMT Model

The derivation of the BEMT model closely follows that of Leishman [62] which may be consulted for additional details. The model presented is modified to include arbitrary radial variation of the externally imposed axial inflow, as well as lookup table based aerodynamics for airfoil lift and drag.

Consider a thin annulus, shown in figure 2.2, around the rotor disk at a radius r with induced inflow velocity $v_i(r)$ and imposed axial velocity $V_{ax}(r)$. From momentum theory the incremental thrust produced by this annulus is:

$$dC_T = 4(\lambda_{ax} + \lambda_i)\lambda_i r dr \tag{2.17}$$

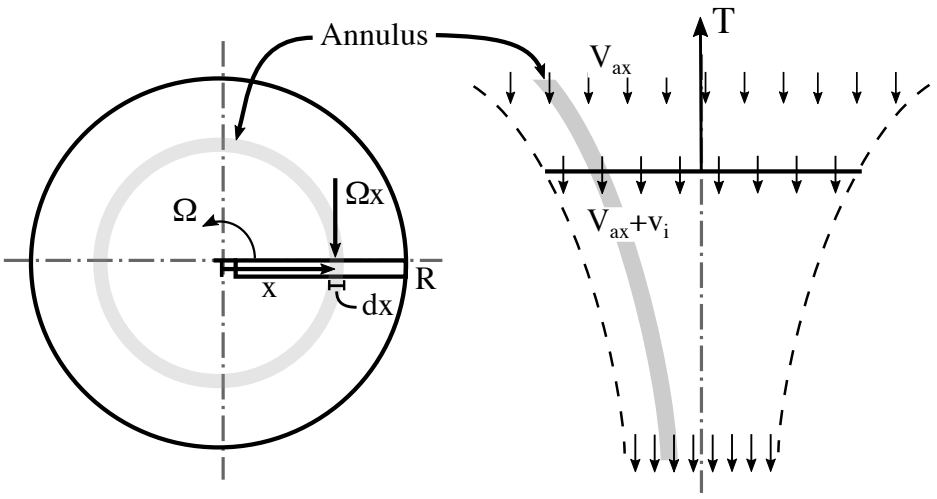

Figure 2.2: Rotor disk and cross sectional view of annulus used for BEMT calculations

The blade section at this radial station sees a relative inflow velocity composed of the rotational velocity and the inflow velocities as shown in figure 2.3. With a lookup table for the airfoil lift and drag coefficients as a function of angle of attack, α, the sectional lift and incremental thrust produced are:

$$dL = \frac{1}{2}\rho V^2 c\, C_l(\alpha) dx \tag{2.18}$$

$$dD = \frac{1}{2}\rho V^2 c\, C_d(\alpha) dx \tag{2.19}$$

$$dF_z = dL\cos\phi - dD\sin\phi \tag{2.20}$$

With the assumptions that the inflow velocity is small relative to the rotational velocity:

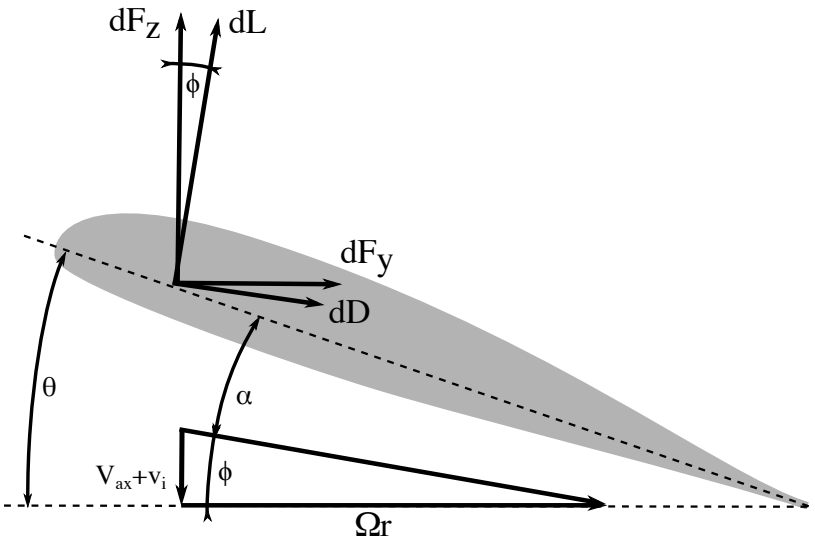

Figure 2.3: Blade sectional geometry at rotor radius x with inflow from axial and induced velocities

$$V \approx \Omega r \tag{2.21}$$

$$\cos\phi \approx 1 \gg \sin\phi \approx \phi \tag{2.22}$$

$$dC_T = \frac{1}{2}\sigma C_l(\alpha) r^2 dr \tag{2.23}$$

Equating 2.23 and 2.17 and solving for the unknown total inflow ratio, $\lambda = \lambda_{ax} + \lambda_i$:

$$\frac{1}{2}\sigma C_l(\alpha) r^2 = 4\lambda(\lambda - \lambda_{ax})r \tag{2.24}$$

$$\lambda = \frac{\lambda_{ax} \pm \sqrt{\lambda_{ax}^2 + \frac{\sigma r}{2} C_l(\alpha)}}{2} \tag{2.25}$$

Additionally the Prandtl tip loss correction factor, F, is added to equation 2.25 to account for the loss of thrust near the blade tip by modifying the inflow:

$$\lambda = \frac{\lambda_{ax} \pm \sqrt{\lambda_{ax}^2 + \frac{\sigma r}{2F} C_l(\alpha)}}{2} \tag{2.26}$$

$$F = \frac{2}{\pi} \arccos -f \tag{2.27}$$

$$f = \frac{N_b}{2} \frac{(1-r)}{r \sin\phi} \tag{2.28}$$

Equation 2.26 must be solved iteratively as both the tip loss factor and the angle of attack are functions of ϕ, which is itself a function of the inflow ratio:

$$\alpha = \theta - \phi \tag{2.29}$$

$$\alpha = \theta - \arctan\left(\frac{V_{ax} + v_i}{\Omega r}\right) \tag{2.30}$$

$$\alpha \approx \theta - \frac{\lambda}{r} \tag{2.31}$$

To solve for the rotor thrust and power the rotor blade is discretized along the radius and at each radial location the unknown inflow solved for using the local blade pitch $\theta(r)$, axial inflow $\lambda_{ax}(r)$, and airfoil lookup table. With the inflow at all radial stations determined the system thrust and torque are then determined by integrating the exact expressions for dC_T and dC_P:

$$C_T = \int_{r_0}^{1} dC_T dr = \int_{r_0}^{1} \frac{1}{2}\left[\sigma C_l(\alpha)\cos\phi - \sigma C_d(\alpha)\sin\phi\right] r^2 dr \tag{2.32}$$

$$C_P = \int_{r_0}^{1} dC_P dr = \int_{r_0}^{1} \frac{1}{2}\left[\sigma C_l(\alpha)\sin\phi + \sigma C_d(\alpha)\cos\phi\right] r^2 dr \tag{2.33}$$

The numerical implementation allows for the code to model arbitrary spanwise variation of blade properties including chord, twist, and airfoil section. Figures 2.4 a-d show the spanwise variation of inflow ratio, angle of attack, dC_T and dC_P respectively for three rotors at $C_T = 0.010$. The BEMT captures the non-uniform inflow across the rotor disk and shows how the addition of twist and taper tends to produce a more uniform thrust distribution. The ability to model these effects makes the code very useful for preliminary rotor design.

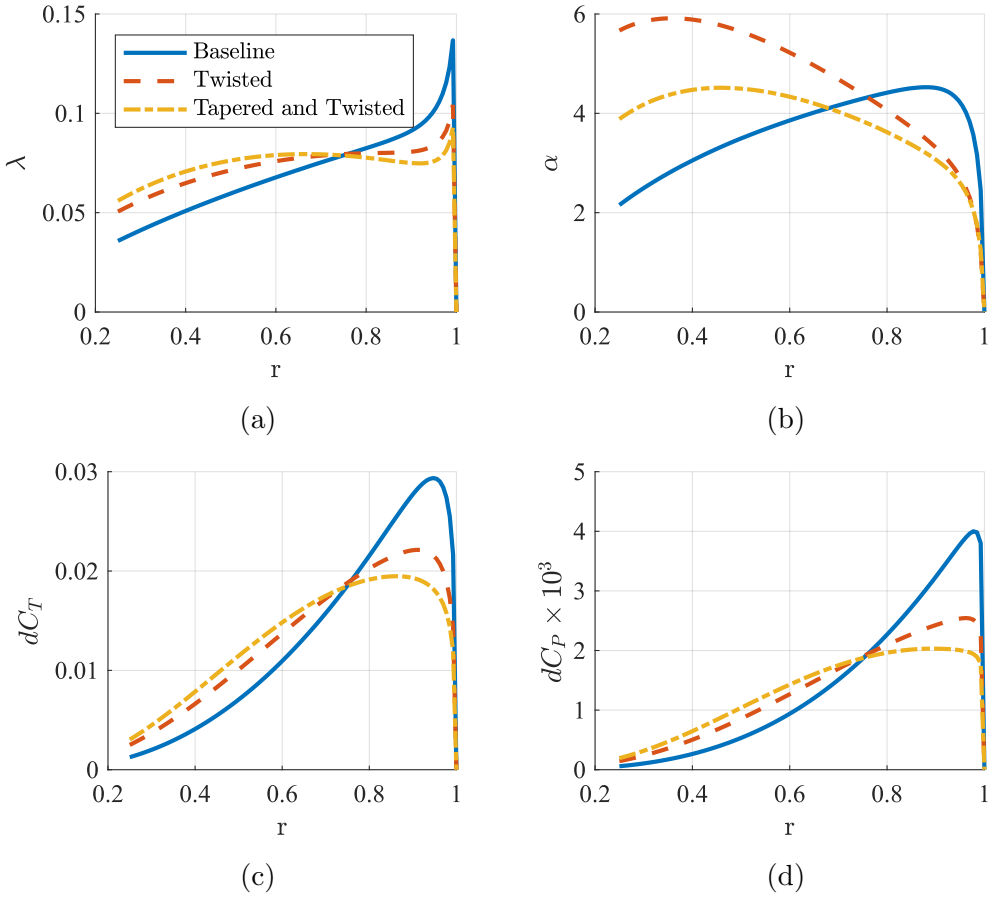

Figure 2.4: Blade element momentum theory predictions for three rotors at $C_T = 0.010$: untwisted and un-tapered, $-10°$ linear twist, $-10°$ linear twist with 2:1 root-tip taper

2.1.2.2 Coaxial Interference Implementation

With the single rotor model formulated for arbitrary radial variation of axial inflow, the extension of the BEMT code to the coaxial case is trivial. Consider the coaxial rotor system shown in figure 2.5. With the assumption that the upper rotor wake has contracted to a radius $r_{wake} = a\,R$ by the time it encounters the lower rotor, the axial inflow experienced by the lower rotor is:

$$V_{ax} = \begin{cases} \frac{(w_u)(r_u = r_l/a)}{a^2} & r_l \leq aR \\ 0 & r_l > aR \end{cases} \tag{2.34}$$

$$w_u = V_{ax} + v_{i,upper} \tag{2.35}$$

Following the method proposed in [64], the upper rotor inflow is mapped from radius r to ar and scaled by $1/a^2$ to enforce mass conservation. The upper rotor wake decreases lower rotor angle of attack, concentrating lift production at the blade tips. The rotor system is trimmed by first solving for the upper rotor wake at a target collective value. Next the lower rotor collective is varied until each rotor consumes equal power.

2.1.3 Free Vortex Wake Model

Where BEMT calculates non-uniform inflow conditions by coupling momentum and blade element theories, FVM [9] explicitly models the vorticity

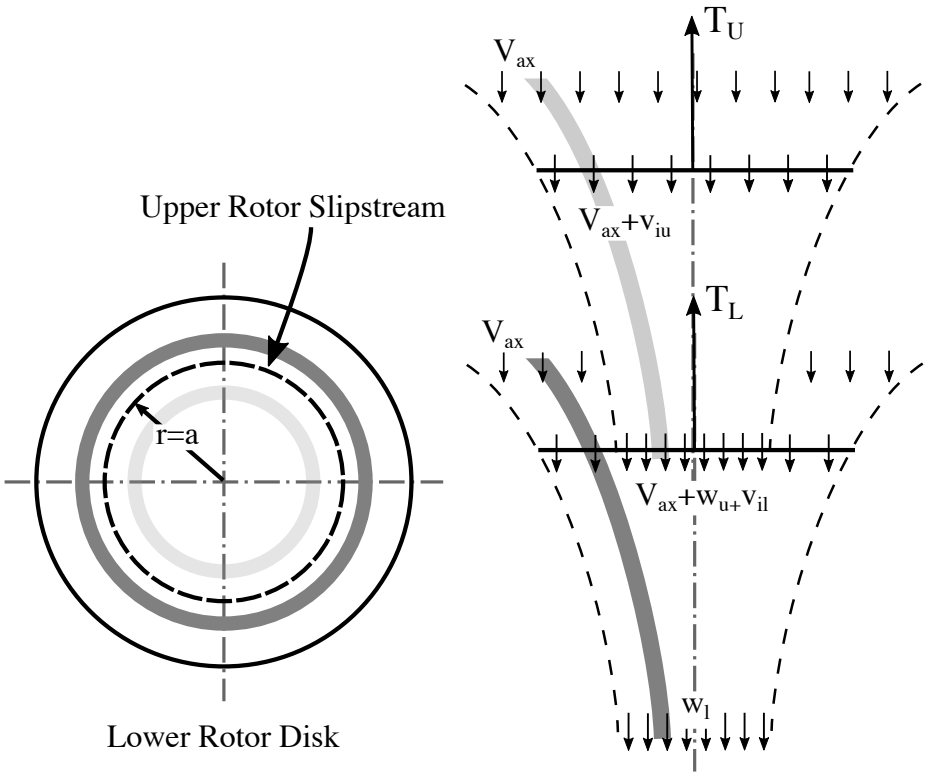

Figure 2.5: Coaxial rotor wake geometry showing contracted upper rotor wake interference with lower rotor

dominated rotor wake dynamics. The wake is modeled as discrete vortex filaments, trailed and shed from the rotor blades. The induced velocities of the filaments on one another are calculated and used to evolve the wake. A panel method is used to calculate the blade-bound circulation and two-dimensional airfoil lookup tables used to calculate lift and drag. Both explicit time-stepping, as well as implicit relaxation based schemes may be used to calculate the wake evolution. Relaxation based techniques assume periodic structure and converge to a steady state result, while time-marching techniques allow for the modeling of unsteady flight conditions including maneuvering flight [14, 16].

The current code is implemented with a fourth order Runge-Kutta time marching method. Figure 2.6 shows a diagram of the wake structure. At each time step wake elements are generated behind the rotor blade. In the near-wake there is trailed vorticity caused by spanwise blade circulation variation and shed vorticity due to temporal circulation variation. The near-wake is consolidated into far wake tip and root vortices after a set number of time steps while the vortex core radii are evolved using a model for viscous diffusion derived from experimental measurements and filament strain [15, 90, 110].

In the coaxial configuration induced velocities are calculated between both rotor wakes and blades. Trim is achieved similar to the BEMT procedure, with the upper rotor collective held fixed and the lower rotor varied until torque balance is achieved. With the explicit time stepping, several rotor revolutions must be simulated before the solution converges. Additional details of the

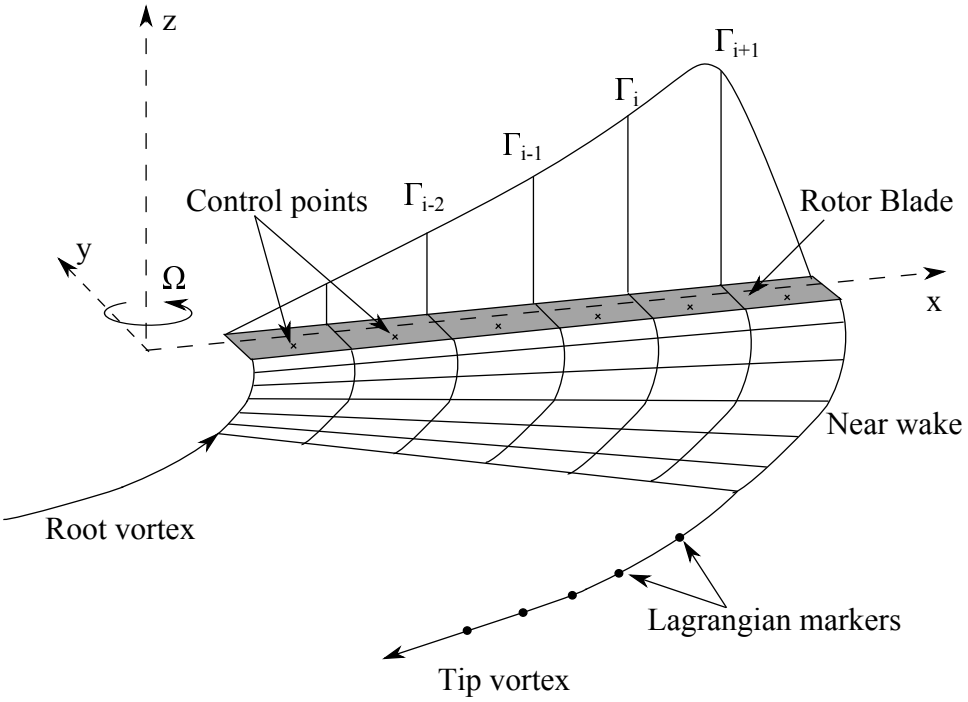

Figure 2.6: Coaxial rotor wake geometry showing contracted upper rotor wake interference with lower rotor

implementation are available in the dissertation by Karpatne [53]. The FVM has advantages over the BEMT including the ability to simulate conditions such as forward flight, descending flight, and maneuvering flight. It also more accurately models diffusion processes in the wake.

2.1.4 Airfoil Tables

Both the BEMT and FVM rely on two-dimensional airfoil lookup tables for calculating lift and drag. As no experimental data was available for the VR-12 airfoil with trailing edge tab, the 2-D sectional airfoil lift/drag data was obtained using a 2-D, incompressible, steady-state simulation run in Fluent, at a Reynolds Number of around 800,000, corresponding to the 3/4 radius location. A structured, quadrilateral mesh with 59,000 elements was generated, with the farfield boundaries ≈15 chord lengths from the airfoil in all directions. The airfoil surface roughness length, 25micron, is used to modify the shear stress calculations at the airfoil wall boundary. The resulting aerodynamic coefficients are shown in figures 2.7 and 2.8.

2.2 Structural Models

This section describes two structural models which were used during the design and evaluation of the rotor blades. The first is a linear Euler-Bernoulli beam model derived for flap-bending motion of the beam in the rotating frame presented in §2.2.1. This model was used for preliminary design evaluation, primarily for evaluating the rotating frame first flap frequency. §2.2.2 presents

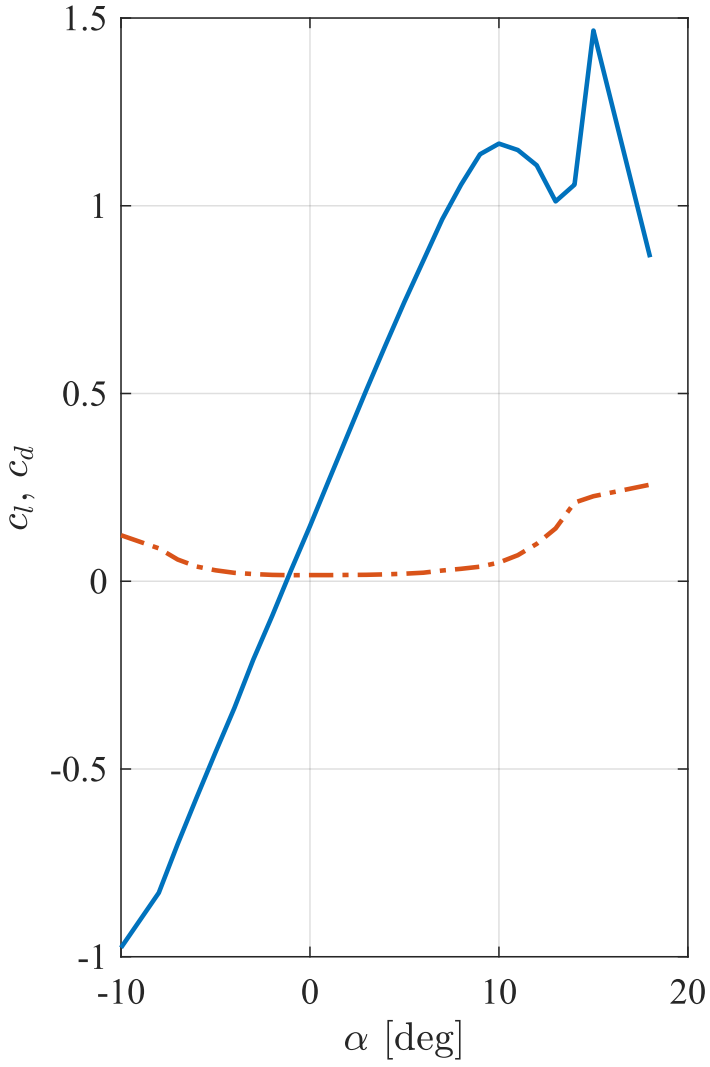

Figure 2.7: Coaxial rotor wake geometry showing contracted upper rotor wake interference with lower rotor

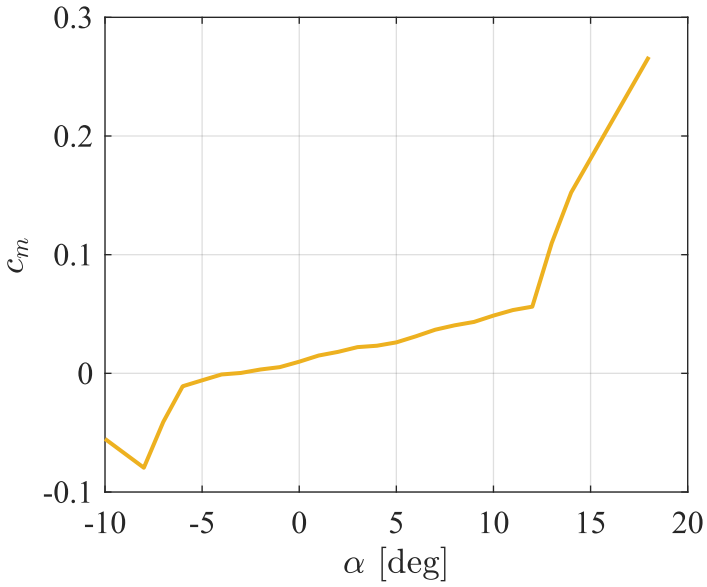

Figure 2.8: Coaxial rotor wake geometry showing contracted upper rotor wake interference with lower rotor

an overview of a nonlinear beam model, which was used for correlation with experimental modal analysis of flap, lag and torsional modes. Both models require the evaluation of certain cross-sectional mass and stiffness properties. A tool for evaluating these integrals on the VR-12 airfoil cross section with arbitrary composite material layups is presented in §2.2.3.

2.2.1 Linear Beam Model

The linear beam model is derived using the Extended Hamilton's Principle. Euler-Bernoulli beam theory assumptions are employed. As such the rotation of a differential beam element is negligible compared to it's translation, and the shear distortion is small relative to the bending deformation.

These assumptions allow for the rotational inertia and shear deformations to be ignored in the kinetic and potential energies. Figure 2.9 shows the beam under consideration. The beam has a root cutout radius e with a torsional spring k_e for modeling compliance in the blade root attachment. The beam bending stiffness, EI, and mass per unit length, m, are allowed to vary arbitrarily over the span. The beam rotates at a constant angular velocity Ω about the z-axis and a spanwise varying forcing f_{ext} is assumed.

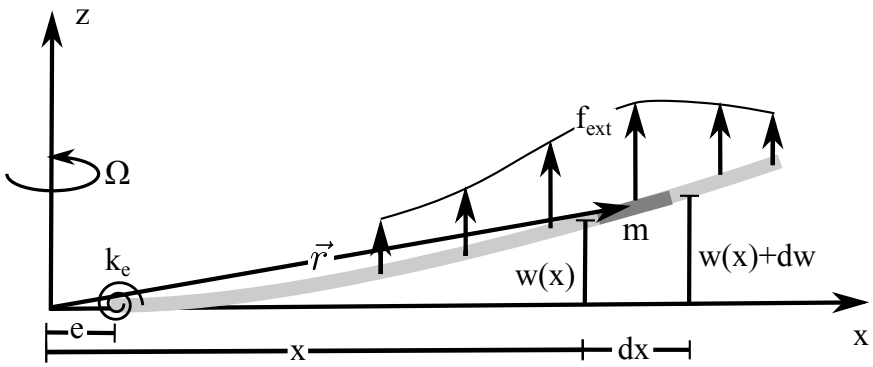

Figure 2.9: Diagram of the linear beam model with coordinate system and displacements, external forcing, and root torsional spring

The Extended Hamilton's Principle [72], provides a framework for deriving the equations of motion and boundary conditions for a dynamic system, using the calculus of variations. The principle states that the evolution of a dynamic system with generalized coordinates, $q_i(t)$ and velocities $\dot{q}_i(t)$, may be found by equating the variation of the action functional equal to zero:

$$S[\vec{q}] \equiv \int_{t1}^{t2} L\left(\vec{q}, \dot{\vec{q}}, t\right) dt \tag{2.36}$$

$$\frac{\delta S}{\delta \vec{q}(t)} = 0 \tag{2.37}$$

Where the system Lagrangian L is equal to the kinetic energy, minus the potential energy, plus non-conservative work :

$$\int_{t1}^{t2} \left(\delta T - \delta V + \delta \bar{W}_{NC}\right) dt = 0 \tag{2.38}$$

The system potential energy arises from strain energy in the blade due to bending deformation as well as energy stored in the root spring. Using the superscript $'$ to indicate spatial partial derivatives with respect to x:

$$V = \int_e^R EI(x) \frac{w''^2}{2} dx + \frac{1}{2} k_e w'^2 \Big|_{x=e} \tag{2.39}$$

The non-conservative work arises form the distributed forcing f_{ext} as:

$$\bar{W}_{NC} = \int_e^R f_{ext}\, w\, dx \tag{2.40}$$

Finally the kinetic energy is derived by first considering the position vector of a differential beam element:

$$\vec{r} = (x - u)\hat{i} + w\hat{j} \tag{2.41}$$

Here u is kinematic foreshortening due to the blade flapping motion as the blade is modeled as inextensible. To derive u consider the diagram in figure 2.10, a close-in view of the differential beam element from figure 2.9. From the displacements shown the differential foreshortening may be related to the differential flap displacement as:

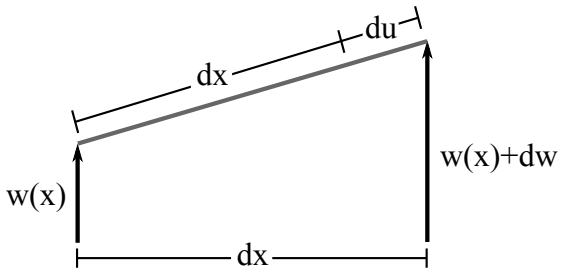

Figure 2.10: Detail view of the differential beam element including the kinematic foreshortening, du

$$(dx + du)^2 = dx^2 + dw^2 \tag{2.42}$$

$$dw = \frac{dw}{dx}dx = w'dx \tag{2.43}$$

$$dx + du = dx\sqrt{1 + w'^2} \tag{2.44}$$

$$du = dx\left(\sqrt{1 + w'^2} - 1\right) \tag{2.45}$$

For small flap-bending slopes, w', the equation above may be expanded and simplified as:

$$du = \frac{w'^2}{2}dx \tag{2.46}$$

The foreshortening at a location x is then obtained by integration:

$$u = \int_e^x \frac{w'^2}{2} d\xi \tag{2.47}$$

Returning to equation 2.41 and taking the derivative with respect to time:

$$\dot{\vec{r}} = (x - u)\Omega\hat{j} + \dot{w}\hat{k} \tag{2.48}$$

The kinetic energy of the system may then be written as:

$$T = \frac{1}{2}\int_e^R m\,\dot{\vec{r}} \cdot \dot{\vec{r}}\, dx \tag{2.49}$$

$$T = \frac{1}{2}\int_e^R m\,\left((x-u)^2\Omega^2 + \dot{w}^2\right) \tag{2.50}$$

$$T \approx \frac{1}{2}\int_e^R m\,\left(\Omega^2(x^2 - 2xu)) + \dot{w}^2\right) \tag{2.51}$$

In equation 2.51 the second order foreshortening term, u^2, is neglected. The expressions for the kinetic energy, potential energy and virtual work are then substituted into equation 2.38, the variation taken, and, after several integrations by parts, the equations of motion and boundary conditions are recovered as:

$$m\ddot{w} + \left[\left(\Omega^2 \int_x^R m\,\xi\,d\xi\right) w'\right]' + (EI(x)w'')'' = f_{ext} \tag{2.52}$$
$$w|_{x=e} = 0\,,\ EIw'' = k_e w'|_{x=e}$$
$$w''|_{x=R} = 0\,,\ w'''|_{x=R} = 0$$

In order to solve the above equations for arbitrary spanwise stiffness and mass distributions a Galerkin finite element approach is taken. The partial differential equation, 2.52, is cast into weak form, multiplying by a test function $v(x,t)$ and integrated by parts to yield the symmetric form:

$$\int_e^R \left(m\ddot{w}v + \left[\Omega^2 \int_x^R m\,\xi\,d\xi\,w'\,v'\right] + EI(x)w''\,v''\right) dx = \int_e^R f_{ext} v dx \tag{2.53}$$

The domain $e < x < R$ is discretized into several subdomains called elements. The trial functions $w(x,t)$ are chosen to be the summation of the products of time varying coefficients and spatially varying shape functions defined with compact support over an element. The test functions $v(x)$ are the set of spatial shape functions used in constructing $w(x,t)$. In discretizing the domain, the integration over the entire domain becomes a summation of integrals over the elements.

$$\begin{aligned} w(x,t) &= \sum_{i=1}^{n} a_i(t)\phi_i(x) \\ v(x) &= \phi_j(x) | 1 \le j \le n \end{aligned} \tag{2.54}$$

To enforce continuity of beam displacement and slope the shape functions are chosen as Hermite cubic polynomials. The polynomials are derived on a master element on which all calculations are performed. A given element $x_1 \leq x \leq x_1 + h_e$ is mapped to $-1 \leq \zeta \leq 1$ in the master element. Equation 2.55 shows the equations for the four Hermite cubic functions, with h_e equal to the original element width. The functions H_1 enforce continuity of displacement w, while the H_2 elements enforce continuity of slope w'.

$$\begin{aligned} \phi_1 = H_1^0 &= \frac{1}{4}\left(2 - 3\zeta + \zeta^3\right) \\ \phi_2 = H_2^0 &= \frac{1}{4}\left(1 - \zeta - \zeta^2 + \zeta^3\right) \\ \phi_3 = H_1^1 &= \frac{1}{4}\left(2 + 3\zeta - \zeta^3\right) \\ \phi_4 = H_2^1 &= \frac{1}{4}\left(-1 - \zeta + \zeta^2 + \zeta^3\right) \end{aligned} \tag{2.55}$$

Substituting the discrete shape functions into the weak form 2.53 and evaluating the integrals with a Gaussian quadrature rule, a set of linear ordinary differential equations in $a(t)$ is recovered:

$$\begin{bmatrix} m_{11} & m_{12} & \dots \\ m_{21} & m_{22} & \ddots \\ \vdots & \ddots & \ddots \end{bmatrix} \begin{Bmatrix} \ddot{a}_1 \\ \ddot{a}_2 \\ \vdots \end{Bmatrix} + \begin{bmatrix} k_{11} & k_{12} & \dots \\ k_{21} & k_{22} & \ddots \\ \vdots & \ddots & \ddots \end{bmatrix} \begin{Bmatrix} a_1 \\ a_2 \\ \vdots \end{Bmatrix} = \begin{Bmatrix} F_1 \\ F_2 \\ \vdots \end{Bmatrix} \tag{2.56}$$

$$m_{ij} = \int m\phi_i\phi_j \, dx \tag{2.57}$$

$$k_{ij} = \int \left(EI\phi_i\phi_j + \left[\Omega^2 \int_x^R m\,\xi \, d\xi \right] \phi_i'\phi_j' \right) dx \tag{2.58}$$

$$f_j = \int f\phi_j \, dx \tag{2.59}$$

Substituting for the time varying terms as $a_i(t) = e^{i\lambda t}$ and considering the homogeneous solution, the eigenvalue problem for the beam natural frequencies and mode shapes is recovered:

$$-\lambda^2 \left[M\right] \left\{a\right\} + \left[K\right] \left\{a\right\} = \left\{0\right\} \tag{2.60}$$

The linear beam model was used for rapidly evaluating candidate blade stiffness and mass distributions in an effort to meet a target rotating flap-bending frequency. The model was also used to update theoretical spanwise stiffness distributions by comparison with distributed deformation measurements of a prototype blade under static tip loading.

2.2.2 Nonlinear Beam Model

The nonlinear beam model used in this paper was created by Sicard [105] to modelthe dynamics of extremely flexible micro-aerial vehicle rotor blades. The model follows the derivation by Hodges and Dowell [41] using the extended Hamilton's principle along with assumptions of small strains and finite displacements. The ordering scheme for the model was chosen to

Table 2.2: Ordering scheme for nonlinear beam model

element	order
$\theta_0, \theta, \frac{x}{R}, \frac{\delta}{\delta x}, \frac{\delta}{\delta t}$	$\mathcal{O}(1)$
$\frac{v}{R}, \frac{w}{R}, \frac{\eta}{R}, \frac{\xi}{R}, \frac{c}{R}$	$\mathcal{O}(\epsilon)$
$\frac{u}{R}$	$\mathcal{O}(\epsilon^2)$

capture the large twist deformations observed in the extremely flexible rotor blades and is shown in table 2.2. The blade elastic twist is $\mathcal{O}(1)$, the elastic bending deformations are $\mathcal{O}(\epsilon)$ and extensional deformation $\mathcal{O}(\epsilon^2)$. Details of the derivation along with physical insight into several of the terms that arise including the trapeze effect and determination of the shear center for extremely flexible blades are presented in [103].

The resulting equations of motion are solved using 14 degree of freedom beam finite elements. The flap and lag-bending degrees of freedom are represented by Hermite cubic polynomials, while the extensional and torsional degrees of freedom are modeled by quadratic Lagrange polynomials. The solution procedure is initialized by finding the system equilibrium position using a Newton-Raphson iteration scheme. Once the equilibrium position is found the system is linearized and then modal and stability analyses may be performed. The current study used this nonlinear code for more accurate mode shape and natural frequency estimation than the linear beam model. This was important for comparison with experimentally measured modal charactersitics, especially at higher frequencies.

Table 2.3: Nonlinear beam model elastic cross-sectional constants

$\iint_A E\, d\eta d\xi = EA$	$\iint_A E\eta^2\, d\eta d\xi = EI_\eta$	$\iint_A E\left(\eta^2 + xi^2\right)^2\, d\eta d\xi = B_1$
$\iint_A \eta\, d\eta d\xi = A\, e_\eta$	$\iint_A E\xi^2\, d\eta d\xi = EI_\xi$	$\iint_A E\eta\left(\eta^2 + xi^2\right)\, d\eta d\xi = B_2$
$\iint_A \xi\, d\eta d\xi = A\, e_\xi$	$\iint_A E\xi\eta\, d\eta d\xi = EI_{\eta\xi}$	$\iint_A E\xi\left(\eta^2 + xi^2\right)^2\, d\eta d\xi = B_3$
$\iint_A G\left(\eta^2 + \xi^2\right)\, d\eta d\xi = GJ = G\, A\, k_A^2$		

Table 2.4: Nonlinear beam model inertial cross-sectional constants

$\iint_A \rho\, d\eta d\xi = m_0$	$\iint_A \rho\eta^2\, d\eta d\xi = m_0 k_{m\xi}^2$	$\iint_A \rho\left(\eta^2 + xi^2\right)\, d\eta d\xi = m_0 k_m^2$
$\iint_A \rho\eta\, d\eta d\xi = m_0\, d_\eta$	$\iint_A \rho\xi^2\, d\eta d\xi = m_0 k_{m\eta}^2$	
$\iint_A \rho\xi\, d\eta d\xi = m_0\, d_\xi$	$\iint_A \rho\xi\eta\, d\eta d\xi = m_0 k_{m\xi\eta}^2$	

2.2.3 Cross Section Analysis

Beam analyses operate by separating a three-dimensional structural dynamics problem into a one-dimensional problem along the beam span and a series of two-dimensional problems at each beam cross section. This cross-sectional analysis involves computing various integrals over the cross section to determine mass and stiffness properties. For the linear beam model the required cross section properties are simply the bending stiffness EI and the mass per unit length m. For the nonlinear beam model the required integrals for the elastic and inertial properties are given in tables 2.3 and 2.4.

For the rotor blades considered in [103] these integrals were calculated analytically, as there was only a single material and a simple cross sectional shape such as a circular arc. In the current study the rotor blade cross section, shown in figure 2.11 is composed of several different materials, with geometry that is not defined in terms of closed form functions. As a result the integrals must be calculated computationally. A code was developed which evaluates the integrals for each cross-section component individually. The airfoil outer profile geometry is input, then the laminate mid-planes, and foam core outer envelopes are calculated using a level set method described in 2.2.3.2. The integrals are then computed, with line integral approximations for the thin composite laminates:

$$\iint_A f(\eta, \xi)\, d\eta d\xi \approx \int_S t\, f(S)\, dS \tag{2.61}$$

Here S is a parameterization of a curve through the laminate midplane and t is the laminate thickness. For use with the nonlinear beam code, reference elastic and shear moduli are defined, and equivalent area integrals for the complete structure calculated. For example consider the flap-bending area moment of inertia I_η for a blade with n components.

$$I_\eta = \frac{1}{E_{ref}} \sum_{i=1}^{n} E_i]\, I_{\eta,i} \tag{2.62}$$

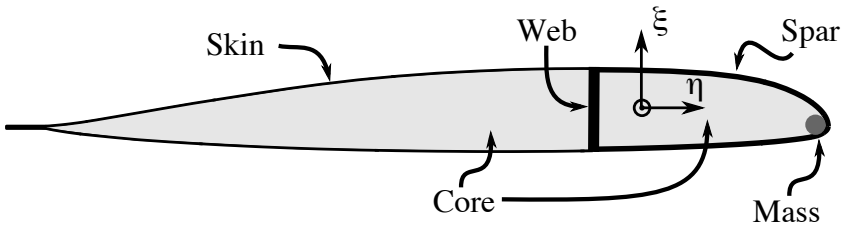

Figure 2.11: Blade cross section with labeled components

2.2.3.1 Composite Materials

In order to calculate the integrals for the composite laminates, the elastic properties must be known. The required properties are: longitudinal and transverse elastic moduli (E_{11}, E_{22}), major Poisson's ratio (ν_{12}), and in-plane shear modulus (G_{12}). Individual lamina elastic properties are obtained from experimental measurements when available, or approximated via the rule of mixtures [28]. For the rule of mixtures, first the fiber and resin volume fractions (v_r and v_f) are calculated from manufacturer supplied mass fractions as:

$$v_f = \frac{\frac{m_f}{rho_f}}{\frac{m_f}{rho_f} + \frac{m_r}{rho_r}} \tag{2.63}$$

$$v_r = 1 - v_f \tag{2.64}$$

For an orthotropic composite lamina the four elastic properties necessary for the analysis are calculated as:

$$E_{11} = E_f v_f + E_r v_r \tag{2.65}$$

$$\frac{1}{E_{22}} = \frac{v_f}{E_f} + \frac{v_r}{E_r} \tag{2.66}$$

$$\nu_{12} = v_f \nu_f + v_r \nu_r \tag{2.67}$$

$$\frac{1}{G_{12}} = \frac{v_f}{G_f} + \frac{v_r}{G_r} \tag{2.68}$$

Often fiber or resin ν must be estimated as 0.3 and the shear modulus estimated as $E/(2(1+\nu))$. With the individual lamina properties determined, elastic properties for multiple layer laminates are then calculated using classical laminate theory [28].

2.2.3.2 Midplane Calculations

The laminate midplanes are calculated by offsetting the airfoil profile inwards by one-half the laminate thickness. A level set method is used to avoid degenerate geometry that can occur when the offset is greater than the local radius of curvature. This phenomenon is demonstrated in figure 2.12 where an offset is calculated by propagating points along the local surface normal. The degeneracy occurs near the leading edge radius where the offset curve self-intersects.

To avoid this, the level set algorithm described by Kimmel and Bruckstein [57] was implemented. A continuous scalar function $\phi(x, y, t)$ is introduced, such that the contour $\phi(x, y, 0) = 0$ reproduces the original shape to be offset. The function is defined negative inside the shape and positive outside.

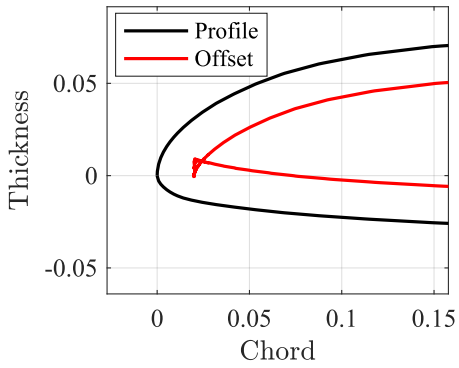

Figure 2.12: Example of degenerate geometry produced during blade offset

The problem of offsetting the original curve then becomes one of tracking the contour $\phi(x, y, t) = 0$ as the scalar function is evolved according to the partial differential equation:

$$\frac{\partial \phi}{\partial t} - \|\nabla \phi\| = 0 \tag{2.69}$$

With $\|\nabla \phi\| = \nabla \phi^2$, a finite difference solution is introduced. A first order, conservative flux scheme with upwinding and explicit time stepping is used to propagate the scalar function and naturally enforces the condition that the offset curve may not self intersect. The discrete time stepping formula is as follows:

$$\phi\left(i\Delta x, j\Delta y, n\Delta t\right) \equiv \phi_{ij}^{n} \tag{2.70}$$

$$\phi_{ij}^{n} + 1 = \phi_{ij}^{n} - \Delta t\, g\left(D_{-}^{x}\phi_{ij}^{n}, D_{+}^{x}\phi_{ij}^{n}, D_{-}^{y}\phi_{ij}^{n}, D_{+}^{y}\phi_{ij}^{n}\right) \tag{2.71}$$

$$g\left(D_{-}^{x}\phi_{ij}^{n}, D_{+}^{x}\phi_{ij}^{n}, D_{-}^{y}\phi_{ij}^{n}, D_{+}^{y}\phi_{ij}^{n}\right) =$$

$$\left(min\left(D_{-}^{x}\phi_{ij}^{n}, 0\right)^{2} + max\left(D_{+}^{x}\phi_{ij}^{n}, 0\right)^{2} + min\left(D_{-}^{y}\phi_{ij}^{n}, 0\right)^{2} + max\left(D_{+}^{y}\phi_{ij}^{n}, 0\right)^{2}\right)$$

$$D_{-}^{x}\phi_{ij}^{n} \equiv \frac{\phi_{ij}^{n} - \phi_{i-1j}^{n}}{\Delta x} \quad D_{+}^{x}\phi_{ij}^{n} \equiv \frac{\phi_{i+1j}^{n} - \phi_{ij}^{n}}{\Delta x}$$

$$D_{-}^{y}\phi_{ij}^{n} \equiv \frac{\phi_{ij}^{n} - \phi_{ij-1}^{n}}{\Delta y} \quad D_{+}^{y}\phi_{ij}^{n} \equiv \frac{\phi_{ij+1}^{n} - \phi_{ij}^{n}}{\Delta y}$$

While higher order flux schemes are available, e.g. Lax-Friedrichs, the above formulation is sufficient for the current work. Figure 2.13a shows the initialized scalar function with $\phi = 1$ outside the contour boundary and $\phi = -1$ inside. The resulting offset curves, with a spacing of 0.3 mm normal to the blade profile, are presented in figure 2.13b. The curves remain continuous with no overlap due to the level set method.

2.3 Uncertainty and Statistical Analysis

A major goal of the current study is to apply rigorous uncertainty analysis, error propagation, and statistical principles to rotor system measurements. Previous studies largely neglect reporting measurement uncertainties, creating difficulty in evaluating theoretical and numerical models which attempt to replicate the experimental results. The following sections describe

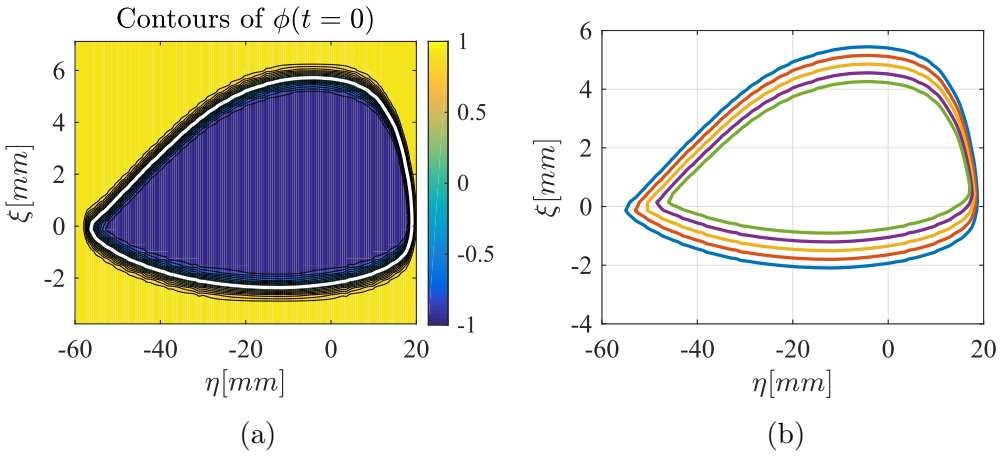

Figure 2.13: Level set offset method, (a) Contours of initial scalar function ϕ with zero-level in white, (b) Offsets of 0.3mm from the initial contour

the approaches used for estimating measurement uncertainty, working with regressions and model fits, and propagating error.

2.3.1 Precision and Bias Uncertainties

Measurement uncertainties are considered following guidelines outlined by NIST [3]. Uncertainties are split into two categories, precision (type A) uncertainties, and bias (type B) uncertainties. Precision uncertainties are due to random sources of error which are characterized with repeated measurements. Ideally these repeated measurements would be made at several different time scales, ranging from multiple samples during a single experiment (repeatability), to samples taken on different days (reproducibility), to samples taken between complete overhauls of the experiments(long-term). In practice only repeatability and, sometimes, reproducibility may be captured due to limited

time and equipment availability. To compute the measurement uncertainty for a mean measurement value calculated from multiple independent samples, first the standard error of the mean, $s_{\bar{x}}$, is calculated:

$$\bar{x} = \sum_{i=1}^{N} \frac{x_i}{N} \tag{2.72}$$

$$s_x = \sqrt{\frac{\sum_{i=1}^{N} (x_i - \bar{x})^2}{N-1}} \tag{2.73}$$

$$s_{\bar{x}} = \frac{s_x}{\sqrt{N}} \tag{2.74}$$

The mean measurement value is then assumed to follow a Student's-t distribution with degrees of freedom $\nu = N - 1$. The distribution, shown in figure 2.14, approaches the normal distribution as the degrees of freedom increase, with larger tails at lower degrees of freedom. The precision uncertainty is calculated for a specified confidence level, α, typically chosen as 95%, as:

$$u_{\bar{x}}^{prec} = t_{(1-\alpha)/2,N-1} s_{\bar{x}} \tag{2.75}$$

Here $t_{(1-\alpha)/2,n-2}$ is the t-statistic calculated at the 95% confidence level for a Student's-t distribution with $N-1$ degrees of freedom, i.e., $\alpha = 0.95$ and the p-value is $(1-\alpha)/2 = 0.025$.

Bias uncertainties arise from sources other than variation in repeated measurements. They typically are a characteristic of a given measurement device or an environmental variable that was not sampled such as a physical

constant. In the current study bias uncertainties are primarily associated with measurement instruments. In the case of externally supplied instruments the bias uncertainty is estimated using a manufacturers calibration or data sheet when available, or, in the case of devices such as scales or rulers, estimated as one-half the least count of the device. For custom measurement devices bias uncertainties are frozen from the calibrations as shown in §2.3.3. With the bias uncertainty, $u_{\bar{x}}^{bias}$ estimated, the total uncertainty of a measurement is then calculated as:

$$u_{\bar{x}} = \sqrt{(u_{\bar{x}}^{prec})^2 + (u_{\bar{x}}^{bias})^2} \tag{2.76}$$

2.3.2 Propagation of Error

Often individual measurements are combined together to produce derived values. For example, upper and lower rotor lift measurements may be combined to calculate a thrust ration, T_U/T_L. The question then arises; for a quantity that is a function of several measurements, each with uncertainties, what is the uncertainty in the derived value? To answer this question a derivation following reference [6] is presented. Consider a scalar function of n random variables $Y = f(X_1, X_2, ..., X_n)$. Then, taking the Taylor expansion about the mean expected values μ_i and discarding higher order terms:

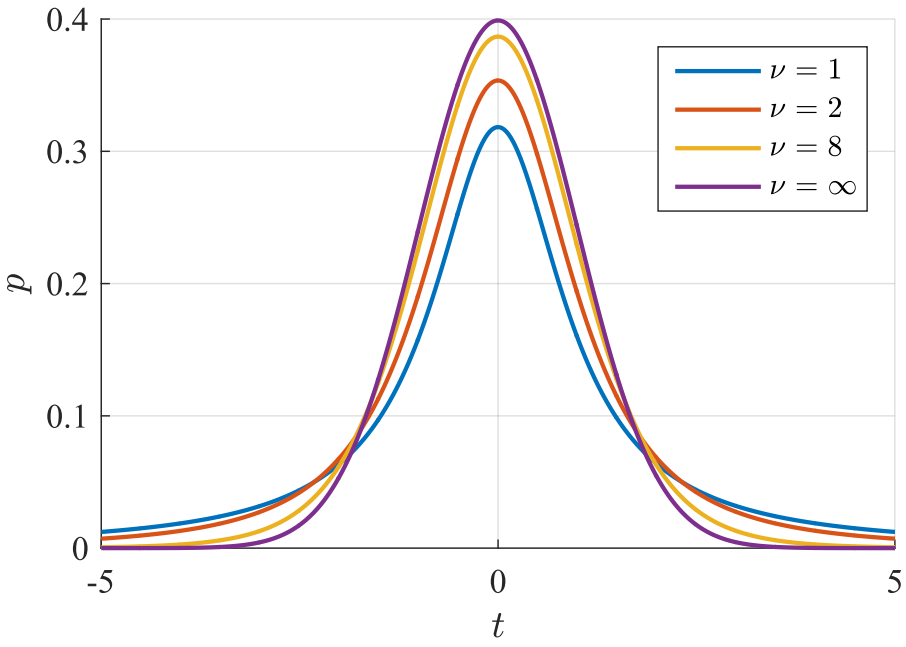

Figure 2.14: Student's-t probability distribution function for various degrees of freedom

$$Y \approx Y(\mu_1, \mu_2, ..., \mu_n) + \sum_i^n \left[\frac{\partial f}{\partial X_i}(\mu_1, \mu_2, ..., \mu_n) \right] [X_i - \mu_i] \tag{2.77}$$

$$a0 \equiv Y(\mu_1, \mu_2, ..., \mu_n) \tag{2.78}$$

$$ai \equiv \frac{\partial f}{\partial X_i}(\mu_1, \mu_2, ..., \mu_n) \tag{2.79}$$

$$Y \approx a0 + \sum_i^n a_i(X_i - \mu_i) \tag{2.80}$$

Because the approximation is linear, and given normally distributed random inputs X_i, the output Y is also gaussian. The expected value of Y can be shown, after some manipulation, to be:

$$E[Y] = \mu_y = f(\mu_1, \mu_2, ..., \mu_n) \tag{2.81}$$

And the variance of Y is derived as:

$$E[(Y - \mu_Y)^2] = \sigma_Y^2 = E[(\sum_i^n a_i(X_i - \mu_i))^2] \tag{2.82}$$

$$\sigma_Y^2 = E[\sum_i^n a_i(X_i - \mu_i) \sum_j^n a_i(X_j - \mu_j)] \tag{2.83}$$

$$\sigma_Y^2 = \sum_i^n a_i^2 E[(X_i - \mu_i)^2] + \sum_{i \neq j}^n \sum^n a_i a_j E[(X_i - \mu_i)(X_j - \mu_j)] \tag{2.84}$$

$$\sigma_Y^2 = \sum_i^n \left(\frac{\partial f}{\partial X_i} \right)^2 \sigma_i^2 + \sum_{i \neq j}^n \sum^n \left(\frac{\partial f}{\partial X_i} \right) \left(\frac{\partial f}{\partial X_y} \right) \sigma_{ij} \tag{2.85}$$

Typically the above result is often presented for uncorrelated inputs X_i as:

$$\sigma_Y = \sqrt{\sum_i^n \left(\frac{\partial f}{\partial X_i}\right)^2 \sigma_i^2} \tag{2.86}$$

The standard deviations in 2.86 may be replaced with the uncertainties given in equation 2.76 to calculate the fully propagated uncertainty in the value of Y. The process is presented graphically for a function of one variable in figure 2.15. The uncertainty bounds on the dependent variable x are projected onto the partial derivate, slope, of the function $f(X)$ to calculate the resulting uncertainty in μ_y. In higher dimensions the variances are summed, maintaining orthogonality of the uncorrelated measurement uncertainties.

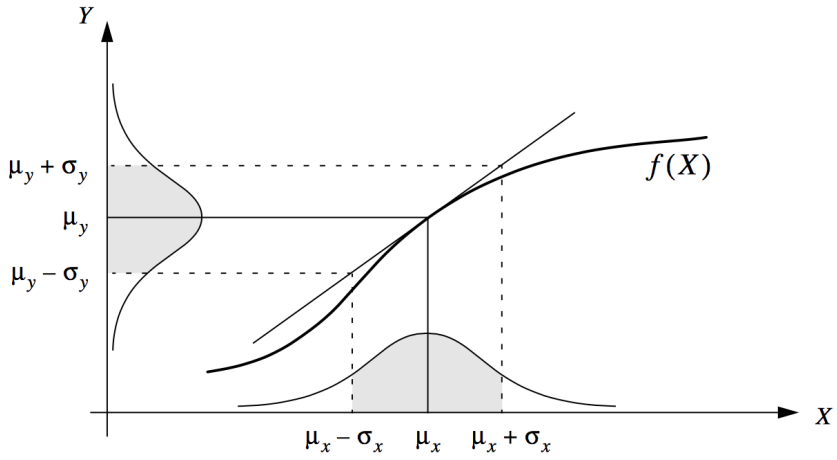

Figure 2.15: Graphical illustration of the propagation of uncertainty in μ_x, σ_x to uncertainty in $\mu_y = f(X)$, σ_y, from Ref. [6]

2.3.2.1 Sequential Perturbation

Calculation of the partial derivatives in equation 2.86 may be difficult or impossible for very complicated functions. An alternative method for

propagating error is that of sequential perturbations. In this technique the nominal value of the function $Y_0 = f(\bar{x}_1, \bar{x}_2, ..., \bar{x}_n)$ is computed. Then the inputs x_i are perturbed, one at a time, by their corresponding uncertainties u_{x_i}. Uncertainty in the final value of Y is then calculated as:

$$u_Y = \sqrt{\left[(Y_0 - f(\bar{x}_1 + u_{\bar{x}_1}, \bar{x}_2, ...\bar{x}_n))^2 + (Y_0 - f(\bar{x}_1, \bar{x}_2 + u_{\bar{x}_2}, ...\bar{x}_n))^2 ...\right]} \tag{2.87}$$

The formula in 2.87 uses positive perturbations of the input variables. Negative perturbations, or the average of the positive and negative perturbations may also be used in cases when the function f is highly nonlinear. Sequential perturbation is easy to implement computationally as a wrapper function around the already existing data processing code.

2.3.2.2 Covariance and Numerical Jacobian

While sequential perturbation works for uncorrelated input measurements, it is not accurate for cases with correlated input measurements. It is therefore desirable to develop a method for calculating the uncertainty of functions with correlated inputs, featuring the same ease of implementation as sequential perturbation. To accomplish this consider equation 2.85, rewritten in matrix form as:

$$\sigma_Y^2 = \{J\}[\mathbf{\Sigma^X}]\{J\}^T \tag{2.88}$$
$$\vec{J} = \left[\frac{\partial f}{\partial X_1}, \frac{\partial f}{\partial X_2} ...\right]$$

$$\mathbf{\Sigma^X} = \begin{bmatrix} \sigma_1^2 & \sigma_{12} & \dots \\ \sigma_{12} & \sigma_2^2 & \ddots \\ \vdots & \ddots & \ddots \end{bmatrix}$$

Here $\vec{J}$ is the Jacobian of f evaluated at $\vec{\mu}$ and $\mathbf{\Sigma^X}$ is the covariance matrix of the measurements X_i. A Matlab package, Adaptive Robust Numerical Differentiation [29], is used to numerically approximate the Jacobian through central differences, with Richardson expansion for acceleration and error estimation. The measurement uncertainty is then calculated according to 2.88. The covariance terms under consideration generally arise from the precision uncertainty. Bias uncertainties are included by adding their square to the corresponding diagonal term in the covariance matrix. The final code is interchangeable with the sequential perturbation code mentioned previously, acting as a wrapper function around an existing data processing function.

2.3.2.3 Example Calculations

Consider the previously mentioned thrust sharing ratio T_U/T_L. Table 2.5 shows example parameters including the mean measurements, bias uncertainties, as well as measurement variance and covariance. Defining the thrust ratio as y:

Table 2.5: Example uncertainty propagation parameters

T_U	200	[N]
T_L	180	[N]
u_{TU}^{bias}	8	[N]
u_{TL}^{bias}	8	[N]
σ_{TU}^2	16	$[N^2]$
σ_{TL}^2	25	$[N^2]$
$\sigma_{TU,TL}$	-5	$[N^2]$

$$\sigma_y = \sqrt{\left(\frac{\partial Y}{\partial T_U}\right)^2 \sigma_{TU}^2 + \left(\frac{\partial Y}{\partial T_L}\right)^2 \sigma_{TL}^2 + 2\frac{\partial^2 Y}{\partial T_U \partial T_L}\sigma_{TU,TL}} \tag{2.89}$$

$$= \sqrt{\left(\frac{1}{T_L^2}\right)\sigma_{TU}^2 + \left(\frac{T_U^2}{T_L^4}\right)\sigma_{TL}^2 - \frac{2T_U}{T_L^3}\sigma_{TU,TL}} \tag{2.90}$$

Adding the square of the bias uncertainties to the measurement variances $\sigma^2 + (u^{bias})^2$ in the above equation, the resulting uncertainty in the thrust sharing ratio, $y = 1.053$ is calculated as $\sigma_y = 0.072$. If the covariance term is neglected the uncertainty becomes $\sigma_y = 0.070$, while neglecting the bias uncertainties results in $\sigma_y = 0.035$. In this example the influence of covariance is small, and may reasonably be neglected. The bias uncertainty must be included as it accounts for nearly half the derived measurement uncertainty.

.

2.3.3 Model Fits and Regressions

Regressions are used for two main purposes in the current study. The first is for generating calibrations for custom measurement devices such as the pushrod load cells or pitch angle instrumentation described in §3.2. The second is for fitting analytical models to experimental data. In both cases the uncertainties in the regression coefficients and the regression outputs are of interest. These simple linear regressions take the form:

$$y = \beta_1 x + \beta_0 \tag{2.91}$$

Statistical analysis is used to evaluate the regression coefficients and accuracy of the analytical fits. Detailed descriptions and derivations of the statistical analysis techniques can be found in the textbook by Ryan [94].

Shaded confidence intervals, plotted with the analytical model, may provide a visual indication of the uncertainty of the estimates $\hat{y}_i$ for various values of x_i. These confidence intervals also serve as a basis for defining the bias uncertainty for a calibrated instrument. A 95% confidence interval is defined such that, with repeated sampling, 95% of the generated confidence intervals about the estimated values $\hat{y}_0$ are expected to contain the true value y_0. The expression for this confidence interval is given as (2.92).

$$P(\hat{y_0} - \delta_y \leq y_0 \leq \hat{y_0} + \delta_y) = 0.95 \tag{2.92}$$

Here, given a set of n measurements used to generate the analytical fit,

$$\delta_y = t_{0.025,n-2}\ s_\epsilon \sqrt{\frac{1}{n} + \frac{(x_0 - \bar{x})^2}{S_{xx}}} \tag{2.93}$$

$$s_\epsilon = \sqrt{\frac{\sum_{i=1}^{n} (y_i - \hat{y}_i)^2}{n-2}} \tag{2.94}$$

$$S_{xx} = \sum_{i=1}^{n} (x_i - \bar{x_i})^2 \tag{2.95}$$

The expression for the confidence interval δ_y, includes a term that increases as the value of x_0 moves away from the mean value of x. For calibrations based on regressions a conservative estimate of the bias uncertainty may be obtained from the value of the confidence interval furthest from the mean values used for the regression. In addition to these fit confidence intervals, the 95% confidence intervals for the coefficients of the analytical fits are calculated as follows:

$$P(\hat{\beta_0} - \delta_{\beta 0} \leq \beta_0 \leq \hat{\beta_0} + \delta_{\beta 0}) = 0.95 \tag{2.96}$$

$$P(\hat{\beta_1} - \delta_{\beta 1} \leq \beta_1 \leq \hat{\beta_1} + \delta_{\beta 1}) = 0.95 \tag{2.97}$$

$$\delta_{\beta 1} = t_{0.025,n-2}\ \sqrt{\frac{\sum_{i=1}^{n} (y_i - \hat{y}_i)^2}{(n-2)S_{xx}}} \tag{2.98}$$

$$\delta_{\beta 0} = t_{0.025,n-2}\ s_\epsilon \sqrt{\frac{\sum_{i=1}^{n} x_i^2}{nS_{xx}}} \tag{2.99}$$

For example, this approach is used to calculate the uncertainties in the induced power and profile power coefficients, fit to the measured thrust and power using the momentum theory derived in §2.1.1. With the analytical fit coefficients and their uncertainties, the Student's-t test may then be used to compare measurements from different experimental configurations. The null hypothesis for comparing coefficients from two fits, a and b, is that they are equal; the resulting t-statistic is calculated using the coefficients and their standard errors as:

$$t = \frac{\hat{\beta}_{n,a} - \hat{\beta}_{n,b}}{\sqrt{s^2_{\hat{\beta}_{n,a}} + s^2_{\hat{\beta}_{n,b}}}} \tag{2.100}$$

A p-value is computed using this t-statistic and a t-distribution with $n-2$ degrees of freedom, where n is the lesser of the number of points used to create the two fits. This p-value is the probability of observing a test statistic at least as extreme as that calculated (from equation (2.100)). If this p-value is greater than 0.025, the null hypothesis is accepted, which means that the coefficients are found to have no statistical difference with a confidence level of 95%. On the other hand, if this p-value is less than 0.025, the null hypothesis is rejected, in which case there is a significant difference between the coefficients at the chosen p-value.

Chapter 3

Experimental Design

This chapter documents the design, fabrication and validation of the Mach-scale CCR test stand and instrumentation. The range of nominal The chapter is divided in three sections. In §3.1 the design of the drive system transmission, hubs and pitch control system, including linear servos, is covered. In §3.2 the instrumentation used for key measurements is presented, including calibrations and characterizations of uncertainty. Finally §3.3 describes the data acquisition and real time test monitoring systems.

3.1 Test Stand Hardware

3.1.1 Drive System

The heart of the test stand is a belt driven transmission assembly. Shown in figure 3.1, the transmission uses two synchronized toothed belts to transmit power from the input drive shaft to the rotor shafts. The two input pulleys rotate together on the same shaft. The inner shaft drives the upper rotor, while the outer shaft drives the lower, as seen in the cross-sectional view in figure 3.2. The upper rotor is driven counter-clockwise, as is conventional for North American rotorcraft, while the lower rotor spins clockwise due to

the serpentine belt arrangement with idler pulley. The toothed belts and pulleys, with a 1:1 drive ratio, ensure that the rotors remained synchronized over time. The 36-tooth pulleys allow for adjusting the upper-lower rotor phase relationship, and therefore the location of upper-lower rotor blade crossings, in 10 degree increments. Power is provided through a hydraulic drive system, consisting of a remote reservoir and pump, with a compact, stand mounted, bent axis hydraulic motor (Rexroth AA2FM-63). Maximum power is 105 kW at 4000 RPM, while 50 kW is available at the maximum nominal testing speed of 1800 RPM.

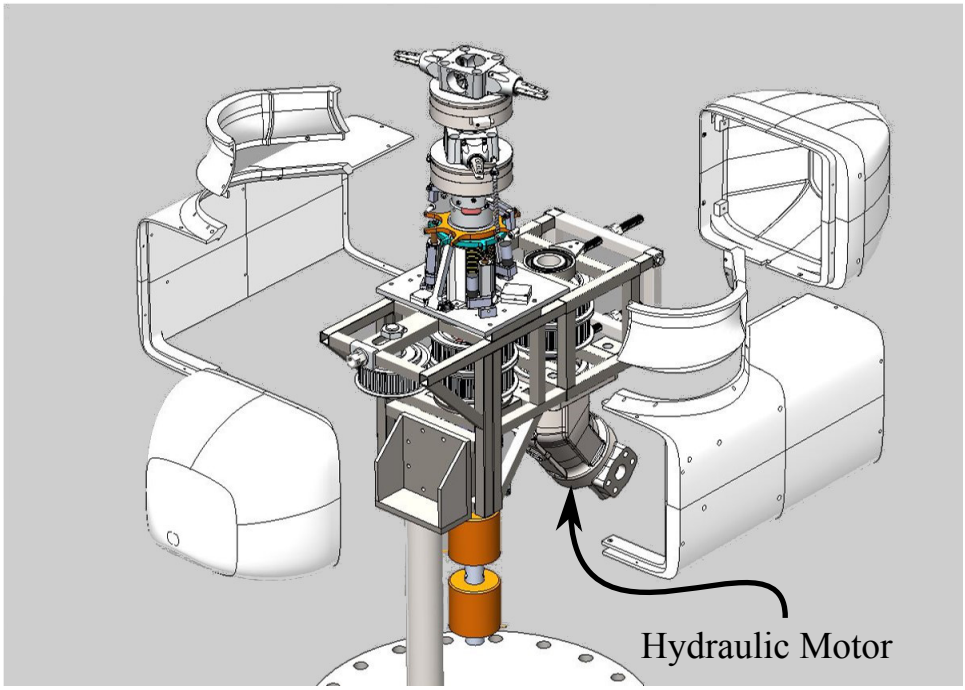

Figure 3.1: Belt driven coaxial transmission with hydraulic motor

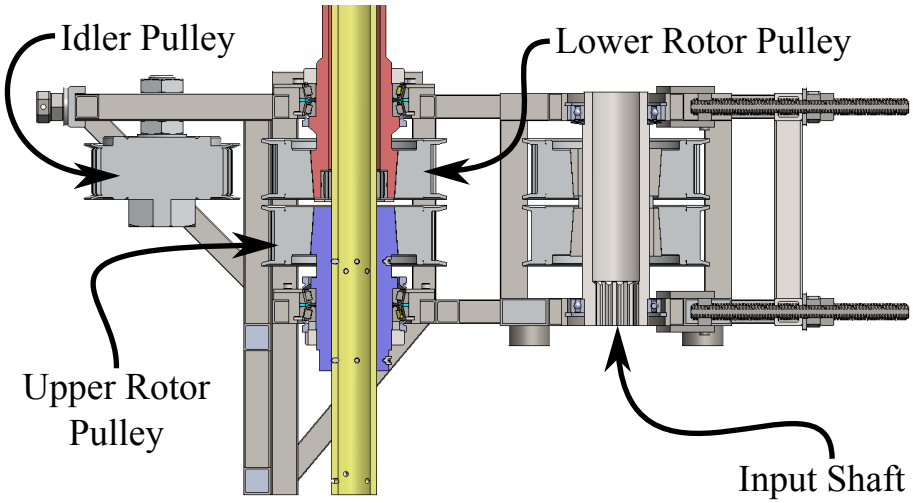

Figure 3.2: Coaxial transmission cross sectional view

3.1.2 Hub Design

The design of the rotor hubs contained several challenges unique to the closely spaced CCR rotor system under investigation. Traditionally, rotor hubs feature bearings allowing blade motion in the pitch, flap and lag directions. These hub designs, referred to as fully articulated, do not support bending moments at the blade root, reacting only the blade forces, greatly reducing stresses. A CCR rotor system, designed for use with lift offset, must react large bending loads at the blade root to ensure that the upper and lower rotor blades do not collide. These large bending moments, as well as the centrifugal loading from the blade are the driving factors in the hub design. The BEMT and linear beam codes were used to derive estimates of the hub loads which are listed in table 3.1. The moment load due to the distributed blade thrust was taken

Table 3.1: Design Loads for Hub

Rotational Velocity	1800	RPM
Blade Mass	0.3	kg
Centrifugal Loading	4200	N
Blade Thrust	250	N
Flap Bending Moment	177	Nm

directly from the BEMT model. This is a conservative estimate of the bending moment seen by the hubs, as blade-flapping combined with centrifugal force produces a negative flap-bending moment, partially countering the positive flap-bending moment due to the rotor thrust.

The space available for the hub also introduced design constraints. The inside of the lower rotor hub must clear the 50 mm upper rotor shaft, and the hub height is limited to 50 mm by the upper rotor drive flange. The hub outer diameter must be minimized to avoid excessive drag and the final design must mate to the 4×120 mm bolt pattern of the main load cells. The final design, shown in figure 3.3a consists of a central hub with modular bearing carrier and bladegrip assemblies. The bearing carriers house three bearings, visible in figure 3.3b: one axial roller bearing for centrifugal loads, and two needle roller bearings reacting thrust and flap-bending moments.

Given the high forces involved, accurate predictions of the stresses experienced by the blade grip and hub is important. Central to the prediction of the stresses is the modeling of the bearings. Roller bearings are inherently complicated mechanisms, with non-linear, load dependent stiffness determined

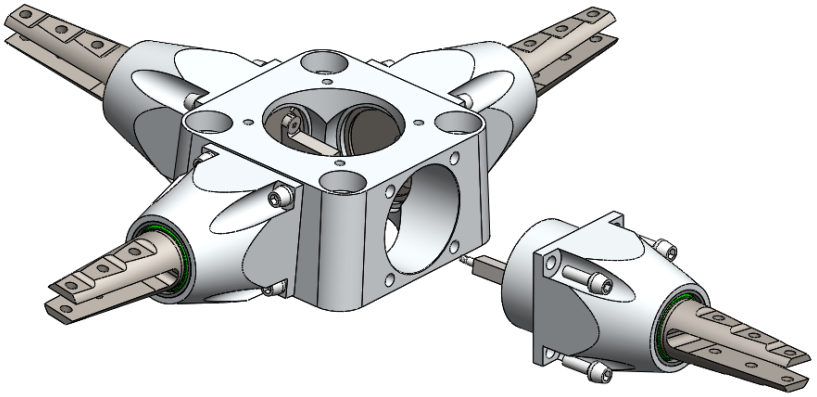

(a)

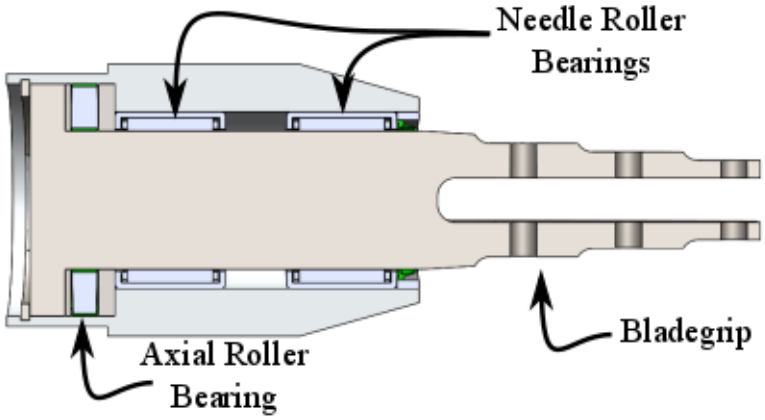

(b)

Figure 3.3: Modular, rigid rotor hub design (a) Central hub with bearing carriers (b) Cross-sectional view of bearing carrier and bladegrip

by Hertzian contact stress. Several strategies have been proposed for reduced order modeling of bearings for finite element analysis. Following one approach by Molnár et al. [73], the bearings are modeled as solid bushings with elastic moduli tailored to reproduce the appropriate stiffness response. Three degrees of precone angle is added to the hubs to reduce root bending moments utilizing the inertial flapping moment.

3.1.3 Pitch Control System

Controlling blade pitch is crucial for proper operation of the rotor stand. In hover, collective pitch determines the power and thrust produced, and differential adjustment of upper and lower rotor collective is used for balancing rotor torques. Forward flight introduces the additional requirement of sinusoidally varying the rotor blade pitch once per revolution in order to trim rolling moments. The following sections describe the various pitch control systems that were built and utilized during the testing performed on the rotor stand.

3.1.3.1 Fixed Pitch

During early hover testing, pitch control was accomplished by manual adjustment of individual blade pitch links. These upper and lower rotor manual pitch control systems are labeled in figure 3.4. The upper rotor pitch control consists of female rod-ends attached to socket head cap screws captured in spherical bearings. Turning the cap screw moved the rod-end vertically with

a resulting pitch resolution of 3.5°/turn. While the upper rotor system was entirely contained on the hub, the lower rotor system used pushrods mounted to fixed arms below the rotor system with pitch resolution of 4.3°/turn. As demonstrated in §3.2.3 the lower rotor pushrod forces were measured to correct the hub loads. This was accomplished by instrumenting the support arms with full-bridge bending strain gauge arrangements, as shown in figure 3.5. Programmable instrumentation amplifiers (RAETECH SG1169) were mounted to the support so only amplified signals were sent through the sliprings.

3.1.3.2 Swashplates and Linkages

While the fixed pitch system was sufficient for limited hover testing, wind tunnel testing requires significantly more advanced control. Typical helicopter main rotor controls consist of three degrees of freedom: collective blade pitch (θ_0), longitudinal cyclic pitch (θ_{1C}), and lateral cyclic pitch (θ_{1S}). The resulting blade root pitching motion from these three degrees of freedom is described by the equation:

$$\theta = \theta_0 + \theta_{1C} \cos\psi + \theta_{1S} \sin\psi \tag{3.1}$$

For the coaxial rotor system, each rotor has independent control settings (θ_0, θ_{1C}, θ_{1S}) for a total of six degrees of freedom. The collective and cyclic controls are implemented using custom built swashplate linkage assemblies. The lower rotor swashplate and linkages, shown in figure 3.6, are in a configuration traditionally used on helicopters. Three fixed-frame linear servo

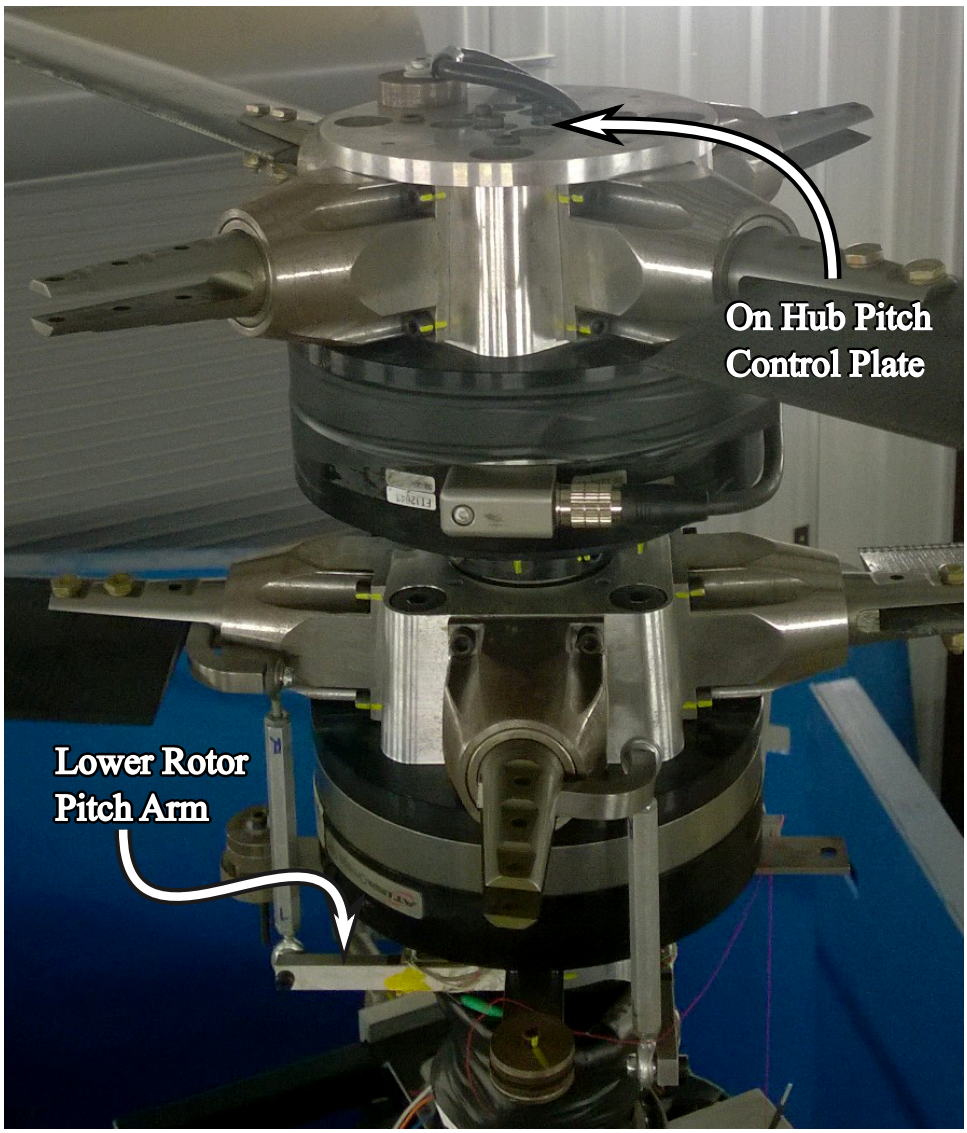

Figure 3.4: Manually adjusted pitch control system for hover experiments

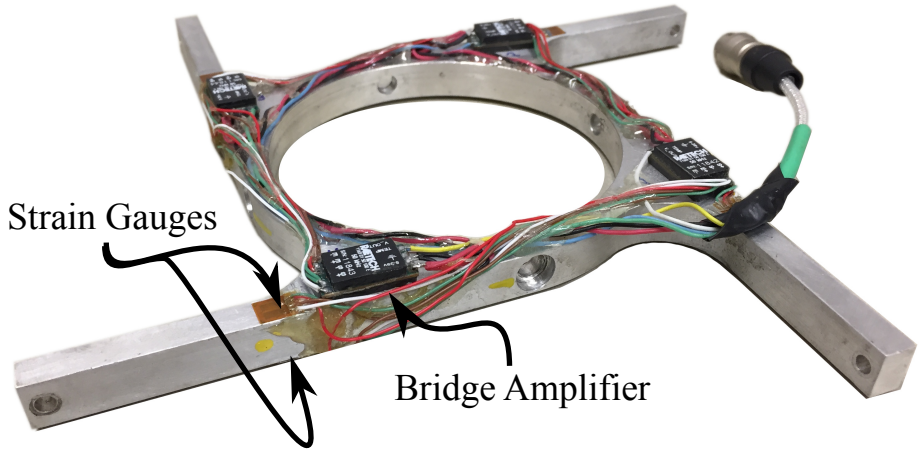

Figure 3.5: Lower rotor pushrod support with full-bridge strain gauge instrumented arms

actuators translate and tilt the non-rotating swashplate riding on a central spherical bearing. The non-rotating swashplate transmits motion to the rotating swashplate through a thin section ball-bearing. The rotating swashplate (rotating with the blades at the rotor angular velocity) is connected to the lower rotor pitch horns via adjustable carbon fiber pitch links. Linear translation of the swashplate changes the collective (mean) pitch angle, while tilting the swashplate fore to aft and side to side changes the longitudinal and lateral cyclic pitch amplitudes respectively.

The upper rotor swashplate and linkage assembly is considerably more complicated. Shown in figure 3.7, the pitch control system runs through the inner shaft for a compact, aerodynamic implementation. The linear servos

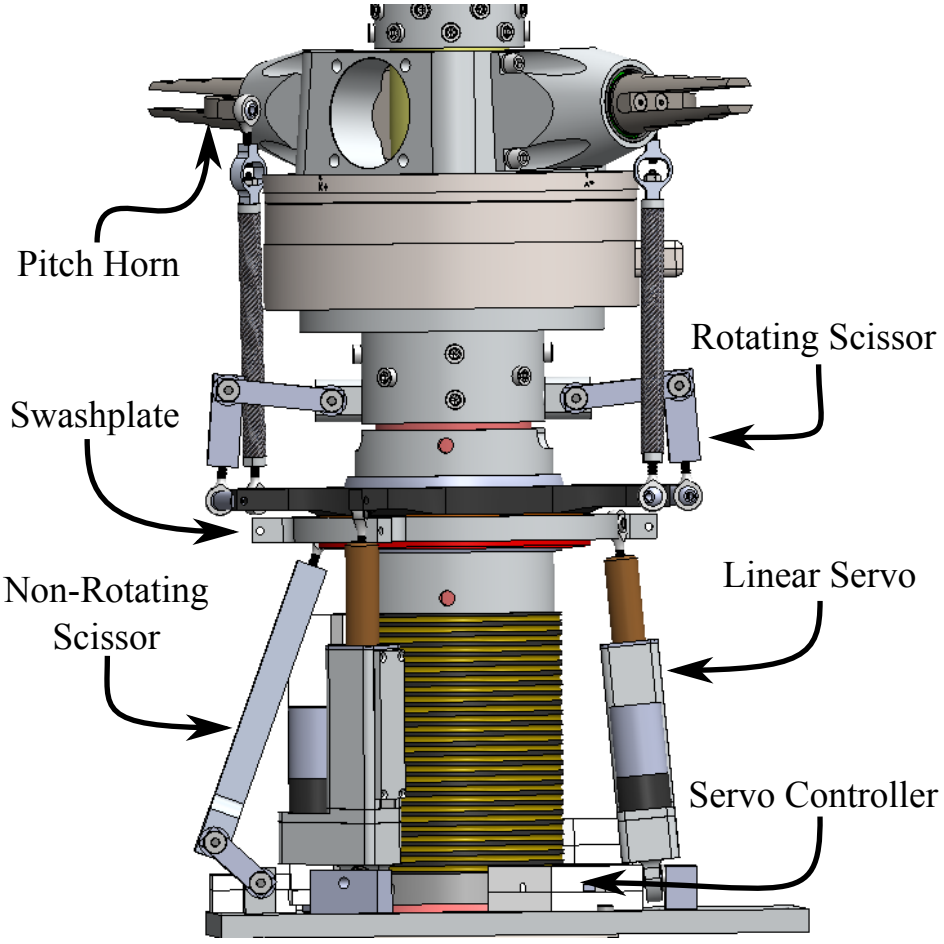

Figure 3.6: Lower rotor swashplate and linkage assembly

and swashplate, similar to those of the lower rotor, are mounted upside down, below the transmission assembly. External, rotating pitch links connect to ball-bearing supported bellcranks which reverse the pitch direction, connecting to the internal pitch links running to the inside of the upper rotor.

Running the upper rotor pushrods internally results in different upper and lower rotor pitch horn geometry. Shown in figures 3.8a and 3.8b, the lower rotor pitch horn length of 23 mm is 1.78 times larger than that of the upper rotor (13 mm). This variation in pitch horn length results in distinct upper and lower rotor pitch control loads and pitch control stiffnesses. The rotor blade pitching forces, including inertial and aerodynamic loads, result in linear pushrod loads in the control system proportional to $1/L_{horn}$:

$$F_{PR} = \frac{M_{pitch}}{L_{horn}} \tag{3.2}$$

Similarly the torsional stiffness of the control system, measured at the blade root, is related to the linear stiffness of the pushrods and components by:

$$k_\theta = k_{linear} L_{horn}^2 \tag{3.3}$$

Finally, free-play hysteresis enters the system largely through rod-end and ball-joint positioning tolerances. The total linear hysteresis is then related to the pitch angle hysteresis as:

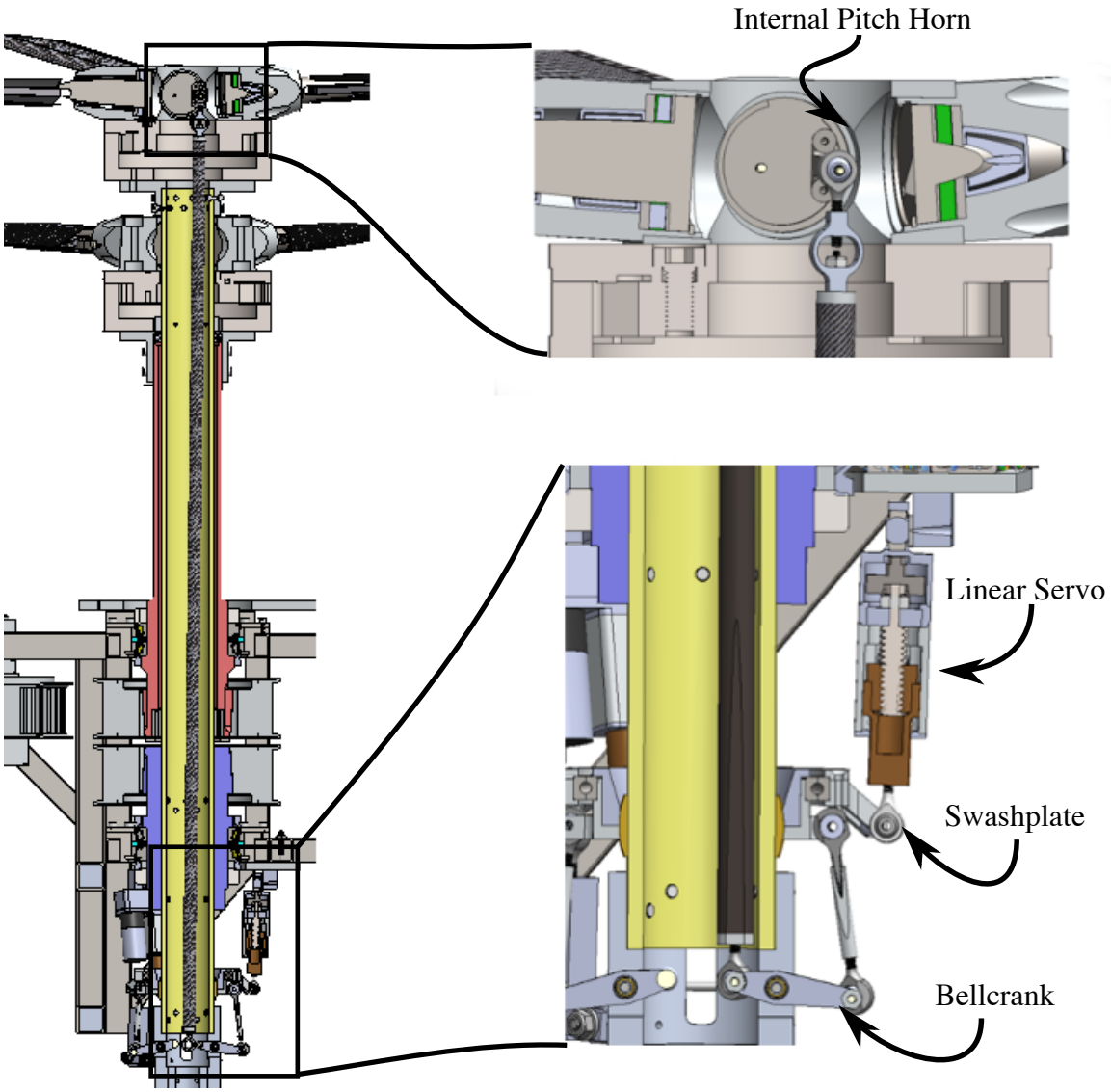

Figure 3.7: Upper rotor swashplate and linkage assembly

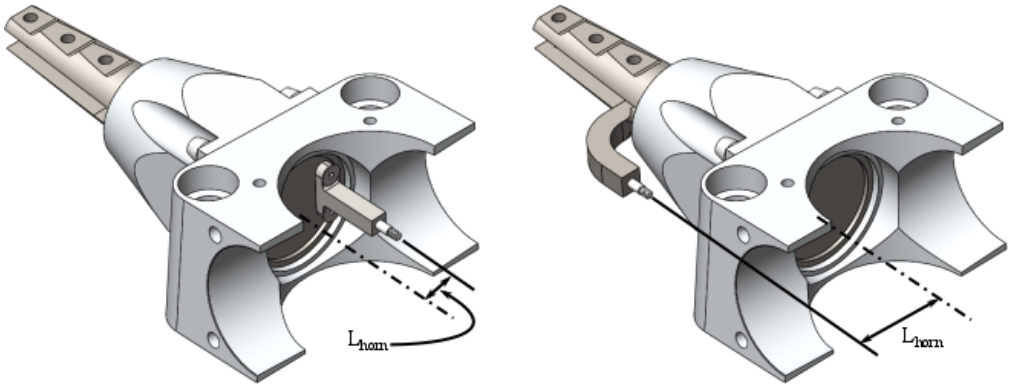

(a) (b)

Figure 3.8: Pitch horn geometry, (a) Upper rotor, (b) Lower rotor

Table 3.2: Upper and lower rotor pitch dynamics

	Upper Rotor	Lower Rotor	
L_{horn}	0.013	0.023	[m]
$\frac{F_{PR}}{M_{pitch}}$	78.7	44.2	[1/m]
k_θ	118	388	[Nm/rad]
$\delta\theta$	2.1	0.5	[deg]

$$\delta\theta = \frac{\delta PR}{L_{horn}} \tag{3.4}$$

Table 3.2 shows these values computed for the upper and lower rotors. Torsional stiffness is built up from individual system components using a combination of linear elasticity and FEA calculations, and the hysteresis measured for the installed system.

3.1.3.3 Servo Controller and Calculations

A diagram of the servo control system is shown in figure 3.9. A central unit, located in the control room, manages user inputs and servo command outputs. The control unit has a LCD display, and toggle switch controls for all six rotor degrees of freedom. The control unit main microprocessor (ATmega2560) reads the switch inputs, calculates the servo throws from the commanded control angles, and updates the output screen. The servo throws are calculated via a series of scalings and transformation matrices as follows. The first transformation is between servo displacements (Δ_i) and the resulting swashplate control plane angles (θ^{CP}):

$$\begin{bmatrix} \frac{1}{3} & \frac{1}{3} & \frac{1}{3} \\ 0 & \frac{-1}{2L_{non}\cos 60^\circ} & \frac{-1}{2L_{non}\cos 60^\circ} \\ \frac{-1}{L_{non}} & \frac{-1}{2L_{non}\sin 60^\circ} & \frac{-1}{2L_{non}\sin 60^\circ} \end{bmatrix} \begin{Bmatrix} \Delta_0 \\ \Delta_1 \\ \Delta_2 \end{Bmatrix} = \begin{Bmatrix} \theta_0^{CP} \\ \theta_{1S}^{CP} \\ \theta_{1C}^{CP} \end{Bmatrix} \tag{3.5}$$

Here L_{non} is the distance from the ceter of swashplate rotation to the non-rotating pushrod attachments. To account for the azimuthal offset, ϕ_h, between the blade pitch axis and the pitch horn location a rotation matrix is introduced, then collective and cyclic pitches are scaled by the distance from the center of swashplate rotation to the rotating pushrod attachments (L_{rot}) and pitch horn length (L_{horn}):

$$\begin{bmatrix} -\frac{1}{L_{horn}} & 0 & 0 \\ 0 & -\frac{L_{rot}}{L_{horn}} & 0 \\ 0 & 0 & -\frac{L_{rot}}{L_{horn}} \end{bmatrix} \begin{bmatrix} 1 & 0 & 0 \\ 0 & \cos\phi_h & \sin\phi_h \\ 0 & -\sin\phi_h & \cos\phi_h \end{bmatrix} \begin{Bmatrix} \theta_0^{CP} \\ \theta_{1S}^{CP} \\ \theta_{1C}^{CP} \end{Bmatrix} = \begin{Bmatrix} \theta_0 \\ \theta_{1S} \\ \theta_{1C} \end{Bmatrix} \tag{3.6}$$

With the desired servo throws calculated, a daughter board (PCA9685) is used to output commanded positions via six pulse width modulated (PWM) signals. These signals run to a distribution panel, mounted on the test stand transmission. Here the signals, along with 12 Volt power, are routed to the individual servo microcontrollers (Pololu Jrk 21v3) which drive the servos to the commanded position with PID feedback.

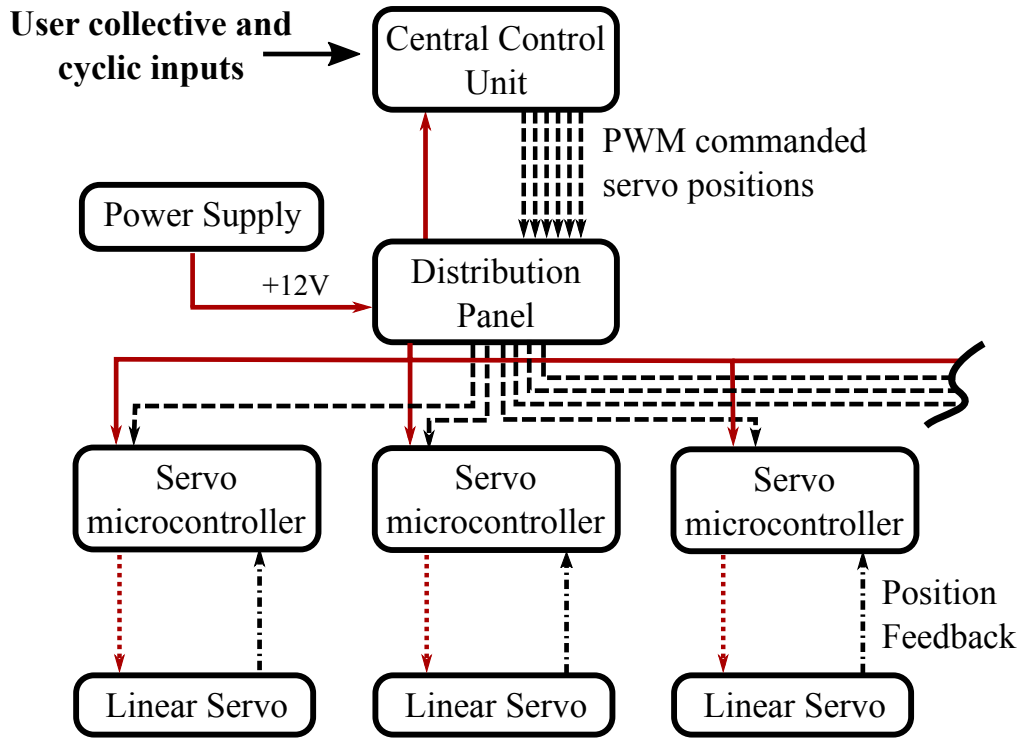

Figure 3.9: Diagram of the servo control system, red arrows are power, black arrows are control and feeback signals

3.1.3.4 Linear Servo Design

The first iteration of the servo control system utilized off-the-shelf hobby servo-actuators (Hitec HS-M7990TH) shown in figure 3.10. This design performed well in hover testing however, under higher forcing in the wind tunnel, the hobby servos exhibited unacceptable play and insufficient resolution for properly trimming the rotor system with cyclic controls. The cyclic control resolution issues occurred due to the coupling in the transformation between commanded control angles and servo throws, combined with the finite servo resolution. Figures 3.11 a-c show contour plots of the error between commanded and actual pitch angles for the lower rotor with the Hitec angular servo actuators over a range of commanded cyclic pitches. The error exhibits a periodic pattern, and is greatest in θ_{1C}. Figure 3.11d shows the relationship between pitch angle error and servo resolution.

In response to the shortcomings of the Hitec servos, custom linear servo actuators were designed. The goals of this design were to increase servo force capability, increase servo resolution, and decrease compliance. The design, shown in figure 3.12a and 3.12b, uses a leadscrew actuator rod driven by a brushed DC motor through a gear reduction system. To simplify the design, parts of the geartrain from the hobby servo actuators were adapted for the linear servos. The leadscrew and nut where purchased from Nook industries featuring 6 turns per inch (tpi) lead and 60% efficiency. With this low lead, the screw cannot be back driven by axial input forces. This means that the servo will hold its position even with no input power, a safe failure mode. The

Figure 3.10: Hitec angular servo actuator with custom arm

geartrain stages and total reduction are listed in table 3.1. The servo housing integrates a spherical bearing for kinematically correct, compact mounting and the all-metal construction with direct load paths minimizes compliance.

Position feedback is measured using a compact membrane linear potentiometer (Spectra Symbol TSP-L) actuated by the servo output shaft using a rapid prototyped ABS plastic wiper, visible to the right in the unassembled servo components shown in figure 3.13. The completed servo characteristics are presented in table 3.4. The custom actuator achieves four times greater positioning resolution, while generating 20 times the force output at peak power as the Hitec servo. The Hitec servo achieves higher maximum pitch velocities which, while useful for certain types of dynamic testing, is not necessary for

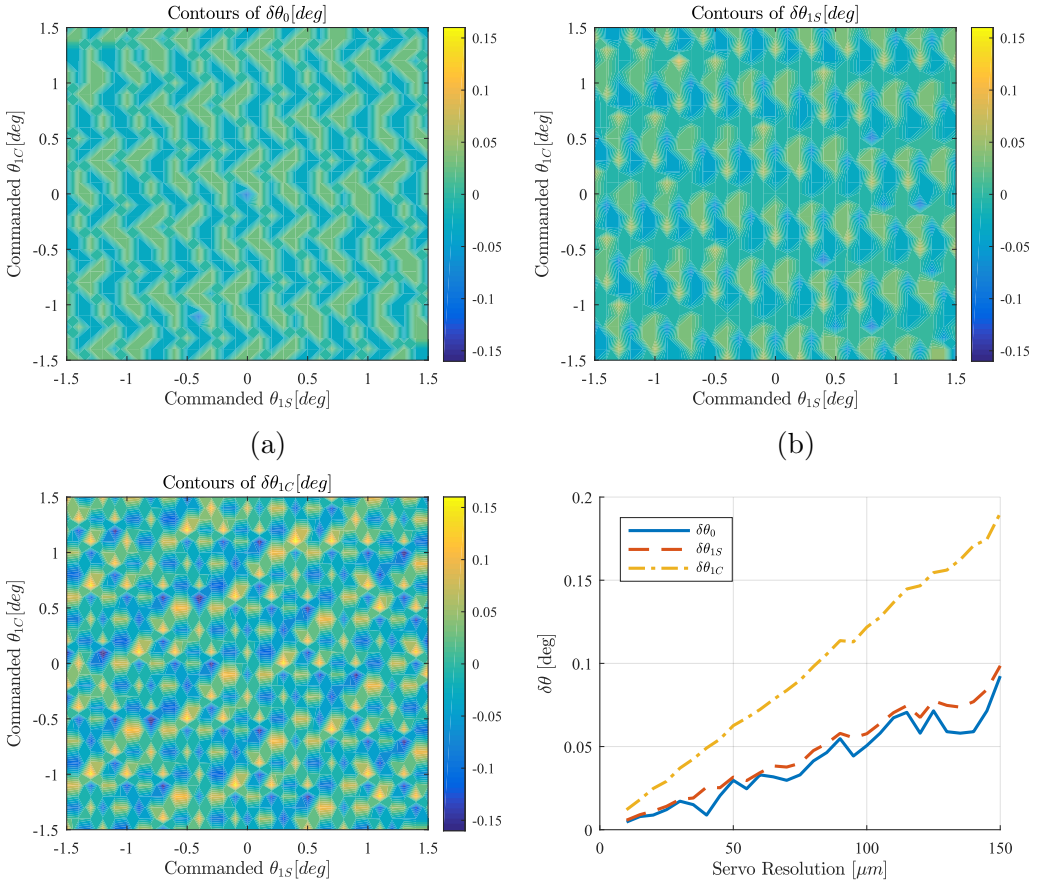

Figure 3.11: Characterization of pitch angle error due to servo resolution, (a) Error in θ_0, (b) Error in θ_{1S}, (c) Error in θ_{1C}, (d) Variation of maximum error with servo resolution

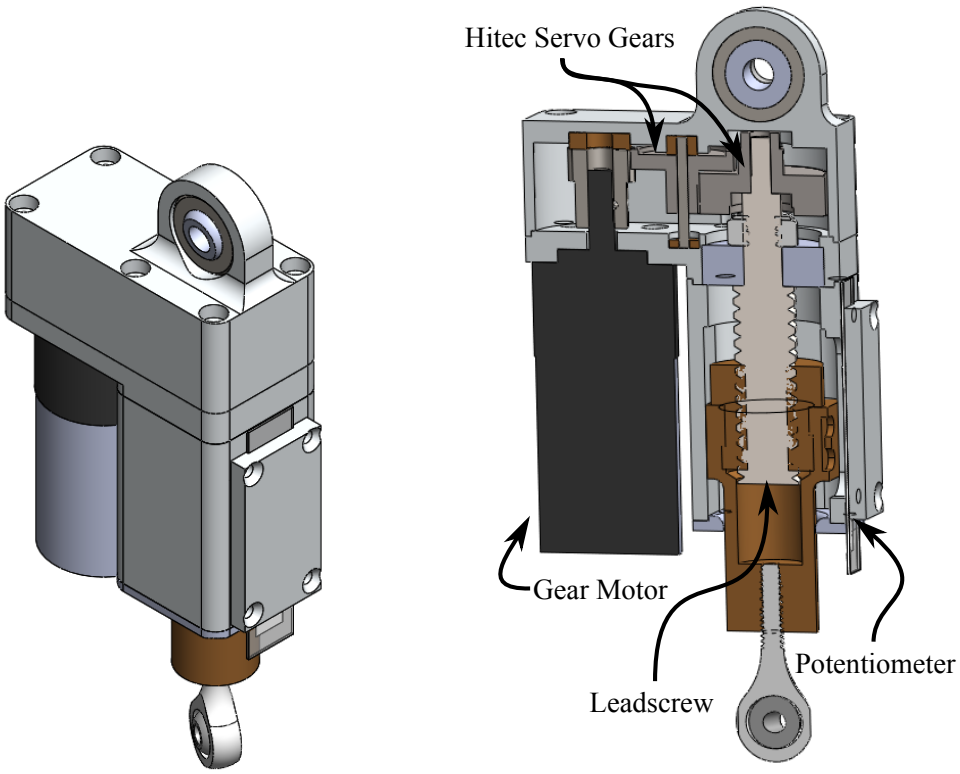

(a) (b)

Figure 3.12: Upper rotor linear servo-actuator CAD views (a) Isometric (b) Cross-sectional view

Table 3.3: Geartrain stages and reductions

Component	Reduction
Planetary Gearbox	43:1
Stage 1	40:24
Stage 2	48:10
Total Gear Reduction	344:1
Leadscrew	6 tpi
Total	2064 tpi

Table 3.4: Servo actuator characteristics

	Hitec Servo	Linear Servo
Resolution [μm]	98	16
Repeatability [μm]	-	25
Maximum pitch error (lower rotor) [deg]	0.25	0.05
Maximum pitch velocity (lower rotor) [deg/s]	150	7.7*
Force at maximum power [N]	85	1750*

*theoretical

standard hover and wind tunnel tests.

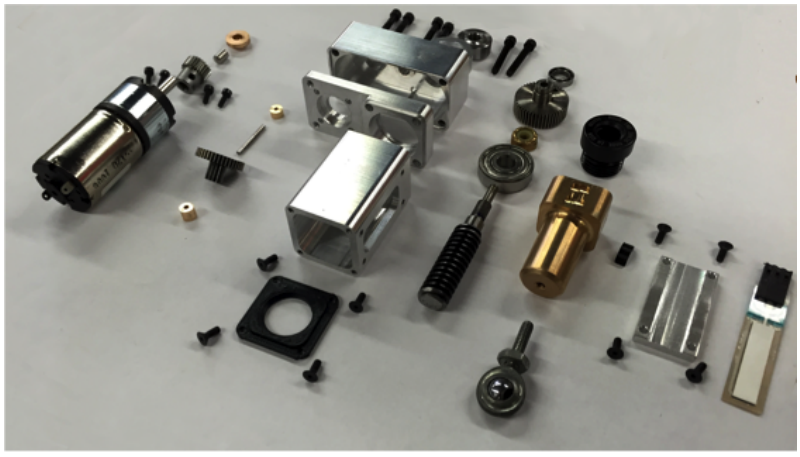

Figure 3.13: Finished linear servo actuator components before assembly

3.2 Instrumentation

3.2.1 Fixed Frame Instrumentation

Permanent fixed frame instrumentation both monitors test stand safety, and is used for analysis. Four integrated circuit, thermocouple based temper-

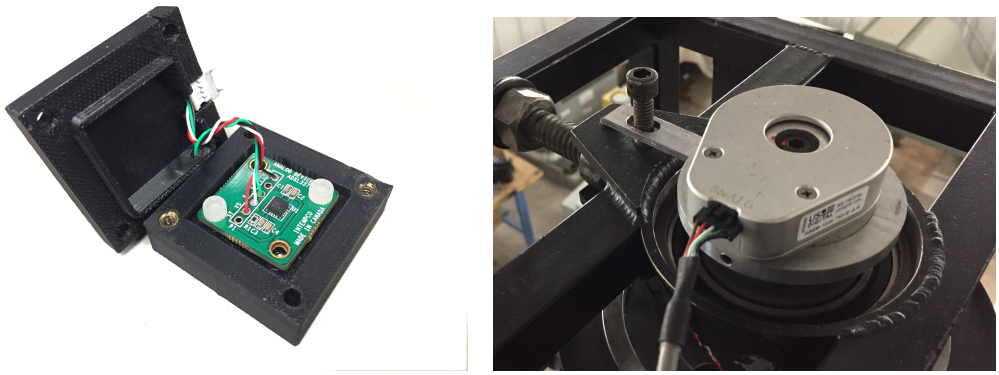

(a) (b)

Figure 3.14: Fixed frame instrumentation, (a) MEMS accelerometer with rapid prototyped mount, (b) Optical incremental encoder

ature transducers (Texas Instruments LM35) are mounted to each of the major bearing housings to monitor heat buildup and bearing health. A two-axis MEMS accelerometer (ADXL-330), shown in figure 3.14a monitors fixed-frame vibrations. It is used for dynamic balancing of the rotor system before testing, as well as for monitoring loads during tests where unsteady aerodynamic forcing may become significant. Finally a 4096 count/revolution optical encoder (US Digital HB6M) is mounted to the input drive-shaft as shown in figure 3.14b. This encoder is used to measure azimuth angle and RPM, and is also used for post-processing data via synchronous averaging of multiple revolutions. Additionally the encoder signal may be used to trigger external strobe lights, lasers, and cameras, precisely aligning measurements at repeatable azimuthal locations.

With the majority of the instrumentation located in the rotating frame, electrical slip-rings are necessary to transfer the signals back to the fixed frame

data acquisition. Two sliprings, supplied by Fabricast, are used. One with 24 channels for the upper rotor, and a second with 26 channels for the lower rotor. The upper rotor slipring is mounted below the test stand with wires running alongside the upper rotor pushrods through the inner shaft. The lower rotor slipring is mounted above the test stand, with wiring passing inside a protective sleeve that also serves as the inner shaft for locating the lower rotor swashplate. As sliprings introduce noise into the signals it is beneficial that only amplified signals pass from the rotating to fixed frames, a factor that is taken into consideration in the design of the rotating frame instrumentation.

3.2.2 Main Load Cells

A key requirement for the experimental setup was the ability to measure static and dynamic loads in all 6-axes for the upper and lower rotors separately. Two custom modified 6-component load cells (ATI Omega-160) [7], are mounted in the rotating frame directly below the upper and lower rotor hubs. The load cells feature on-board signal conditioning ensuring that only high level voltage signals are passed through the slip rings. The high-gain silicon semiconductor strain gages allow for a very stiff construction, with isolated load cell natural frequencies greater than 1000 Hz in all directions.

3.2.2.1 Calibration and Drift Corrections

The load cells are supplied with factory static calibrations for two of three load cases: low, medium and high. For all testing the medium calibra-

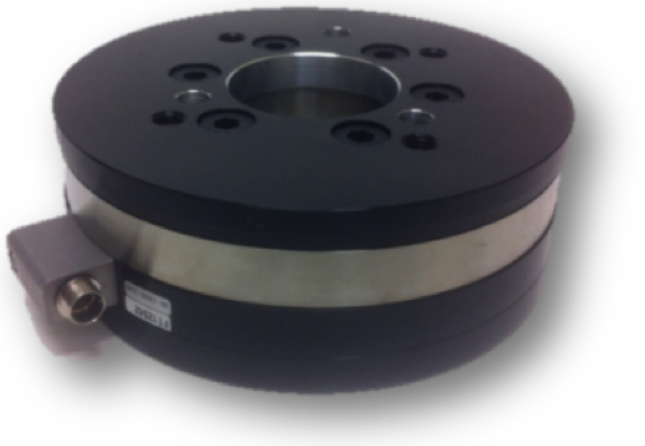

Figure 3.15: ATI Omega-160 6-component load cell

tion range was used. Table 3.5 shows the calibrated range, resolution, and uncertainty for all six load cell components. The load cell calibration is shown in equation 3.7. The 6×6 matrix of coefficients transforms the strain gauge outputs to the orthogonal forces and moments. A noteworthy characteristic of this calibration is the highly coupled nature, with resolved forces predominantly featuring a combination of two or three strain gauge signals. The stiffnesses listed in table 3.5, combined with rotor inertial properties, provide an estimate of the upper bound of the frequency response of the system. With a two-bladed rotor, aligned along the x-direction, the F_x, F_y and F_z force, and M_x moment measurements have natural frequencies greater than 700 Hz. M_z, rotor torque, has a natural frequency of 260 Hz while M_y, perpendicular to the blade-span, has a natural frequency of 200 Hz. Using this as an upper bound on the usable frequency range of the load cell, the highest rotor harmonics

Table 3.5: Omega-160 load cell factory calibration

Component	Range	Uncertainty	Stiffness
F_x, F_y	±1400N	4N	$7x10^7$N/m
F_z	±3750N	8N	$1.2x10^8$N/m
M_x,M_y	±240Nm	0.75Nm	$3.3x10^5$Nm/rad
M_z	±240Nm	0.5Nm	$5.2x10^5$Nm/rad

that may be measured range between six-per revolution at 1800 RPM and twelve-per-revolution at 900 RPM.

$$\begin{bmatrix} 3.43 & -0.37 & -7.26 & -175 & 3.88 & 154 \\ 7.06 & 187 & -2.00 & -101 & -4.21 & -89.0 \\ 266 & 0.76 & 273 & 2.79 & 270 & 1.52 \\ -0.22 & 0.12 & -17.5 & -0.29 & 17.0 & 0.08 \\ 19.4 & 0.11 & -10.0 & 0.01 & -9.89 & -0.18 \\ -0.24 & -9.38 & -0.28 & -10.6 & -0.46 & -9.09 \end{bmatrix} \begin{bmatrix} SG0 \\ SG1 \\ SG2 \\ SG3 \\ SG4 \\ SG5 \end{bmatrix} = \begin{bmatrix} F_x \\ F_y \\ F_z \\ M_x \\ M_y \\ M_z \end{bmatrix} \tag{3.7}$$

With the measured rotor loads not spanning the complete range for all load cell components there was a need to make corrections to certain calibration constants. Specifically the supplied calibration did not adequately decouple in-plane forces (F_x and F_y) from in-plane moments (M_x and M_y) at the low absolute values encountered during testing. While the error was not out of the possible uncertainty range for the load cell, it was much too large for the measurements acquired during wind tunnel testing. Correction factors were measured by applying in-plane moments using a vertical F_z force and a moment arm. Figure 3.16 shows the observed couplings for the lower rotor

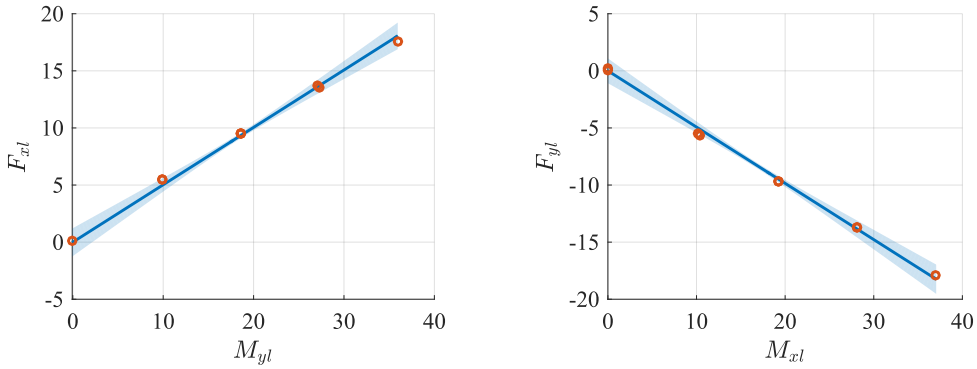

Figure 3.16: Lower rotor load cell in-plane moment-force couplings with linear fits and confidence bounds, (a) F_x-M_y coupling, (b) F_y-M_x coupling

Table 3.6: In-plane moment-force coupling correction factors

Components	Correction Factor [1/m]	Corrected Force Uncertainty [N]
M_y-F_x Upper	0.532	0.77
M_x-F_y Upper	0.502	2.00
M_y-F_x Lower	-0.465	0.85
M_x-F_y Lower	-0.492	0.30

load cell. To correct for these couplings the data was fit with a linear trend-line with zero intercept. Table 3.6 shows the correction factors for all four couplings as well as uncertainties in the resulting corrected forces. The uncertainty listed was calculated for a moment of equal magnitude but opposite sign to the maximum applied moment. This produces a conservative estimate of the error, as this value is farthest from the mean value of the moments used for creating the fit.

Finally, the load cells displayed a tendency to drift over time while

spinning. This was compensated by taking pre and post-test, zero RPM tare readings immediately following each test condition. Then working from the assumption that the load cell drift is linear with time the force readings were compensated as follows:

$$F_{z,corrected}(t_i) = F_z(t_i) - \left(\frac{t_i - t_0}{t_f - t_0}\right)[F_z(t_f) - F_z(t_0)] \tag{3.8}$$

Here t_i is the time of the measurement to be corrected, t_0 the time of the first tare reading and t_f the time of the final tare reading. Figure 3.17 shows both raw and corrected F_z data for the upper rotor spinning with no blades attached. The uncorrected force shows a clear linear drift away from zero as the test progresses. After applying the correction factor the force is steady, near $F_z = -5N$ for all test points except for the first and last non-rotating points. The residual $5N$ force may be accounted for by mechanical coupling from load cell wiring, as well as pushrod forces which may be compensated for, as shown in the following section 3.2.3.

3.2.3 Pitch Link Load Cells

Pitch link loads are an important design parameter for rotorcraft, and large pitch link loads due to retreating blade dynamic stall may be the limiting factor in increasing flight speeds. While this alone makes measurement of pitch link loads desirable, the unique main load cell configuration of the current test stand also necessitates measuring these loads so that the true rotor forces may be recovered. Figure 3.18 shows a free body diagram of the pushrod-hub-load

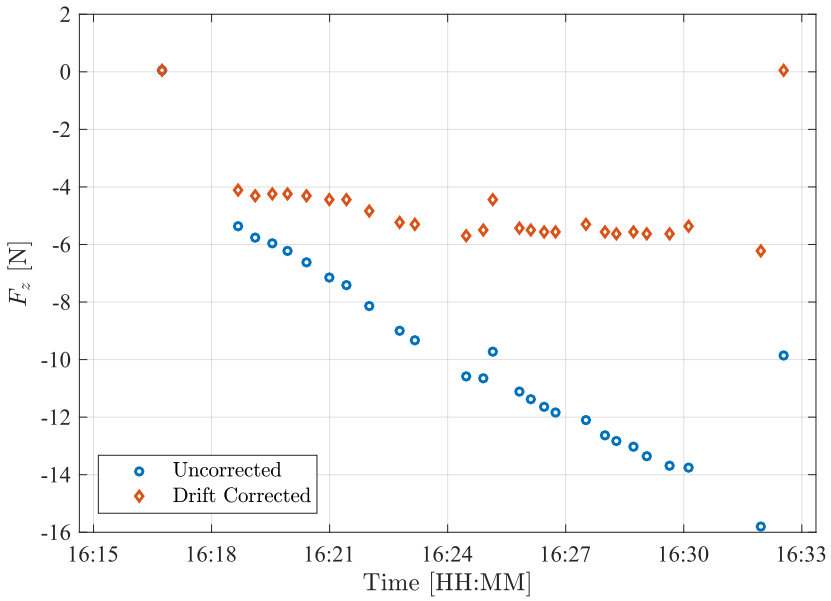

Figure 3.17: Raw and drift corrected upper rotor F_z with no applied rotor loads

cell system. The load cell reaction force is composed of the target hub load measurement as well as the pushrod forces, $F_{load} = F_{hub} - F_{PR1} - F_{PR2}$. These pushrod forces enter into both the F_z as well as M_x and M_y through moment arms associated with the pitch horn geometry. Equations 3.9 and 3.10 show the transformations of the pushrod loads to the load cell frame for both upper and lower rotor geometries.

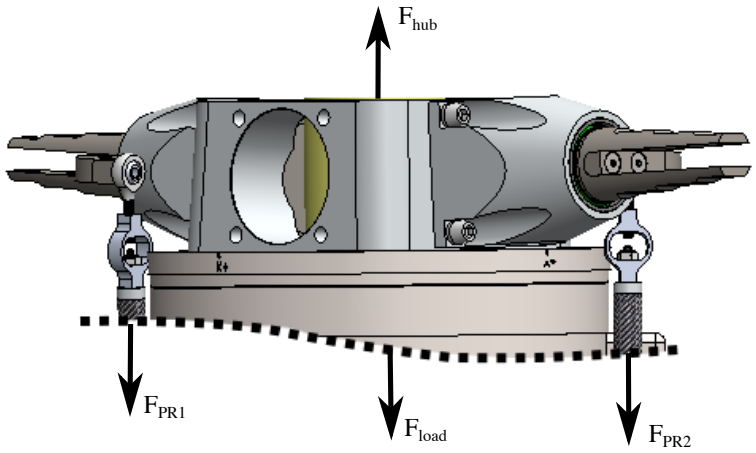

Figure 3.18: Free body diagram of pushrods, hub and load cell

$$\begin{bmatrix} 0 & 0 \\ 0 & 0 \\ -1 & -1 \\ -0.0127 & 0.0127 \\ -0.0069 & 0.0069 \\ 0 & 0 \end{bmatrix} \begin{bmatrix} F_{PR1,U} \\ F_{PR2,U} \end{bmatrix} = \begin{bmatrix} F_{xU} \\ F_{yU} \\ F_{zU} \\ M_{xU} \\ M_{yU} \\ M_{zU} \end{bmatrix} \tag{3.9}$$

$$\begin{bmatrix} 0 & 0 \\ 0 & 0 \\ -1 & -1 \\ -0.0834 & 0.0834 \\ -0.0348 & 0.0348 \\ 0 & 0 \end{bmatrix} \begin{bmatrix} F_{PR1,L} \\ F_{PR2,L} \end{bmatrix} = \begin{bmatrix} F_{xL} \\ F_{yL} \\ F_{zL} \\ M_{xL} \\ M_{yL} \\ M_{zL} \end{bmatrix} \tag{3.10}$$

The compensation of pushrod loads is very important for forward flight where the cyclic pitching motion required for rotor trim introduces pushrod forces of the same order of magnitude as the rotor thrust. Figure 3.19 shows how, even with no thrust or rotor cyclic, the subtraction of pushrod forces increases the accuracy of the measured hub loads. Subtracting pushrod loads brings the measured rotor thrust to within $2N$ of the expected zero thrust value for all points whereas the drift compensated measurements were $4-6N$ too low.

In order to fit inside the upper rotor shaft a full-bridge strain gauge instrumented hoop, with an integral instrumentation amplifier, was designed as shown in figure 3.20. Pure tension and compression forces applied to the hoop ends induce bending loads in the thin hoop arms. Figure 3.21 shows the normal and transverse strain components along the hoop arms for a tension loading. Here we see the outer hoop surfaces placed into compression while the inner surfaces are placed in compression. The hoops were wire EDM machined from 2024-T4 aluminum for high accuracy and quality surface finish. Preliminary rotor system simulations produced a target load range of $\pm 250N$ for high speed forward flight. The load cells were designed to ensure adequate fatigue life

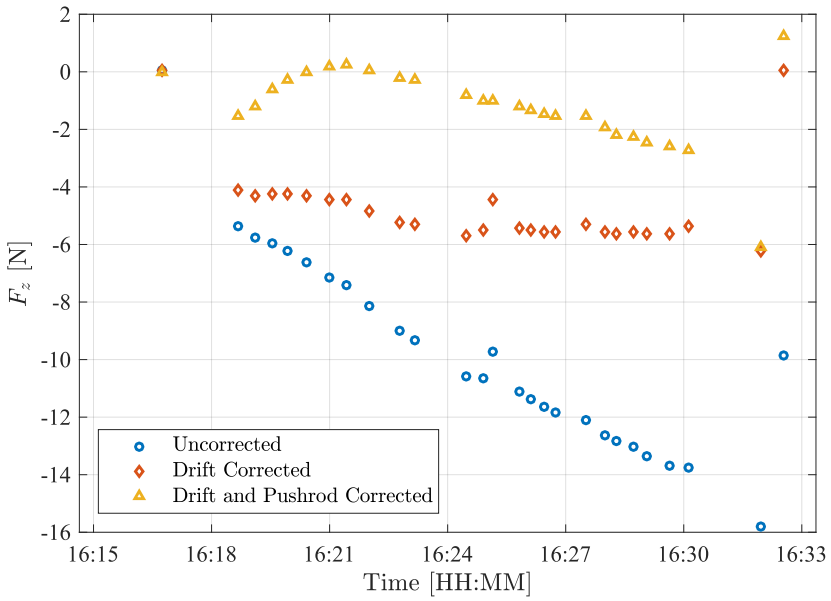

Figure 3.19: Raw and drift corrected upper rotor F_z with no applied rotor loads

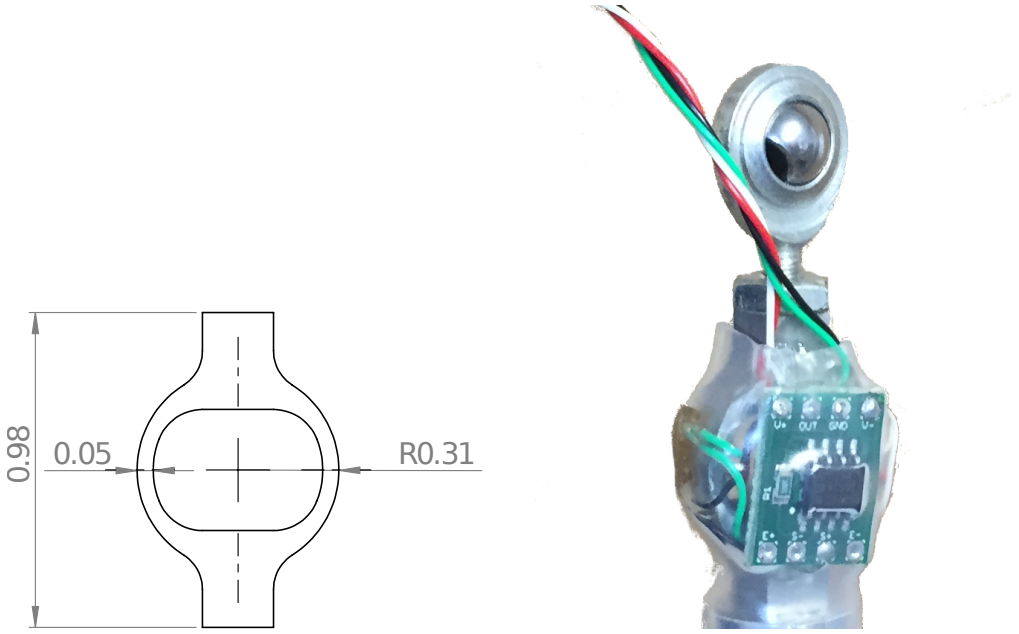

Figure 3.20: Strain gauge hoop (a) Dimensioned drawing (in) (b) Assembly with amplifier board

using resultant stress from the FEA analysis and stress-life calculations from the Metallic Material Properties Development and Standardization (MMPDS) Handbook [91]. For the fully reversed design load, fatigue life was found to be greater than 10^7 cycles, or more than 140 hours at 1200 RPM.

The strain distribution in the hoop arms, with opposite sides in tension and compression leads to the choice of strain gauge arrangement shown in figure 3.22. The arrangement is similar to that for a beam in bending, however the compressive and tensile strains are not equal in magnitude. Therefore the bridge sensitivity is calculated starting from first principles.

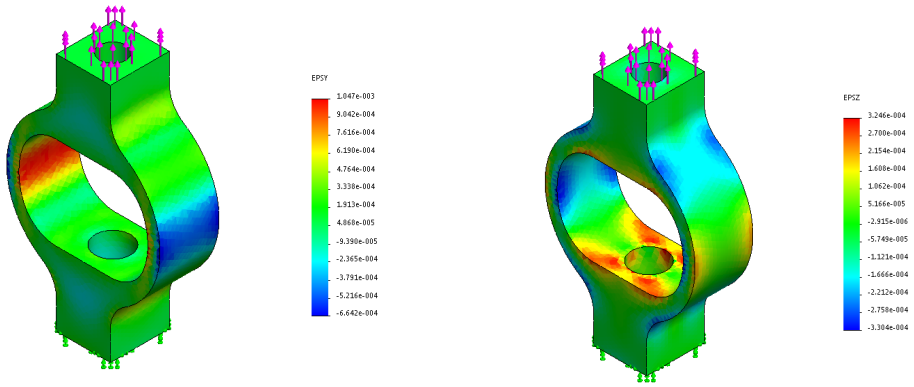

(a) (b)

Figure 3.21: FEA calculated strain under $220N$ tension loading (a) Tangential strain (b) Transverse strain

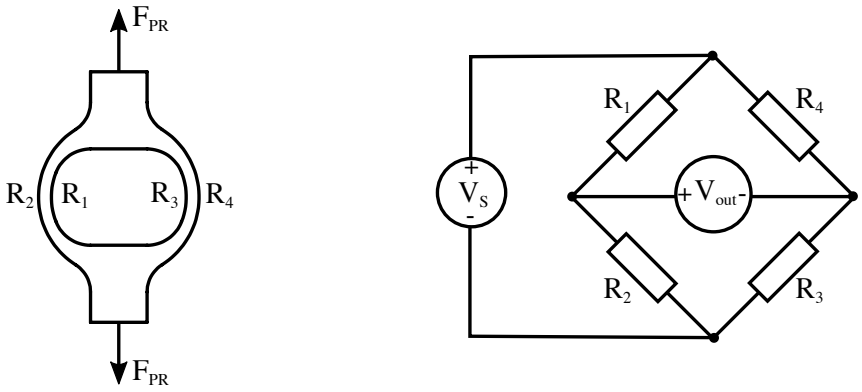

(a) (b)

Figure 3.22: Pitch link load cell strain gauge arrangement, (a) Gauge location on hoop, (b) Electrical arrangement in Wheatstone bridge

$$V_{out} = V_S \left(\frac{R_1}{R_1 + R_2} - \frac{R_4}{R_3 + R_4} \right) \tag{3.11}$$

$$V_{out} = V_S \left(\frac{R_1 (R_3 + R_4) - R_4 (R_1 + R_2)}{(R_1 + R_2)(R_3 + R_4)} \right) \tag{3.12}$$

With $R = R + \Delta R$ where $\Delta R << R$ and $R_1 = R_2 = R_3 = R_4$ equation 3.12 may be rewritten, ignoring higher order terms, as:

$$V_{out} = \frac{V_S}{4} \left(\frac{\Delta R_1}{R_1} - \frac{\Delta R_2}{R_2} + \frac{\Delta R_3}{R_3} - \frac{\Delta R_4}{R_4} \right) \tag{3.13}$$

For the constantan foil strain gauges used (Omega SGT-3J/350-TY43) resistance is related to strain through a gauge factor (GF) as:

$$\frac{\Delta R_g}{R_g} = GF\epsilon \tag{3.14}$$

For strain gauges of equivalent gauge factor and initial resistance substitute 3.14 into 3.12 and assume symmetric strains in each hoop arm:

$$V_{out} = \frac{V_S GF}{4} (\epsilon_T - \epsilon_C + \epsilon_T - \epsilon_C) \tag{3.15}$$

From the FEA analysis the relationship between pushrod force and strain was found to be $\epsilon_T = 4.727 \times 10^{-6}/N$ and $1.56\epsilon_C = -\epsilon_T$. The gauge factor is 2.11 ± 0.1 and the maximum allowable excitation voltage is $10V$. Therefore the theoretical relationship between output voltage and pushrod force for the bridge is:

$$V_{out} = 81.8 \pm 4.0 \mu \text{V/N} \tag{3.16}$$

In order to prevent excessive noise from entering the pushrod loadcell signals, compact instrumentation amplifiers were designed to mount directly to the hoops. The instrumentation amplifier (Analog Devices AD623) gain is determined by a single resistor, minimizing part count. The boards were designed with surface mount components including power supply decoupling capacitors. The board ciruit diagram, bill of materials, and layout schematics are included in Appendix 1. With a target full-scale measurement range of $\pm 250N$ the gain was set at 99 using precision 1kΩ resistors resulting in a final amplified output sensitivity of:

$$V_{amp} = 8.10 \pm 0.40 \text{mV/N} \tag{3.17}$$

The chosen sensitivity results in a full-scale measurement voltage range of $\pm$1.9V. While this gain does not utilize the full $\pm$5V supply voltage range, it does allow a margin for initial bridge imbalances.

The loadcells were calibrated in tension using a series of proof masses. The results of the four calibrations are presented in table 3.7. The bias error is calculated for the maximum compressive load for a conservative estimate. The measured sensitivities fall within the uncertainty of the calculated value, validating the design analysis. Despite significant offsets in three sensors, the

Table 3.7: Pushrod loadcell calibrations

Sensor	Sensitivity [mV/N]	Offset [V]	Calibration Bias Error [N]
Upper 1	7.93 ± 0.08	2.88	2.23
Upper 2	8.28 ± 0.03	0.13	0.51
Lower 1	7.83 ± 0.08	2.88	1.25
Lower 2	7.83 ± 0.08	2.87	1.13

full scale range does not exceed ±5V. After digitization the nominal sensor resolutions are 0.02N.

3.2.4 Root Pitch Angle Sensors

Root pitch angle measurements are required, both for rotor control trimming as well as for analyzing elastic control system deflections due to the blade pitching dynamics. Traditional optical or magnetic encoders were not able to fit in the limited space available, especially for the lower rotor in proximity to the upper rotor shaft. As a result a pitch measurement system, with a linear Hall effect sensor (Honeywell SS495A1) and two Neodymium magnets, was designed to fit inside the existing hub envelope. The system, pictured in figure 3.23, operates with the stationary Hall effect sensor measuring the magnetic field as the two magnets of opposite polarity rotate with the bladegrip.

The response of the system was sensitive to both the axial gap between the Hall effect sensor and the magnets, as well as to the radial separation distance between the magnets. With a measurement range target of 30°, several

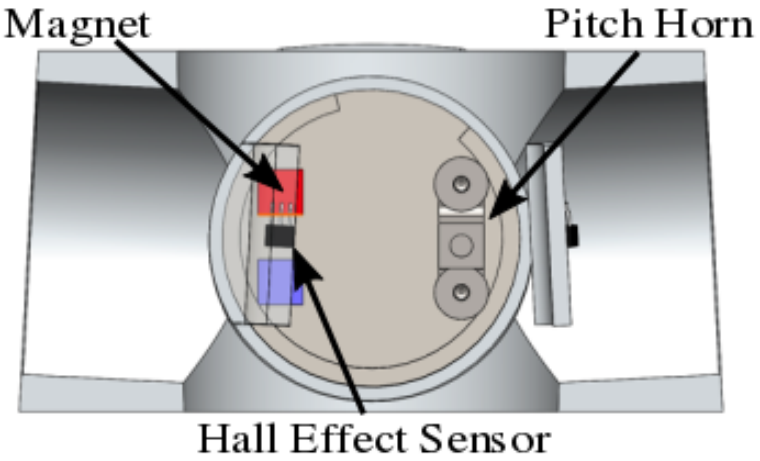

Figure 3.23: Diagram of upper rotor root pitch angle sensor and magnets

combinations of axial and radial distances were tested using an adjustable jig. Figure 3.24 shows two of the tested configurations. Significant non-linearity, as well as output saturation and extreme angles is apparent for the curve with 2.5 mm separation. Increasing the axial separation from 2.5 to 4.1 mm, the maximum allowable by packaging constraints, reduces the sensitivity of the sensor preventing saturation. Here the Hall effect output is nearly linear over the entire 30° range of motion. Figure 3.25a shows an installed sensor calibration with both first and third order polynomial fits. The fit bias uncertainties are ±0.6178° and ±0.41° for the first and third order fits respectively. From the fit residuals in figure 3.25b it is clear that the first order fit residuals are not normally distributed and the third order calibration is most appropriate. For real time monitoring the first order fits were used while the experimental data was post-processed with the third order fits for higher accuracy.

With the final configuration dimensions determined, jigs for magnet

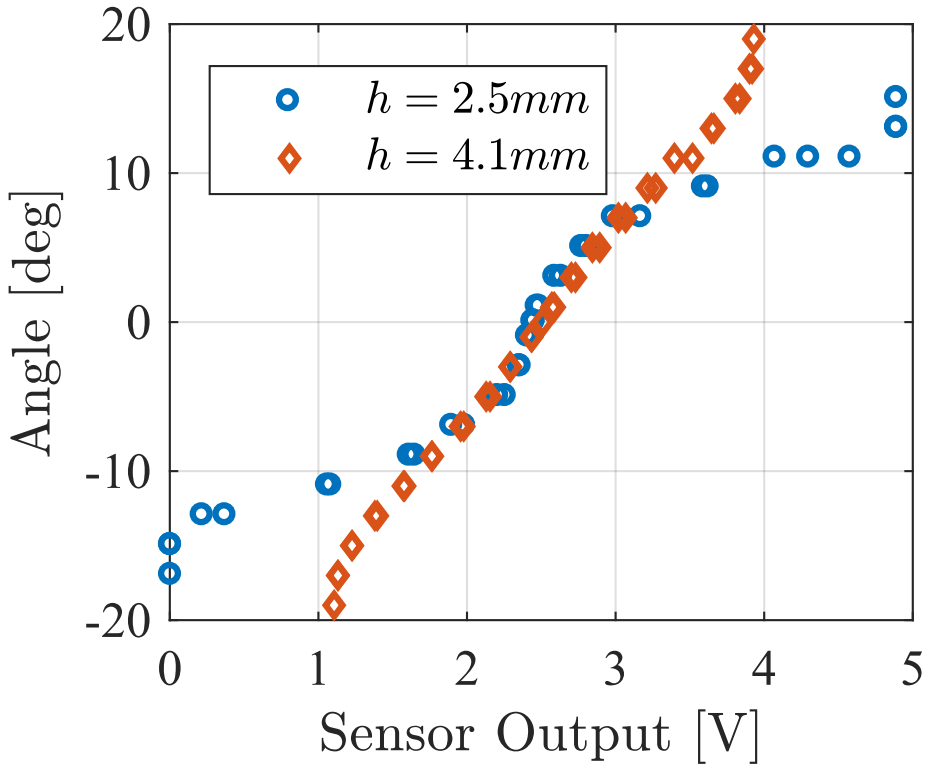

Figure 3.24: Variation of Hall effect output with variation in axial separation distance (radial separation = 6.2 mm)

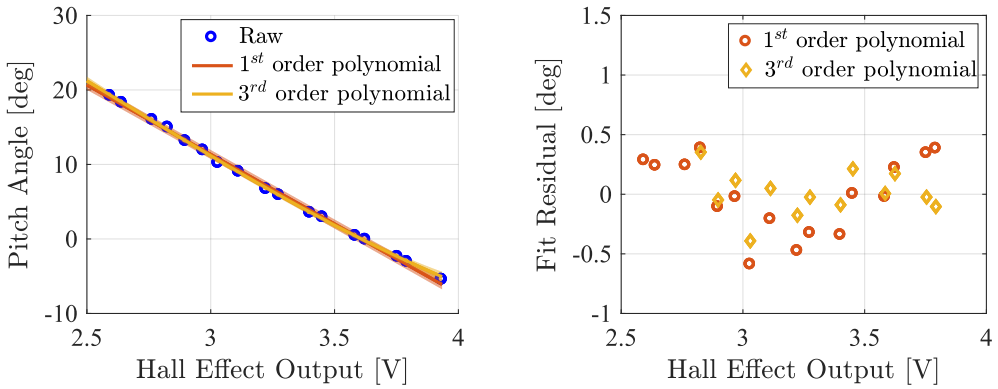

(a) (b)

Figure 3.25: Installed sensor calibration, (a) Raw data with first and third order polynomial fits, (b) Fit residuals for first and third order polynomials

and Hall effect mounting were made. Shown in figure 3.26, the Hall effect sensor jig is rapid prototyped from ABS plastic and designed to interface with the bearing carrier mount bolts, while the magnet mounting jig is laser cut from plywood. The magnets are mounted with a 10° offset such that the effective root pitch angle measurement range runs from −5° to 25°.

3.2.5 Blade Tip Clearance Sensor

During testing with lift offset, the advancing rotor blades produce excess thrust, flapping upwards, while the retreating blades flap downwards. In the coaxial configuration the lower rotor blades flap upwards near $\psi = 270°$, where the upper rotor blades simultaneously flap downwards. This decreases tip clearance as lift offset is increased, and in extreme cases can lead to collisions and blade destruction.

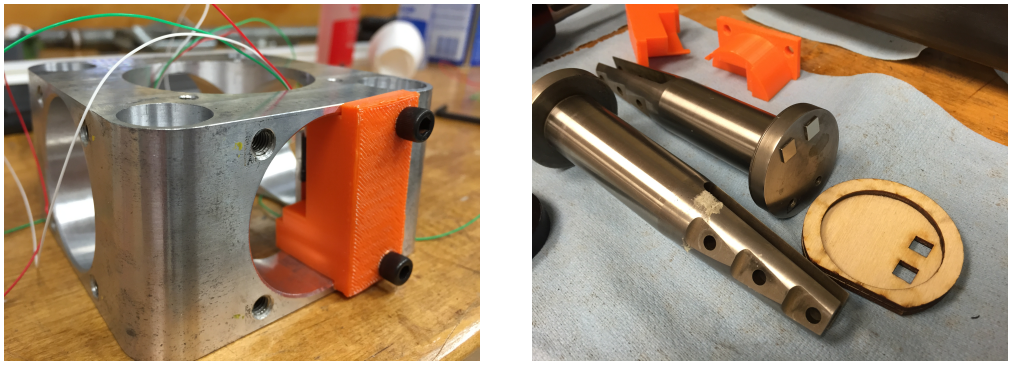

(a) (b)

Figure 3.26: Jigs for pitch angle sensor construction (a) Rapid prototyped fixture for Hall effect mount (b) Laser cut magnet locating jig with bladegrips

In order to ensure safety during testing at high lift offsets, the blade tip clearance was monitored using an optical sensor embedded in the lower surface of an upper rotor blade as shown in figure 3.27. The primary goal of the sensor was to ensure that tip clearance remained greater than 5% radius ($\approx$ 50mm) during testing, with a secondary goal of measuring trends in tip clearance. Two related designs were implemented. The first, shown in figure 3.28a consisted of an integrated circuit infrared distance sensor (Vishay VCNL4020) and a microcontroller located at the upper rotor hub. The Vishay sensor packages an IR LED with a photodetector and hardware for ambient light compensation. Custom circuit boards for embedding the sensors in the blades were produced, with schematics and board layouts included in appendix 1. The digital sensor communicated with the central microcontroller using a digital serial interface for triggering acquisition and returning the measured clearance. While the sensor performed well in stationary testing, it exhibited

unexplained drift followed by saturation with the rotor system spinning.

The second sensor, shown in figure 3.28b consists of a discrete IR LED and accompanying photodiode. Signal conditioning located on the upper rotor hub converts the photodiode output into a voltage that is related to the intensity of light reflected from the lower rotor blade tips, which are painted white to enhance the signal. This analog sensor was simultaneously sampled with the other test stand instrumentation, and captured all four blade crossings per revolution. Tests with the analog sensor were performed without external illumination to ensure accurate readings without ambient light contamination.

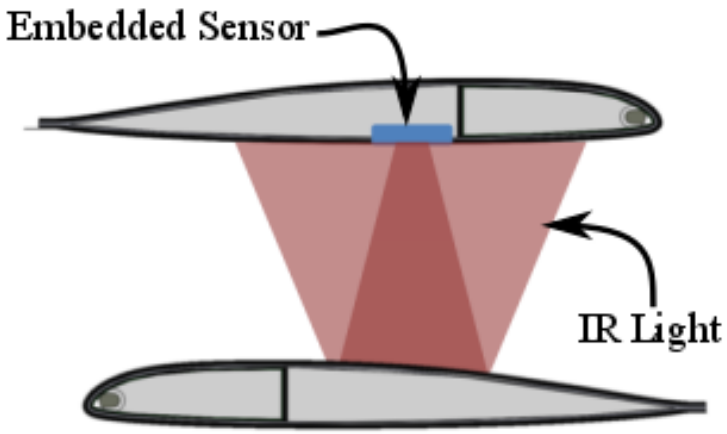

Figure 3.27: Blade clearance sensor operational diagram

Located at approximately 0.9R and immediately aft of the blade spar, the sensor is connected to wires inserted during the blade curing process and potted in place with epoxy adhesive. Calibrations were performed with the

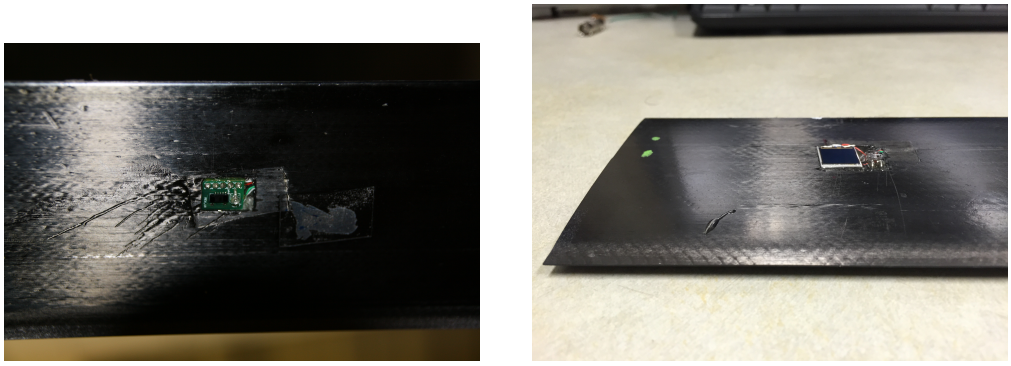

(a) (b)

Figure 3.28: Embedded blade clearance sensors (a) Digital sensor (b) Discrete analog sensor

blades mounted to the rotor system. The relationship between sensor voltage and clearance is well captured by a quadratic polynomial curve fit as shown in figure 3.29. The calibration curve uncertainty, shown as a shaded region in figure 3.29, varies between 5–10 mm (0.5–1% R). This uncertainty is sufficiently small to allow measurement of trends in tip clearance with rotor system operating conditions in addition to functioning as a safety limit sensor.

3.3 Data Acquisition

The data acquisition (DAQ) system uses a National Instruments (NI) PXIe modular instrumentation system for all input and output. Three multifunction DAQ cards are used, two NI PXI-6358 cards with simultaneously sampled analog inputs, and one PXI-6225 with up to 80 sequentially sampled analog inputs. The specifications of all three cards are summarized in table 3.8. All three cards may share sampling clocks through the PXI chassis back-

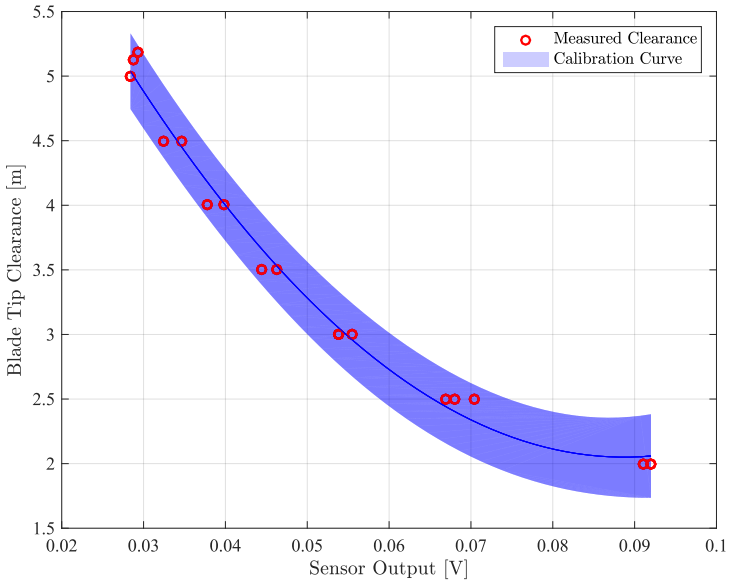

Figure 3.29: Blade clearance sensor calibration curve

pane to ensure synchronization. The two 6358 cards, with their simultaneous sampled inputs, were used for all analog sensors which were simultaneously sampled at 30 kHz, corresponding to 1000 samples-per-revolution at the maximum nominal rotor speed of 1800 RPM. One high speed counter on the 6225 card was used for measuring the azimuthal angle output from the optical encoder. The incremental A channel of the optical encoder was also used for driving a second high speed counter to generate an output pulse train phase locked to the rotor rotational frequency. This channel was used for triggering of external sources including strobe and laser lights for illumination at integer multiples of the fundamental rotational frequency. Phase offset of this output was adjustable in steps of 1/1024 revolutions. Finally a single digital

Table 3.8: Data acquisition card specifications

	PXI-6358	PXI-6225
Analog Inputs	32	80
ADC Resolution	16 Bit	16 Bit
Simultaneous Sampling?	Yes	No
High Speed Counters	4	2
Digital Input/Outputs	48	24

input is available for recording trigger signals from external instrumentation for measurement synchronization during post-processing.

3.3.1 LabView Virtual Instrument

A series of LabView Virtual Instruments (VIs) were created for conducting experiments, monitoring test stand safety, and saving test data. The VIs were constructed with a modular architecture, shown in figure 3.30. The data acquisition process begins with the initialization and synchronization of the three DAQ cards. Data collection begins and data is read in a high speed loop with no additional processing. The data then passes via an asynchronous queue to an initial processing loop, where measurements are scaled by calibration constants and tare readings removed. A VI divides the data into complete revolution blocks (if test stand is stationary data is divided into 0.5 second blocks) which are then passed via a second asynchronous queue to the main state machine loop. This loop provides tools for realtime evaluation of data and test stand safety, including raw sensor readings, control angle measure-

ments and trim conditions. Data may be synchronously averaged to reduce noise, and both raw and averaged data recorded to text files in integer multiples of revolutions. Strobe and external trigger output is controlled by a secondary loop running in parallel with the main loop. The state machine architecture enables rapid modification and expansion of the VI for integrating additional sensors or analysis capabilities. During wind tunnel testing the status of the test stand was monitored from the trimming panel. Shown in figure 3.31, the panel includes key readings for evaluating system trim as well as safety margins. The labeled readout are as follows:

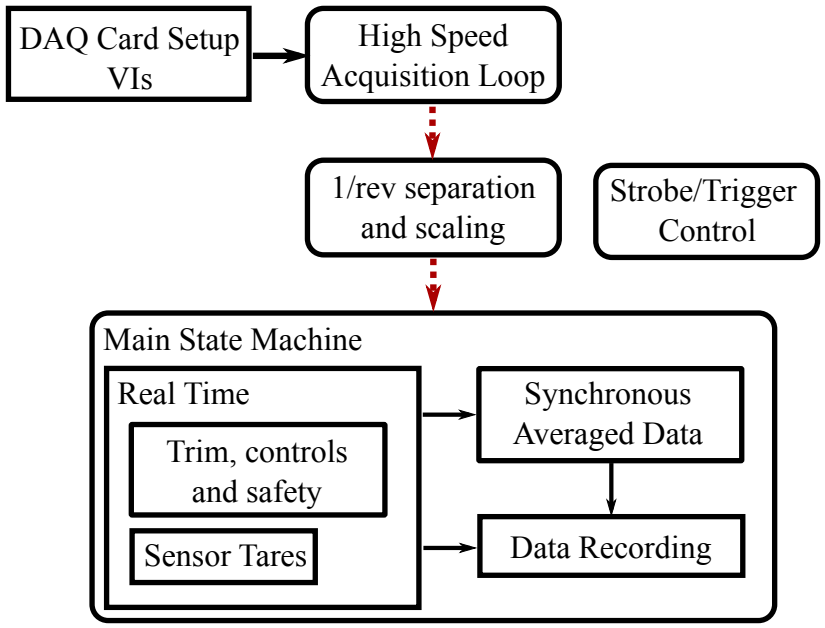

Figure 3.30: Diagram of LabView VIs, red dashed lines indicate asynchronous queue communication

1. Synchronous averaging and data storage
2. RPM strip chart
3. Torque balance and rolling moments with targets for trimming
4. Upper and lower rotor control settings (θ_0,θ_{1S},θ_{1C})
5. Pushrod force and accelerometer harmonic amplitudes
6. Blade clearance sensor readout

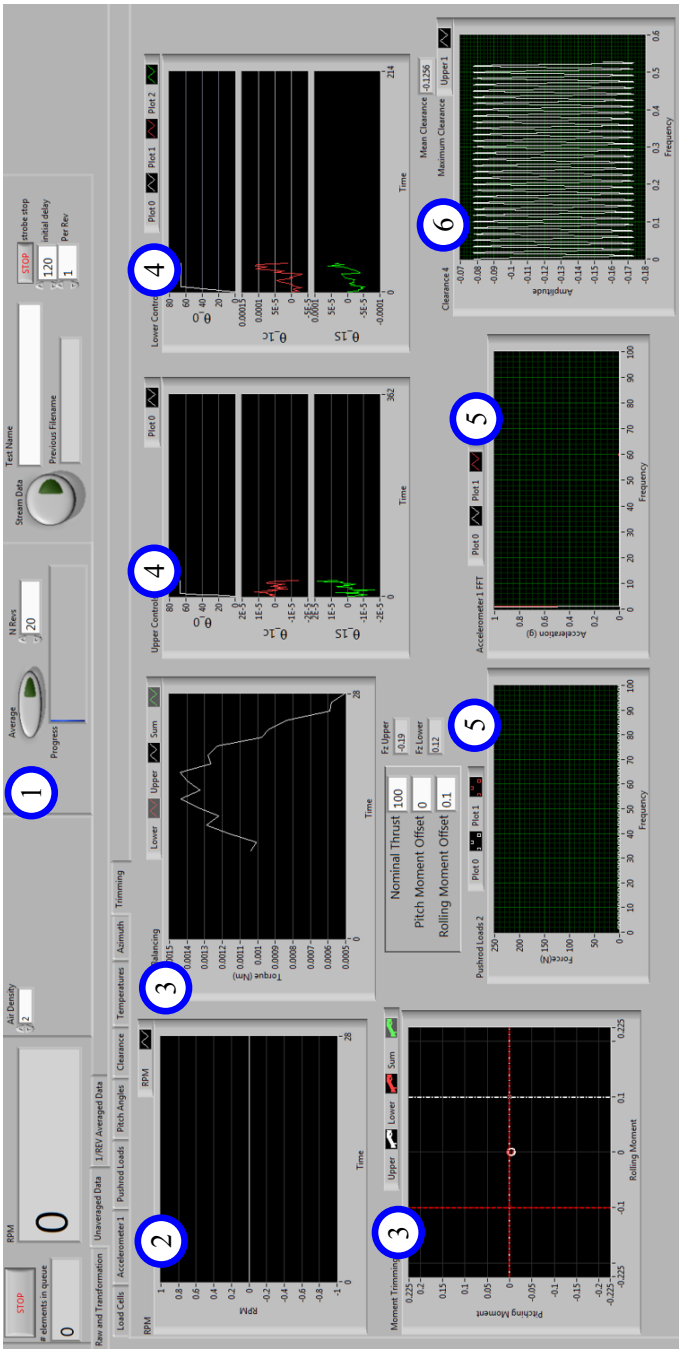

Figure 3.31: Diagram of LabView VI trimming and safety panel

Chapter 4

Blade Construction and Characterization

This chapter describes the construction and characterization of the rotor blades. §4.1 covers the construction of two different rotor blade designs, an initial reference blade, and a stiff reinforced design. Next, static characterization of the blade elastic properties is presented in §4.2. The digital image correlation technique is introduced in §4.2.2.1 and used to measure the displacements of the non-uniform reinforced blade. Dynamic characterization of the reinforced blade modal properties is presented in §4.3. High speed digital image correlation is combined with modal analysis techniques to extract blade natural frequencies and mode shapes. The results of the static and dynamic characterization are compared with, and used to update blade numerical model properties.

4.1 Blade Construction

The rotor blade is based on a uniform VR-12 cross section with zero twist and zero taper. The VR-12 airfoil, developed by Boeing Vertol, is a second generation helicopter airfoil, designed using coupled potential flow and boundary layer simulations [62]. Dadone [27], describes the complex trade-offs

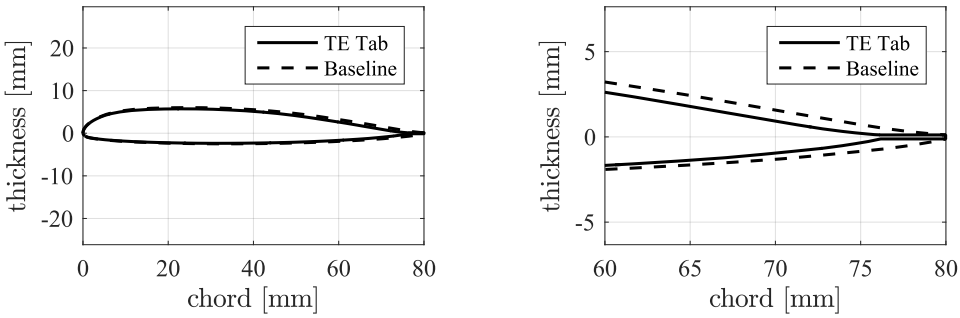

Figure 4.1: Comparison of VR12 airfoil baseline with 5% trailing edge tab (a) Complete airfoil (b) Trailing edge detail

involved in helicopter airfoil design, as factors including, maximum lift, drag divergence Mach number, pitching moment and dynamic stall characteristics must be considered. The VR-12 airfoil provides high lift while maintaining a modest drag divergence Mach number greater than 0.77 [62]. The current blades add a trailing edge tab, with 5% chord length, to the baseline VR-12 airfoil as shown in figure 4.1a. The trailing edge tab, detailed in 4.1b, adds reflex camber near the airfoil trailing edge. This helps to reduce pitching moment and control forces magnitudes.

4.1.1 Materials

The blades are constructed with solid foam cores wrapped with preimpregnated (prepreg) carbon fiber reinforced epoxy composites. Two carbon-epoxy composite materials are used, a plain weave AS4/3501-6 prepreg, and a IM7/3501-6 uni-directional tape. The material properties for both were estimated from several sets of experimental data. Data for composites using

Table 4.1: 3501-6 and 8552 epoxy comparison

	3501-6, Neat	8552, Neat	AS4/3501-6	AS4/8552
ρ[g/cm^3]	1.265	1.301	1.136	1.136
E_{11} [GPa]	4.24	4.67	141	141
ν_{12}	0.365	-	-	-
Fiber volume fraction	0	0	0.62	0.58
t [mm]	-	-	0.132	0.132

3501-6 epoxy matrix are extremely limited. As a result, test data from composites cured with 8552 epoxy are substituted. To justify this substitution, consider the data in table 4.1, taken from Hexcel material data sheets [38, 39]. Both neat resin and unidirectional AS4 prepreg tape properties are considered. While there is variation in the resin properties including elastic modulus, when cured with carbon fibers with approximately 60% volume fraction there is minimal variation in the reported properties between the two epoxies. As complete blade stiffness properties will be verified experimentally, the 8552 resin prepreg data is sufficient for preliminary design analyses. Tables 4.2 and 4.3 show properties for the unidirectional IM7 tape and plain weave AS4 fabric respectively. Data is presented from the previously mentioned Hexcel datasheets [39], the Department of Defense Composite Materials Handbook [2], and from tests performed by the National Center of Advanced Materials Performance for the FAA [69, 70].

The AS4 plain-weave fabric is used exclusively in the $\pm 45°$ orientation to provide torsional stiffness. The lamina elastic properties when rotated

Table 4.2: IM7/8552 unidirectional tape properties

	Ref. [39]	Ref. [69]	Ref. [2]	Compiled
ρ[g/cm^3]	1.57	1.58	-	1.57
E_{11} [GPa]	168	162	-	165
E_{22} [GPa]	-	10.1	-	10.1
ν_{12}	-	0.36	-	0.36
G_{12} [GPa]	-	4.69	-	4.69
v_f	0.58	0.573	-	0.58
t[mm]	0.132	0.183	-	0.183

Table 4.3: AS4/8552 plain weave properties

	Ref. [39]	Ref. [69]	Ref. [2]*	Compiled
$\rho\,[g/cm^3]$	1.57	1.58	1.55	1.57
E_{11} [GPa]	68	64.5	67.5	66
E_{22} [GPa]	68	65.5	67.5	66
ν_{12}	-	0.031	-	0.031
G_{12} [GPa]	-	4.96	-	4.96
v_f	0.553	0.553	0.525	0.55
t[mm]	0.195	0.198	0.203	0.198

*3501-6 Epoxy Matrix

Table 4.4: AS4/8552 plain weave elastic properties, ±45° orientation

E_x [GPa]	17.3
E_y [GPa]	17.3
G_{xy} [GPa]	32.0

Table 4.5: Additional blade construction materials

	FM-300K	Rohacell IG31-F	Tungsten
ρ [g/cm^3]	1.15	0.052	19.25
E [GPa]	-	0.070	-
G [GPa]	-	0.019	-
t [mm]	0.20	-	-

45°, as calculated using classical lamination theory, are presented in table 4.4. Additional materials used in the blade construction include FM-300K film adhesive [26], Rohacell IG31-F closed cell foam [32], and tungsten for mass balancing. The relevant properties for these materials are given in table 4.5.

4.1.2 Reference Blades

The base blade construction is based on a method used by Bao [11]. A two-cell construction technique with solid foam cores is used. The design, shown in figure 4.2, results in a forward D-spar section, housing the tungsten balancing weights and aluminum root insert, joined to an aft section with reduced layup thickness. In contrast to designs featuring a separately cured spar, this construction technique allows for the blade to be cured as a single assembly. The blade is cured in a 36 inch long aluminum female mold. The

two mold halves are located with dowel pins and compression provided by 18 bolts distributed along each side. The detailed blade fabrication steps are outlined in the next three sections.

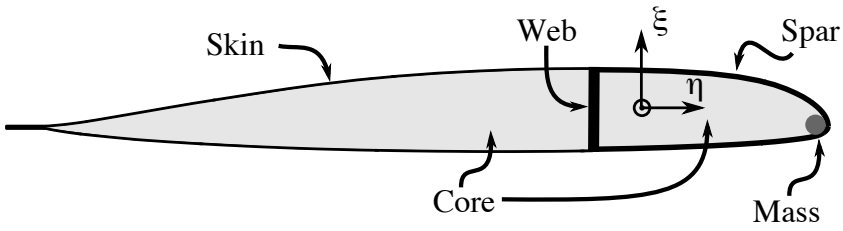

Figure 4.2: Blade cross section with labeled components

4.1.2.1 Core and Insert Preparation

The first step in producing a blade is forming the foam core. The core acts as a mandrel for the composite material, while also providing buckling resistance to the finished blade. The foam core material is sanded to near-net shape using rapid-prototyped guides, then compressed in the aluminum mold and heated to 250°F for thermoforming and smoothing. Next the core is separated into fore and aft pieces using a sliding razor-blade jig. The fore foam core is machined to accept leading edge tungsten weights for controlling the blade center of gravity, as shown in figure 4.3a. Visible on the right hand side of figure 4.3a is a rectangular cutout in the blade-root for an aluminum insert. This insert provides compressive strength where the blade will be clamped in the hub blade-grips. The tungsten masses are cut from pure tungsten welding rods into 2 inch lengths, and distributed along the leading edge with 1" spacing.

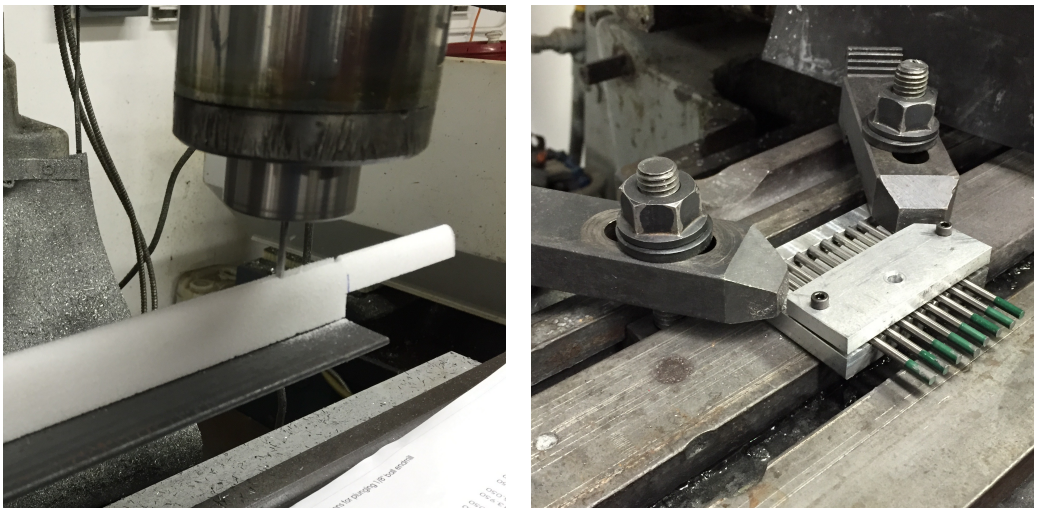

(a) (b)

Figure 4.3: Foam core and insert machining, (a) Milling leading edge slots for tungsten inserts, (b) Cutting tungsten leading edge masses to length using diamond cutting wheel

Figure 4.3b shows the jig designed for cutting the tungsten using an abrasive diamond cutting wheel.

4.1.2.2 Composite Layup and Curing

The first step in the layup is assembling the D-spar. Film adhesive is used to bond the aluminum and tungsten inserts into the foam core as shown in figure 4.4. The excess aluminum insert protruding from the foam core serves as a datum for post-cure machining. Next the core is wrapped in a single ply of film adhesive, followed by a unidirectional im7/3501-6 ply, with fibers oriented in the spanwise direction. The unidirectional ply is overlapped on the aft edge of the spar, forming a web with two plies thickness. The completed spar is

then joined with the aft foam core as shown in figure 4.5a. The blade skin, a single ply of ±45° AS4 is then wrapped around the two cores and joined at the trailing edge, forming the trailing edge tab. Figure 4.5b shows the fully assembled blade, wrapped in release film for achieving a high quality surface finish, and placed in the aluminum mold.

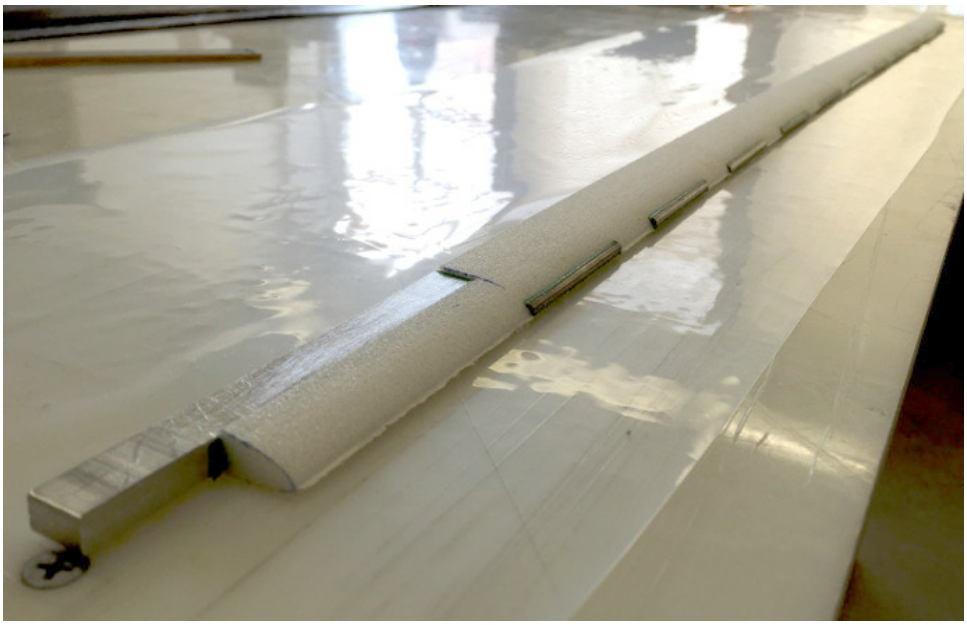

Figure 4.4: Foam core with bonded root insert and tungsten leading edge masses

The blade is cured in a high temperature autoclave oven shown in figure 4.6. The autoclave is kept at atmospheric pressure as compression is provided by the aluminum mold. The cure cycle for the 3501-6 epoxy involves two stages. First the temperature is ramped at 5°F/min to 250°F and held for one hour. Then the temperature ramps to 350°F for the final two hour cure. When the cure cycle is complete the oven is powered off, opened, and the blade left

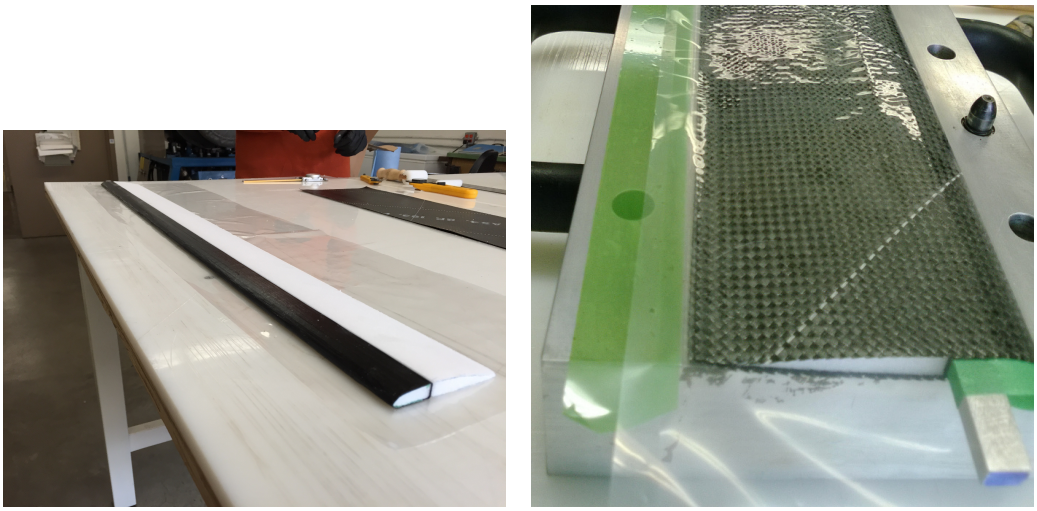

(a) (b)

Figure 4.5: Blade construction, (a) Completed D-spar joined to aft foam core, (b) Blade wrapped with outer skin and release film in mold

to cool overnight.

4.1.2.3 Finish Machining

After curing, the blade undergoes two finishing steps shown in figure 4.7. First the blade root, tip, and trailing edge are trimmed using a diamond abrasive cutoff wheel mounted on a horizontal mill. Then the blade is mounted to a vertical mill and holes drilled for the bladegrip bolts using a tungsten carbide drill bit. The finished blade dimensions are shown in figure 4.8.

4.1.3 Reinforced Blades

While the reference blades were sufficient for hover testing, it was determined that they were incapable of sustaining high lift offset testing in forward

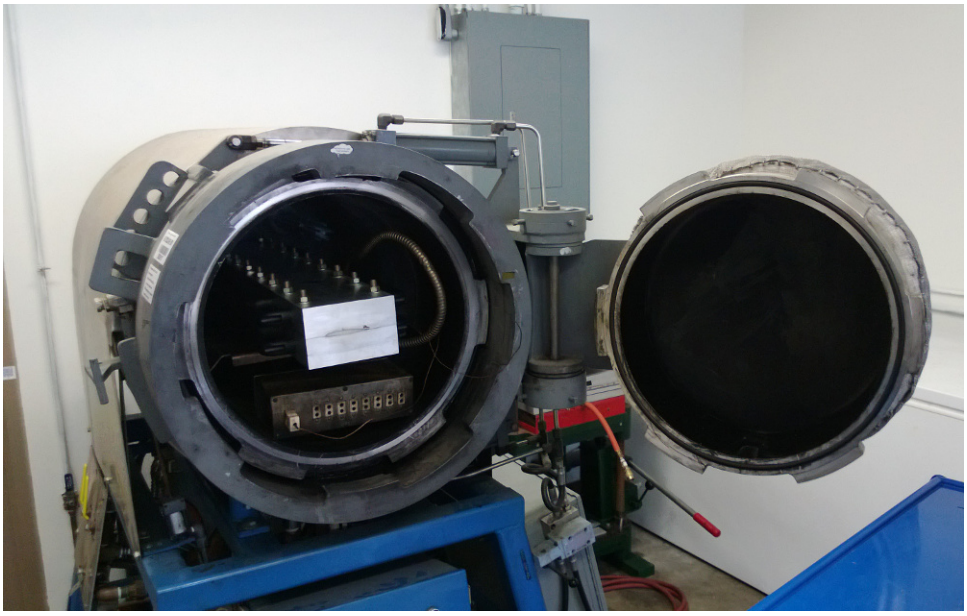

Figure 4.6: Closed mold in autoclave oven

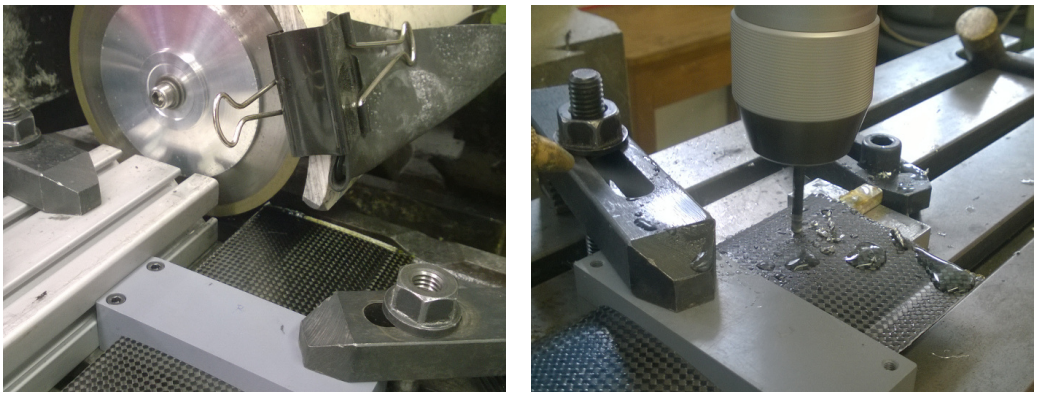

(a) (b)

Figure 4.7: Blade finish machining, (a) Trimming blade tip with diamond cutoff wheel, (b) Drilling holes for bladegrip bolts

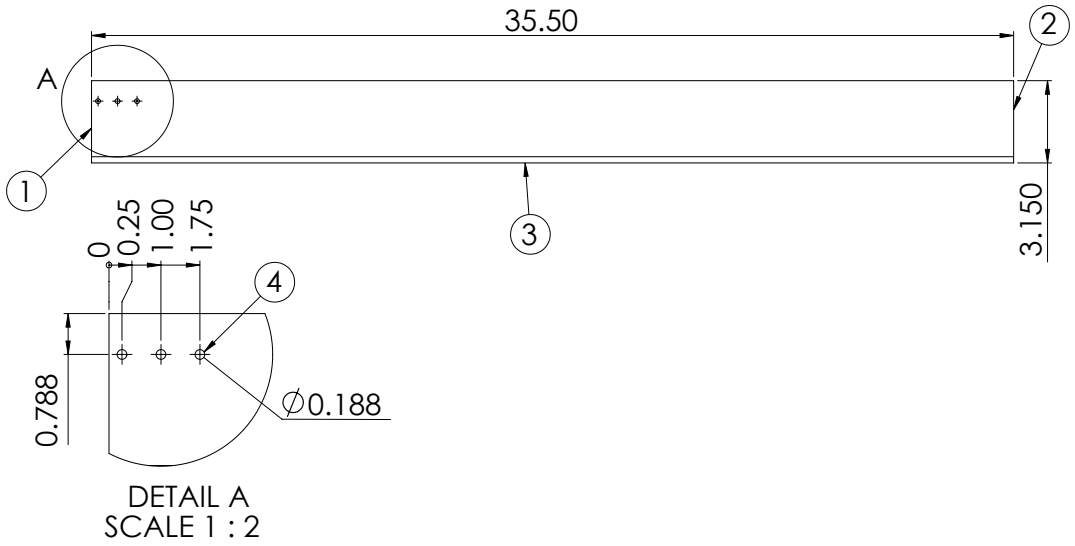

Figure 4.8: Finished blade dimensions, numbers indicate order of finish machining

flight. In a study by Schmaus and Chopra [96], a comprehensive analysis code was used to predict tip clearance for various blade properties. The reference blades were found to be capable of only 10% lift offset before the tip clearance safety limit of 5% radius was exceeded. Two major design factors were identified as targets for a new set of blades. The first is the blade first flapping frequency, closely related to the flap-bending stiffness, EI_η. The second is the blade Lock number, γ, a non-dimensional parameter that relates the blade aerodynamic flapping moments to the opposing inertial moments. The Lock number is a measure of the ratio of aerodynamic to inertial blade flap-bending moments. It is derived from the equations of motion of a spinning, rigid, articulated blade with linear aerodynamics as:

$$\gamma = \frac{\rho a \, c R^4}{I} \tag{4.1}$$

$$I = \int_e^R x^2 m \, dx \tag{4.2}$$

To decrease blade flapping the first flap frequency must increase while the Lock number decreases. Figure 4.9 shows the relationship between these design variables and the maximum achievable lift offset. The reference blades are indicated on the diagram along with the design target for a new set of reinforced blades. While decreasing the Lock number is accomplished simply by adding mass, thereby increasing the flap inertia; increasing the first flap frequency is more challenging. In the end a two step approach to achieving the new targets was chosen. The baseline VR12 blade composite layup was

modified, adding both mass and stiffness, and a post-cure bonded root reinforcement cuff was designed to increase stiffness. The linear beam model was used to predict the rotating flap stiffness for different combination of composite layup and cuff profile, iterating until an acceptable solution was found.

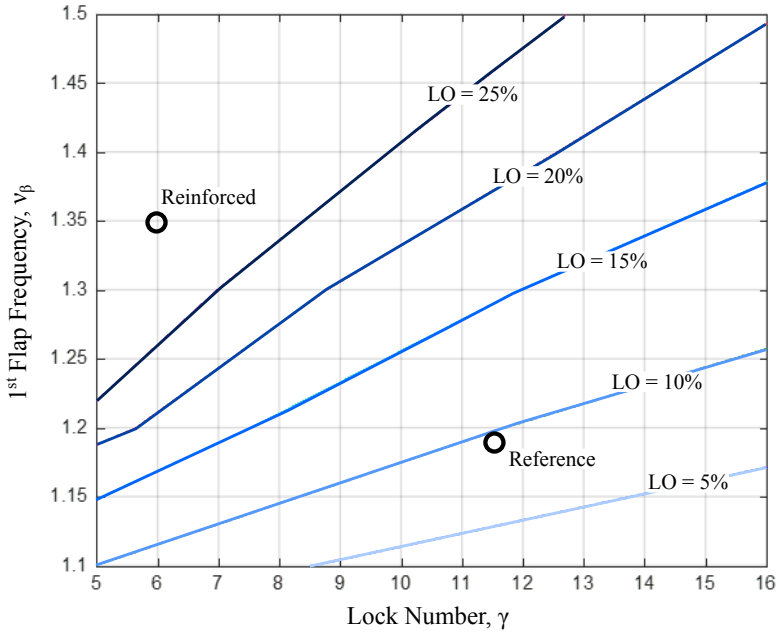

Figure 4.9: Maximum lift offset capability vs. Lock number and flap frequency, reference and reinforced blades marked

The main blade construction follows the same method as for the reference blades, with the only differences being in the laminates. The D-spar thickness is doubled, with two plies of unidirectional IM7, doubled on the aft edge creating a four-ply web. An additional ply of unidirectional IM7 is added on top of the AS4 skin, doubling the skin thickness. The final modification from the reference blade is that additional and larger tungsten counterweights

Table 4.6: reference and reinforced blade composition

	reference Blade	Reinforced
Spar	[FM300,0°IM7,±45°AS4]	[FM300,0°$IM7_2$,±45°AS4,0°IM7]
Web	[FM300,0°$IM7_2$]	[FM300,0°$IM7_4$]
Skin	[±45°AS4]	[±45°AS4,0°IM7]
Tungsten	10 x (2.00"x0.095")	11 x (2.00"x0.188")

are necessary to bring the chordwise center of gravity to the quarter chord. The composition of both blades, including laminates as labeled in figure 2.11 and tungsten rod properties are summarized in table 4.6.

4.1.3.1 Root Reinforcement Cuff

A diagram of the root reinforcement cuff including cross sections is shown in figure 4.10. The cuff extends to 31.5% of the blade radius, tapering from a root thickness of 33% chord, down to the VR12 profile at the outboard edge. Aluminum female molds were machined in two halves, with dowel pins for location. The female molds along with a male mandrel cast in silicone are shown in figure 4.11a. The blade cuff layup consists of a base ply of ±45° AS4 with two outer layers of unidirectional IM7 oriented in the spanwise direction. The laminate is wrapped around the male mandrel and compressed in the aluminum mold. The cure cycle is the same as for the main blade, although a hot press is used in lieu of the autoclave oven.

The cured blade cuff, shown in figure 4.11b, is removed from the mandrel and trimmed of excess material. The cuff and main blade are bonded

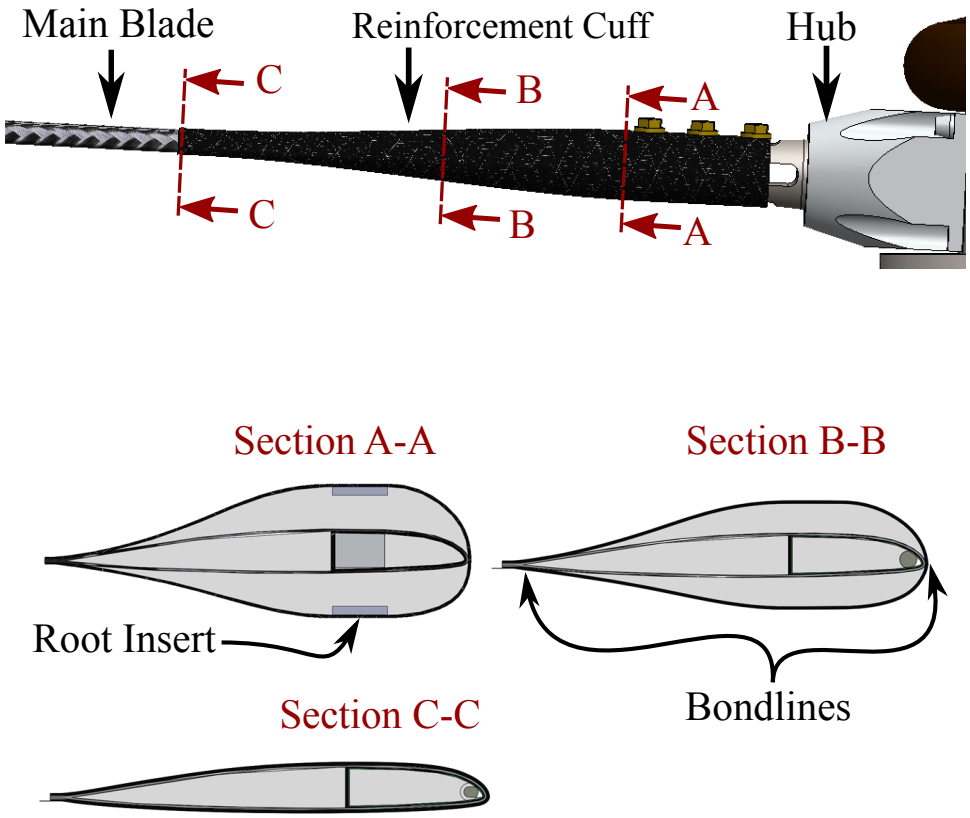

Figure 4.10: Diagram of blade root reinforcement cuff with cross sectional views

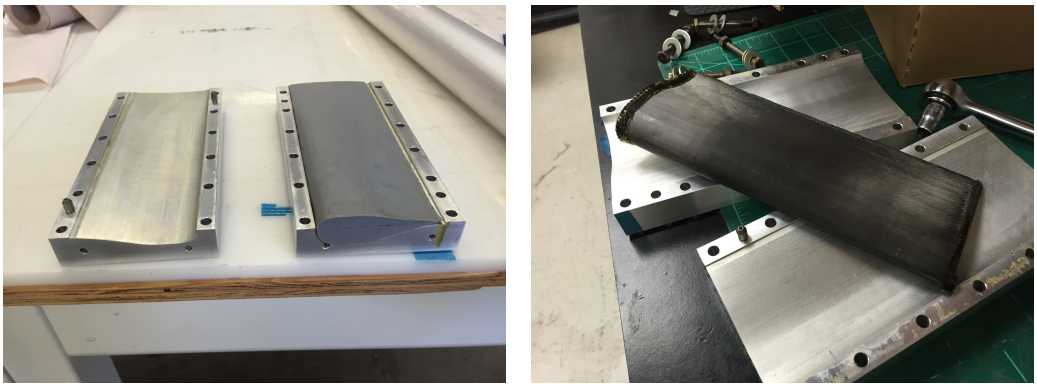

(a) (b)

Figure 4.11: Blade cuff construction, (a) Female and male cuff molds, (b) Unfinished blade cuff post-curing

together using high strength Hysol EH-120P epoxy, with the female mold acting as a fixture. As with the main blade, holes are drilled in the cuff for the bladegrip bolts to pass through. Finally, a dummy bladegrip and root inserts, labeled in figure 4.10, are attached to the blade and cuff and two-part, expanding urethane foam used to fill the bladegrip cavity. When cured this foam provides compressive strength, preventing buckling of the thin root cuff shell.

4.2 Static Characterization

Characterization of the blade structural properties is necessary, both for ensuring uniformity of blade construction and for accurate simulations which model the blade structural dynamics. While the nonlinear structural code in 2.2.2 requires many cross sectional properties, three stiffness properties have the majority of the influence on blade behavior: the flap-bending and

lag-bending stiffnesses, EI_η and EI_ξ, and the torsional stiffness GJ. These properties, as well as the total mass were measured for both the reference uniform blades, as well as the reinforced blades.

4.2.1 Uniform Beam

Measurements of the reference blades were simplified by assuming uniform cross sectional properties along the beam span. With this assumption, exact expressions for cantilevered beam bending slopes and twist at a spanwise location x were derived for concentrated force and torsional loads at the same location as:

$$\begin{aligned} w'(x) &= \frac{f^{\xi}_{tip} x^2}{2EI_\eta} \\ v'(x) &= \frac{f^{\eta}_{tip} x^2}{2EI_\xi} \\ \theta(x) &= \frac{M_\zeta x}{GJ} \end{aligned} \tag{4.3}$$

Next a benchtop experiment was designed to apply tip forces and moments to the blades and measure the resulting tip slopes and twists. The experimental setup, diagrammed in figure 4.12, consists of a rotor blade, cantilevered from a rigidly mounted bladegrip at the root, with a tip force applied using proof masses and pulleys. A mirror attached to the blade tip, reflects a collimated laser source, and projects it onto a target located a distance L from the blade root. The measured laser displacement d is then related to the tip slope as:

$$\beta = \frac{1}{2}\arctan\left(\frac{d}{L}\right) \tag{4.4}$$

Here β may be the flap-bending slope, lag-bending slope, or blade twist, depending on the applied tip load. Relating equations 4.4 to those in equations 4.3 the blade stiffnesses are recovered as:

$$EI = \frac{f_{tip}x^2}{\arctan\left(\frac{d}{L}\right)} \tag{4.5}$$

$$GJ = \frac{2M_{tip}x}{\arctan\left(\frac{d}{L}\right)} \tag{4.6}$$

Figure 4.13 shows the jig used for applying these tip loads. Pure flap-bending loads were applied at the blade quarter chord, while pure moment loads were generated using opposing pulleys to apply a couple to the aluminum beam. The details of the experimental setup dimensions, and applied loads are shown in table 4.7. Figure 4.14 shows the results from flap-bending stiffness tests of four blades. As seen in figure 4.14b the propagated uncertainty in the measurement variables does not entirely account for the blade-to-blade variation in EI_η indicating some variation in manufacturing tolerances. Table 4.8 summarizes the measured mean blade properties along with the values calculated from the cross sectional analysis. There is good agreement between the calculated and measured flap-bending stiffness, as well as between the calculated and measured mass. The lag-bending stiffness is overestimated by 15%, while the calculated and measured torsional stiffnesses differ by more than an

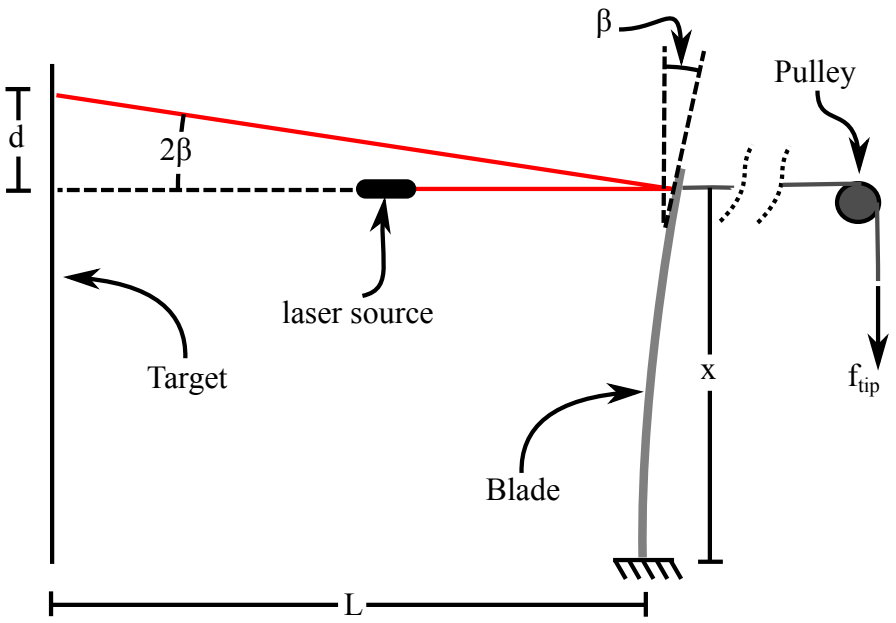

Figure 4.12: Diagram of blade tip slope experimental setup, pictured are the flap-bending slope w' and associated tip load

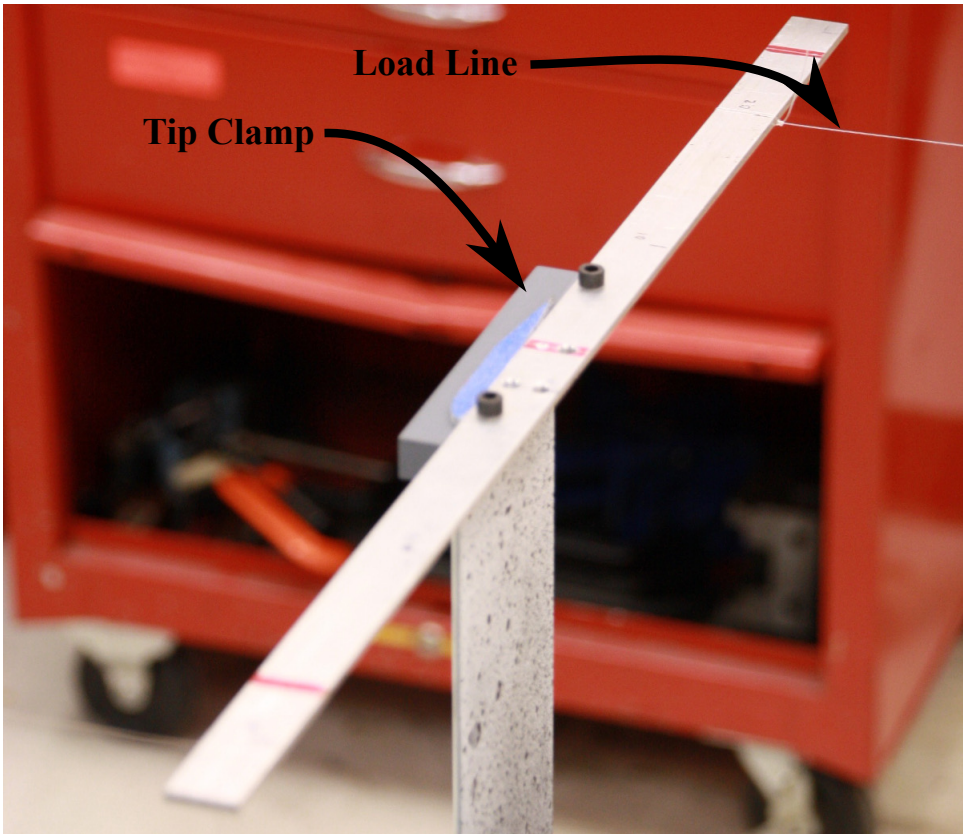

Figure 4.13: Picture of the jig for applying tip loads, combined flap-bending torsion load shown

Table 4.7: Dimensions for tip bending slope experiments

$L[m]$	3.68 ± 0.03
$x[m]$	0.794 ± 0.005
max f_{tip} [N]	1.96 ± 0.02
max M_{tip} [Nm]	0.167 ± 0.002
max d [m]	0.212 ± 0.001

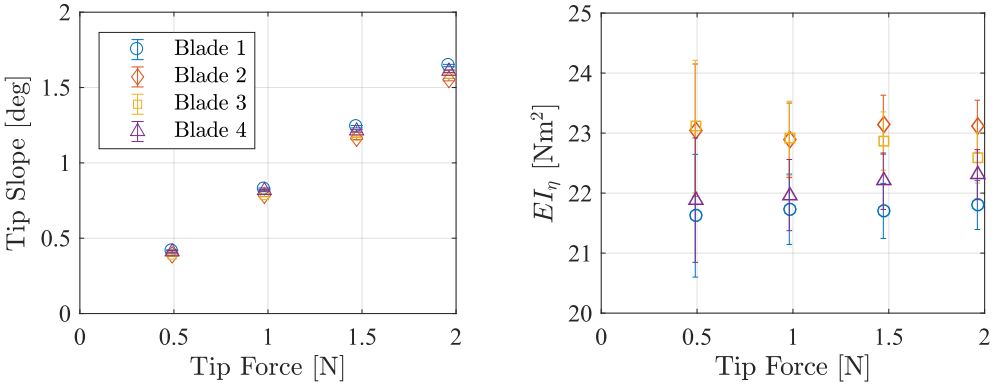

(a) (b)

Figure 4.14: Results from flap-bending stiffness tests for four blades, (a) Tip slope vs. applied force, (b) Derived flap-beding stiffness vs. applied force

order of magnitude. This discrepancy is due to the thin shell construction of the blade cross section. In the cross-sectional analysis code presented in 2.2.3 the entire beam is treated as a prismatic section with varying material properties. To achieve a more accurate estimate of the shear properties of the section, the shear flow through the thin laminates would need to be considered.

Table 4.8: Mean blade properties for reference blades

	Calculated	Measured
$\bar{EI}_\eta$ [Nm^2]	23.7	22.4 ± 0.32
$\bar{EI}_\xi$ [Nm^2]	771	676 ± 15
$\bar{GJ}$ [Nm^2]	939	23.0 ± 0.22
$\bar{m}$ [kg/m]	0.170	0.169 ± 0.006

4.2.2 Non-Uniform Beam

While the assumption of uniform cross sectional properties with span allowed for the the analysis of the reference blades, the root cuff reinforcement of the reinforced blades precludes such simplification. Instead the full field deformation response of the blades under tip loading conditions, similar to the reference blades, is required to characterize the spanwise variation of the cross-sectional properties. This is accomplished using digital image correlation techniques as described in §4.2.2.1. The resulting deformations are then compared to FEM beam models and used to adjust the estimated cuff and uniform blade section properties to match the experimental results as described in §4.2.2.2.

4.2.2.1 Digital Image Correlation

The digital image correlation technique (DIC) calculates test article deformations through cross correlations between deformed and undeformed images taken with digital cameras. Stereoscopic DIC uses the two-dimensional deformation results from at least two cameras, along with stereophotogramme-

try principles to recover full three-dimensional displacement fields. Care must be taken during sample preparation, image acquisition and image processing to ensure that accurate results are achieved. The preparation of the sample under test has, perhaps, the largest influence on the quality of DIC results. In order for the DIC technique to recover unique peaks in the cross-correlation field, a high contrast, stochastic speckle pattern is applied. A reinforced blade, shown in figure 4.15 , is prepared by applying a base layer of matte white paint, followed by randomly distributed black speckles. Several techniques are used for speckle application. For small test articles the speckle pattern may be applied by spraying or flicking paint droplets on the article. For the larger rotor blades of the current study, the speckle is applied using a permanent ink marker. The speckles should be of uniform density, with several dots per DIC interrogation window (typically 16×16 to 32×32 pixels), and speckles should be $\approx 3-5$ pixels in the final digital images.

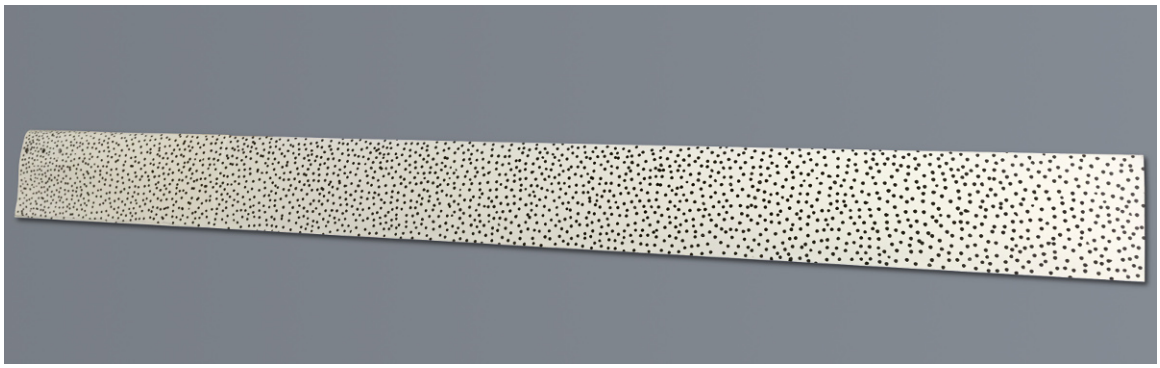

Figure 4.15: Blade prepared for DIC with stochastic speckle pattern

With the specimen prepared, the imaging system is setup and calibrated. Figure 4.16 shows the arrangement of the specimen, cameras and

lighting used for the benchtop testing. The high speed cameras (Phantom MIRO-M310) feature 12-Bit 1280x800 pixel CMOS sensors capable of recording 3,000 frames per second at full resolution. They are mounted to adjustable tripods and placed at an angle ϕ from the image plane. Highest accuracy for out of plane deformations is achieved for $\phi = 45°$. Scheimpflug adapters, which tilt the lens relative to the camera body, are used to rotate the lens focal plane to align with the desired image plane. In an ideal setup the lens plane, image plane, and camera sensor plane will all intersect at a single spatial axis. 25 mm, AF Nikon NIKKOR f/2D lenses are mounted to the cameras. The cameras are positioned, as shown in figure such that the long sensor axis with 1280 pixels is oriented along the blade span, maximizing resolution. LaVision DaVis 8.3.0 [1] software is used for image acquisition, calibrations, and DIC processing. The camera calibration establishes the exact positions of both cameras relative to a coordinate system defined by a calibration plate, shown in figure 4.17b. The calibration plate targets, located at two distinct out of plane levels, are used to fit a modified pinhole model to each camera, which is valid across the entire volume of focus. This calibration is used for image dewarping and, more important, for the stereophotogrammetic reconstruction of the three dimensional displacements.

With the calibration complete, images are acquired of the blade in the undeformed state, as well as at various deformed states due to applied loads. The LaVision DIC software then computes the deformation fields through a series of steps:

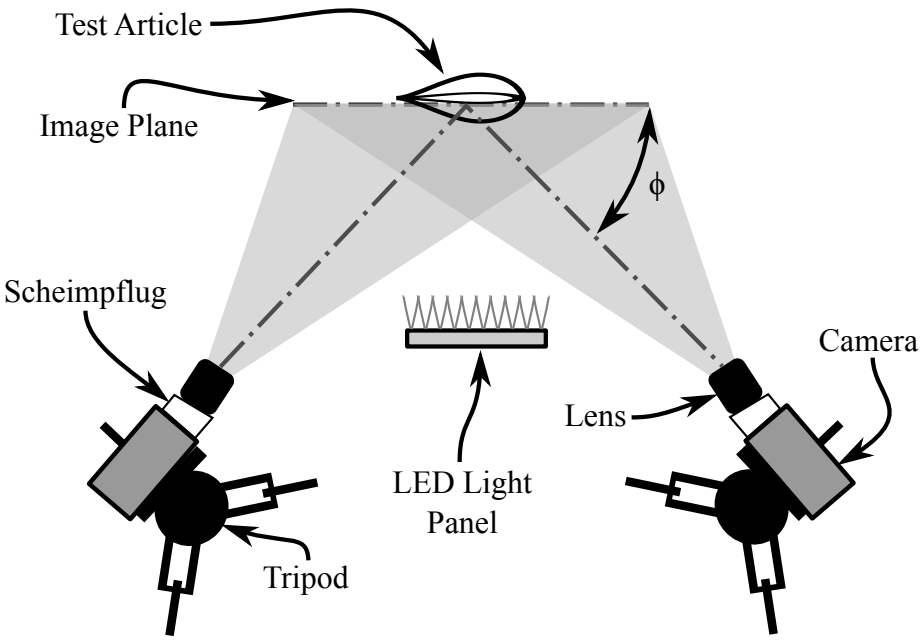

Figure 4.16: Overhead view of DIC imaging setup for bench-top structural property validation

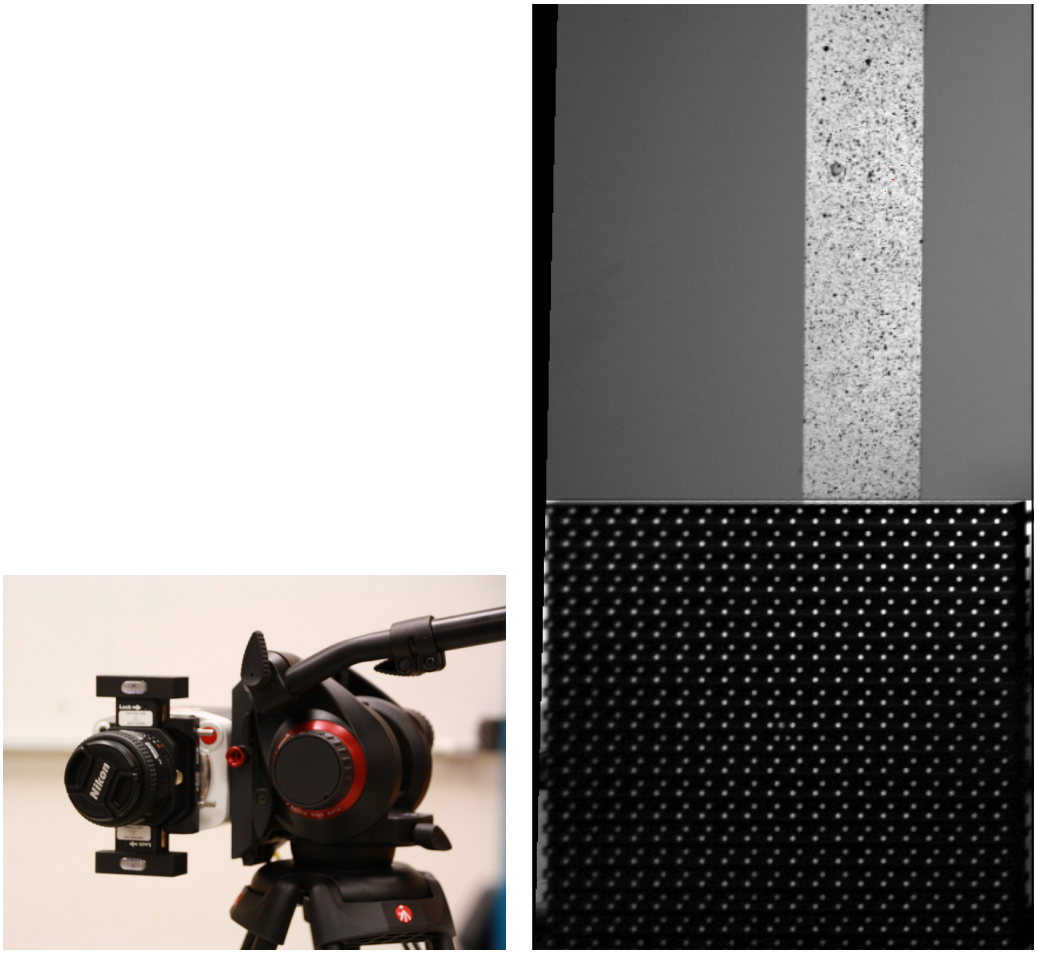

(a) (b)

Figure 4.17: DIC Camera arrangement, (a) MIRO M310 camera mounted sideways to maximize blade resolution, (b) Reference image with split-plane calibration plate

- A mask is applied to the images, retaining only the speckle patterned blade
- The remaining image is subdivided into interrogation windows (33×33 px) with 8 px overlap
- Two-dimensional cross correlations are computed between corresponding interrogation windows between the undeformed and deformed reference images
- A peak finding algorithm identifies the peak correlation value and calculates the corresponding displacement with sub-pixel accuracy
- The resulting in-plane deformations from both cameras are combined using the stereo calibration to recover the three-dimensional displacements

The spatial measurement resolution of the displacement vector field is determined by the window size and overlap. For the bench-top experiments, with 32×32 pixel windows, 8 pixel overlap, and a calibration constant of 1.26 mm/pixel, the measurement spacing is 10 mm or $\approx$ 1% of the blade radius. The LaVision documentation provides an estimate of 3D displacement vector uncertainty. For the 32×32 interrogation window used with high dynamic range from the LED lighting, a conservative displacement uncertainty estimate is 0.1 pixels, or 0.13 mm, less than 0.01% rotor span.

4.2.2.2 Linear Beam Model Fit

With the DIC system in place, tip bending and torsional loads were applied to the reinforced blade with the same pulley and clamp system used for the reference blade tip-slope tests. A reference blade image and images at each deformation level were captured and DIC processing performed. The resulting deformation vectors were imported into Matlab and processed to extract elastic axis (assumed located at the quarter chord), flap, lag and torsional deformations. The flap and lag deformations were directly interpolated from the measured x and z displacements. The torsional deformation at a spanwise station was calculated by fitting a linear regression to the chordwise distributed w deformations ($w(y) = \beta_0 + \beta_1(y - y_{QC})$. The slope of this linear fit, β_1, was then related to the twist angle as:

$$\theta(x) \approx \arctan \beta_1 + \mathcal{O}(\epsilon^4) \tag{4.7}$$

The approximated twist angle is accurate to order ϵ^4, as defined in table 2.2. The measured spanwise flap, lag, and torsion responses were then compared to the output of the linear finite element beam model, constructed from estimated cross sectional properties of the reinforced blade. The L_2 norm was used to formulate an objective function to quantify the error between the measured and simulated responses as:

$$O(\vec{d}_{sim}, \vec{d}_{meas}) = \sqrt{(\vec{d}_{sim} - \vec{d}_{meas}) * (\vec{d}_{sim} - \vec{d}_{meas})^T} \tag{4.8}$$

Here $\vec{d}$ may be the vectors of spanwise flap, lag or torsional deflections, depending on the applied tip loads. The distributed blade stiffness is then split into two components, the contribution of the root cuff and the contribution of the uniform blade. The original computed stiffness of these sections may then be scaled by multiplicative constants α^{cuff} and α^{blade} respectively:

$$\vec{EI}_{\eta} = \alpha_{\eta}^{cuff}\vec{EI}_{\eta}^{cuff} + \alpha_{\eta}^{blade}\vec{EI}_{\eta}^{blade} \tag{4.9}$$

$$\vec{EI}_{\xi} = \alpha_{\xi}^{cuff}\vec{EI}_{\xi}^{cuff} + \alpha_{\xi}^{blade}\vec{EI}_{\xi}^{blade} \tag{4.10}$$

$$\vec{GJ} = \alpha_{\zeta}^{cuff}\vec{GJ}^{cuff} + \alpha_{\zeta}^{blade}\vec{GJ}^{blade} \tag{4.11}$$

The objective function is then minimized by varying the α^{cuff} and α^{blade} stiffness terms using the Matlab function fmincon. Figures 4.18 through 4.20 show the DIC measured flap, lag and torsion in response to tip loadings. Overlaid are the finite element model predictions after fitting the blade structural properties using the objective function and minimization routine. The optimization routine was performed for each load case independently, then the mean correction and precision error calculated. The bending deflection cases show excellent agreement and smooth experimental data. The blade torsion measurement is more sensitive to noise, as it is calculated from the raw displacements according to equation 4.7.

The multiplicative factors, α, are shown in table 4.9. Here we see good agreement between the predicted main-blade flap and lag bending stiffness and measurements, while the blade torsional stiffness is significantly over-predicted

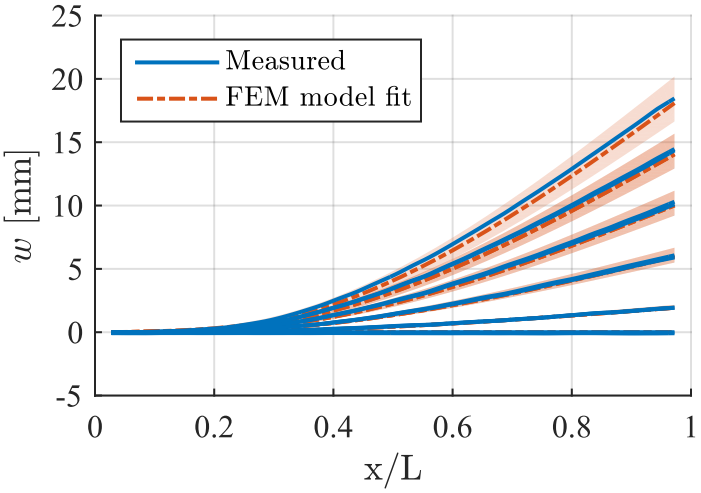

Figure 4.18: DIC measured blade flap-bending deflections at several tip loadings with computational model fits and uncertainty bounds

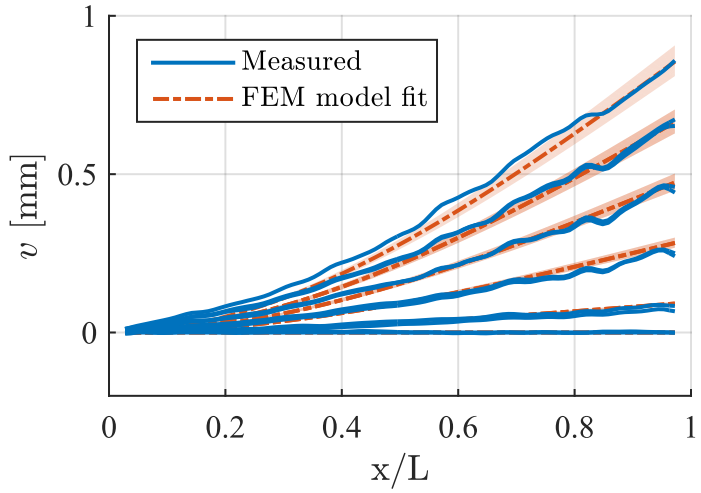

Figure 4.19: DIC measured blade lag-bending deflections at several tip loadings with computational model fits and uncertainty bounds

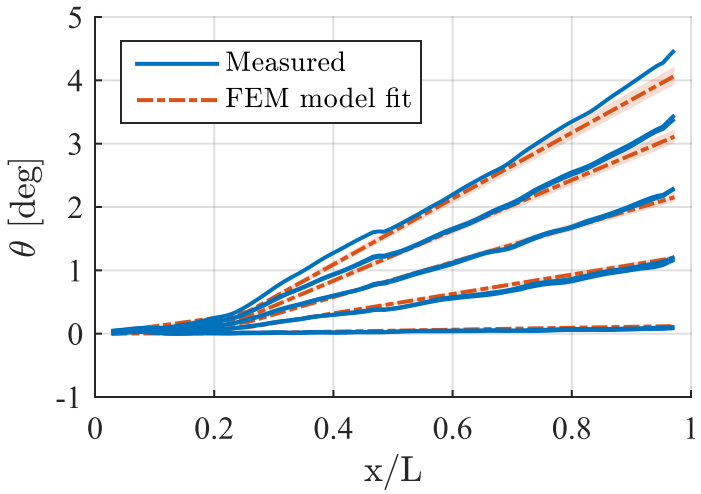

Figure 4.20: DIC measured blade torsional deflections at several tip loadings with computational model fits and uncertainty bounds

Table 4.9: Cuff and blade stiffness scaling factors

	α^{cuff}	α^{blade}
Flap (α_η)	0.46 ± 0.08	1.02 ± 0.04
Lag (α_ξ)	0.066 ± 0.004	1.03 ± 0.02
Torsion (α_ζ)	0.043 ± 0.003	0.024 ± 0.008

as explained in §4.2.1. The measured cuff flap stiffness was approximately one half the calculated value, while cuff the lag and torsional stiffnesses were over predicted by a factor of approximately 20. This over prediction is unsurprising given the proximity of the cuff to the beam fixed boundary, as well as the non-ideal cantilever root condition introduced by the bladegrip. Figure 4.21 plots the distributed blade properties as a function of span after applying the measured corrections.

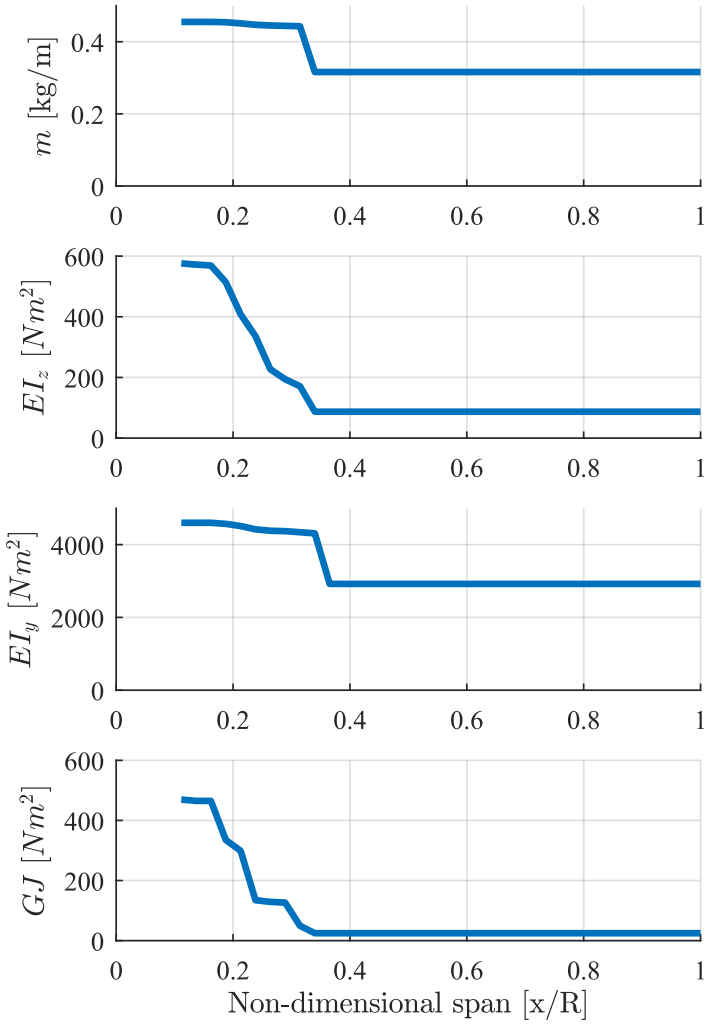

Figure 4.21: Reinforced blade distributed structural properties after model fitting

4.3 Dynamic Characterization

While the static characterization techniques are able to measure and adjust the blade elastic properties, dynamic characterization provides an assessment of the coupled mass and stiffness properties. The dynamic properties of the reinforced blade are measured using a combination of high speed DIC and operational modal analysis techniques. Two tests were performed. In the first, the stationary blade is excited with white noise input from an electromechanical shaker, while the second set of tests were performed on a rotating blade with transient gust excitation.

4.3.1 Modal Analysis Techniques

Two modal analysis techniques were used to characterize the blade structural properties, the Ibrahim Time Domain (ITD) technique, and the Eigensystem Realization Algorithm (ERA). Both methods work by estimating the discrete state space system representation of the signals under test. The discrete state space system representation is derived, starting from a second order, continuous time structural dynamic system as:

$$M\ddot{\vec{y}}(t) + C\dot{\vec{y}}(t) + K\vec{y}(t) = \vec{u}(t) \tag{4.12}$$

$$\begin{bmatrix} \dot{\vec{x}}(t) \\ \ddot{\vec{x}}(t) \end{bmatrix} = \begin{bmatrix} 0 & I \\ -(K/M) & -(C/M) \end{bmatrix} \begin{bmatrix} \vec{x}(t) \\ \dot{\vec{x}}(t) \end{bmatrix} + \begin{bmatrix} 0 \\ (1/M) \end{bmatrix} \vec{u}(t) \tag{4.13}$$

$$\begin{bmatrix} \vec{y}(t) \end{bmatrix} = \begin{bmatrix} I & 0 \end{bmatrix} \begin{bmatrix} \vec{x}(t) \\ \dot{\vec{x}}(t) \end{bmatrix} \tag{4.14}$$

The equations are then rewritten as:

$$\dot{\vec{x}}(t) = A_c\vec{x}(t) + B_c\vec{u}(t) \tag{4.15}$$

$$\vec{y}(t) = C_c\vec{x}(t) \tag{4.16}$$

These are the linear, time invariant state space equations in continuous time form with no feedback control. Matrix A_c is square and referred to as the continuous time state transition matrix, B_c is the continuous time input matrix and C_c the continuous time output matrix. In performing modal analysis on digitized data, sampled with period T, the discrete time formulation of these equations is required:

$$\vec{x}(k+1) = A\vec{x}(k) + B\vec{u}(k) \tag{4.17}$$

$$\vec{y}(k) = C\vec{x}(k) \tag{4.18}$$

$$x(k) \in \mathbb{R}^n \tag{4.19}$$

$$A = e^{A_c T} \tag{4.20}$$

The eigenvalues of the discrete state transition matrix, λ_i are related to the continuous time system natural frequencies and damping ratios by:

$$\lambda_c^i = \frac{1}{\Delta t} \ln\left(\lambda^i\right) \tag{4.21}$$

$$\omega_n^i = |\lambda_c^i| \tag{4.22}$$

$$\zeta^i = \frac{-Re(\lambda_c^i)}{\omega_n^i} \tag{4.23}$$

Here ΔT is the discrete time step between times k and $k+1$.

4.3.1.1 Ibrahim Time Domain

The Ibrahim Time Domain (ITD) [44] technique estimates the discrete state transition matrix through a least squares matrix inversion. The inputs to the ITD technique are the free responses of the system signals to an impulse. These discrete time free responses, $Y_i(t_j)$, referred to as Markov parameters, may be obtained from traditional modal testing where the input forcing as well as the output are measured, or from operational modal analysis techniques. Two matrices are assembled from the Markov parameters as:

$$\Phi = \begin{bmatrix} Y_i(t_j) \\ Y_i(t_j + \Delta t) \end{bmatrix} \tag{4.24}$$

$$\hat{\Phi} = \begin{bmatrix} Y_i(t_j + \Delta t) \\ Y_i(t_j + 2\Delta t) \end{bmatrix} \tag{4.25}$$

These two matrices have dimension $2m \times n$ where m is the number of channels Y_i, and n is the number of time instants t_j with the constraint $n \geq 2m$. The rows of Φ and $\hat{\Phi}$ are separated by a time step Δt which is chosen

by the analyst. The discrete state transition matrix is then estimated from Φ and $\hat{\Phi}$ as:

$$A\Phi = \hat{\Phi} \tag{4.26}$$

$$A = \frac{1}{2}\left(\left[\hat{\Phi}\Phi^T\right]\left[\Phi\Phi^T\right]^{-1} + \left[\hat{\Phi}\hat{\Phi}^T\right]\left[\Phi\hat{\Phi}^T\right]^{-1}\right) \tag{4.27}$$

Equation 4.27 is an average of two least squares solutions, designed to remove bias errors in the eigenvalues of A [43]. The system natural frequencies and damping ratios are calculated as derived in equation 4.3.1 and the eigenvectors of A are the corresponding mode shapes. The state transition matrix A has rank equal to the number of channels, m, generally higher than the number of true modes in the system. The additional modes contain system noise and are discarded by considering several heuristics. The restriction that the number of time steps n be greater than twice the number of measurement channels is troublesome when applied to DIC measurements which may contain thousands of spatial measurements. With a limited number of time steps available, spatial data must be discarded to satisfy the constraint. The large number of channels also results in many spurious noise modes to discard as the number of modes returned is equal to $2m$.

4.3.1.2 Eigensystem Realization Algorithm

The Eigensystem Realization Algorithm (ERA) [52] overcomes these limitations through the use of the singular value decomposition (SVD). Where

the ITD estimates the state transition matrix A, the ERA estimates a complete system realization of A, as well as the input matrix B and output matrix C. The technique begins with Markov Parameters $Y_i(k)$ assembled into a block Hankel matrix:

$$H_{rs}(k-1) = \begin{bmatrix} Y_i(k) & Y_i(k+1) & \dots & Y_i(k+s-1) \\ Y_i(k+1) & Y_i(k+2) & \dots & Y_i(k+s) \\ \vdots & \vdots & \vdots & \vdots \\ Y_i(k+r-1) & Y_i(k+2) & \dots & Y_i(k+s+r-2) \end{bmatrix} \tag{4.28}$$

Here r and s are arbitrary integers and the resulting dimension of H_{rs} is $mr \times s$. There is no restriction on the ratio of time steps to channels as with the ITD. Introducing the SVD of H_{rs} as:

$$H_{rs}(k-1) = R\Sigma Q^T \tag{4.29}$$

The diagonal matrix Σ contains the singular values of $H_{rs}(k-1)$, which may be used to limit the rank of the identified system by discarding small singular values. This limits the number of noise modes to discard after the analysis is completed. A rule of thumb is to keep at least four times the number of expected modes as singular values. The state space system realization is then calculated using the first n singular values of the SVD along with $H_{rs}(k)$, the Hankel matrix constructed a time step forward from $H_{rs}(k-1)$.

$$A = \Sigma^{-1/2} R^T H_{rs}(k) Q \Sigma^{-1/2} \tag{4.30}$$

$$B = \Sigma^{1/2} Q^T E_r \tag{4.31}$$

$$C = E_m^T R \Sigma^{1/2} \tag{4.32}$$

Where E_r and E_m are block selection matrices for extracting the values of B and C. The natural frequencies and damping ratios are calculated as defined in §4.3.1, while the mode shapes at the measurement locations are recovered from the combination of the observer matrix C and the eigenvectors of A as:

$$\Psi = C\Psi_A \tag{4.33}$$

4.3.1.3 Natural Excitation Technique

In traditional modal testing the Markov parameters used in the ITD and ERA are generated by calculating the impulse response functions of the system using the input forcing. If the input forcing is unknown other methods for estimated Markov parameters must be used. The Natural Excitation Technique (NExT) [46] estimates Markov parameters for a system under ambient white noise excitation, using cross-correlations between output measurements:

$$Y_i(t) = \int_{-\infty}^{\infty} y_{ref}(t) y_i(t+\tau) d\tau \tag{4.34}$$

In practice the cross-correlations are determined by calculating the cross-spectral densities at all measurement locations with a single reference location, and then taking the inverse Fourier transform. In calculating the cross-spectral densities ensemble averaging may be employed to reduce measurement noise. The output of the NExT analysis is then used as an input to either ITD or ERA.

4.3.1.4 Eliminating Noise Modes

In both the ITD and ERA techniques the system realization includes both the desired structural modes as well as spurious noise modes. Separating the structural and noise modes requires the input of an experienced analysts along with several empirical indicators of modal quality. For a structural dynamic system, the first criteria considered is the modal damping ratio. Modes with negative damping are unphysical and discarded. In cases where structural damping is known to be low, modes with large damping ratios may also be discarded as unphysical.

This process is repeated for multiple realizations of the system. For ITD multiple realizations are achieved by varying the channels under consideration or the time step, Δt. For ERA multiple realizations are achieved by varying the number of singular values retained during the decomposition. The mode shapes from the multiple realizations are then compared using the modal assurance criteria (MAC):

$$MAC_{ij} = \frac{|q_i q_j^*|}{(|q_i q_i^*||q_j q_j^*|)^{1/2}} \tag{4.35}$$

Here the q_i and q_j are mode shapes from two different system realizations, and $(\ )^*$ the conjugate transpose. The MAC varies from one for identical mode shapes to zero. Generally MAC values greater than 0.95 indicate repeatedly identified modes. The results for the different realizations are used to create a stabilization diagram, shown for multiple ERA singular values in figure 4.22. The x-axis is the frequency range and the y-axis covers the repeated realizations. Markers are placed at the identified modal frequencies and are colored by their mean MAC value. Accepted modes are plotted as x's with spurious noise modes as o's. The identified modes form columns on the stabilization diagram, which generally occur near peaks in the underlying Markov parameter spectral density, shown in gray. These stabilization diagrams provide a visual tool for assessing the quality of identified modes.

4.3.2 Dynamic DIC Shaker Test

Using the camera and lighting setup as described in §4.2.2.1 the vibration response of the reinforced rotor blade was measured using DIC. Figure 4.23 shows a diagram of the instrumentation and hardware used for the test. A LabView VI and NI PCIe-6351 DAQ card are used to generate an arbitrary waveform output signal. That signal is amplified (AE Techron LV 3620) and sent to an electrodynamic shaker (LDS V201). The shaker is connected via a slender sting to a bridge-based load cell (Omega LCMFD-20N) as shown in

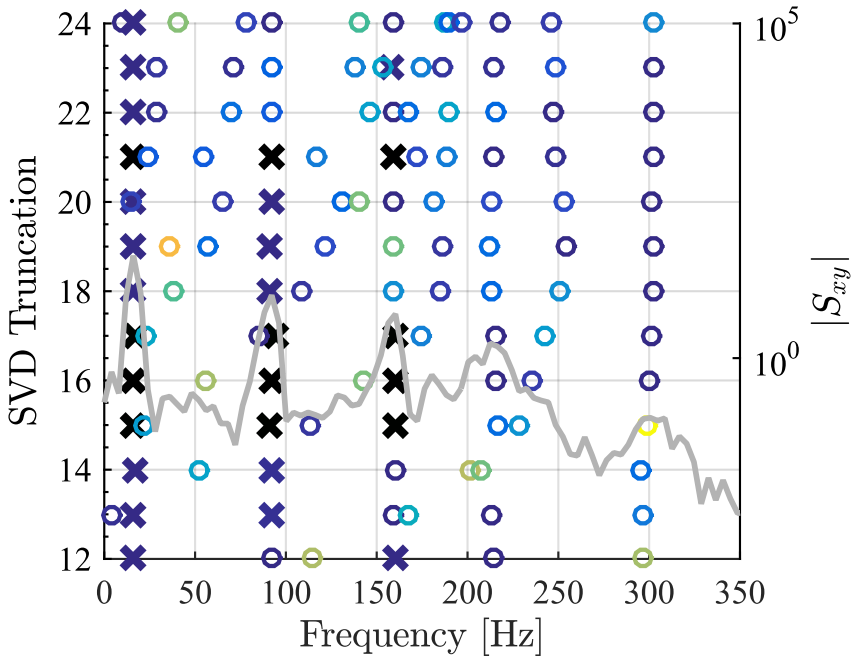

Figure 4.22: Stabilization diagram for out-of-plane displacements overlaid on Markov parameter power spectrum, x's are accepted modes

figure 4.24. The load cell is attached to a stud, bonded to the blade trailing edge ≈ 8 in from the blade root, and it's output sent through a Vishay 2120A signal conditioner before being digitized by the DAQ card. The DAQ analog input signal and start trigger are shared with the camera timing and synchronization box for the LaVision imaging system. This allows for synchronized acquisition of input forcing and camera images of the blade displacement.

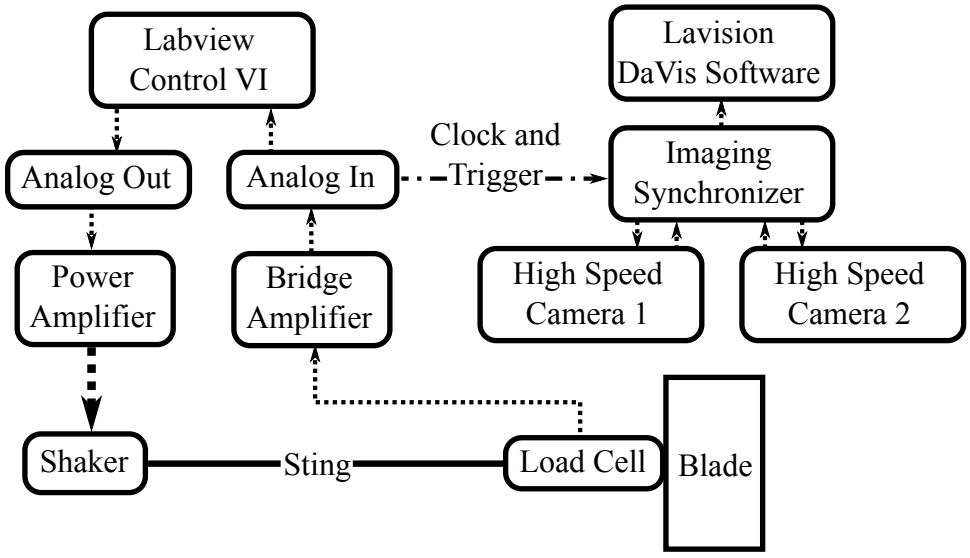

Figure 4.23: Diagram of shaker test setup showing synchronization between NI and LaVision hardware

A series of uniform, random white noise signal, band-limited from 0-300Hz with peak to peak forcing of ±20N, was applied to the blade. Two seconds of images and force measurements were taken, sampled at 2 kHz. The beam displacement images were post-processed using the same DIC settings as

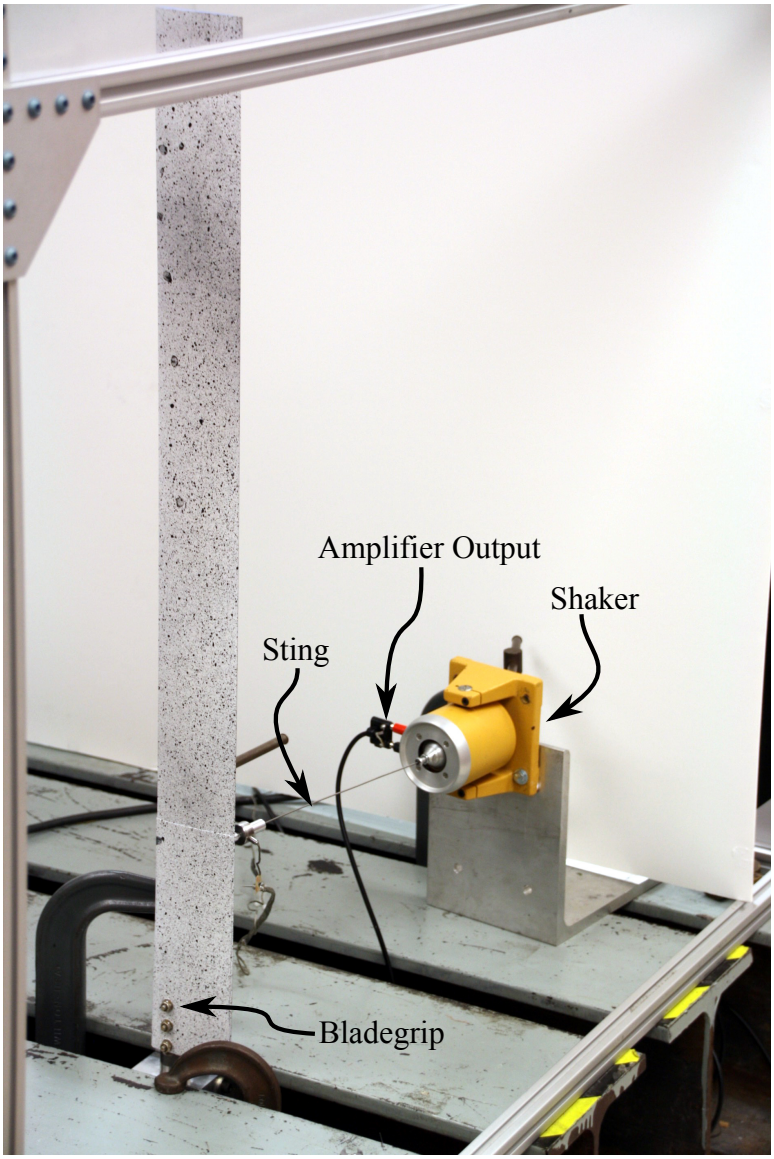

Figure 4.24: Electrodynamic shaker with sting attachment to load cell and blade

the static tests. The post-processed images were then imported into Matlab for modal analysis. The NExT technique was used to generate the system Markov parameters given the white noise forcing. Figure 4.25a shows a subset of the raw beam displacement measurements, while figure 4.25b shows the output of the NExT technique with 500 sample ensemble averages. The NExT Markov parameters demonstrate the expected damped sinusoidal behavior associated with a free response.

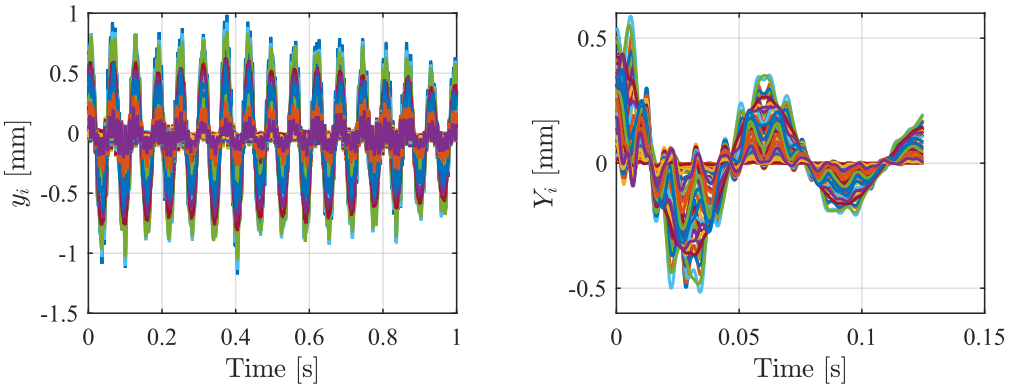

Figure 4.25: Natural Excitation Technique signals, (a) Raw blade displacements, (b) Output Markov parameters from cross-correlations

The ERA was run on the full-field displacements (1374 spatially distributed measurements), retaining between 12 and 24 singular values. The block rows were chosen equal to the number of singular values, and the number of block columns equal to three times the the number of rows. Two of the identified raw mode shapes are shown in figures 4.26a and 4.26c. The two-dimensional mode shapes are then projected onto flap, lag and torsional

displacements along the blade quarter chord. The resulting mode shapes, shown in figures 4.26b and 4.26d demonstrate uncoupled behavior, with one dominant displacement. The extracted modes are identified as the first flap and torsion modes respectively. Table 4.10 shows the natural frequencies and damping ratios of the four identified modes.

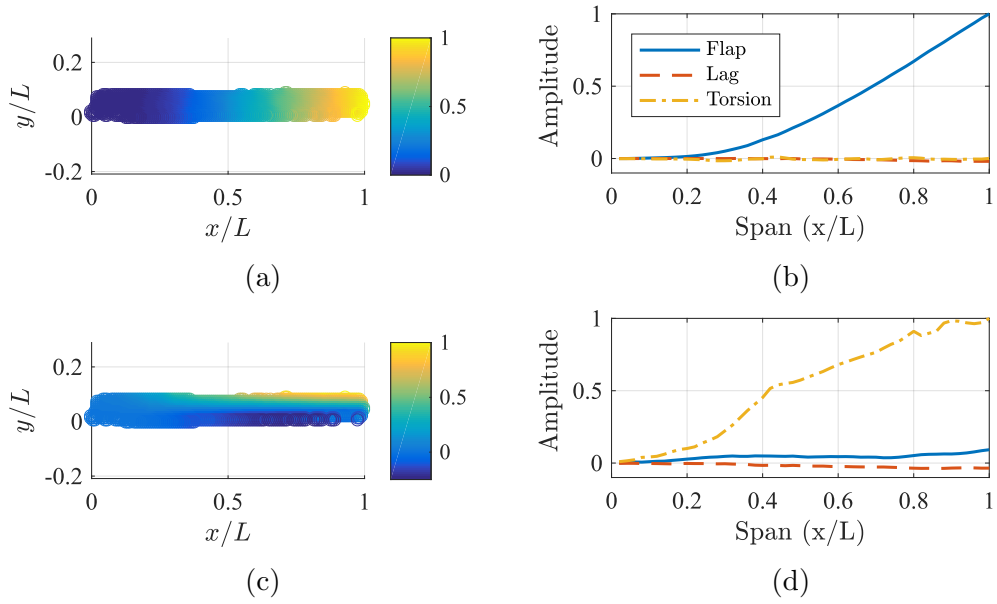

Figure 4.26: ERA extracted mode shapes projected to quarter chord, (a)Raw 1st flap, (b)Projected 1st flap, (c)Raw 1st torsion, (d)Projected 1st torsion

The results are overlaid on the natural frequencies calculated using the nonlinear beam code with the calibrated blade properties from §4.2.2.2 in figure 4.27. Excellent agreement is shown with all four extracted frequencies. The primary components of the measured and computed mode shapes are compared in figure 4.28. The two flap-bending mode shapes are nearly identical, while the measured lag-bending mode shape exhibits a large amount of

Table 4.10: Shaker test identified modal frequencies and damping ratios

	$\omega_n\,[Hz]$	ζ
1st Flap	16.25 ± 0.22	0.066 ± 0.017
1st Lag	65.0 ± 1.0	0.016 ± 0.013
2nd Flap	92.09 ± 0.59	0.014 ± 0.008
1st Torsion	159.7 ± 1.1	0.050 ± 0.020

root compliance. This results in a measured mode shape with characteristics similar to rigid body rotation about the blade root. There is good agreement in the shape of the torsion modes, although the measured mode shape is noisy in comparison with the bending modes. This is similar to the results from the static testing where the derived nature of the twist deflection introduced noise.

4.3.3 Rotating Frame Modal Extraction

As shown in figure 4.27 the modal characteristics of the blade are influenced by the rotational velocity through inertial and aerodynamic effects. In order to characterize these effects DIC was performed on a spinning rotor blade. The two high-speed cameras are located approximately ten feet below the rotor plane, angled at 45°, with 50 mm, Nikon NIKKOR f/1.8D lenses. Figure 4.30b shows the calibration setup, with a 1 x 0.8m single level calibration plate (Type A 1000). The field of view is limited to one quarter of the rotor disk. This results in an incomplete time history which disallows the use of the NExT and ERA analysis from the non-rotating experiment.

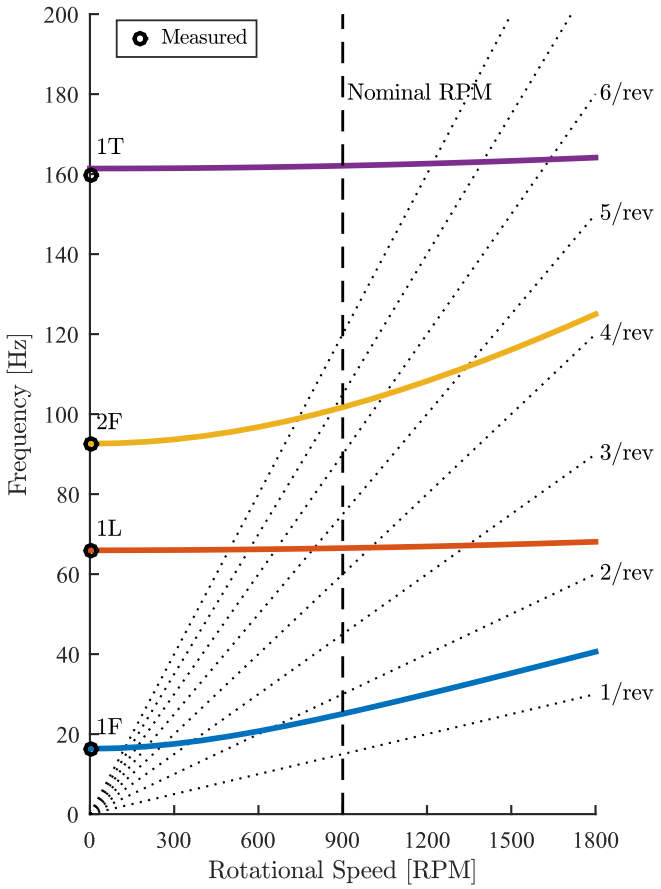

Figure 4.27: Fanplot of nonlinear beam code natural frequencies with non-rotating frequencies measured using NExT ERA

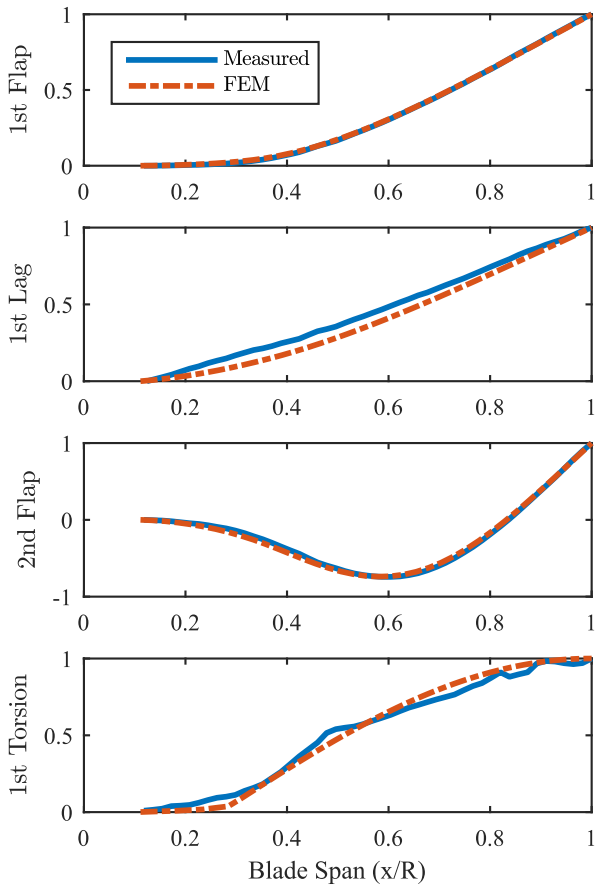

Figure 4.28: Mode shapes extracted using NExT ERA of DIC images with nonlinear beam code predictions

Figure 4.29: Calibration setup for rotating DIC testing

Instead, a formulation of the ITD proposed by Rizo-Patron [93] is used. The experimental setup is shown in figures 4.30a and 4.30b. In order to measure the system Markov parameters directly, an air excitation source is placed beneath the rotor plane at approximately $3/4R$. The air jet induces a gust response which is then measured by the DIC setup over the next quarter revolution. The test stand optical encoder is used to generate a camera sampling clock with fixed, 11.25° azimuthal spacing and data is collected over 100 revolutions. In populating the matrices used for the ITD analysis (equations 4.24 and 4.25) $\vec{Y}(t_j)$ is a vector of flap displacement at revolution j, while Δt is chosen within a single quarter revolution. This is in contrast to traditional ITD, where a single impulse response is sampled for both the t_j and Δt terms.

Reference images are captured at each azimuthal location with no gust excitation and the relative blade displacements calculated using the DaVis software. Figure 4.31 shows the raw DIC displacements along with uniform interpolation grids used to transform the measurements to a blade-fixed coordinate system. The ITD is formulated using 25 spanwise points at a single chord location resulting in a 4:1 ratio of spatial to time samples. By varying the chordwise location, and the initial time step of the sampled displacements, the ITD technique is performed several times for each dataset. The repeated results are then compared, and the consistently identified modes retained.

Data was measured for a single-bladed, counter-balanced rotor with zero collective pitch at 300 and 600 RPM. The first flapping mode was successfully identified for both 300 and 600 RPM. Figure 4.32 compares the measured

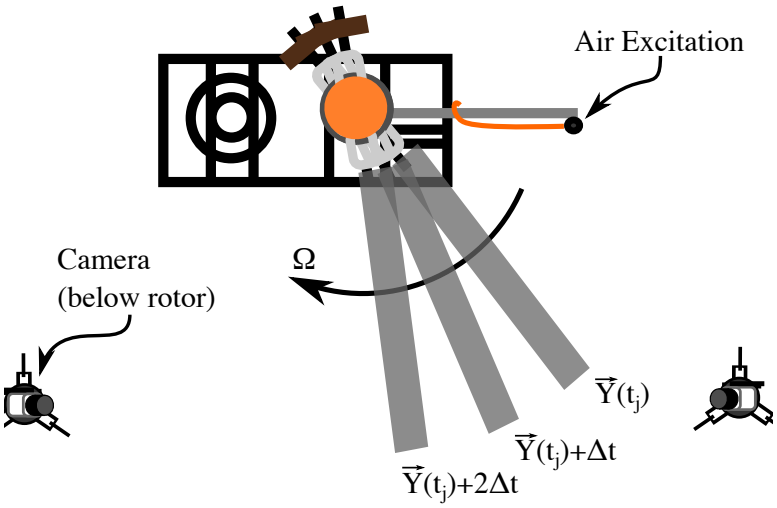

(a)

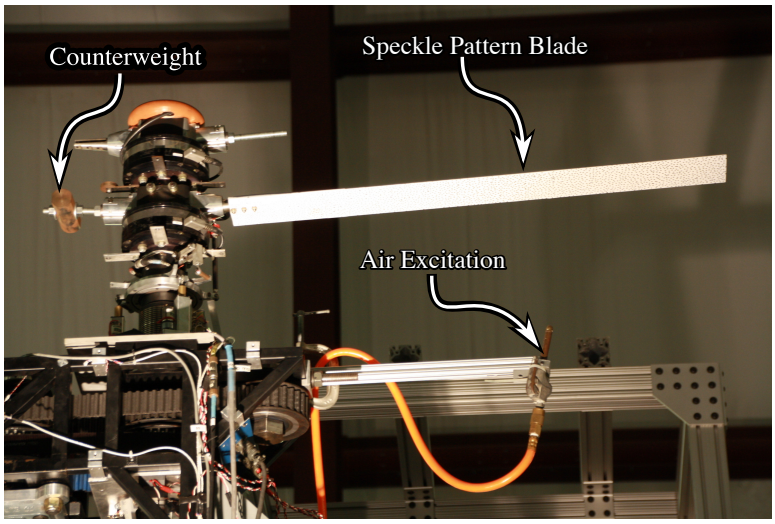

(b)

Figure 4.30: Air excitation DIC experiment, (a) Diagram of excitation, cameras and ITD Markov parameters, (b) Photograph of excitation implementation

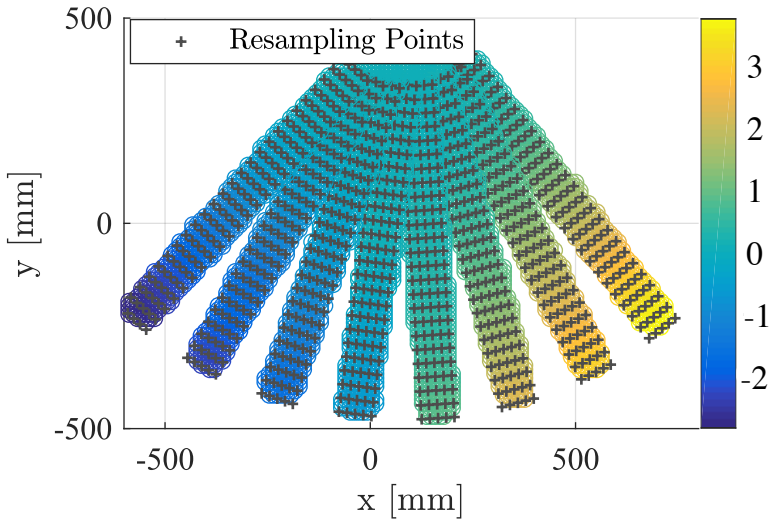

Figure 4.31: Raw flap displacements with uniform interpolation grids

first flap frequency, ν_β (normalized by rotational frequency), and damping ratio, ζ, to computational results. The damping ratio is estimated from the equation of motion of a rigid flapping blade with linearized aerodynamics:

$$\overset{**}{\beta} + \frac{\gamma}{8}\overset{*}{\beta} + \nu_\beta^2\beta = M_{aero} \tag{4.36}$$

$$2\zeta\nu_\beta = \frac{\gamma}{8} \tag{4.37}$$

$$\zeta = \frac{\gamma}{16\nu_\beta} \tag{4.38}$$

Here γ is the Lock number and superscripts * indicates a derivative with respect to azimuth angle. The results are summarized in table 4.11. There is excellent agreement between the identified and predicted modal natural fre-

quencies, and the predicted damping ratios fall within the uncertainty bounds of the measured values. In contrast to the non-rotating mode shapes, the identified rotating mode shapes, shown in figure 4.33, contain significant noise and uncertainty. Longer time samples and increased excitation amplitude could improve the signal to noise ratio, possibly allowing for the identification of higher frequency modes.

The results compare favorably with the previous work done by Rizo-Patron and Sirohi [93]. While the current study was only able to identify one, as opposed to three flapping modes, unlike in the previous work, the aerodynamic damping was successfully extracted. The difference is likely due to a modification of the sampling technique used. In the current study eight images were captured each revolution, separated by the inter-sample azimuth angle of 11.25°. The sampling technique in [93] captured one image-per-revolution at a single sampling azimuth, taking 1000s of images in a single data-set. Then the sampling azimuth was incremented by Δt and another set of images captured. The resulting ITD analysis was constructed using these images that were properly separated in azimuth angle, but not in time as the images were taken during different captures. This sampling technique did not properly account for natural revolution to revolution unsteadiness in the deformations, likely disrupting the observation of consistently decaying modal amplitudes necessary for damping ratio identification. By sampling all azimuthal locations during a single revolution the deformation unsteadiness is captured and the damping ratio extracted.

Table 4.11: Rotating ITD and predicted natural frequencies and damping ratios

	$\nu_\beta\,[1/rev]$	ζ
300 RPM Measured	3.52 ± 0.10	0.110 ± 0.046
300 RPM Predicted	3.51	0.107
600 RPM Measured	2.08 ± 0.08	0.218 ± 0.071
600 RPM Predicted	2.07	0.181

The correct identification of the aerodynamic damping is an important step toward fully characterizing the dynamics of a rotating blade. Accurate damping measurements would be especially useful when applied to rotors with marginal stability, such as the extremely flexible rotor systems examined by Sicard and Sirohi [104]. Increasing the number of revolutions captured and the corresponding ITD matrix sizes would likely lead to increased accuracy of the identified mode shapes, although camera memory becomes an issue. Alternatively additional cameras could be used to capture the complete blade deformation time history around the rotor disk. This would and allow for the use alternative OMA techniques such as NExT ERA which provide more flexibility in the identification process.

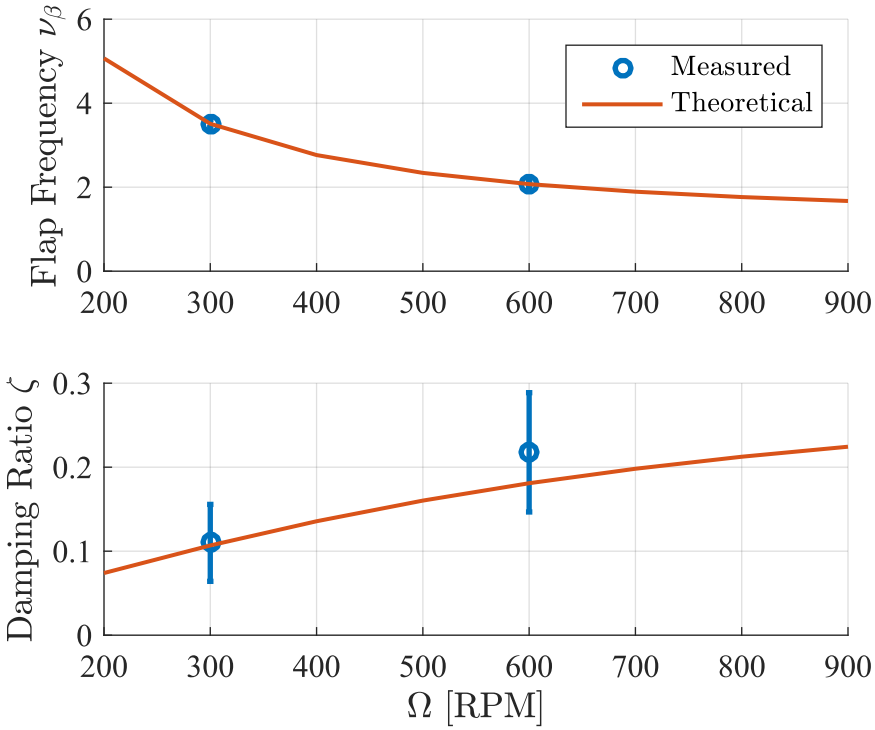

Figure 4.32: Measured and theoretical 1st flap frequency and damping ratio vs. RPM

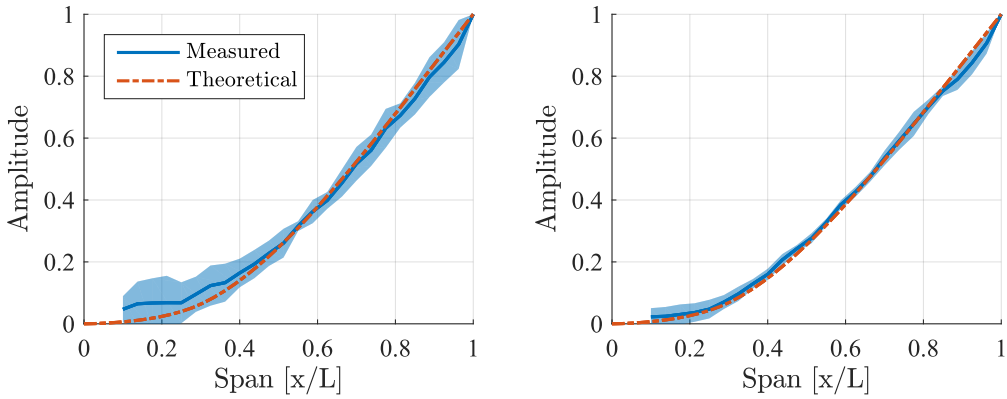

Figure 4.33: Measured and theoretical 1st flap mode shapes, (a) 300 RPM, (b) 600 RPM

Chapter 5

Hover Testing

Three rounds of hover testing were performed, as summarized in table 5.1. The first two tests were performed using the reference rotor blades and incomplete instrumentation, while the final test featured complete instrumentation and the reinforced blades used in the wind tunnel experiments. The results presented from the first two tests are combined to compare coaxial and isolated rotor steady performance and loads in §5.2. The interference effects are quantified and compared to the BEMT and FVM models. Complementary results from the third round of testing include collective measurements in §5.2.6, as well as vibratory loads from upper-lower rotor interaction in §5.3. All tests were performed at the University of Texas Rotor Test Facility, shown in figure 5.1. The lower rotor plane is more than two diameters above the ground, and the stand is located in the middle of the $50 \times 33 \times 60$ft tall room to minimize recirculation effects.

Portions of this chapter were previously published as "Performance of a mach-scale coaxial counter-rotating rotor in hover" [22] in the AIAA Journal of Aircraft. All writing and figures included in this chapter are the original work of the author, incorporating free vortex wake computational data from Dr. Anand Karpatne, with editing by Dr. Jayant Sirohi.

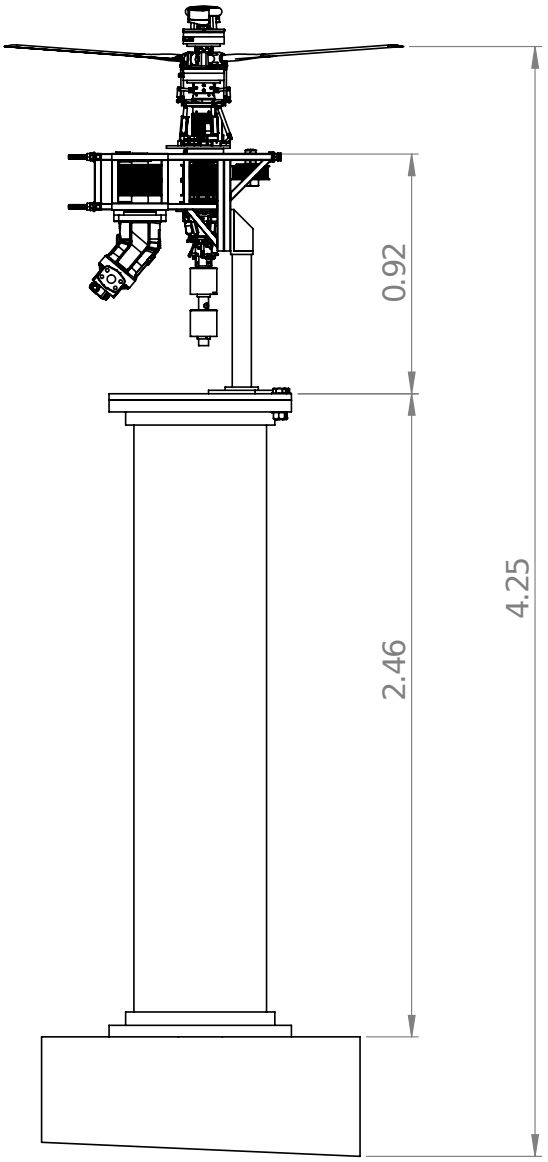

Figure 5.1: Dimensions (m) of rotor system on hover tower

5.1 Experimental Procedure

In the first set of tests, data for each rotor configuration was acquired at five blade loadings. At each test condition 100 revolutions of data were captured and phase averaged. Typical plots of phase averaged thrust and push rod loads for the lower coaxial rotor are shown in Figure 5.2 at a tip speed of 190 m/s and $C_T/\sigma = 0.089$. In processing the performance data the mean of each revolution is treated as a statistically independent sample. The mean and standard deviation of each of these 100 independent samples are then used to calculate the mean value and precision uncertainty of quantities at that test condition. For this first test, multiple runs were performed at each desired blade loading of the coaxial rotor, varying the torque balance between the upper and lower rotors. Torque balance τ is defined as the difference between upper and lower rotor torque normalized by total system torque as shown in Equation (5.1).

$$\tau = \frac{(C_{QL} - C_{QU})}{(C_{QL} + C_{QU})} \tag{5.1}$$

Data was taken as near to torque balanced as possible, which was found to occur at nearly equal upper and lower collectives. The torque balance was very sensitive to collective, with changes of approximately 0.25 degrees collective resulting in up to a 10% change in torque balance. Due to this sensitivity, additional data was taken with small torque imbalances between upper and lower rotor at each blade loading. These data points, along with the

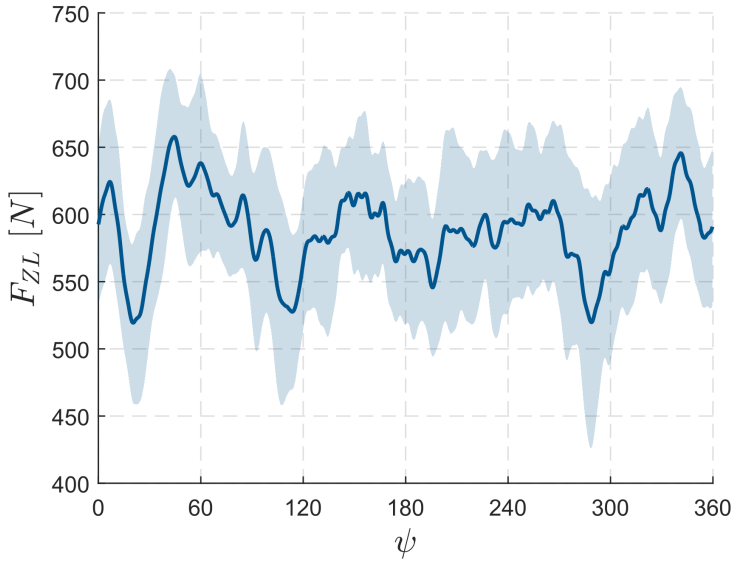

(a)

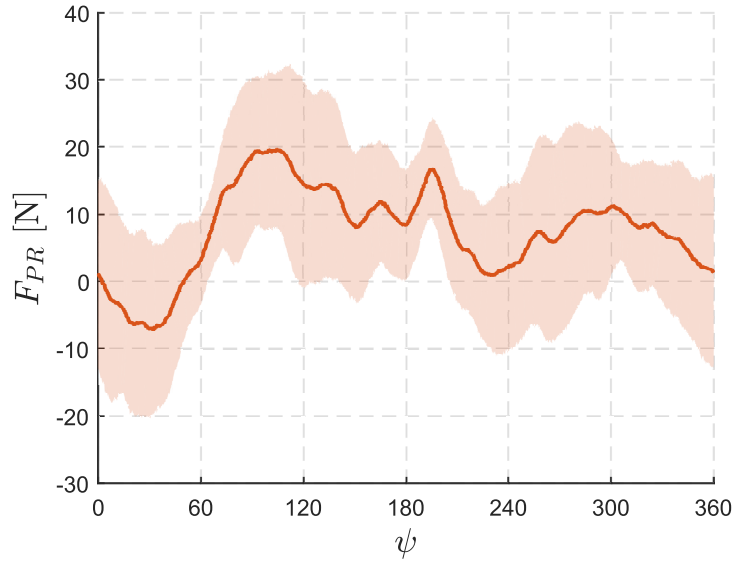

(b)

Figure 5.2: Phase averaged data over one rotor revolution (Tip speed = 190 m/s and $C_T/\sigma = 0.089$) (a) Lower rotor thrust (F_{ZL}), (b) push rod force (F_{PR})

nearly torque balanced data, were then used to generate linear fits in order to interpolate the exactly torque balanced condition, as well as $\pm 5\%$ unbalanced conditions. An example of raw C_T data with overlaid linear fits is shown in Figure 5.3.

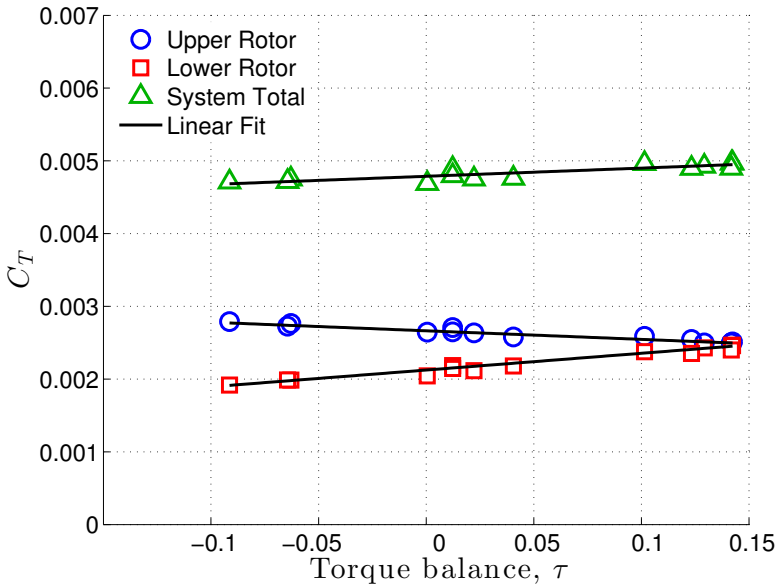

Figure 5.3: Coaxial rotor thrust vs. torque balance τ with linear fits for estimating thrust at exactly torque balanced condition

For the second set of tests, the availability of servo-actuated swashplate controls simplified the trimming and data processing procedure. At each test condition, an upper rotor collective pitch was set and the lower rotor collective pitch adjusted until the system was as close to torque balanced as possible. Post-processing the second test data consisted of checking torque balance values and discarding any points with $\tau > 0.03$. As no push rod forces were

recorded during this second set of tests, quartic polynomials were fit to the mean push rod forces from the first set of tests; these were used to compensate the thrust loads in the second set of tests. The measured load cell forces are a combination of the desired hub forces and the pushrod loads as described in section 3.2.3. The measured push rod forces, along with the polynomial fits and uncertainties used to compensate the second set of thrust data are presented in Figure 5.4. The interpolated push rod force is multiplied by the number of pushrods and subtracted from the measured thrust value. For the upper rotor, the push rod forces are multiplied by an additional factor to account for the pitch link geometry.

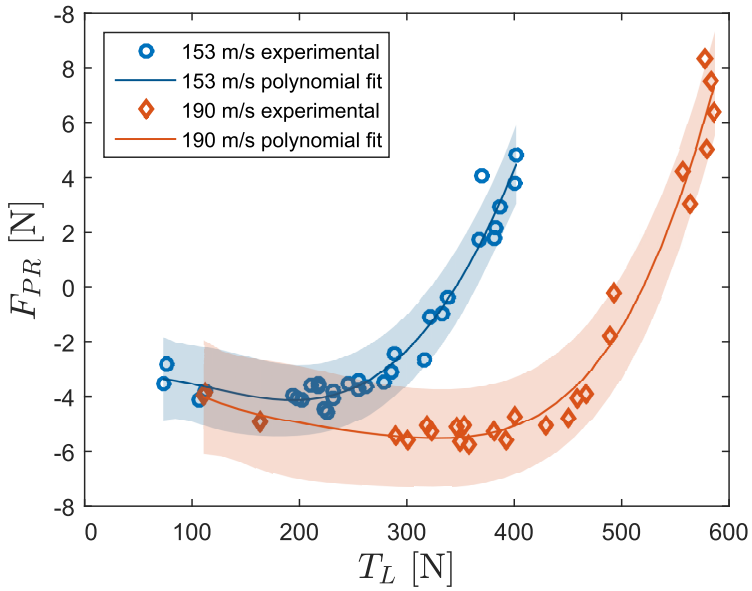

Figure 5.4: Measured push rod load vs rotor thrust including polynomial fits with 95% confidence intervals

The final round of testing with the reinforced blades, included the complete control and instrumentation system described in chapter 3. The test procedure was similar to that for the second round of testing. The upper rotor collective was fixed and the lower rotor adjusted to torque balance. These tests were performed for comparison of the reinforced to reference blades, and to measure root pitch angles and pushrod forces using the additional instrumentation. The measurement of pushrod forces allows for analysis of the vibratory hub loads for these tests.

In all test cases the azimuthal encoder is used to project forces from the rotating load cell frame to the fixed frame coordinate system as shown in figure 5.5. The fixed frame coordinate system is oriented with X positive over the rotorcraft tail, Y positive to the right, and Z positive upward.

5.2 Performance and Steady Loads

The performance of the rotor system concentrates on the relationship between rotor thrust and power. In §5.2.1 - 5.2.3 the effects of tip speed, test setup, and torque balance on thrust and power are examined. Statistical analysis using momentum theory model fits and the Student's-t test justify the compilation of data from several different test runs. Coaxial and isolated configurations of the rotor system are compared using the same method in §5.2.4, while the individual upper and lower coaxial rotor performance is investigated in §5.2.5. Finally the effects of rotor configuration on collective pitch control response are presented in §5.2.6.,

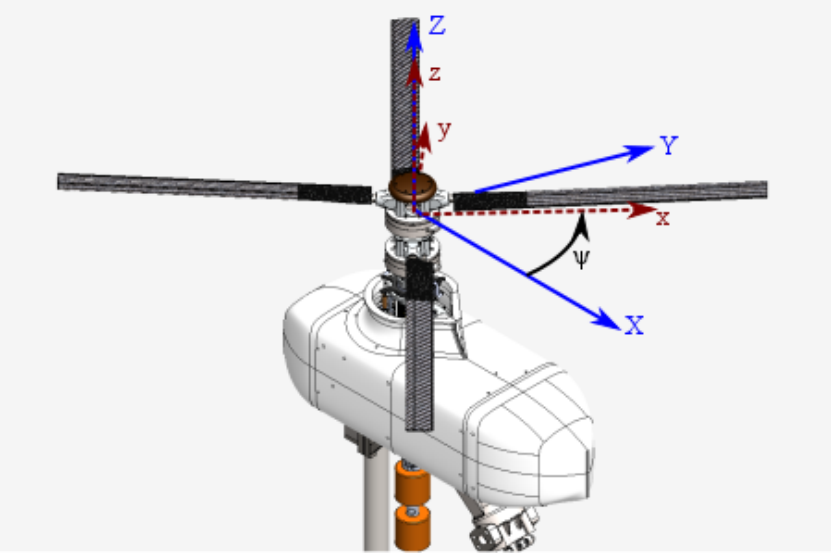

Figure 5.5: Rotating frame load cell coordinate system (red) and fixed frame coordinate system (blue)

5.2.1 Tip speed effect

During the first set of tests, data was collected at two different tip speeds, 153 and 190 m/s, corresponding to blade chord-based Reynolds numbers of 5.8×10^5 and 7.4×10^5 at the 3/4 span location. In order to compare the performance of the rotor systems, an analytical model derived from momentum theory, shown in equation (5.2), was fit to the measured data using a linear least-squares regression. In this Reynolds number regime, it is important to check for the impact of tip speed on the performance characteristics of the rotor, especially as related to the profile power, as the airfoil C_d is sensitive to the Reynolds number. The coaxial rotor system performance data at both tip speeds is plotted in Figure 5.6 and the induced power coefficient and profile

power are given in table 5.3 along with 95% confidence intervals. There is no statistical difference in induced power or profile power of the rotor system at the two tip speeds (p =0.349 and p = 0.387 respectively). These p-values, calculated using the Student's-t test, represent the probability of the observed data given the null hypothesis that both rotors perform identically. Small p-values, generally less than 0.05, indicate that the null hypothesis is unlikely and there may be a performance difference between two rotor systems. With p-values greater than 0.3, the two tip speeds are combined in the following sections.

$$C_P/\sigma = \kappa \sqrt{\sigma}\frac{(C_T/\sigma)^{3/2}}{\sqrt{2}} + \frac{C_{P0}}{\sigma} \tag{5.2}$$

5.2.2 Different test setups

As previously described, a second set of tests were performed six months after the first set. In between tests, the rotor system was completely dismantled and reassembled with a new pitch control system. The two sets of test data were compared by the same methods used to compare the effect of tip speed; the results are shown in Figure 5.7 and table 5.3. The second set of tests was performed at lower blade loadings; as such, the extrapolated momentum theory model shows greater disagreement with the first set of tests at higher blade loadings. However, as in the case of the different tip speeds, there was no statistically significant difference in induced power or profile power between tests 1 and 2 (p= 0.167 and p = 0.325 respectively). This indicates good re-

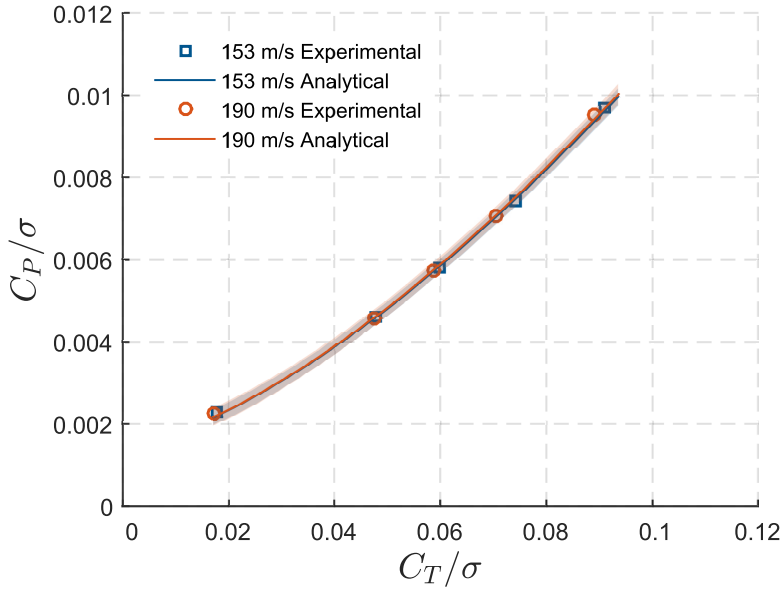

Figure 5.6: Comparison of coaxial rotor performance data between 153 and 190 m/s tip speeds

peatability in the performance measurements, even separated by six months and with completely different pitch control systems.

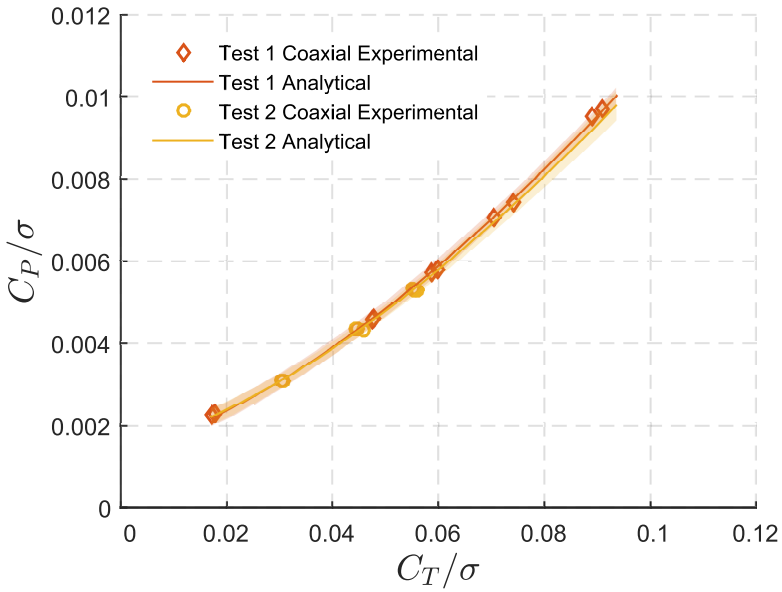

Figure 5.7: Comparison of coaxial rotor performance data from Test 1 and Test 2 conducted six months apart

5.2.3 Effect of torque balance

The same linear fits used to interpolate an exactly torque balanced condition in the test 1 data were also used to interpolate the performance of the rotor system with torque unbalances of $\tau = \pm 0.05$. This data is plotted along with the torque balanced data in figure 5.8. Note that due to the nature of the linear fits, there is increased uncertainty in the unbalanced performance curves. However, there is no statistically significant difference in rotor performance

between the three conditions. This result is in agreement with the momentum theory derivations by Leishman and Syal [65]. They showed a negligible change in system induced power coefficient (less than 0.1%) between torque balanced and thrust balanced rotor systems. Further measurements targeting various torque balance conditions could reduce the uncertainty of the unbalanced data as well as reveal trends in performance at higher imbalance ratios, however, the typical operating condition for a helicopter with a CCR rotor system is with the torque balanced, i.e., yaw trim condition.

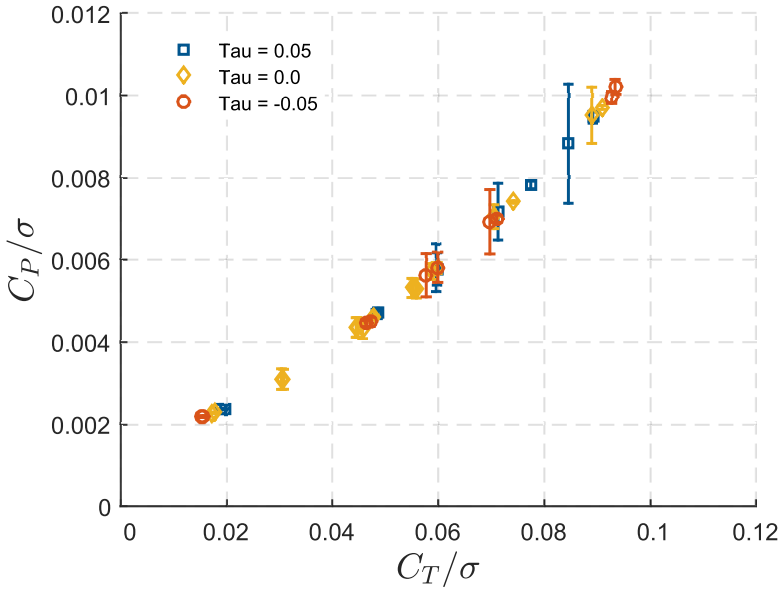

Figure 5.8: Effect of torque balance on coaxial rotor hover performance

5.2.4 Coaxial and Isolated Rotor System Performance

First, both isolated rotor configurations were processed and the thrust versus power curves compared to the FVM predictions (Figure 5.9). The experimental data is plotted with 95% confidence intervals based on the combination of the observed measurement precision and the load cell bias error. This data was used to verify the VR-12 lift and drag polars used in the FVM simulations. Good agreement is seen without any additional modification to the lookup tables calculated in Fluent. The FVM simulations appear to slightly under-predict the measured power requirements for both the two and four-bladed isolated rotors at higher thrust levels while falling within the uncertainty bounds. The BEMT model is accurate at lower thrusts, but underpredicts power at high C_T by a larger margin than for the FVM calculations. In Figure 5.10, the FVM and BEMT predictions are compared to the measured performance of the two-bladed coaxial rotor. It is clear that the FVM model is able to achieve good correlation to the experimental results across all investigated thrust values, while the BEMT underpredicts power at low and high thrust. This indicates an issue with the induced power, and therefore inflow calculated by the BEMT.

To compare the isolated rotor systems to the coaxial system, thrust vs. power is plotted normalized by rotor solidity in Figures 5.11a and 5.11b. Plotted with the experimental data are analytical momentum theory fits with shaded 95% confidence intervals; the coefficients of which are listed in table 5.3. Figure 5.11a shows the two-bladed single rotor consuming significantly

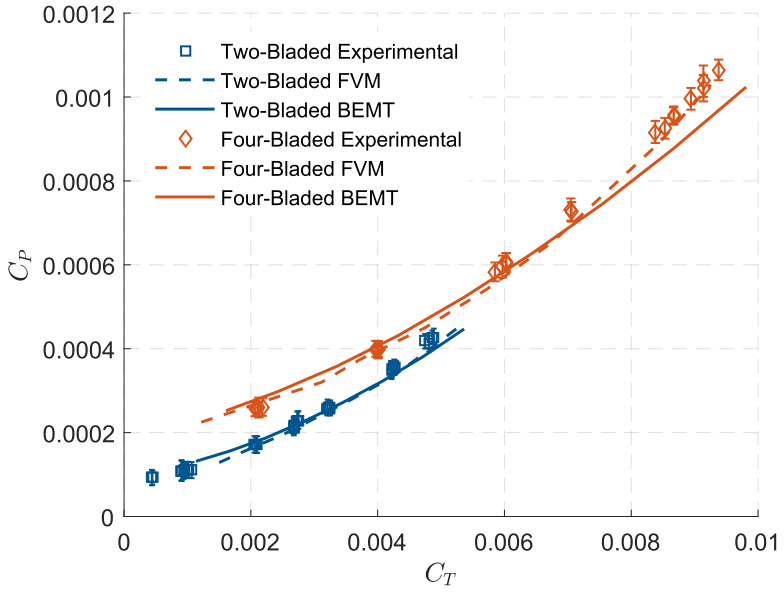

Figure 5.9: Mean thrust vs. power, measurements with FVM and BEMT predictions of single rotor configurations

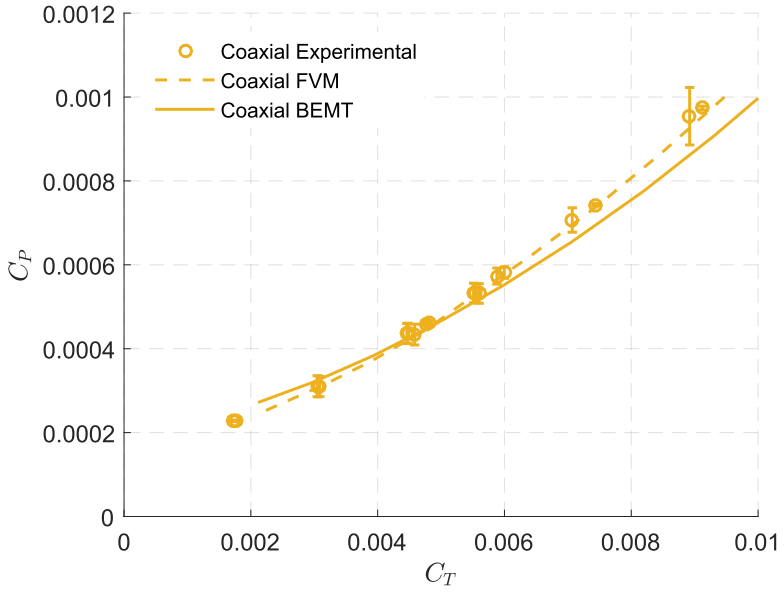

Figure 5.10: Mean thrust vs. power, measurement and FVM and BEMT prediction of the two-bladed coaxial rotor system

less power on a per blade basis than the coaxial rotor system at higher thrust values. This is due to the reduced solidity of the two-bladed isolated rotor affecting the per-blade induced power as seen in the factor of $\sqrt{\sigma}$ multiplying the induced power term in equation (5.2). The two-bladed isolated rotor may consume less power per blade at a given blade loading but has an overall thrust capacity of approximately half the coaxial rotor system. A better comparison is between systems that are geometrically identical in blade planform and solidity, differing only in rotor configuration. This is shown in Figure 5.11b where the coaxial rotor system is compared to the isolated four-bladed rotor. Here the two systems appear similar, with the coaxial rotor consuming slightly less power at higher blade loadings. This result is significant, as the coaxial rotor consumes less power than the isolated rotor, even before additional power savings from the lack of tail rotor are accounted for. This advantage in hover efficiency makes the coaxial rotor system attractive, even at low flight speeds.

Table 5.4 shows the induced power coefficients and profile powers of the rotor systems with 95% confidence intervals calculated from the regression. The four-bladed isolated rotor and the two-bladed coaxial system, having equal solidity, show no statistical difference in profile power, while the difference in the induced power coefficient is significant with $p = 3.5 \times 10^{-4}$. The induced power coefficient of the two-bladed isolated rotor is slightly higher than that of the four-bladed rotor, however the difference is not statistically significant. Additionally the two-bladed isolated rotor exhibits approximately one-half the profile power of the four-bladed isolated and two-bladed coaxial rotors, a result

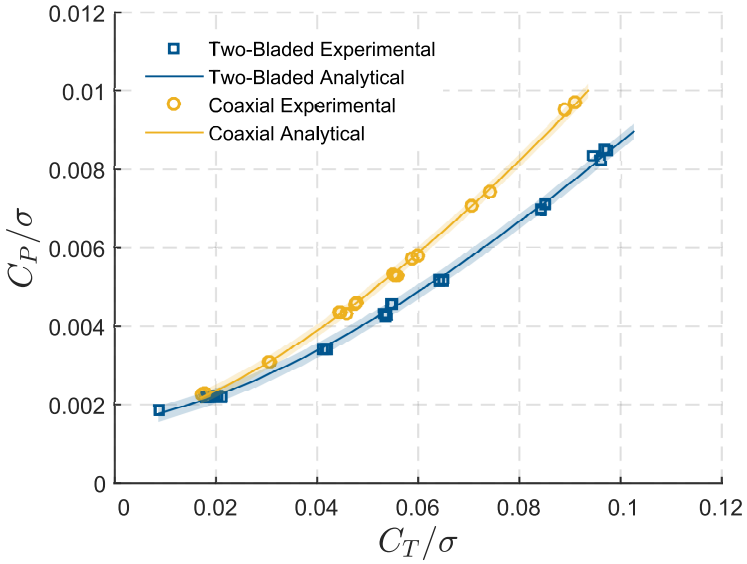

(a)

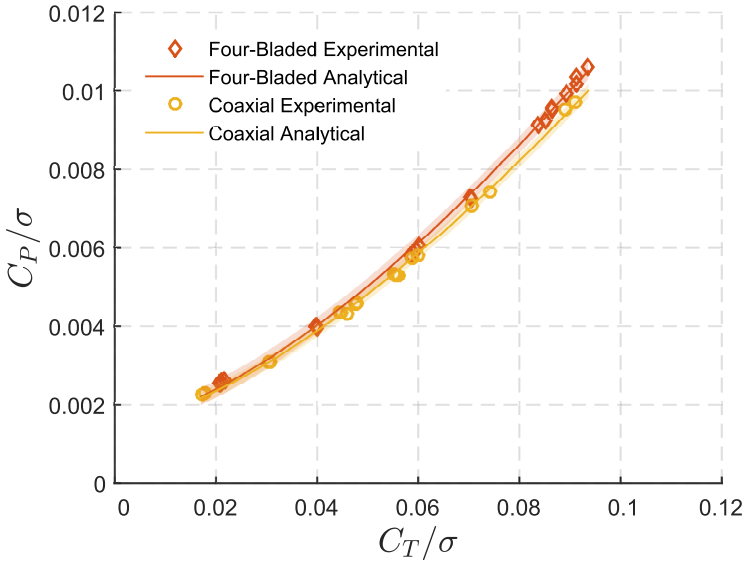

(b)

Figure 5.11: Comparison of 2-bladed coaxial rotor performance to, (a) 2-bladed single rotor, (b) 4-bladed single rotor

expected from BEMT.

The ratio of the two-bladed coaxial induced power coefficient to that of the four-bladed rotor system, referred to by Ramasamy [89] as a separation coefficient, κ_{sep}, is 0.942 ± 0.022 for the current rotors. This means that the coaxial rotor system consumes 6% less induced power than the equivalent isolated rotor system. This result is in agreement with the conclusions drawn from the reexamination of the momentum theory model of Leishman and Syal, described in §2.1.1.2. These measurements also validate computational results reported by Kim and Brown [55] for the Harrington coaxial rotor and a notional equivalent four-bladed isolated rotor. Similar experimental results were obtained by Nagashima et al. [75] who found that a coaxial rotor system consumed up to 6% less power than the equivalent solidity single rotor as well as by Ramasamy [89] who showed a 10% decrease in induced power for an equivalent solidity coaxial rotor.

The FVM model is used to further explore the components of the rotor system power (Figure 5.12). Here, there is a clear difference in induced power between the two-bladed isolated rotor and both the four-bladed isolated and two-bladed coaxial rotor. Indeed, the agreement between the rotor systems of equivalent solidity suggests that the difference in per-blade power with the two-bladed rotor system is simply due to a solidity effect. Note also that the predicted profile power remains nearly constant across all test conditions. This is important as it validates the useage of the momentum theory model in equation (5.2) which was derived assuming a constant profile power coefficient.

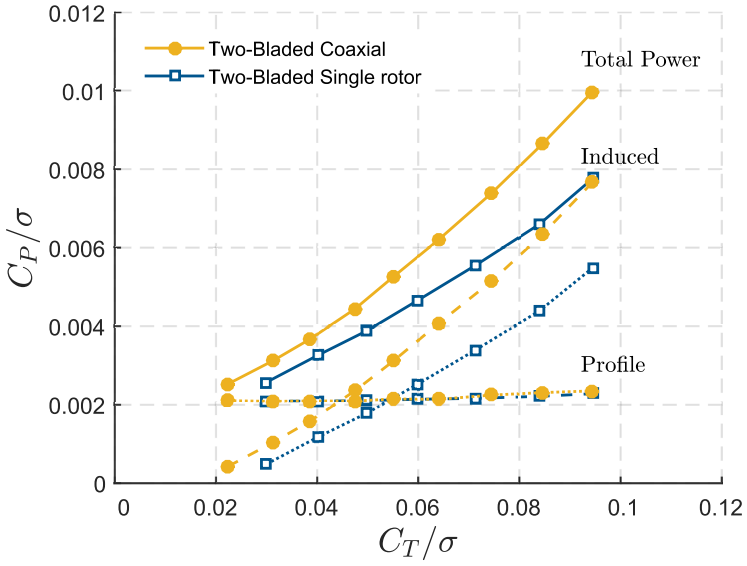

(a)

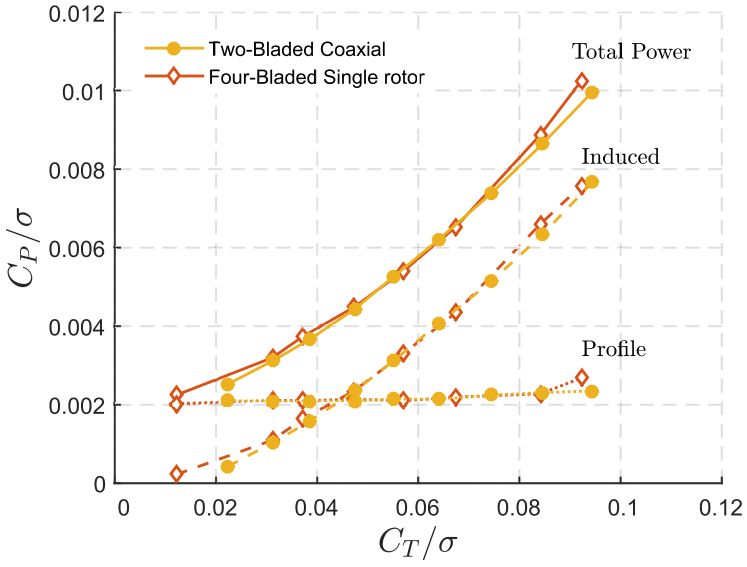

(b)

Figure 5.12: Power breakdown of 2-bladed coaxial, 2-bladed single, and 4-bladed single rotor systems calculated using the FVM

5.2.5 Upper and Lower Coaxial Rotor Performance

Considering upper and lower rotor hub load data separately, the interactional effect on the performance of the upper and lower coaxial rotors are investigated by comparing each with an isolated two-bladed single rotor of equivalent solidity and planform. Figure 5.13 compares the performance of the upper and lower rotors with the data measured from the isolated two-bladed rotor. The upper and lower rotor performances are greatly impacted due to aerodynamic interaction resulting in increased power consumption. This behavior is well captured by the FVM model. The BEMT model, shown in figure 5.14 provides a fairly accurate prediction of lower rotor power, with the prediction falling within the upper uncertainty bounds of the experimental results. On the other hand, the interference effect on the upper rotor is not captured at all, with coaxial upper and isolated two-bladed results coinciding. This result is expected, as the model derivation included no allowance for the lower rotor to interact with the upper.

The same analytical model used to fit overall rotor system performance is used for the individual rotors as shown in Figure 5.15 as well as in table 5.4. A quantitative measurement of the interference effect is obtained by taking the ratio of the individual coaxial rotor induced power factors to that of the isolated two-bladed rotor system. This quantity, referred to as the rotor on rotor influence factor by Ramasamy [89], is found to be $\kappa_U = 1.178 \pm 0.035$ and $\kappa_L = 1.490 \pm 0.030$ for the upper and lower rotors respectively. The lower rotor suffers the greater performance impact with 49% increased induced

power compared to an isolated two-bladed single rotor, while the upper rotor only shows 18% increase. The mean power increase of the system (33.4%) falls between momentum theory estimates of induced power interference factor given by Leishman and Syal [65] as $\kappa_{int} = 1.414$ for co-planar rotors and $\kappa_{int} = 1.2818$ for a lower rotor operating in the fully-developed slipstream of the upper rotor.

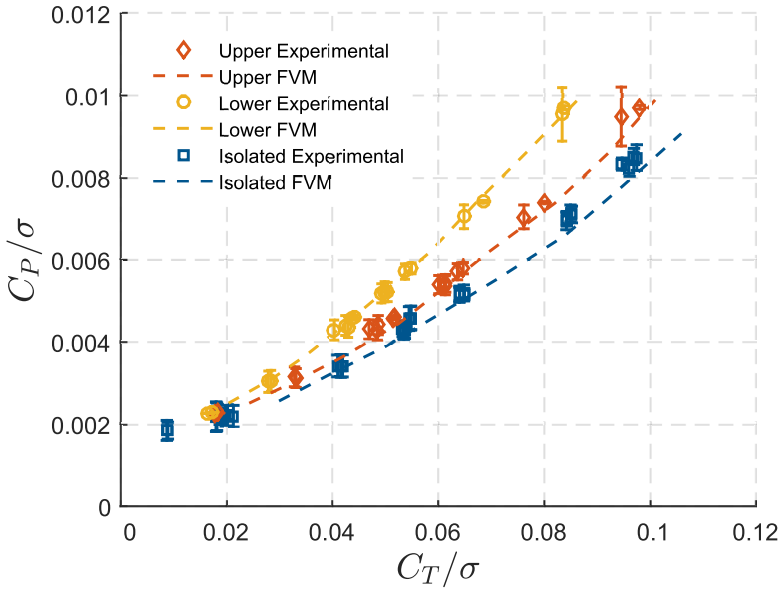

Figure 5.13: Performance comparison of two-bladed isolated rotor to upper and lower coaxial rotors with FVM predictions

The relationship between upper and lower rotor thrust in the torque balanced condition is explored further in Figure 5.16a. Here the thrusts are seen to follow linear trends of different slopes with increasing system thrust. Predictions from the FVM are overlaid and show excellent agreement with

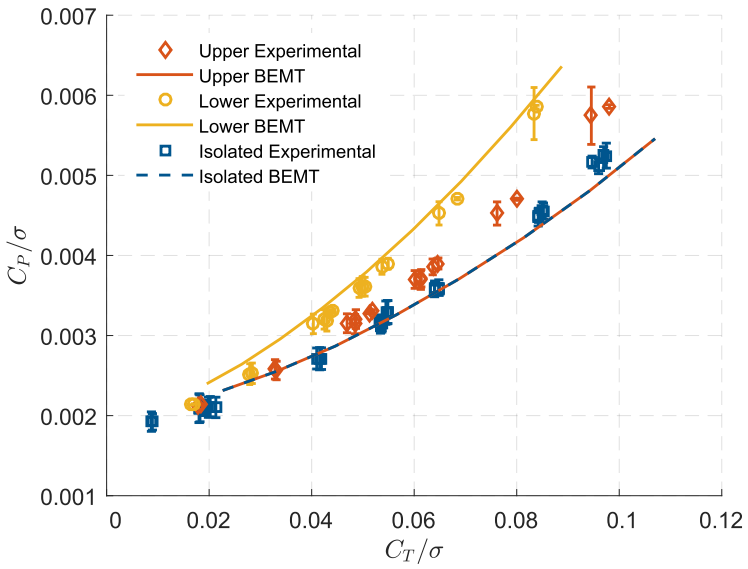

Figure 5.14: Performance comparison of two-bladed isolated rotor to upper and lower coaxial rotors with BEMT predictions

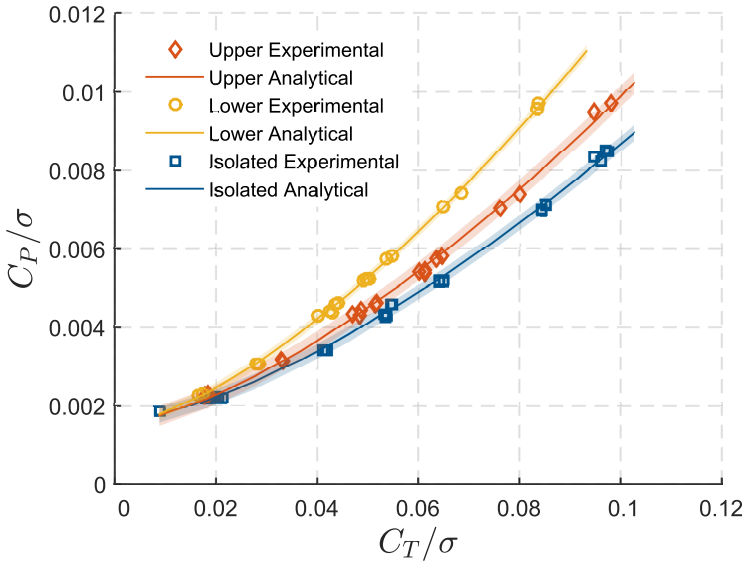

Figure 5.15: Performance comparison of two-bladed isolated rotor to upper and lower coaxial rotors with analytical fit

the experimental data. The BEMT predictions are poor, overpredicting upper rotor thrust while underpredicting lower rotor thrust. Figure 5.16b shows the ratio of upper rotor to total system thrust at both the balanced and unbalanced conditions. In the balanced configuration, the ratio is nearly constant with the upper rotor producing $53.8 \pm 2.0\%$ of the total thrust. This result is consistent with the analysis performed on the Harrington rotor data by Kim and Brown [55], the experimental and analytical results of Nagashima et al. [75] and with the experimental work of Ramasamy [88]. While the uncertainty in the torque unbalanced conditions is significant, the mean thrust ratios are calculated as $49.4 \pm 6.4\%$ and $58.1 \pm 4.4\%$ for the $\tau = 0.05$ and $\tau = -0.05$ cases. Note that the -5% torque unbalance case nearly achieves an equal thrust condition for the upper and lower rotors.

The computations from the FVM and BEMT also give an estimate of the radial variation of rotor inflow and thrust production as shown in Figure 5.17. The inflow ratio, shown in figure 5.17a, is underpredicted for the upper rotor by the BEMT when compared to the FVM, while the opposite is true for the lower rotor. Additionally, with no allowance for viscous diffusion in the wake, the BEMT lower rotor predictions demonstrate a large discontinuity in the inflow velocity at the edge of the upper rotor wake. The allowance for vortex diffusion in the FVM model dissipates this discontinuity by the time the upper rotor wake reaches the lower rotor. Note that the BEMT model has a prescribed converged upper wake radius of $0.85R$ at the lower rotor disk. Similar behavior is seen in the radial thrust distribution in figure 5.17b.

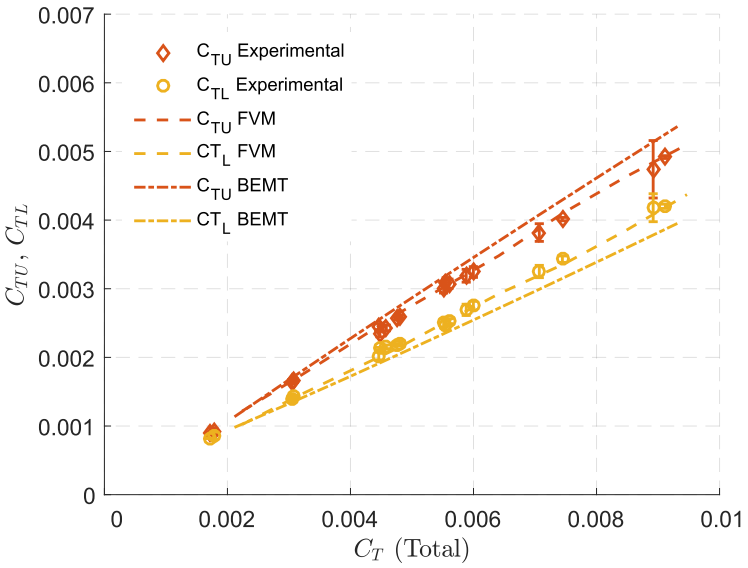

(a)

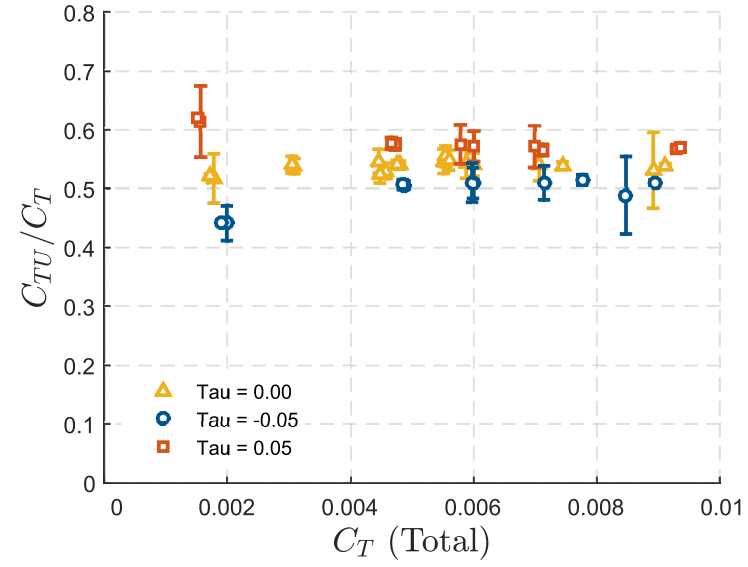

(b)

Figure 5.16: Thrust sharing between upper and lower coaxial rotors, (a) Torque balanced upper and lower rotor thrust vs. total thrust, (b) Ratio of upper to total thrust vs. torqe balance

The BEMT upper rotor thrust is greater than the FVM thrust at all radial stations, with the greatest differences occurring near the rotor tip and mid-span. The large discontinuity in the inflow manifests itself in the lower rotor thrust distribution. The result is thrust production concentrating outside of the upper rotor slipstream.

The coaxial rotor FVM results are next compared to those of the isolated, four-bladed rotor. In Figure 5.18a the inflow ratio λ is plotted against radial location for both the four-bladed isolated rotor as well as the upper and lower coaxial rotors. There is a significant increase in lower rotor inflow due to the upper rotor wake, and upper and lower rotor inflow conditions straddle the four-bladed isolated rotor inflow, especially further from the blade root. This phenomenon, with the four-bladed rotor distribution falling between the upper and lower rotor distributions, is seen again in Figure 5.18b, where the blade thrust distribution is plotted against the radial location. These results agree with the findings of Kim and Brown for the Harrington rotor system [54]. Overall, aerodynamic interference effects cause the increase in upper and lower rotor induced power consumption when compared to the isolated two-bladed rotor, and when averaged result in a total system performance similar to the isolated four-bladed rotor.

5.2.6 Collective Response

The third round of testing included the complete rotor system instrumentation along with the reinforced blades used in wind-tunnel testing at 900,

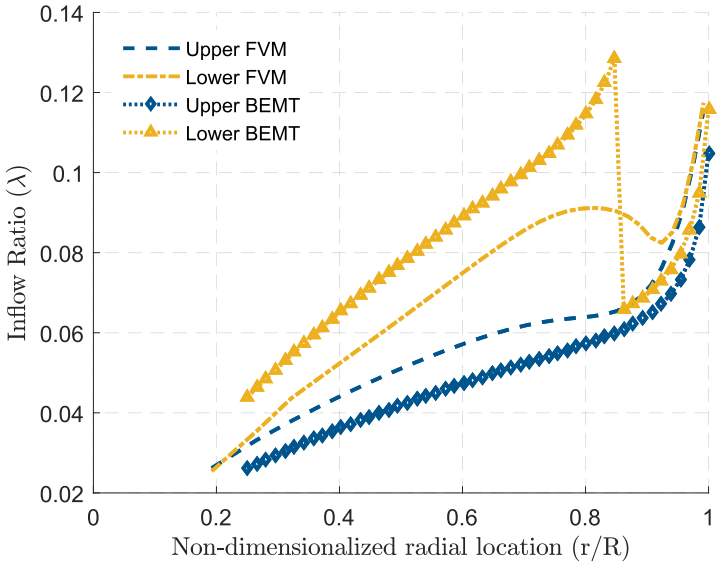

(a)

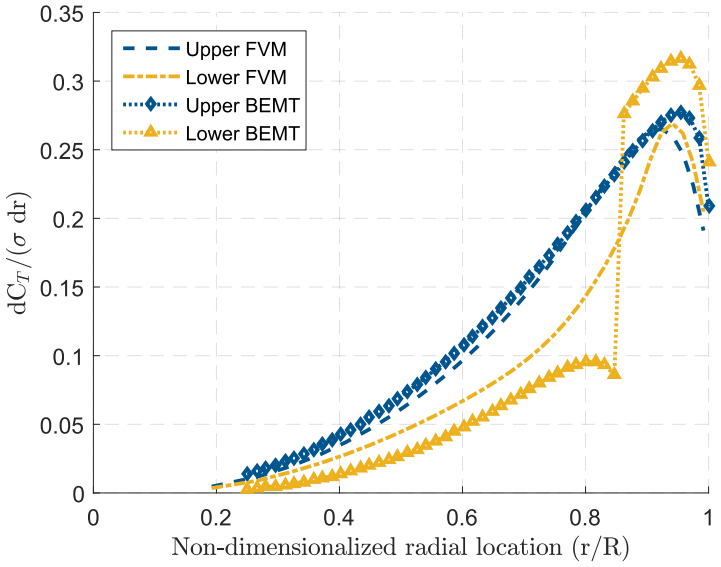

(b)

Figure 5.17: Radial variation of coaxial rotor performance, comparison between BEMT and FVM ($C_T/\sigma = 0.084$), (a) Inflow ratio, (b) Thrust

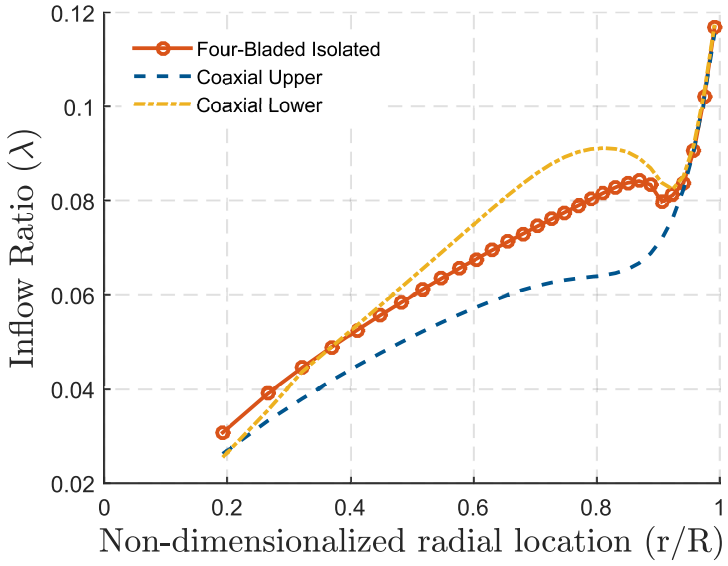

(a)

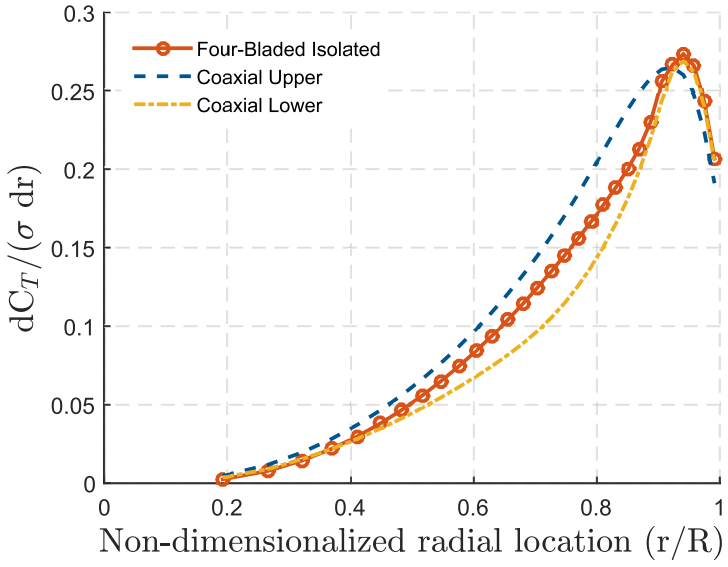

(b)

Figure 5.18: Radial variation of rotor performance, four-bladed isolated and two-bladed coaxial rotors ($C_T/\sigma = 0.084$), (a) Inflow ratio, (b) Thrust

1200 and 1500 RPM. Table 5.5 summarizes the measured induced power factors and profile power constants for the reinforced blades. The reinforced blades exhibit slightly lower induced power coefficients than the reference blades tested, likely due to the extension of the datasets to lower thrusts. The profile power coefficients agree with those of the reference blades to within the measurement uncertainty. Additionally the interference factors, $\kappa_{int} = 1.19 \pm 0.08$ for the upper and $\kappa_{int} = 1.155 \pm 0.18$ agree with those for the reference rotors.

Using the root pitch angle sensors, the interference effect on rotor control angles is explored in figures 5.19a and 5.19b. Figure 5.19a shows blade loading varying with collective. At low collective values the isolated lower rotor thrust is notably higher than the isolated upper rotor, however at higher collectives the two curves coincide. The upper and lower rotors of the coaxial system coincide with the upper isolated rotor at low collective values where the interference effect is smallest. As the collective increases the thrust from both the lower and upper rotors falls off from the isolated cases, with a more prominent decrease in the lower rotor thrust. The slope of a linear regression of thrust vs. collective angle measures the sensitivity of thrust to collective. The thrust sensitivities for all four rotors are listed in table 5.6. The lower rotor collective sensitivity decreases by 21±6% while the upper rotor collective sensitivity decreases by only 11±5%. Figure 5.19b shows the variation of rotor system power with collective. Here the differences between the isolated and coaxial cases is much smaller. The most important trend is the slightly increased lower coaxial rotor collective for a given power level when compared to

both the upper coaxial rotor, as well as isolated upper and lower rotors. This difference results in a positive differential collective between the lower and upper rotors when the system is torque balanced, and is due to the decrease in angle of attack as the upper rotor wake impinges on the lower rotor. The mean differential collective between lower and upper coaxial rotors for the test cases shown is $0.32 \pm 0.095^\circ$. This result is much smaller than the differential collective predicted by BEMT $1.28 \pm 0.13^\circ$.

5.3 Vibratory Loads

Vibratory loads in hover are, in general, much lower than in forward flight, however the aerodynamic interaction between upper and lower coaxial rotors does introduce vibration when compared to isolated rotors. Figure 5.20 shows the first four hub load even harmonics for the isolated lower and upper, as well as coaxial upper and lower rotors in hover. All six components are shown, with forces normalized by the steady rotor thrust and the moments normalized by the steady thrust times the rotor radius. These normalized vibratory forces are, in most cases, less than 5% of rotor thrust, while the normalized moments are generally less than 1%. In all force components and configurations there is a significant two-per-revolution component associated with the two-bladed rotor interaction with the faired transmission assembly. For the coaxial configuration there is a significant increase the in four-per-revolution thrust due to aerodynamic interference at the four upper-lower rotor blade crossings. This effect is largest on lower coaxial rotor operating in

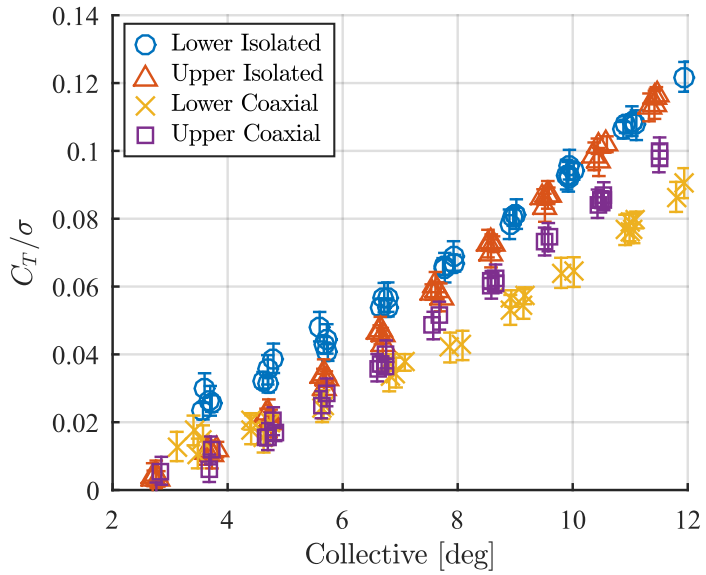

(a)

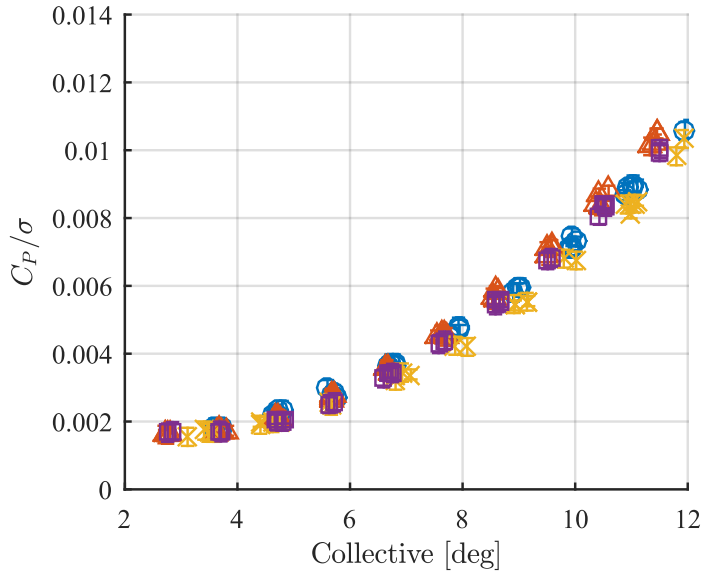

(b)

Figure 5.19: Hover performance vs. collective angle (a) Blade loading (b) Power

the downwash from the upper rotor where the normalized four-per-revolution thrust approaches 10% of the steady thrust. The effect of the lower rotor on the upper rotor is much smaller, with the vibratory four-per-revolution thrust remaining below 5%.

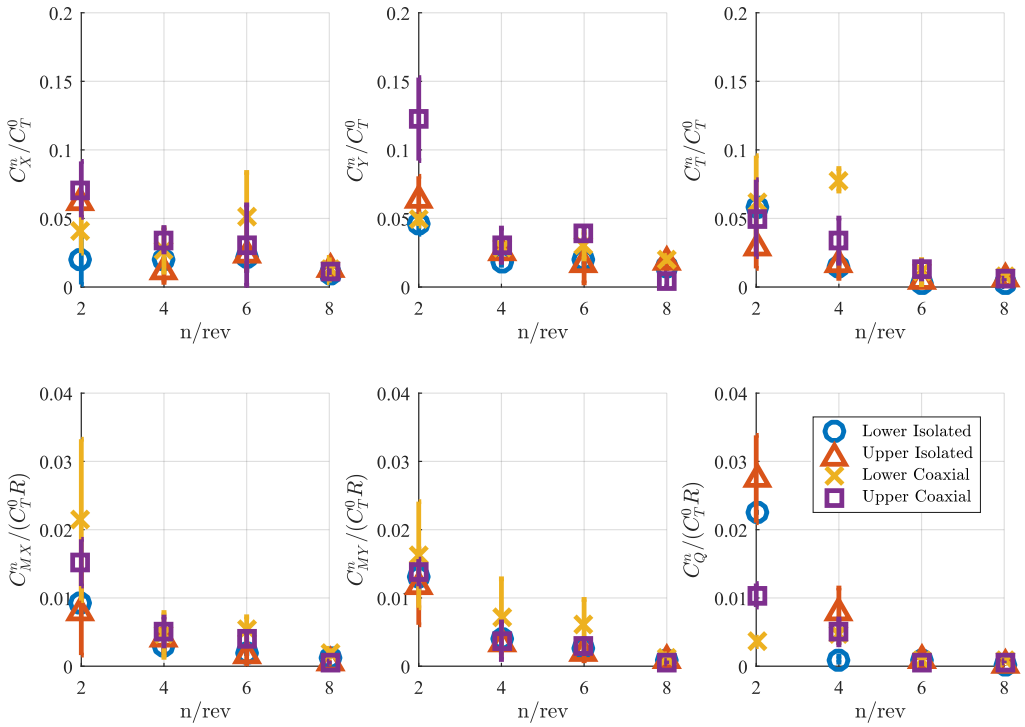

Figure 5.20: Isolated and coaxial upper and lower rotor vibratory hub load amplitudes in hover, ($\theta_0 = 8°$)

An example of the lower rotor azimuthal thrust variation is shown in figure 5.21. The dominant four-per-revolution component is apparent with thrust peaks occuring near the upper-lower rotor blade crossings, marked by vertical dashed lines. In addition to the initial, larger peaks in thrust, sec-

ondary peaks occur approximately 30° delayed. This indicates that there is more than one mechanism generating the unsteadiness. Lakshminarayanan and Baeder [60] suggest a combination of blade bound-vortex interaction and a Venturi effect from the displacement thickness of the blades. While the bound vortex interaction may be captured by a lifting-line based code, a full CFD analysis is necessary to capture thickness effects.

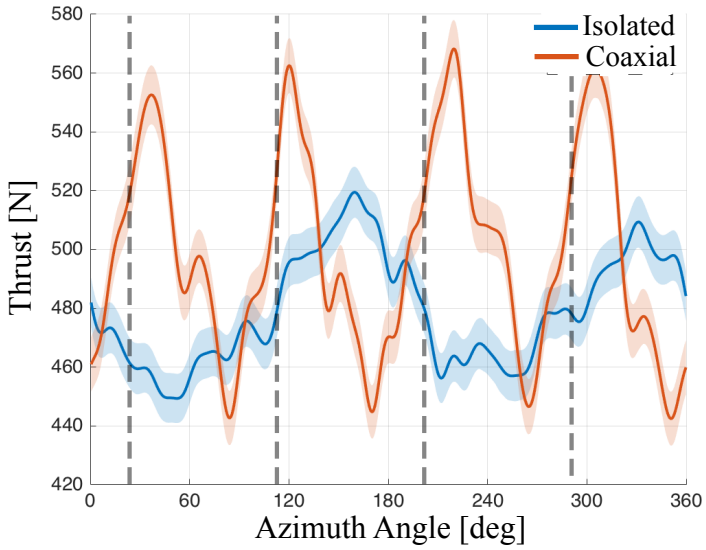

Figure 5.21: Azimuthal variation of isolated and coaxial rotor thrust in hover, blade crossings indicated by dashed lines at $20° + n \times 90°$

Table 5.1: Hover test matrix

	Configurations	Pitch Control	Tip Speeds [m/s]	Max Blade Loading
Test 1	Two-bladed Isolated Four-bladed Isolated Two-bladed Coaxial	Manual	190, 150	0.10
Test 2	Two-bladed Isolated Two-bladed Coaxial	Hitec Servos	190, 150	0.06
Test 3	Two-bladed Isolated Two-bladed Coaxial	Linear Servos	150, 127, 95	0.13

Table 5.2: Summary of rotor properties (hover testing)

	Two-bladed single	Four-bladed single	Two-bladed coaxial
Rotor Spacing			0.140 m
Solidity	0.050	0.100	0.100
Rotor Radius (R)		1.016 m	
Root Cutout		12%R	
Precone Angle		3°	
Airfoil		VR-12	
Chord		0.080 m	
Tip Speed [m/s]		96, 128, 153, 191	
Rotor Speed [RPM]		900, 1200, 1430, 1795	

Table 5.3: Comparison between tests: momentum theory fits to measured rotor system performance, including 95% confidence intervals

Rotor system	Induced power coefficient κ	Profile power $C_{P0} \times 10^4$
Test 1 (ΩR= 150 m/s)	1.320 ± 0.034	1.511 ± 0.105
Test 1 (ΩR = 190 m/s)	1.330 ± 0.041	1.514 ± 0.132
Test 2	1.281 ± 0.077	1.585 ± 0.177

Table 5.4: Reference blade rotor systems: momentum theory fits to measured rotor system performance, with 95% confidence intervals

Rotor system	Induced power coeff. κ	Profile power $C_{P0} \times 10^4$
Two-bladed isolated	1.419 ± 0.022	0.793 ± 0.028
Four-bladed isolated	1.406 ± 0.021	1.506 ± 0.087
Two-bladed coax	1.325 ± 0.023	1.513 ± 0.074
Two-bladed coax upper	1.672 ± 0.044	0.765 ± 0.056
Two-bladed coax lower	2.115 ± 0.029	0.753 ± 0.030

Table 5.5: Reinforced blade rotor systems: momentum theory fits to measured rotor system performance, with 95% confidence intervals

Rotor system	Induced power coeff. κ	Profile power $C_{P0} \times 10^4$
Two-bladed isolated	1.32 ± 0.07	0.64 ± 0.11
Two-bladed coax	1.27 ± 0.05	1.37 ± 0.25
Two-bladed coax upper	1.60 ± 0.10	0.76 ± 0.15
Two-bladed coax lower	2.01 ± 0.12	0.61 ± 0.20

Table 5.6: Rotor thrust collective sensitivity for isolated and coaxial rotors

Rotor system	Thrust sensitivity $((C_T/\sigma)/\theta_0)\times 10^3$
Two-bladed isolated upper	11.6 ± 0.5
Two-bladed isolated lower	13.3 ± 0.5
Two-bladed coaxial upper	9.2 ± 0.6
Two-bladed coaxial lower	11.8 ± 0.5

Bibliography

[1] *La Vision 2016 DaVIs StrainMaster 3-D, Software Package Version 8.1.* La Vision, Goettingen, Germany.

[2] Composite materials handbook, vol. 2. Handbook MIL-HDBK-17-2F, Department of Defense, 2002.

[3] Nist/sematech e-handbook of statistical methods, October 2013.

[4] A. I. Abrego, L. E. Olson, E. A. Romander, D. A. Barrows, and A. W. Burner. Blade displacement measurement technique applied to a full-scale rotor test. In *American Helicopter Society 68th Annual Forum Procedings (Fort Worth, TX, 1-3 May)*, 2012.

[5] D. N. Arents. An assessment of the hover performance of the XH-59A advancing blade concept demonstration helicopter. Technical Report USAAMRDL-TN-25, U. S. Army Air Mobility Research and Development Laboratory, May 1977.

[6] K. O. Arras. An introduction to error propagation: Derivation, meaning and examples of equation $c_y = f_x c_x f_x^t$. Technical Report EPFL-ASL-TR-98-01 R3, EPFL, September 1998.

[7] ATI Industrial Automation. *Six Axis Force/Torque Sensor System Installation and Operation Manual*, April 2012.

[8] A. Bagai. Aerodynamic design of the x2 technology demonstrator^{TM} main rotor blade. In *Proceedings of the American Helicopter Society 64th Annual Forum, Montréal, Québec*, April 29 - May 4 2008.

[9] A. Bagai and J. G. Leishman. Rotor free-wake modeling using a pseudo-implicit technique-including comparisons with experimental data. *Journal of the American Helicopter Society*, 40(3):29–41, 1995.

[10] A. Bagai and J. G. Leishman. Free-wake analysis of tandem, tilt-rotor and coaxial rotor configurations. *Journal of the American Helicopter Society*, 41(3):196–207, 1996.

[11] J. Bao. *Development of Mach Scale Rotor With Composite Tailored Couplings for Vibration Reduction.* PhD thesis, The University of Maryland, College Park, 2004.

[12] J. B. Barlow, W. H. Rae, and A. Pope. *Low Speed Wind Tunnel Testing.* Wiley-Interscience, Hoboken, NJ, 3rd edition, 1999.

[13] B. Berry and I. Chopra. *Wind Tunnel Testing of an Instrumented Rotor at High Advance Ratio.* American Institute of Aeronautics and Astronautics, 2016/08/25 2015.

[14] M. J. Bhagwat and J. G. Leishman. Stability, consistency and convergence of time-marching free-vortex rotor wake algorithms. *Journal of the American Helicopter Society*, 46(1):59–71, 2001.

[15] M. J. Bhagwat and J. G. Leishman. Generalized viscous vortex core models for application to free-vortex wake and aeroacoustic calculations. In *Proceedings of the 58th Annual Forum of the American Helicopter Society, Montréal Québec*, 2002.

[16] M. J. Bhagwat and J. G. Leishman. Rotor aerodynamics during maneuvering flight using a time-accurate free-vortex wake. *Journal of the American Helicopter Society*, 48(3):143–158, 2003.

[17] R. Blackwell and T. Millott. Dynamics design characteristics of the sikorsky x2 technology demonstrator^{TM} aircraft. In *Proceedings of the American Helicopter Society 64th Annual Forum, Montréal, Québec*, April 29 - May 4 2008.

[18] R. E. Brown and A. J. Line. Efficient high-resolution wake modeling using the vorticity transport equation. *AIAA Journal*, 43(7):1434–1443, July 2005.

[19] B. N. Burtsev. The coaxial helicopter vibration reduction. In *Proceedings of the 18th European Rotorcraft Forum, September, 1992*, 1992.

[20] C. Cameron, A. Karpatne, and J. Sirohi. Performance and vibratory hub loads of a mach-scale coaxial rotor in hover. In *Proceedings of the American Helicopter Society 70th Annual Forum, Montréal, Québec*, May 20 - 22 2014.

[21] C. Cameron, D. Uehara, and J. Sirohi. Transient hub loads and blade deformation of a mach-scale coaxial rotor in hover. In *56th AIAA/ASCE/AHS/ASC Structures, Structural Dynamics, and Materials Conference*. American Institute of Aeronautics and Astronautics Inc., January 5-9 2015.

[22] C. G. Cameron, A. Karpatne, and J. Sirohi. Performance of a mach-scale coaxial counter-rotating rotor in hover. *Journal of Aircraft*, 53(3):746–755, 2016/08/11 2016.

[23] T. G. Carne and G. H. J. III. The inception of {OMA} in the development of modal testing technology for wind turbines. *Mechanical Systems and Signal Processing*, 24(5):1213 – 1226, 2010. Special Issue: Operational Modal Analysis.

[24] M. Cheney. The abc helicopter. *Journal of the American Helicopter Society*, 14(4):10–19, 1969.

[25] C. P. Coleman. A survey of theoretical and experimental coaxial rotor aerodynamic research. *NASA TP 3675*, 1997.

[26] Cytec Industries Inc. *FM 300 Epoxy Film Adhesive*, October 2013.

[27] L. U. Dadone. Design and analytical study of a rotor airfoil. Contractor Report 2988, NASA Langley Research Center, 1980.

[28] I. M. Daniel and O. Ishai. *Engineering Mechanics of Composite Materials*. Oxford University Press, New York, NY, 2006.

[29] J. D'Errico. Adaptive robust numerical differentiaion, December 2014.

[30] R. C. Dingeldein. Wind-tunnel studies of the performance of multirotor configurations. Technical Report TN-3236, NACA, August 1954.

[31] M. Drela and H. Youngren. *XFOIL 6.9 User Primer*. Massachesetts Institute of Technology, Cambridge, MA, 2001.

[32] Evonik Resource Efficiency GmbH. *Rohacell IG/IG-F*, March 2016.

[33] F. F. Felker. Performance and loads data from a wind tunnel test of a full-scale, coaxial, hingeless rotor helicopter. Technical Report TM-81329, NASA, October 1981.

[34] G. A. Fleming and S. A. Gorton. Measurement of rotorcraft blade deformation using projection moiré interferometry. *Shock and Vibration*, 7(3):149–165, 2000.

[35] G. A. Fleming, H. L. Soto, and B. W. South. Projection moiré interferometry for rotorcraft applications: deformation measurement of active twist rotor blades. In *American Helicopter Society 58th Annual Forum Preceedings (Montréal, Quebec 11-13 June)*, 2002.

[36] R. D. Harrington. Full-scale-tunnel investigation of the static-thrust performance of a coaxial helicopter rotor. *NASA TN 2318*, 1951.

[37] L. Hermans and H. V. D. Auweraer. Modal testing and analysis of structures under operational conditions: Industrial applications. *Mechanical Systems and Signal Processing*, 13(2):193 – 216, 1999.

[38] Hexcel. *3501-6 Epoxy Matrix Product Data*, 1998.

[39] Hexcel. *8552 Epoxy Matrix Product Data*, February 2013.

[40] J. Ho, H. Yoo, and M. Bhagwat. Validation of rotorcraft comprehensive analysis performance predictions for coaxial rotors in hover. In *Proceedings of the American Helicopter Society 71st Annual Forum, Virginia Beach, Virgina, May 5-7*, 2015.

[41] D. H. Hodges and E. H. Dowell. Nonlinear equations of motion for the elastic bending and torsion of twisted nonuniform rotor blades. Technical Report NASA-TN-D-7818, NASA Ames Research Center, 1974.

[42] S. R. Ibrahim. Random decrement technique for modal identification of structures. *Journal of Spacecraft*, 14(11):696–700, 1977.

[43] S. R. Ibrahim. Doulbe least squares approach for use in structural modal identification. *AIAA Journal*, 24(3), 1986.

[44] S. R. Ibrahim and E. C. Milkulcik. The experimental deterimination of vibration test parameters from time responses. *The Shock and Vibration Bulletin*, 46(5):187–196, 1976.

[45] G. H. J. III, T. G. Carne, and P. S. Veers. Damping measurements using operational data. *Journal of Solar Energy Engineering*, 118(3):190 – 193, 1996.

[46] G. H. James, T. G. Carne, and J. P. Lauffer. The natural excitation technique (next) for modal parameter extraction from operating structures. *The International Journal of Analytical and Experimental Modal Analysis*, 10(4):260–277, October 1995.

[47] W. Johnson. *Helicopter Theory*. Priceton University Press, 1980.

[48] W. Johnson. Technology drivers in the development of camrad ii. In *Proceedings of the American Helicopter Society Aeromechanics Specialists Conference, San Francisco, California, January 19-21*, 1994.

[49] W. Johnson. Influence of lift offset on rotorcraft performance. Technical Report TP-2009-215404, NASA, Nov 2009.

[50] W. Johnson, A. M. Moodie, and H. Yeo. Design and performance of lift-offset rotorcraft for short-haul missions. In *Proceedings of the American Helicopter Society Future Vertical Lift Aircraft Design Conference, San Francisco, California, January 18-20*, 2012.

[51] F. J. B. Jr. A simplified theoretical method of determining the characteristics of a lifting rotor in forward flight. Technical Report 716, NACA, 1941.

[52] J.-N. Juang and R. S. Pappa. An eigensystem realizaiton algorithm for modal parameter identification and modal reduction. *Journal of Guidance, Control and Dynamics*, 8(5):620–627, 1985.

[53] A. Karpatne. *Study of Compressible Flow Through a Rotating Duct*. PhD thesis, The University of Texas at Austin, 2015.

[54] H. W. Kim and R. E. Brown. A comparison of coaxial and conventional rotor performance. *Journal of the American Helicopter Society*, 55, 2010.

[55] H. W. Kim and R. E. Brown. A rational approach to comparing the performance of coaxial and conventional rotors. *Journal of the American Helicopter Society*, 55(1):12003–1 – 12003–9, 2010.

[56] H. W. Kim, K. Duraisamy, and R. Brown. Aeroacoustics of a coaxial rotor in level flight. In *Proceedings of the American Helicopter Society 64th Annual Forum, Montréal, Québec*, April 29 - May 4 2008.

[57] R. Kimmel and A. M. Bruckstein. Shape offsets via level sets. *Computer-Aided Design*, 25(3):154–162, March 1993.

[58] R. Kube, W. Splettstoesser, W. Wagner, U. Seelhorst, Y. Yu, C. Tung, P. Beaumier, J. Prieur, G. Rahier, P. Spiegel, A. Boutier, T. Brooks, C. Burley, D. Boyd, E. Mercker, and K. Pengel. Hhc aeroacoustic rotor tests in the german-dutch wind tunnel: Improving physical understanding and prediction codes. *Aerospace Science and Technology*, 2(3):177 – 190, 1998.

[59] R. Kufeld, D. L. Balough, J. L. Cross, K. F. Studebaker, C. D. Jennison, and W. G. Bousman. Flight testing of the uh-60a airloads aircraft. In

American Helicopter Society 50th Annual Forum Proceedings, (Alexandria, VA May), 1994.

[60] V. K. Lakshminarayan and J. D. Baeder. High-resolution computational investigation of trimmed coaxial rotor aerodynamics in hover. *Journal of the American Helicopter Society*, 54:042008 (21 pages), 2009.

[61] H.-J. Langer, R. L. Peterson, and T. H. Maier. An experimental evaluation of wind tunnel wall correction methods for helicopter performance. In *Proceedings of the American Helicopter Society 52nd Annual Forum, Washington, D.C.*, June 4-6 1996.

[62] J. G. Leishman. *Principles of Helicopter Aerodynamics*. Cambridge University Press, New York, NY, 2nd edition, 2006.

[63] J. G. Leishman. Aerodynamic performance considerations in the design of a coaxial proprotor. *Journal of the American Helicopter Society*, 54(1), 2009.

[64] J. G. Leishman and S. Ananthan. An optimum coaxial rotor system for axial flight. *Journal of the American Helicopter Society*, 53(4):366–381, 2008.

[65] J. G. Leishman and M. Syal. Figure of merit definition for coaxial rotors. *Journal of the American Helicopter Society*, 53(3):290–300, 2008.

[66] J. M. Leuridan, D. L. Brown, and R. J. Allemang. Time domain parameter identification methods for linear modal analysis: A unifying

approach. *Journal of Vibration, Acoustics, Stress, and Reliability in Design*, 108(1):1–8, 1986.

[67] J. W. Lim, K. W. McAlister, and W. Johnson. Hover performance correlation for full-scale and model-scale coaxial rotors. *Journal of the American Helicopter Society*, 54(3):32005, 2009.

[68] T. Lundstrom, J. Baqersad, and C. Niezrecki. *Using High-Speed Stereophotogrammetry to Collect Operating Data on a Robinson R44 Helicopter*, pages 401–410. Springer New York, New York, NY, 2013.

[69] K. Marlett. Hexcel 8552 im7 unidirectional prepreg 190 gsm 35material property data report. Contractor Report CAM-RP-2009-015 Rev A, FAA,NCAMP, 2011.

[70] K. Marlett. Hexcel 8552s as4 plain weave fabric prepreg 193 gsm 38qualification material property data report. Contractor Report CAM-RP-2010-006 N/C, FAA,NCAMP, 2011.

[71] K. W. McAlister and C. Tung. Experimental study of a hovering coaxial rotor with highly twisted blades. In *Proceedings of the American Helicopter Society 64th Annual Forum, Montréal, Québec*, April 29 - May 4 2008.

[72] L. Meirovitch. *Principles of Helicopter Aerodynamics*. Waveland Press Inc., Chicago, IL, 1st edition, 2001.

[73] L. Molnár, K. Váradi, G. Bódai, P. Zweirczyk, and L. Oroszváry. Simplified modeling for needle roller bearings to analyze engineering structures by fem. *Periodica Polytechnica Mechanical Engineering*, 54(1):27–33, 2010.

[74] T. Nagashima and K. Nakanishi. Optimum performance and wake geometry of a coaxial rotor in hover. *Vertica*, 7(225-239), 1983.

[75] T. Nagashima, H. Ouchu, and F. Sasaki. Optimum performance and load sharing of coaxial rotor in hover. *Journal of Japan Society for Aeronautics and Space Sciences*, 26(293):325–333, June 1978.

[76] L. E. Olson, A. I. Abrego, D. A. Barrows, and A. W. Burner. Blade deflection measurement of a full-scale uh-60a rotor system. In *American Helicopter Society Aeromechanics Specialists' Conference Proceedings (San Francisco, CA, 20-22 Jan.)*, 2012.

[77] M. Ozbek, F. Meng, and D. J. Rixen. Challenges in testing and monitoring the in-operation vibration characteristics of wind turbines. *Mechanical Systems and Signal Processing*, 41(1–2):649 – 666, 2013.

[78] M. Ozbek and D. J. Rixen. Operational modal analysis of a 2.5mw wind turbine using optical measurement techniques and strain gauges. *Wind Energy*, 16(3):367–381, 2013.

[79] M. Ozbek and D. J. Rixen. A new analysis methodology for estimating the eigenfrequencies of systems with high modal damping. *Journal of*

Sound and Vibration, 361:290 – 306, 2016.

[80] V. M. Paglino. Forward flight performance of a coaxial rigid rotor. In *Proceedings of the 27th American Helicopter Society Forum, Washington, D.C.*, May 1971.

[81] R. S. Pappa and S. R. Ibrahim. A parametric study of the ibrahim time domain modal identification algorithm. Technical report, NASA Langley Research Center, 1985.

[82] B. Peeters and G. De Roeck. Stochastic system identification for operational modal analysis: A review. *Journal of Dynamic Systems, Measurement, and Control*, 123(4):659–667, 2001.

[83] B. PEETERS and C. VENTURA. Comparative study off modal analysis techniques for bridge dynamic characteristics. *Mechanical Systems and Signal Processing*, 17(5):965 – 988, 2003.

[84] D. A. Peters, C.-J. He, and D. Boyd. A finite-state induced-flow model for rotors in hover and forward flight. *Journal of the American Helicopter Society*, 34(4), 1989.

[85] A. E. Phelps and R. E. Mineck. Aerodynamic characteristics of a counter-rotating, coaxial, hingeless rotor helicopter model with auxiliary propulsion. Technical Report TM-78705, NASA, May 1978.

[86] L. Pirodda. Shadow and projection moire techniques for absolute or relative mapping of surface shapes. *Optical Engineering*, 21(4):214640–214640–, 1982.

[87] N. Rajmohan, J. Zhao, and C. He. A couple vortex particle/cfd methodology for studying coaxial rotor configurations. In *American Helicopter Society Aeromechanics Specialists' Conference Proceedings (San Francisco, CA, 22-24 Jan.)*, 2014.

[88] M. Ramasamy. Measurements comparing hover performance of single, coaxial, tandem, and tilt-rotor configurations. In *Proceedings of the American Helicopter Society 69th Annual Forum, Phoenix, Arizona, May 21-23*, 2013.

[89] M. Ramasamy. Hover performance measurements toward understanding aerodynamic interference in coaxial, tandem, and tilt rotors. *Journal of the American Helicopter Society*, 60:032005 (17 pages), 2015.

[90] M. Ramasamy and J. G. Leishman. The interdependence of straining and viscous diffusion effects on vorticity in rotor flow fields. In *Proceedings of the American Helicopter Society 59th Annual Forum, Phoenix, Arizona, May 6-8*, 2003.

[91] R. C. Rice, J. L. Jackson, J. Bakuckas, and S. Thompson. Metallic materials properties development and standardization (mmpds). Technical Report DOT/FAA/AR-MMPDS-01, Federal Aviation Administration, 2003.

[92] L. F. Richardson and J. A. Gaunt. The deferred approach to the limit. part i. single lattice. part ii. interpenetrating lattices. *Philosophical Transactions of the Royal Society of London A: Mathematical, Physical and Engineering Sciences*, 226(636-646):299–361, 1927.

[93] S. S. Rizo-Patron and J. Sirohi. Operational modal analysis of a rotating cantilever beam using high-speed digital image correlation. In *57th AIAA/ASCE/AHS/ASC Structures, Structural Dynamics, and Materials Conference*. American Institute of Aeronautics and Astronautics, 2016.

[94] T. P. Ryan. *Modern Regression Methods*. Wiley, 2nd edition, 2009.

[95] J. Schmaus and I. Chopra. Aeromechanics for a high advance ration coaxial helicopter. In *Proceedings of the American Helicopter Society 71st Annual Forum, Virginia Beach, VA*, May 5-7 2015.

[96] J. Schmaus and I. Chopra. Performance and loads prediciton for a high advance ratio coaxial helicopter. In *AIAA SciTech 2015, Kissimmee, FL*, 2015.

[97] J. Schmaus and I. Chopra. Performance and loads of a model coaxial rotor part ii: Prediction validations with measurements. In *Proceedings of the American Helicopter Society 73rd Annual Forum, West Palm Beach, Florida, May 17-19*, 2016.

[98] J. Schmaus and I. Chopra. Performance and loads of a model coaxial rotor part ii: Prediction validations with measurements. *Journal of the American Helicopter Society*, Submitted for Review October 2016.

[99] O. Schneider. Analysis of spr measurements from hart ii. *Aerospace Science and Technology*, 9(5):409 – 420, 2005.

[100] M. Sekula. The development and hover test application of a projection moiré interferometry blade displacement measurement system. In *American Helicopter Society 68th Annual Forum Procedings (Fort Worth, TX, 1-3 May)*, 2012.

[101] P. J. Sevenhuijsen. The photonical, pure grid method. *Optics and Lasers in Engineering*, 18(3):173 – 194, 1993.

[102] K. Shinohara. *Optimum aerodynamic character of the coaxial counter rotating rotor system.* PhD thesis, National Defense Academy, February 1977.

[103] J. Sicard. *Development of an Extremely Flexible, Variable-Diameter Rotor for a Micro-Helicopter.* PhD thesis, The University of Texas at Austin, 2014.

[104] J. Sicard and J. Sirohi. Measurement of the deformation of an extremely flexible rotor blade using digital image correlation. *Measurement Science and Technology*, 24(6):065203, 2013.

[105] J. Sicard and J. Sirohi. Modeling of the large torsional deformation of an extremely flexible rotor in hover. *AIAA Journal*, 52(8):1604–1615, August 2014.

[106] R. Singh, H. Kang, C. Cameron, and J. Sirohi. Computational and experimental investigations of coaxial rotor unsteady loads. In *54th AIAA Aerospace Sciences Meeting*, page 1787, 2016.

[107] J. Sirohi and M. S. Lawson. Measurement of helicopter rotor blade deformation using digital image correlation. *Optical Engineering*, 51(4):04603, April 2012.

[108] H. Xin, J. Goss, and C. Parkes. Development of a three-state rotor interference model and application to coaxial rotor inflow modeling. In *American Helicopter Society Aeromechanics Specialists' Conference Proceedings (San Francisco, CA, 22-24 Jan.)*, 2014.

[109] H. Yeo and W. Johnson. Investigation of maximum blade loading capability of lift-offset rotors. In *Proceedings of the American Helicopter Society 69th Annual Forum, Phoenix, Arizona, May 21-23*, 2013.

[110] L. A. Young. Vortex core size in the rotor near-wake. Technical report, NASA Technical Report TM-2003-212275, 2003.

[111] Y. Yu, B. Gmelin, H. Heller, J. J. Philippe, E. Mercker, and J. S. Preisser. Hhc aeroacoustic rotor test at the dnw - the joint german/french/us. In

Proceedings of the Twentieth European Rotorcraft Forum, Amsterdam, October 4-7 1994.

[112] L. Zhang, Y. Yao, and M. Lu. An improved time domain polyreference method for modal identification. *Mechanical Systems and Signal Processing*, 1(4):399 – 413, 1987.

Chapter 6

Wind Tunnel Testing

Forward flight experiments were performed at the University of Maryland Glenn L. Martin Wind Tunnel; the test section with rotor system is shown in figure 6.1. The properties of the coaxial rotor system tested are summarized in table 6.1. Over the course of a full week in the tunnel, over 871 test points were captured. The experimental procedure, including the test matrix, trimming, data processing and wind tunnel corrections are presented in §6.1. Steady loads and performance are examined in §6.2.1 and 6.2.2, with trends in control angles and blade tip clearance discussed in §6.2.3. Vibratory hub loads, including the effect of lift offset and rotor index angle are presented in §6.3.1 and6.3.2, while pushrod forces are summarized in §6.3.3.

6.1 Experimental Procedure

6.1.1 Test Matrix

The forward flight test matrix, shown in table 6.2, was chosen to investigate several key aspects of the lift-offset rotor system. Four advance ratios

Portions of this chapter were previously published as "Performance and Loads of a Model Coaxial Rotor Part I: Wind Tunnel Measurements" in the Proceedings of the AHS 72nd Annual Forum, West Palm Beach, Florida, May 17 to 19, 2016. All writing and figures included in this chapter are the original work of the author, with editing by Dr. Jayant Sirohi

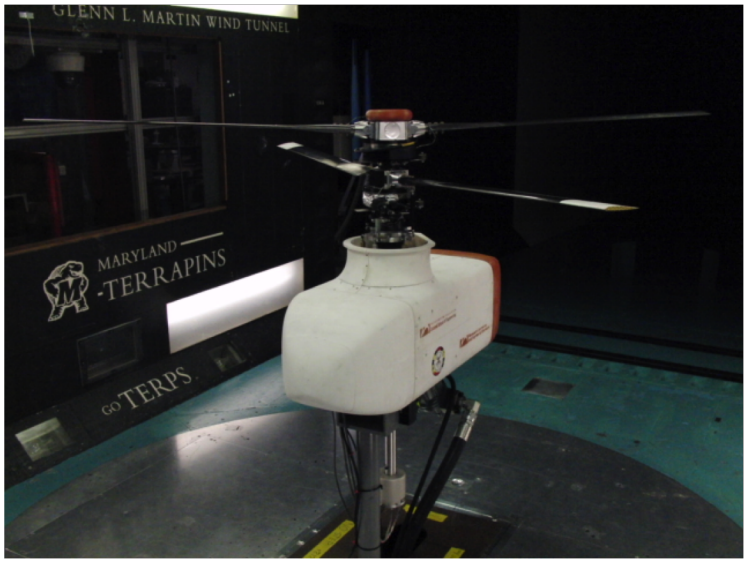

Figure 6.1: Rotor stand installed in the Glenn L. Martin Wind Tunnel

Table 6.1: Summary of rotor properties (wind tunnel)

	Two-bladed coaxial
Inter-rotor Spacing	0.140 m
Rotor Radius	1.016 m
Chord	0.080 m
Solidity	0.10
Tip Speed	85, 128 m/s
Rotor Speed (RPM)	900, 1200
1st flap frequency	1.68/rev (900 RPM)
Lock Number	5.9

were investigated for the isolated rotor system and the coaxial rotor system. Data was acquired for each rotor configuration at four collective values (for the coaxial configuration this corresponds to the upper rotor collective). Due to upper rotor control system actuator limits, the collective values do not agree completely for all tests, with $\theta_0 = 8°$ being the only common collective for all three configurations. At each collective and advance ratio, a sweep of lift offset, from 0% to 20% was performed. Rewriting the definition of lift offset from equation 1.2 using non-dimensional thrust and moments yields:

$$LO = \frac{2 * C_{MX}}{C_{TU} + C_{TL}} \tag{6.1}$$

Additional tests were performed on the coaxial rotor system at a limited set of advance ratios and collective values. The first was a 1200 RPM test to check for the effects of tip speed on the measurements. The second set of tests, performed at 900 RPM, involved varying the azimuth angle at which the upper and lower rotor crossings occurred (index angle). The baseline data, taken for all four collectives and advance ratios, was acquired with blade crossings at 0°, 90°, 180°, and 270°. Defining the azimuth angle of the first crossing, as the inter-rotor index angle ϕ, shown in Figure 6.2, two additional index angles were investigated, $\phi = 20°$ and $\phi = 45°$.

6.1.2 Trimming

Initial shaft balancing was performed to minimize the fixed frame vibrations at the operating speeds using movable masses located below the 6-

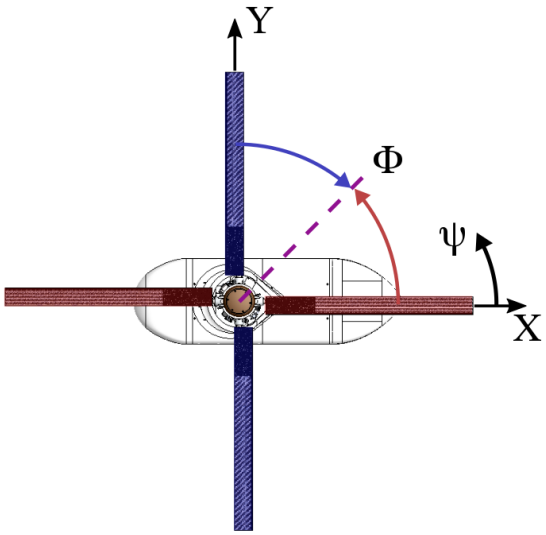

Figure 6.2: Inter-rotor index angle, ϕ, definition, (upper rotor: red, lower rotor: blue)

Table 6.2: Forward Flight Test Matrix

Configuration	RPM	Advance Ratio	Collective [deg]
Lower Rotor Isolated	900	0.21, 0.32, 0.43, 0.53	3, 5, 8, 10
Upper Rotor Isolated	900	0.21	3, 5, 8, 10
		0.32	3, 5, 8
		0.43, 0.53	2, 4, 6, 8
Coaxial Rotor	900	0.21, 0.32, 0.43, 0.53	
	1200	0.2, 0.3	4, 6
Coaxial Rotor (Indexed)	900		

component load cells. After installation of the blades, additional balancing was performed at zero collective with masses added to the blade grips to counteract the rotating frame, in-plane forces measured using the 6-component load cells. Rotor tracking was achieved by varying the rotating frame pitch link lengths. Due to the high flap-bending stiffness of the blades, visual tracking using stroboscopically illuminated blade tips was difficult as deflections were relatively small. As an alternative, the steady rotating frame pitching moment, caused by the steady lift asymmetry of untracked blades, was monitored and minimized. The rotor was considered tracked when this steady pitching moment was less than 2% $C_T R$.

The trim procedure for the coaxial rotor system is outlined in Figure 6.3. Coupling between the upper and lower rotor trim controls was found to act primarily in one direction. The upper forces and moments were found to be fairly insensitive to lower rotor forces and moments. This nearly uncouples the trimming of the rotors to lift offset and torque balance targets,

as the upper rotor lift offset target is set first, then the lower rotor controls modified to achieve lower rotor lift offset and system torque balance. For both upper and lower rotors, torque was found to be highly coupled with pitching moment, while thrust was correlated primarily with rolling moment. Due to the coupling between thrust and rolling moment, achieving exact lift offset targets was difficult and the values listed in table 6.2 are nominal only. Some operating conditions, particularly at low collective values, exhibited multiple torque balanced trim solutions. In these cases, the trim solution was chosen to keep lower rotor collective as close to the upper rotor collective as possible.

6.1.3 Data Processing and Error Analysis

At each operating condition, the azimuthal encoder is used to record 100 rotor revolutions. The data undergoes several post-processing steps in Matlab. First, pre and post-run tare readings are used to correct for load cell drift during the test run and a lowpass filter with a corner frequency of 30/rev is used to remove the forces introduced by the 36 tooth drive pulleys. Steady loads are then computed, treating each revolution as an independent, identically distributed sample, yielding both a mean steady load, as well as a sample standard error. For vibratory loads, the filtered data is resampled from the time domain to the azimuthal domain at 512/rev using the readings from the azimuthal encoder. The resulting resampled data is then synchronously averaged, eliminating non harmonic noise. Blade-off tare measurements are subtracted to correct for hub drag. Rotating frame load cell measurements are

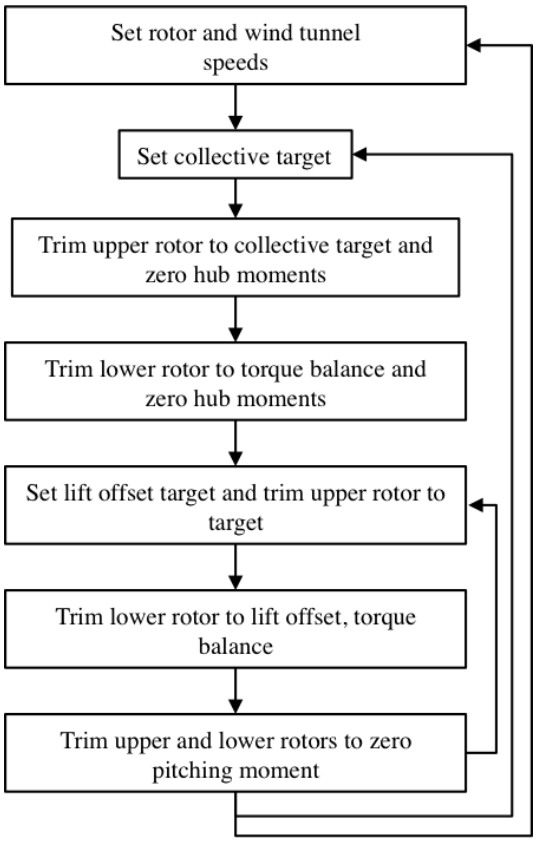

Figure 6.3: Diagram of coaxial rotor trimming procedure

transformed to the fixed frame using the azimuthal encoder readings. The fixed frame coordinate system is oriented with positive X-direction over the fuselage tail, positive Y-direction to starboard, and positive Z-direction upward.

6.1.4 Wind Tunnel Wall Corrections

The effect of the wind tunnel walls on the rotor measurements was estimated following the work of Langer et al. [61]. A modification of the Glauert wall corrections for application to rotorcraft is introduced. The Glauert correction for fixed wings calculates the change in induced angle of attack $\Delta\alpha$ as:

$$\Delta\alpha = \frac{\delta_W A_{wing}}{A_{TS}} C_L \tag{6.2}$$

Here δ_W is a boundary correction factor dependent on the test section shape, the ratio of model span to tunnel width and the position of the model in the wind tunnel. A_{wing} is the wing planform area, A_{TS} the tunnel cross sectional area, and C_L the wing coefficient of lift. Equation 6.2 is adapted for use with a lifting rotor by substituting for C_L in terms of C_T and μ as:

$$C_L \equiv 2C_T \frac{(\Omega R)^2}{V_\infty^2} \tag{6.3}$$

$$\mu = \frac{V_\infty}{(\Omega R)} \tag{6.4}$$

$$\Delta\alpha = \frac{2\delta_W A_{disk}}{\mu^2 A_{TS}} C_T \tag{6.5}$$

Table 6.3: Wall correction factor and parameters

Model Span Ratio ($2R/W_{TS}$)	0.604
Aspect Ratio (H_{TS}/W_{TS})	0.702
δ_W	0.125

The boundary correction factor is determined from tables published by Barlow et al. [12]. The rotor system and test section dimensions are shown in figure 6.4. The section is octagonal and the equivalent correction factor approximated as that of an elliptical section with the same aspect ratio (H_{TS}/W_{TS}). The relevant parameters and final correction factor are listed in table 6.3. The resulting angle of attack, or shaft tilt angle, correction factor is calculated for the range of advance ratios and thrust coefficients observed during testing. The corrections, shown in figure 6.5, reach a maximum of 0.5° at high thrust and low advance ratio, decreasing with the square of advance ratio as indicated in equation 6.5. The rotor system was installed in the tunnel with zero shaft tilt, α, for all test runs. As a result, the correction methodology of interpolating results between shaft angles employed by Langer et al. [61] is infeasible. The results are therefore presented with uncorrected shaft angles, and the calculated shaft angle correction may be implemented in computational studies correlating with the experimental work.

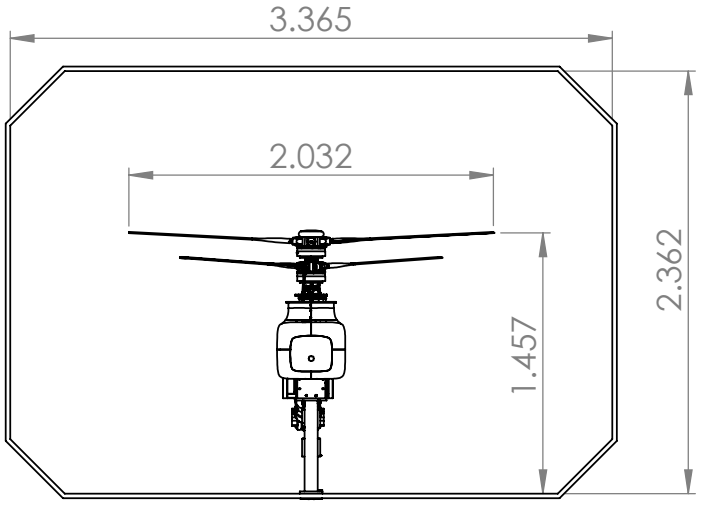

Figure 6.4: Dimensions (m) of rotor system in the Glenn L. Martin wind tunnel

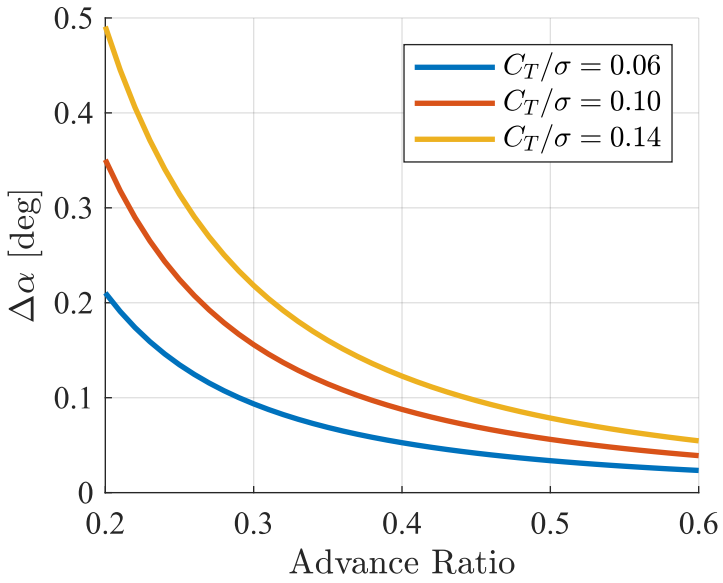

Figure 6.5: Variation of shaft tilt angle correction factor with advance ratio and rotor thrust coefficient

6.2 Steady Loads and Performance

6.2.1 Trimmed Forward Flight

First the isolated lower rotor, and coaxial rotor systems are examined with zero lift offset to determine baseline performance characteristics. Figures 6.6a and 6.7a show the variation of system C_T/σ with advance ratio, μ. From hover to $\mu = 0.21$ there is an increase in thrust in both the isolated and coaxial rotor systems. As advance ratio increases further ($\mu > 0.21$), thrust for the isolated lower rotor decreases for all collectives. In contrast, at lower collective settings the coaxial system thrust remains somewhat constant with advance ratio. At 2° collective, the coaxial rotor thrust decreases by approximately 20% from $\mu = 0.2$ to $\mu = 0.5$. At higher collectives the decrease in thrust is much greater with 8° collective losing nearly 50% thrust over the same advance ratio range. This change in thrust occurs as lift production on the retreating blade decreases due to low dynamic pressures. In order to trim the rolling moments this decrease in retreating blade lift is accompanied by a corresponding decrease in advancing blade lift. Rotor thrust then becomes concentrated at the front and back of the rotor disk, decreasing the total thrust. As advance ratio increases, thrust at all collectives appears to be converging as thrust sensitivity to collective decreases. This phenomenon was explored in single rotors by Berry and Chopra [13] who found that the collective sensitivity continues to decrease, until, at advance ratios greater than one, control reversal occurs with increasing collective leading to decreasing thrust.

Unlike rotor thrust, torque, shown in figures 6.6b and 6.7b, decreases

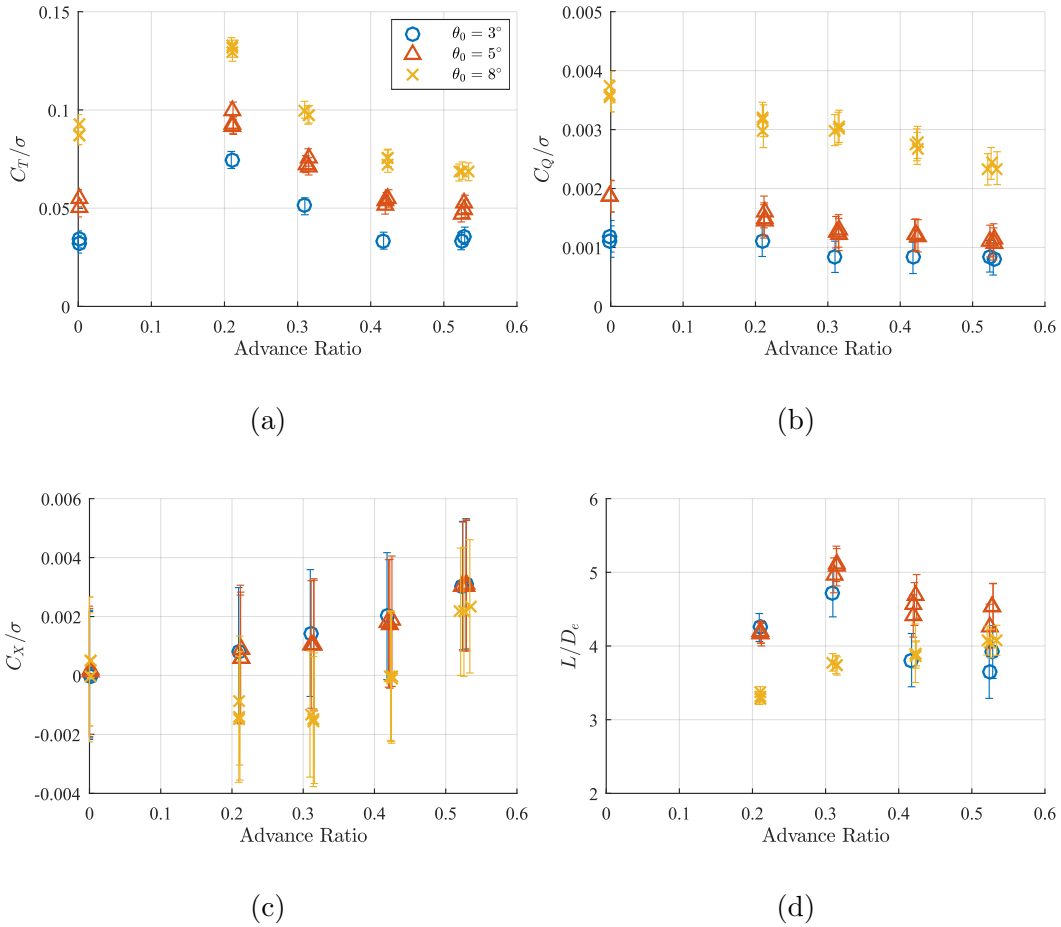

Figure 6.6: Isolated lower rotor performance variation with advance ratio, $LO = 0$

monotonically from hover to low advance ratio forward flight. This, along with the increase in thrust, is more commonly observed as the 'power bucket' experienced by helicopters operating at constant thrust instead of constant collective. As flight speed increases above $\mu = 0.21$, torque tends to decrease, although by a much smaller amount than thrust. Once again, higher collectives experience larger decreases while torque at lower collectives remains nearly constant. The coaxial rotor system at $\theta_0 = 6°$ and $\theta_0 = 8°$ exhibits an initial decrease in torque from $\mu = 0.2$ to 0.3 with more constant behavior at higher advance ratios, similar to the isolated rotor at $\theta_0 = 3°$ and $\theta_0 = 5°$. Figures 6.6c and 6.7c display the variation of drag with advance ratio. From $\mu = 0.2$ to 0.3 there is nearly no change in the rotor X-force (drag), while there is a noticeable rise at $\mu = 0.4$ and 0.5. The relatively large errorbars for the drag force are due to the load cell bias uncertainty of $\pm$4N which, at 900 RPM, is equivalent to $C_X/\sigma = 0.0022$.

These three measures of system performance are combined into an effective rotor lift-to-drag ratio, defined in equation 6.6. This lift-to-drag ratio, shown in figures 6.6d and 6.7d initially increases with increasing advance ratio and then begins to fall as the decreasing thrust and increasing hub drag reduce system efficiency. Isolated lower rotor L/D_e is greatest at 5° collective, with 8° collective showing low efficiency at low advance ratio, and 3° collective dropping off at higher advance ratios. While the variation of lift-to-drag ratio with collective for the coaxial system is small, the L/D_e for 8° collective appears to consistently be lower than 4° and 6° collective. In both isolated and coaxial

rotor systems peak L/D_e is achieved at $\mu = 0.32$ for collectives between 4° and 6°.

$$L/D_e = \frac{C_T}{C_Q/\mu + C_X} \tag{6.6}$$

6.2.2 Lift Offset and Steady Loads

The introduction of lift offset is intended to avoid the decrease in lift-to-drag ratio as advance ratio increases, especially at high collective values. To investigate the effect of lift offset on system performance a single collective ($\theta_0 = 8°$) is examined for both the isolated and coaxial rotor systems. Figures 6.8a and 6.9a show thrust as a function of the applied lift offset for isolated upper and lower rotors, and coaxial upper and lower rotors respectively. At all advance ratios the isolated rotors produce more thrust than the coaxial system. This difference in thrust at a given collective is due to aerodynamic interaction, and is greatest at low advance ratios when the wake skew angle is lowest. For the three higher advance ratios there is a linear relationship between lift offset and thrust output. The slope is similar in all three cases though the initial, zero lift offset, thrust value decreases with increasing advance ratio. Therefore the relative increase in thrust compared to zero lift offset is greater at higher advance ratios, ranging from 26% at $\mu = 0.32$ to 43% at $\mu = 0.53$ for the coaxial rotor system.

Rotor torque, shown in figures 6.8b and 6.9b, displays different behavior

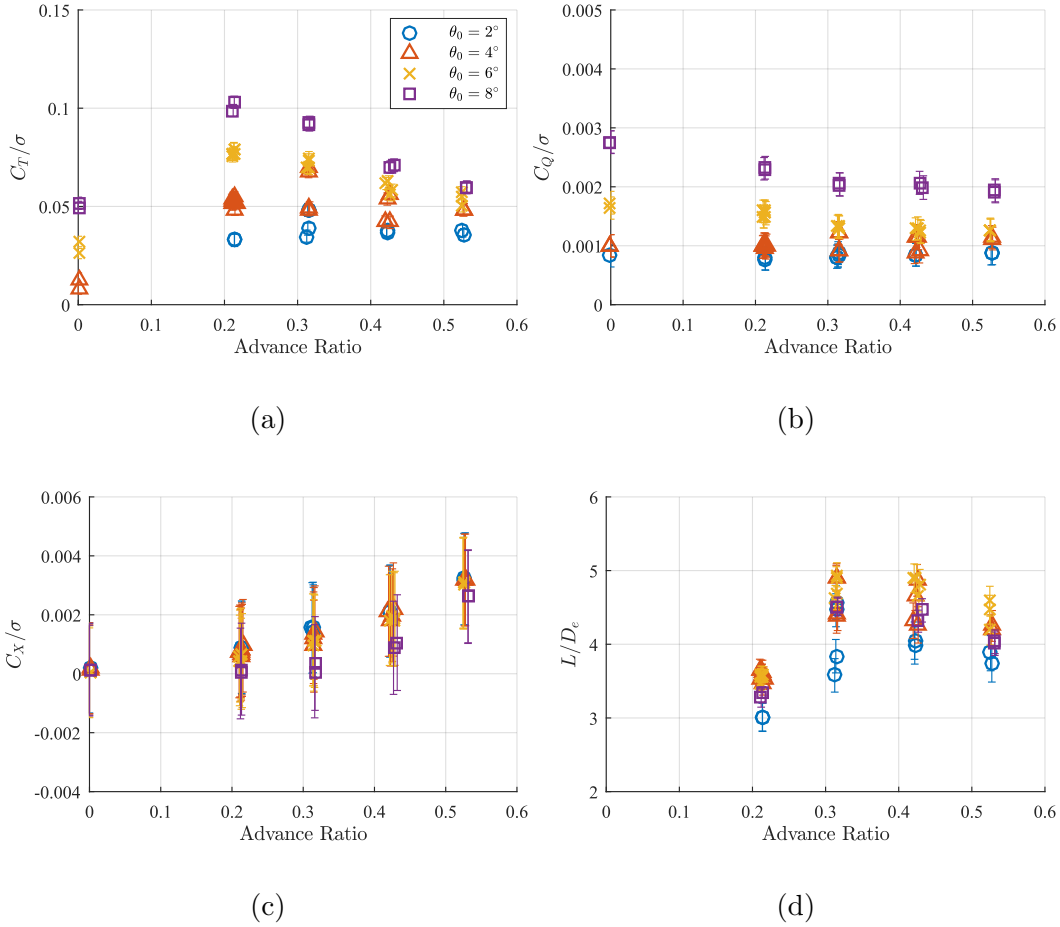

Figure 6.7: Coaxial system performance variation with advance ratio, $LO = 0$

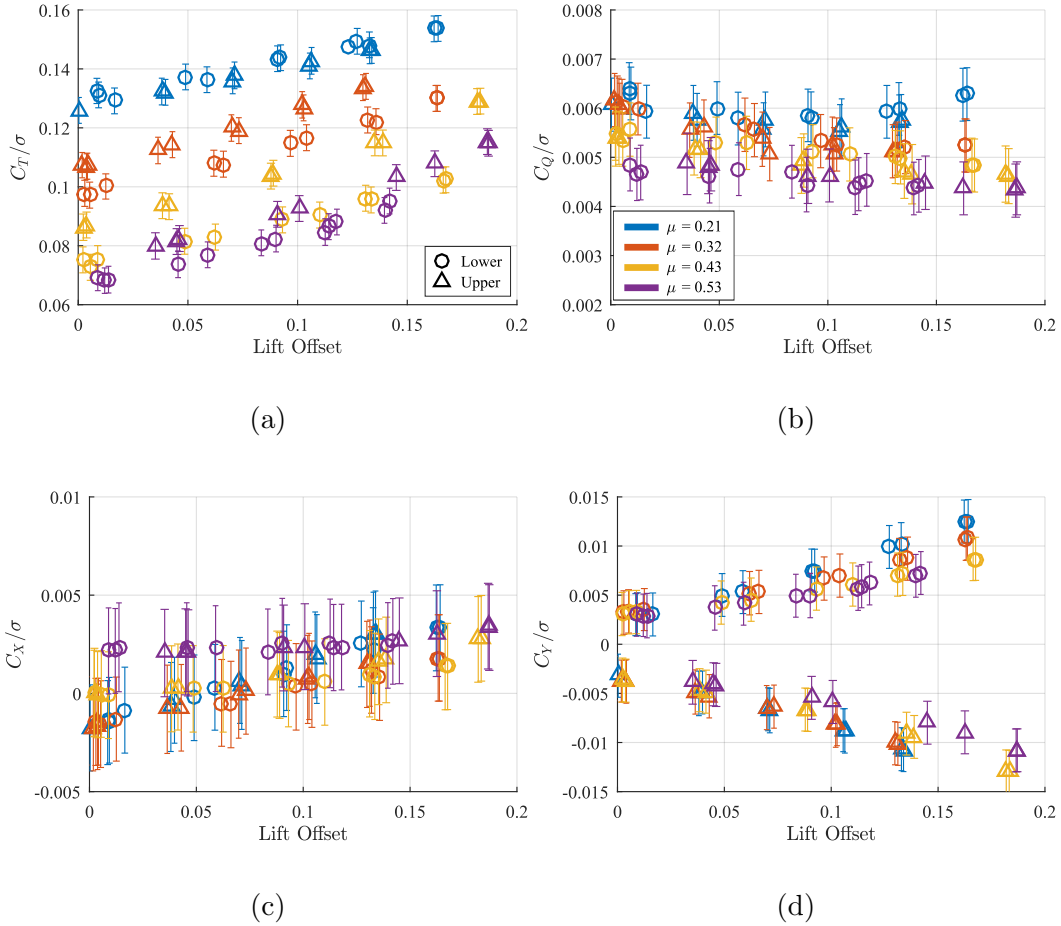

Figure 6.8: Isolated upper and lower rotor hub loads vs. LO, $\theta_0 = 8°$

with lift offset. The isolated rotor systems exhibit initially decreasing torque with lift offset. At $\mu = 0.21$ and $\mu = 0.32$ the isolated rotor torque increases beyond $LO = 0.10$. At higher advance ratios there is no rise in torque at high LO, with torque becoming fairly constant after the initial drop. For the coaxial rotor system torque increases with LO values beyond 0.10 at $\mu = 0.21$ and $\mu = 0.32$, although the initial drop observed in the isolated rotor is not observed. On the other hand, at $\mu = 0.43$ and $\mu = 0.53$ coaxial rotor torque initially decreases with increasing advance ratio. At $\mu = 0.43$ torque reaches a minimum at 17% lift offset before slightly increasing, while at $\mu = 0.53$ torque continues to fall past $LO = 20\%$ down to 87% of the original zero-lift offset value. For both isolated and coaxial rotors the decrease in torque is due to the decreasing dynamic pressure at the retreating blade, forcing higher angles of attack at high advance ratios. As a consequence, at the highest advance ratios lift offset may be increased further before diminishing returns on the torque recovery from the retreating blade are encountered.

Figures 6.8c and 6.9c show drag at higher advance ratios remaining fairly constant with slight increases at LO values greater than 20%. In contrast the $\mu = 0.21$ and $\mu = 0.32$ drag curves steadily increase with increasing lift offset. An additional trend examined is that of rotor side force with lift offset, shown in figures 6.8d and 6.9d. Upper and lower rotor side forces increase in opposite direction with lift offset. This is expected as lift offset is due to the increased effective lift force on one side of the rotorcraft. This force has a component in the in-plane direction due to precone angle and blade

flap-bending. There appears to be a weak trend with side force magnitude decreasing with increasing advance ratio although this is attributable to the decrease in thrust with increasing advance ratio shown in figures 6.8a and 6.9a.

With lift offset having the largest effect on rotor thrust, further data reduction is performed to quantify the influence of lift offset on thrust at all collectives and advance ratios. Figure 6.10 shows how lift offset influences the variation of blade loading with collective pitch for the coaxial rotor system at μ=0.5. As in §5.2.6, collective sensitivity is defined as the slope of a linear regression of blade loading on collective angle. For the three lift offsets in figure 6.10 the collective sensitivity varies between 3.3×10^{-3} at zero lift offset and 6.6×10^{-3} at 20% lift offset. Figure 6.11 shows a contour plot of collective sensitivity vs. lift offset and advance ratio. Increasing advance ratio from 0.2 to 0.5 decreases collective sensitivity by a factor of three. Adding lift offset increases collective sensitivity at all advance ratios, with the relative increase from the zero lift offset case greatest at high advance ratio.

Figures 6.12a and 6.12b show the effect of lift offset on L/D_e for the isolated upper and lower rotors, as well as the coaxial upper and lower rotors respectively. At μ=0.21 the lift-to-drag ratio is nearly constant with lift offset. The isolated rotors show a small increase with lift offset while there is a small decrease near 20% lift offset for the coaxial rotors. At $\mu = 0.32$ lift-to-drag rises steadily through lift offset of 10% where the coaxial rotor L/D_e levels out. For $\mu = 0.43$ and $\mu = 0.53$ the lift-to-drag ratio rises up past a lift offset of 0.2 for both the isolated and coaxial rotors.

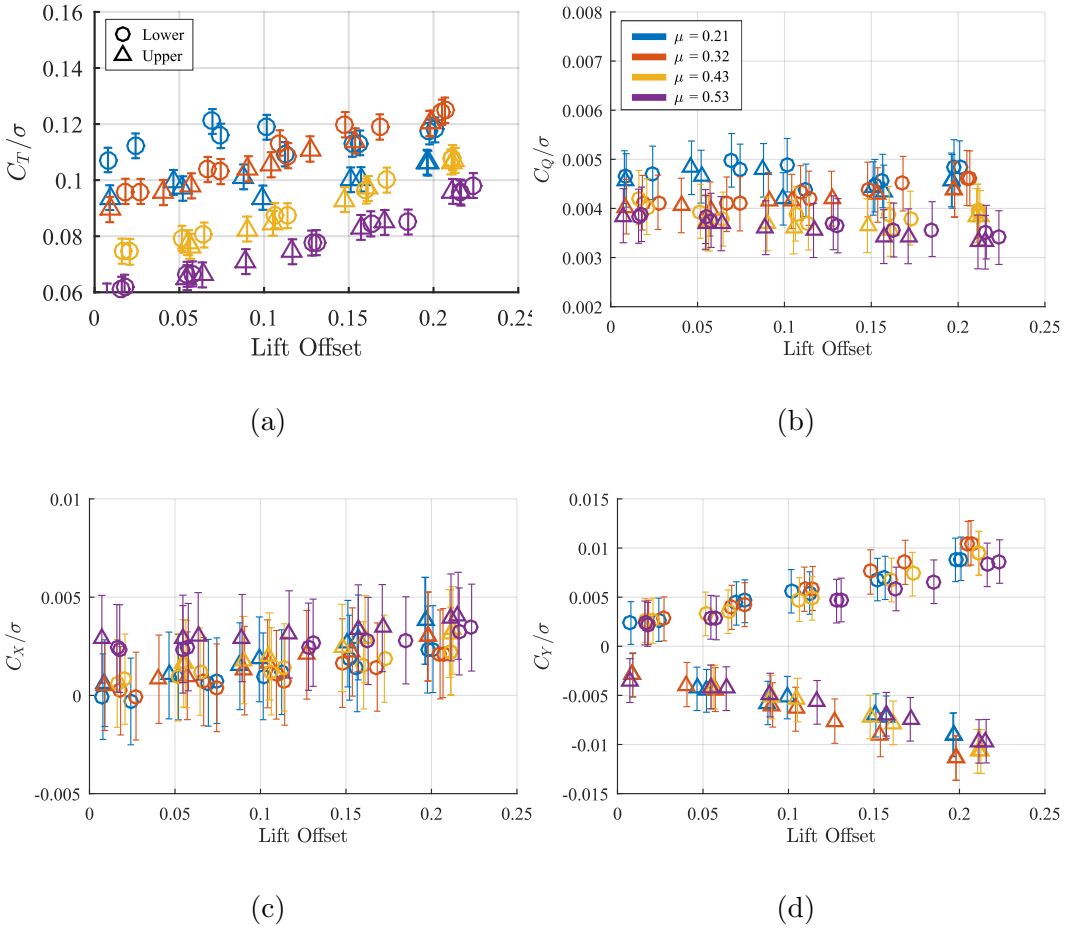

Figure 6.9: Coaxial upper and lower rotor hub loads vs. LO, $\theta_0 = 8°$

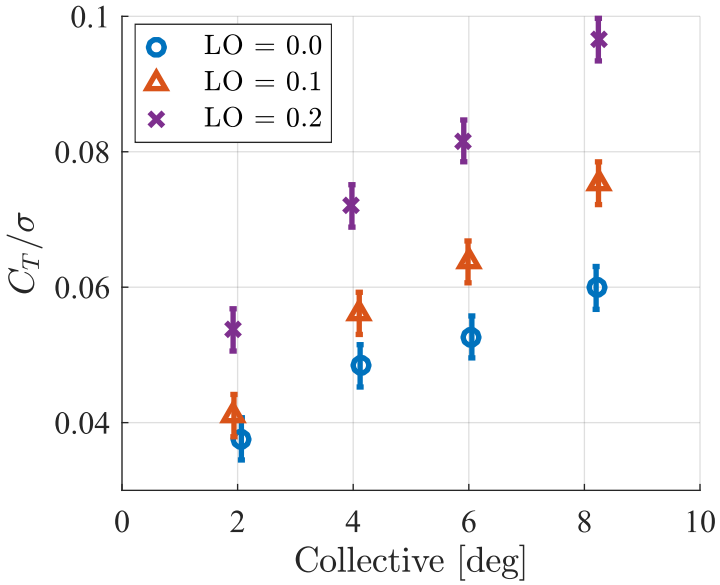

Figure 6.10: Coaxial rotor blade loading vs. collective pitch angle at three LO levels ($\mu = 0.5$)

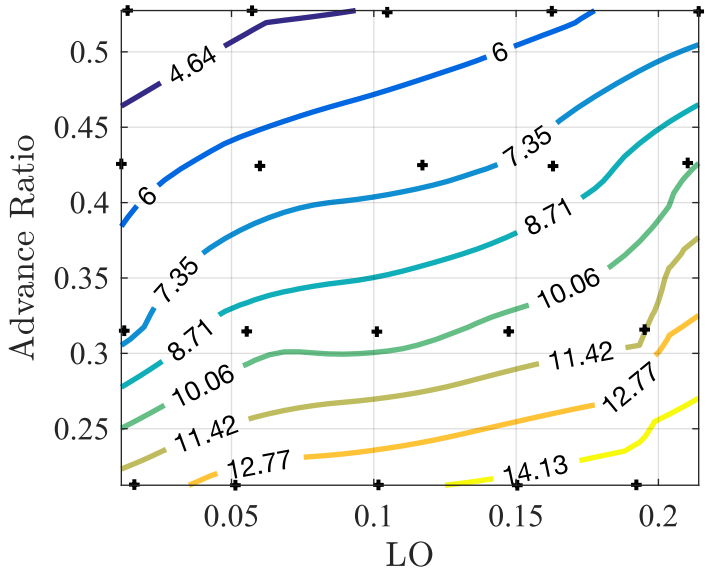

Figure 6.11: Contour plot of coaxial rotor collective sensitivity vs. LO and μ

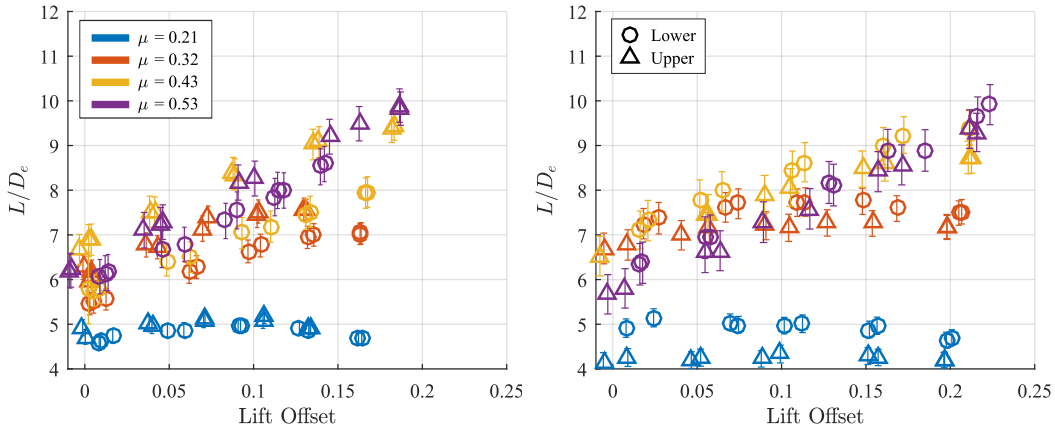

(a) (b)

Figure 6.12: (a) Isolated rotors L/D_e variation with Lift Offset (b) Coaxial upper and lower rotor L/D_e variation with lift offset

The isolated upper and lower rotors have very similar L/D_e curves at $\mu = 0.21$ while the coaxial lower rotor operates at significantly higher L/D_e than the upper rotor at all values of LO. The difference in upper and lower coaxial rotor L/D_e is surprising, as the interference effect between rotors in hover tends to decrease lower rotor performance by a greater factor than for the upper rotor. However, this decrease in lower rotor efficiency in coaxial forward flight is similar to a result from simulations by Yeo and Johnson [109] using CAMRAD II which showed that the interference effect tended to decrease thrust on the upper rotor by a larger amount than the lower. This trend in thrust is examined in figure 6.13. Here the reversal in thrust ratio from hover to forward flight is clear, with a minimum value occurring near $\mu = 0.2$. The lower rotor continues to produce more thrust than the upper rotor at all

advance ratios, with increasing lift offset decreasing the upper rotor thrust deficit. The relatively constant trend in C_{TU}/C_{TL} at advance ratios of 0.3 and greater may be explained by considering the wake-skew angle χ, approximated using cylindrical wake theory [62] as:

$$\chi = \arctan\left(\frac{\mu}{\lambda}\right) \tag{6.7}$$

The resulting wake geometry for the coaxial rotor system at $\mu = 0.2$ and $\mu = 0.3$ is shown in figure 6.14. At $\mu = 0.2$ the leading edge upper rotor wake impinges on the lower rotor near the hub, increasing upwash on the lower rotor disk near $\psi = 180°$. By $\mu = 0.3$ however, the upper rotor wake clears the lower rotor disk entirely and the interaction effect between the two rotors is decreased. While this simple theory provides some insight into the wake dynamics, the reality is much more complicated as the upper rotor wake tends to be accelerated by the lower rotor wake and more complicated mixing occurs. While the CAMRAD II analysis by Yeo and Johnson predicted increased lower rotor thrust, the current findings differ in several ways. Yeo and Johnson predict an increasing difference in upper and lower rotor thrust with lift offset, whereas the opposite trend is observed in the measured data at all advance ratios. Additionally Yeo and Johnson predict a maximum difference in upper and lower rotor thrust of 6% at LO=0.4, while the measured difference varies from 16% to 2% depending on advance ratio and lift offset.

Figure 6.15a shows the summed coaxial system L/D_e vs. LO. Here the increases in efficiency for the coaxial rotor system at $\mu = 0.43$ and $\mu = 0.53$ are

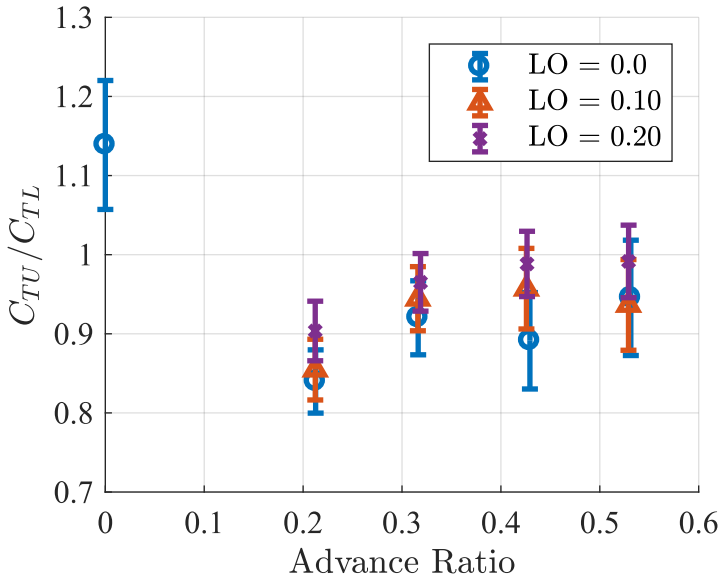

Figure 6.13: Ratio of upper to lower rotor thrust vs. advance ratio at three lift offset values ($\theta_0 = 8°$)

approximately 40% and 60% respectively from the corresponding $LO = 0.0$ cases. The peak efficiency achieved with LO is 30% greater than for the most efficient zero LO case at $\mu = 0.32$. Figure 6.15b shows these trends on a contour plot generated using a surface fit with gradient based smoothing. The contour plot illustrates the insensitivity of L/D_e to lift offset at low advance ratios and the advantages of running at higher advance ratios and lift offset values.

Data was predominantly taken at 900 RPM due to very large pushrod forces and blade flap-bending at higher rotational speed. In order to quantify the effect of tip speed on rotor performance and loads, a limited test matrix was run at 1200 RPM. Figure 6.16 shows lift-to-drag ratio vs. lift offset at

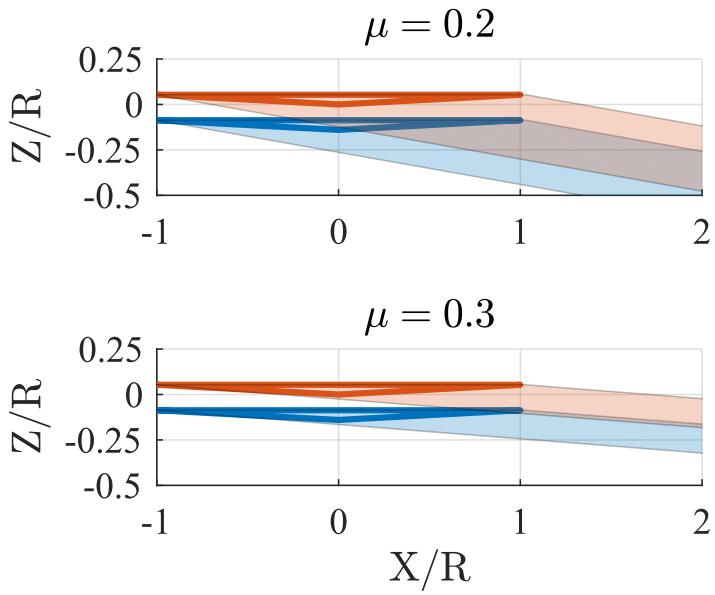

Figure 6.14: Side-view of upper and lower coaxial rotor wake slipstreams at $\mu = 0.2$ and $\mu = 0.3$

900 and 1200 RPM for both advance ratios tested. The good agreement in behavior at both tip speeds indicates that there are not appreciable Reynolds and Mach number effects occurring between 900 and 1200 RPM.

6.2.3 Control Angles and Blade Tip Clearance

Control angles were not explicitly measured during testing. Instead they are extracted using the amplitude and phase of the one-per-revolution (1/rev) component of the blade root pitch angle measurements. While this effectively characterizes the control angles, it is important to note that due to control linkage deflection and free-play the blade undergoes higher harmonic pitching motions in addition to the 1/rev cyclic. Figure 6.17 shows upper rotor

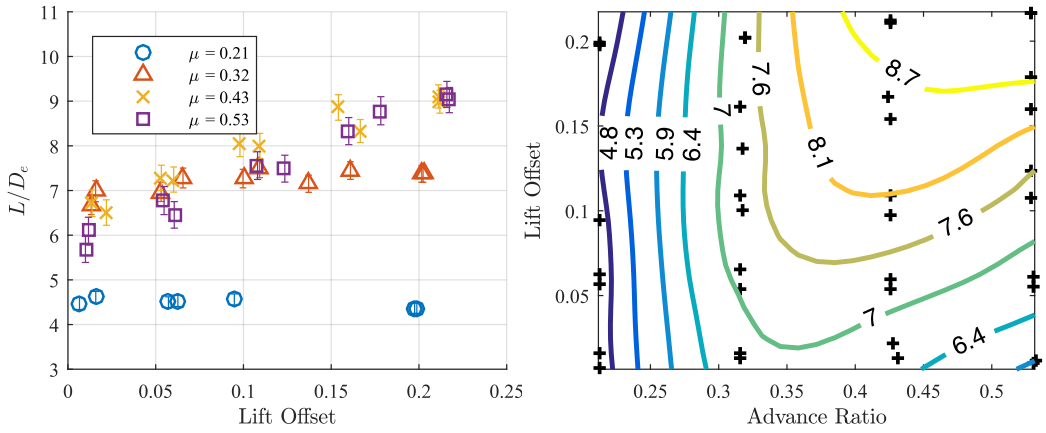

(a) (b)

Figure 6.15: (a) Coaxial system L/D_e variation with lift offset (b) Interpolated contour plot of coaxial system L/D_e variation with lift offset and μ

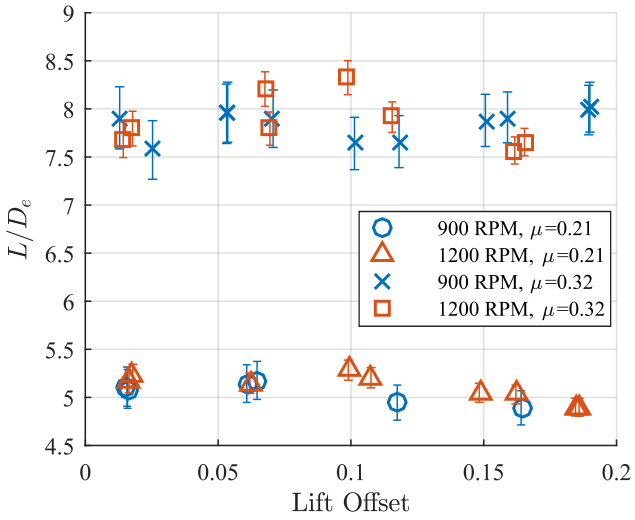

Figure 6.16: Coaxial rotor system effective lift-to-drag ratio vs lift offset at 900 and 1200 RPM, $\theta_0 = 6°$

azimuthal pitch angle variation at various advance ratios. As advance ratio increases the higher harmonic motions become apparent. Figures 6.18a and 6.18b show these higher harmonic amplitudes, normalized by the 1/rev cyclic amplitude for an upper and lower rotor blade respectively. At $\mu = 0.21$ all higher harmonics are less than 2% of the cyclic amplitude. However as advance ratio increases, three, four, and five-per-revolution harmonics increase to around 10% of the 1/rev cyclic amplitude for the upper rotor. Lower rotor higher harmonic pitching amplitudes remain below 5% of the cyclic amplitude. This difference in higher harmonic pitching is due to the increased complexity of the upper rotor pitch control system which introduces additional free-play nonlinearity compared to the lower rotor system. Figure 6.19 shows the variation of cyclic controls with advance ratio and lift offset for the lower rotor at 8° collective and 900 RPM. Note that due to the high first flap frequency of 1.68/revolution the phase lag between cyclic pitch and blade flapping is only 40 degrees. As such, lateral cyclic is referred to as θ_{1S} and longitudinal cyclic as θ_{1C}, in contrast to nomenclature for fully articulated or hingeless rotor systems. The circles are the controls at zero lift offset while the x's show the variation of the controls with lift offset. The variation of longitudinal cyclic with advance ratio is negligible compared to the lateral cyclic necessary to trim the rolling moments. Increasing lift offset involves simultaneously decreasing lateral cyclic while increasing longitudinal cyclic.

As previously noted, the blade tip clearance sensor, originally intended for use as a safety device, was accurate enough to extract trends in tip clearance

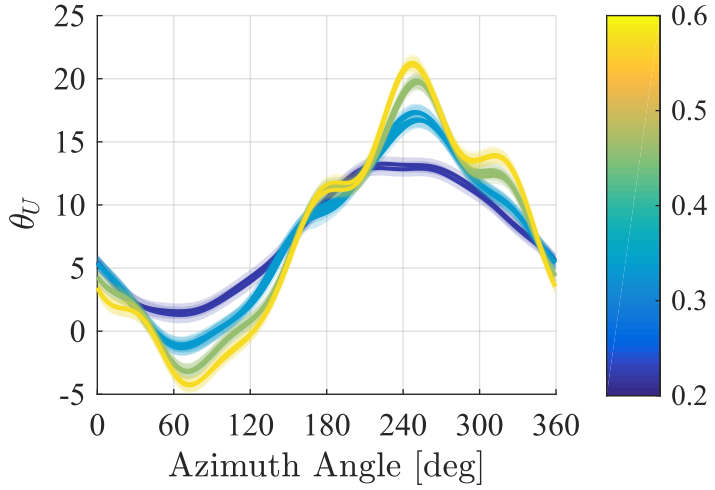

Figure 6.17: Azimuthal variation of upper rotor pitch angle colored by advance ratio, μ

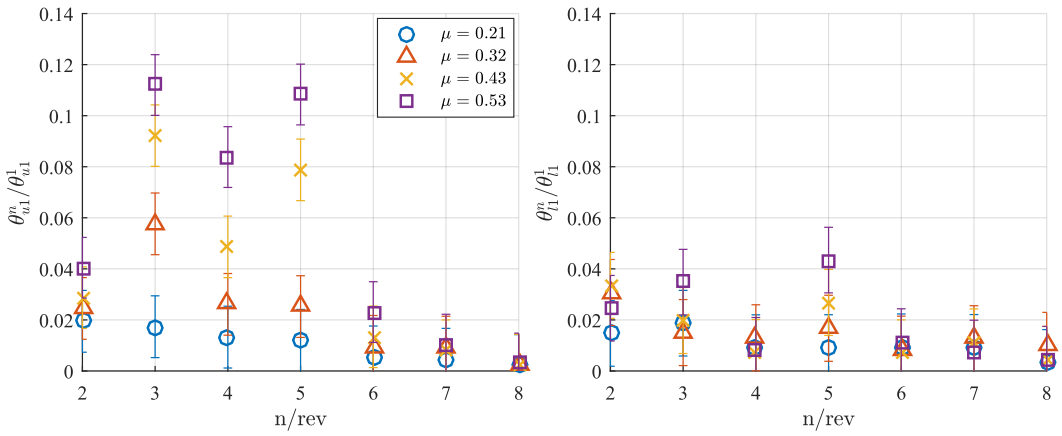

(a) (b)

Figure 6.18: Isolated rotors root pitch harmonics normalized by corresponding 1/rev cyclic pitching amplitude (θ^1), $\theta_0 = 8°$, LO=0 (a) Upper rotor (b) Lower rotor

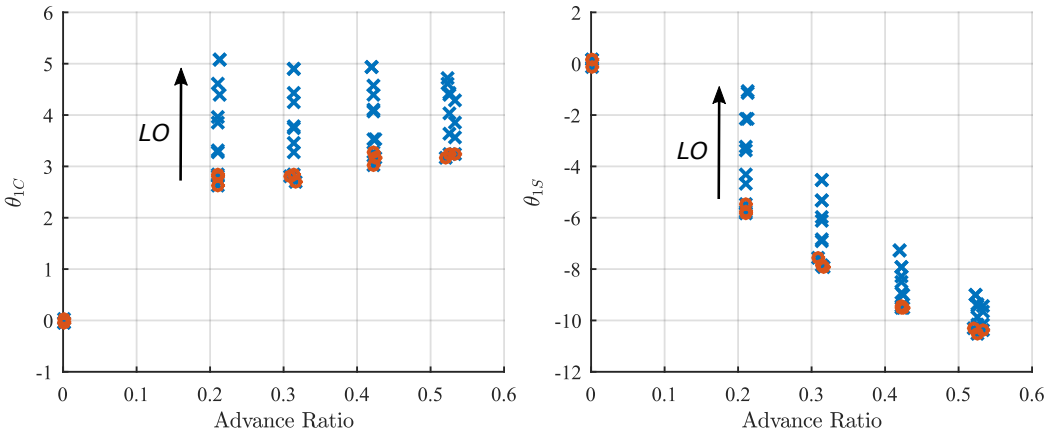

(a) (b)

Figure 6.19: Lower rotor cyclic controls vs. advance ratio and lift offset $\theta_0 = 8°$, (a) θ_{1C} (b) θ_{1S}

with flight condition. Maintaining tip clearance is critical for safety especially during maneuvering flight and the data from the clearance sensor will be very useful for correlating with analyses. Figure 6.20a is the unprocessed azimuthal clearance signal at various advance ratios. All four blade crossings are visible, with tip clearance at the advancing upper rotor blade ($\psi = 90°$) increasing with lift offset, while clearance simultaneously decreases at the retreating upper rotor blade ($\psi = 270°$). Figures 6.20b and 6.20c show variation of tip clearance at $\psi = 270°$ vs. LO for various test cases. Figure 6.20b shows blade tip clearance at 8° collective varying with lift offset and advance ratio. Tip clearance begins near 13% of the rotor radius R, just slightly less than the static blade tip separation of 13.8%R, indicating higher lower rotor thrust than upper rotor thrust. Tip clearance decreases with lift offset down to a

minimum value of 6%R for all four advance ratios. The minimum safe clearance for this test was chosen as 5% R or 5 cm. While the trends are similar for all μ, tip clearance at a fixed lift offset value increases with advance ratio. This is expected due to the relationship between advance ratio and thrust at fixed collective as shown in figure 6.7a.

The effect of collective (indirectly thrust) on clearance is shown in Figure 6.20c. Due to different initial upper and lower rotor trim settings, the 6° collective case has approximately 1% less clearance than the 8° collective case at zero lift offset. The tip clearance at $\theta 0 = 6°$ decreases slower than the higher collective case, with both converging to 6%R clearance at maximum lift offset. This is again due to the effect of the reduced thrust on the lower collective case. Figure 6.20d shows the effect of tip speed on blade tip clearance. Increasing tip speed reduces the relative first flap frequency of the blade causing greater deflections for a given lift offset. During these 1200 RPM tests the minimum safe tip clearance of 5%R limited the system lift offset to 15%.

6.3 Vibratory Loads

Vibratory loads are a major factor in rotor design, especially for helicopters with stiff blades operating at high advance ratios. In order to control high vibratory loads, production helicopters employ passive absorbers and active force generators. Accurate prediction of these loads is therefore important to optimize the sizing and placement of these components, reducing the associated weight and power penalties. In addition to variation of collective and

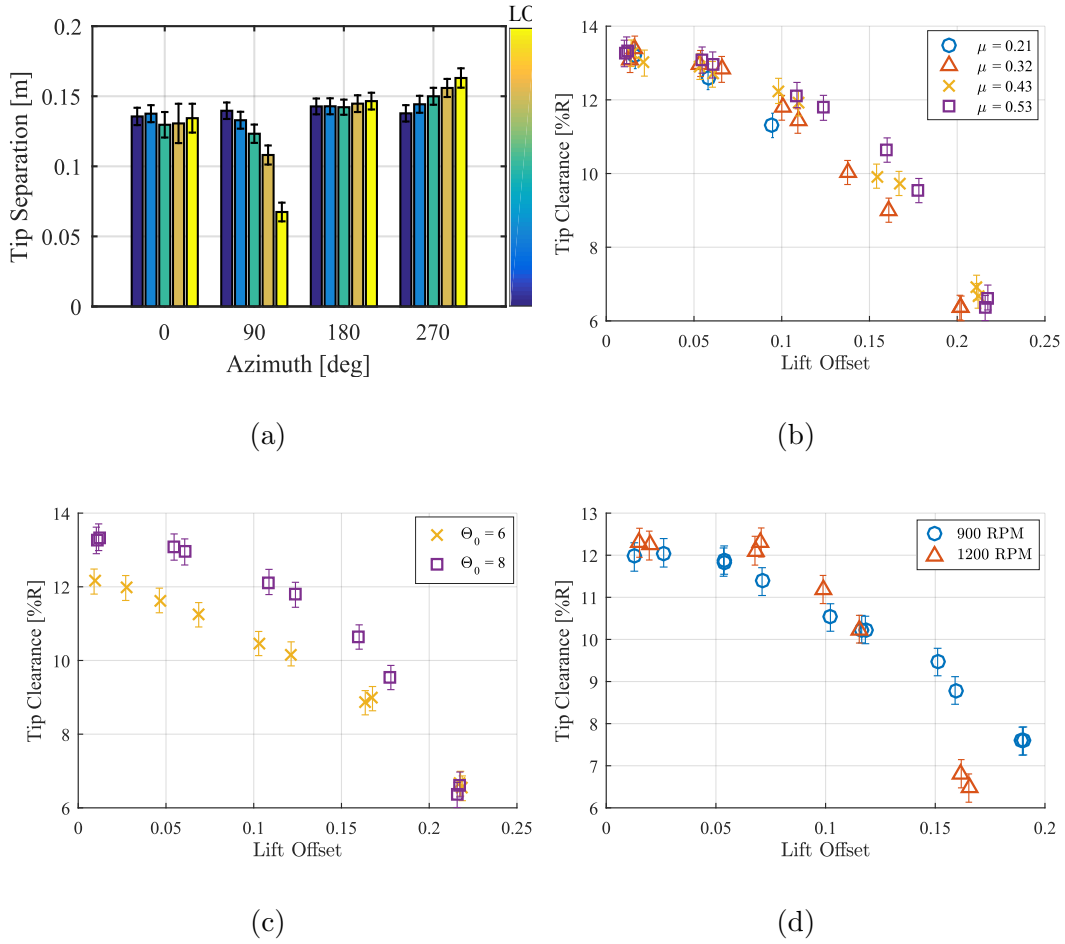

Figure 6.20: Blade clearance vs. LO (a) Raw azimuthal signal($\theta_0 = 8°$, $\mu = 0.53$), (b) Variation of minimum clearance with μ ($\theta_0 = 8°$), (c) Variation of minimum clearance with collective($\theta_0 = 8°$, $\mu = 0.53$), (d) Variation of minimum clearance with tip speed ($\theta_0 = 6°$,$\mu = 0.32$)

advance ratio, the level of lift offset and the presence of two rotors both influence the generation and transmission of vibratory loads to the rotorcraft fuselage.

6.3.1 Isolated Rotor Hub Loads

First consider the vibratory loads of an isolated rotor in forward flight. Figure 6.21 shows the first four even vibratory load harmonics in all six axes. The vibratory forces are normalized by the steady thrust C_{T0}, while the vibratory moments are normalized by $C_{T0}R$. Vibratory loads in all axes increase with advance ratio. The in-plane rotor forces, C_X and C_Y, are dominated by a four-per-revolution component. These large four-per-revolution in-plane forces are likely due to their proximity to the first blade lag mode at 4.5-per-revolution. Lag-bending modes are generally lightly damped, and create large amplification of any forcing near the modal frequency. The rotor thrust and torque vibratory loads are mainly comprised of a two-per revolution component. The pitching moment shows two, four, and eight per-revolution vibratory loads increasing with lift offset, while the rolling moment displays smaller two, four-per-revolution loads.

The azimuthal variation of the rotor thrust with advance ratio, normalized by mean thrust, is plotted in figure 6.22. The two-per-revolution component is predominant, with peaks near $\psi = 110°$ and $\psi = 290°$. The measured hub loads are delayed by a phase lag relative to the input aerodynamic forcing. This phase lag may be approximated using the first flap natural frequency and

damping ratio determined from the rotating frame dynamic measurements in §4.3.3. At 900 RPM the first flap frequency is ν_β=1.67/revolution and the damping ratio is ζ=0.22. The proximity of the first flap mode to the forcing frequency (2/revolution) relative to the second flap mode at 6.8/revolution, allows for the assumption of single degree of freedom response. The phase lag of rotor response to 2/revolution aerodynamic forcing is given in terms of the flap frequency, damping ratio and aerodynamic forcing frequency as:

$$\psi_{lag} = \arctan \frac{2\zeta(\omega_{aero}/\nu_\beta)}{1-(\omega_{aero}/\nu_\beta)} \tag{6.8}$$

The resulting phase lag is 110°. The two-per-revolution aerodynamic forcing creating the large hub load response is therefore concentrated at $\psi = 0°$ and $\psi = 180°$. This indicates the expected concentration of lift on the leading and trailing edges of the rotor disk as the retreating rotor blade lift production capability decreases due to low dynamic pressure.

Figure 6.23 shows the same loads at a fixed advance ratio, $\mu = 0.53$, while lift offset is varied. Increasing lift offset decreases vibratory loads in all three hub forces and in rotor torque. The effect is largest in the primary vibratory load components, four-per-revolution for the in-plane forces and two-per-revolution in thrust and torque. The azimuthal variation of the normalized lower rotor thrust is shown in figure 6.24. Increasing lift offset decreases the two-per-revolution thrust as the advancing rotor blade makes additional lift, however the vibratory load level does not return to the baseline observed in figure 6.22.

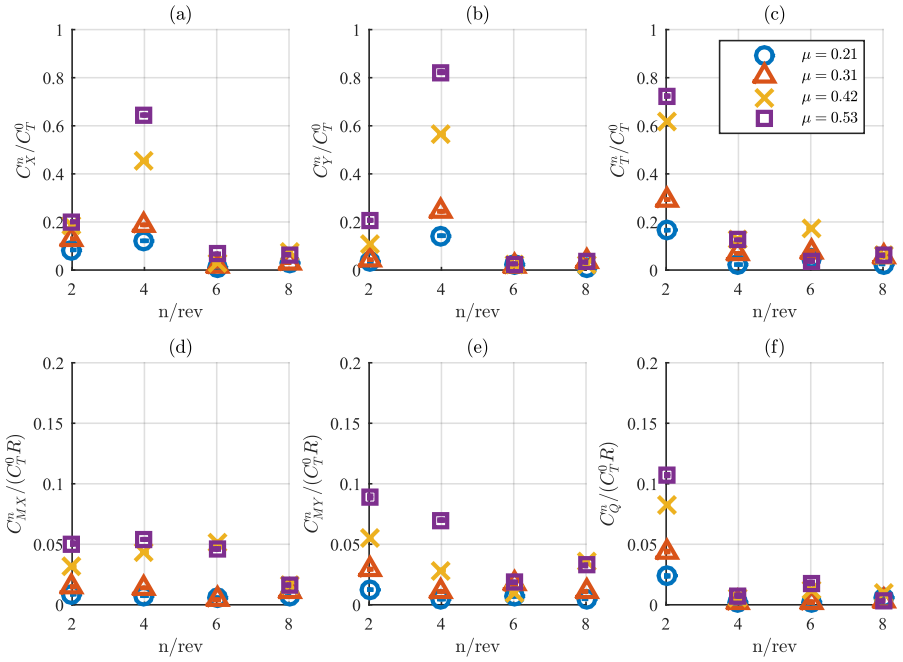

Figure 6.21: Isolated lower rotor vibratory hub load amplitudes, vs. advance ratio ($LO = 0$, $\theta_0 = 8°$)

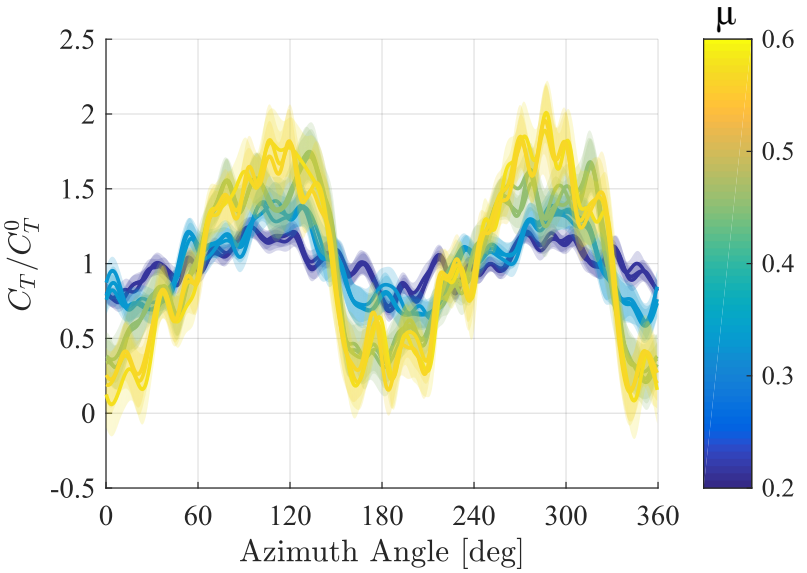

Figure 6.22: Isolated lower rotor azimuthal thrust variation (normalized by mean thrust) vs. advance ratio ($LO = 0$, $\theta_0 = 8°$)

The opposite trend is seen in the rolling and pitching moment where the two-per-revolution vibratory load increases with lift offset, while higher harmonic moments decrease with lift offset. The increase is largest in the rolling moment which is expected as any steady lift offset is accompanied by a two-per-revolution component due to the two-bladed rotor. When lateral cyclic is decreased to induce lift offset, a rotating frame hub overturning moment, $C_{M,rot}$, is created as shown in equation 6.9. When transformed to the fixed frame this rotating moment resolves into a steady rolling moment, which is the lift offset, and a two-per-revolution component as shown in equation 6.10. Note that for a target steady rolling moment the one-per-revolution rotating frame overturning moment must have an amplitude twice the steady fixed

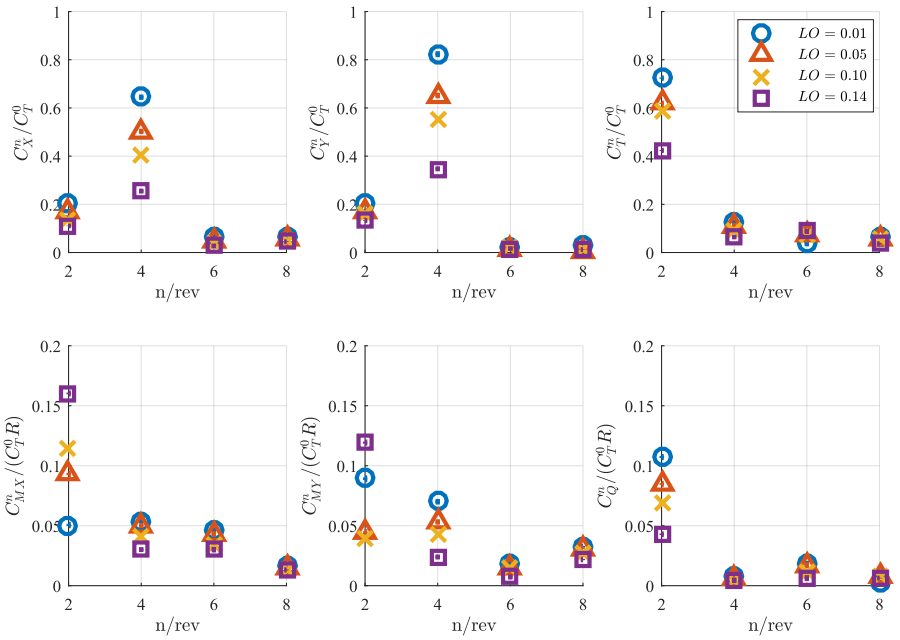

Figure 6.23: Isolated lower rotor vibratory hub load amplitudes vs. LO ($\mu = 0.53$, $\theta_0 = 8°$)

frame value. This rotating moment amplitude drives the choice of the load cell calibration range with a two-bladed rotor. In both figures 6.21 and 6.23 the most significant forces, neglecting the in-plane forces, are two-per-revolution, in agreement with the analysis by Blackwell and Millot [17] that led to the selection of four-bladed main rotors for the X2TD.

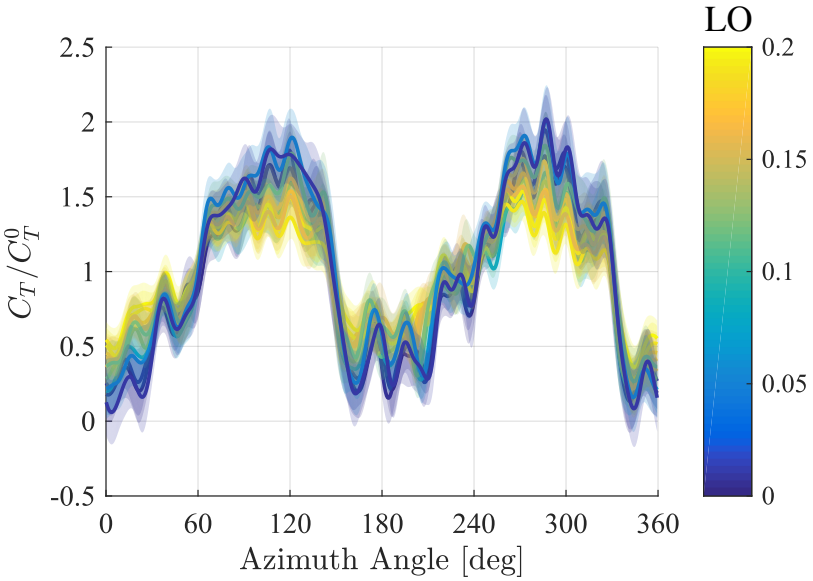

Figure 6.24: Isolated lower rotor azimuthal thrust variation (normalized by mean thrust) vs. lift offset ($\mu = 0.53$, $\theta_0 = 8°$)

$$C_{M,rot} = A\sin(\psi) \tag{6.9}$$

$$\begin{aligned} C_{MX} &= C_{M,rot}\sin(\psi) \\ &= A\sin^2(\psi) \\ &= A/2(1+\sin(2\psi)) \end{aligned} \tag{6.10}$$

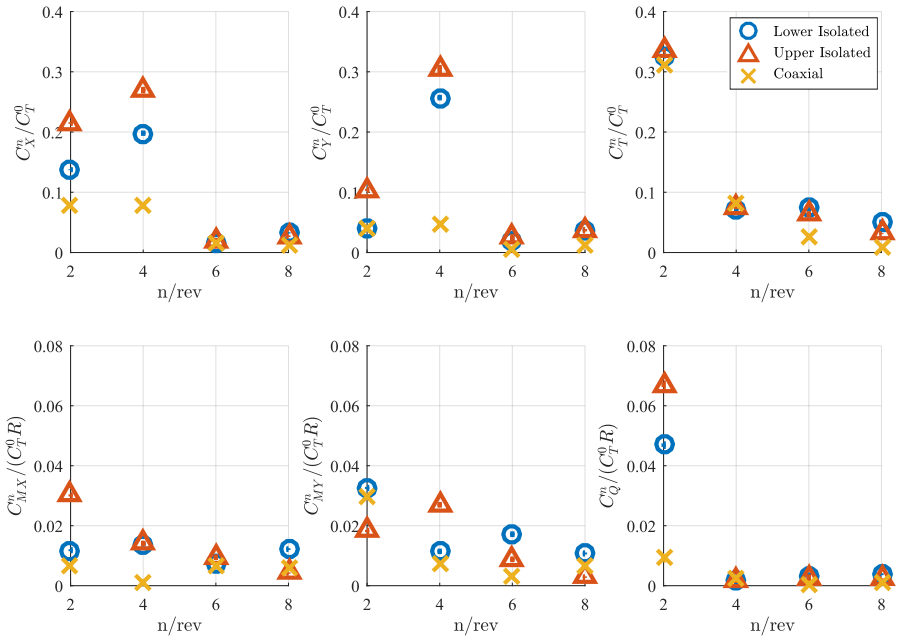

Figure 6.25: Isolated upper and lower rotor vibratory hub load amplitudes vs. summed coaxial rotor hub loads ($LO = 0$, $\theta_0 = 8°$, $\mu = 0.53$)

6.3.2 Coaxial Rotor Hub Loads

When operated with both upper and lower rotors, the resulting loads on the system are the summation of upper and lower rotor loads. The load components can add both in and out of phase, increasing or decreasing the resulting vibratory loads experienced by the system. Figure 6.25 shows the vibratory loads for the isolated upper and lower rotors as well as for the summed coaxial rotor system. The coaxial system eliminates vibratory rolling moment and side force, along with the two-per-revolution torque. There is a small decrease in the four per-revolution drag force while the pitching moment and thrust vibratory loads are effectively unchanged. The constructive and destructive interference between upper and lower rotor loads is dependent on the azimuth angle at which the upper and lower rotor blades cross.

The effect on the summation of upper-lower loads is shown in the azimuthal variation of rolling moment in figure 6.26a. At this index angle, $\phi = 0°$, the upper and lower rotor two-per-revolution rolling moments are 180° out of phase and completely cancel, which explains the trend as previously shown in figure 6.25. Figure 6.26b shows the result of this summation for the three index angles investigated during this experiment. As the index angle increases the two-per-revolution rolling cancellation decreases, until at $\phi = 45°$ the upper and lower rotor vibratory rolling moments add perfectly in phase. Figure 6.27 shows the variation of all six force components with index angle at 20% lift offset. At this high lift offset, the influence of the index angle on the two-per-revolution in-plane forces and moments is apparent. Modifying the

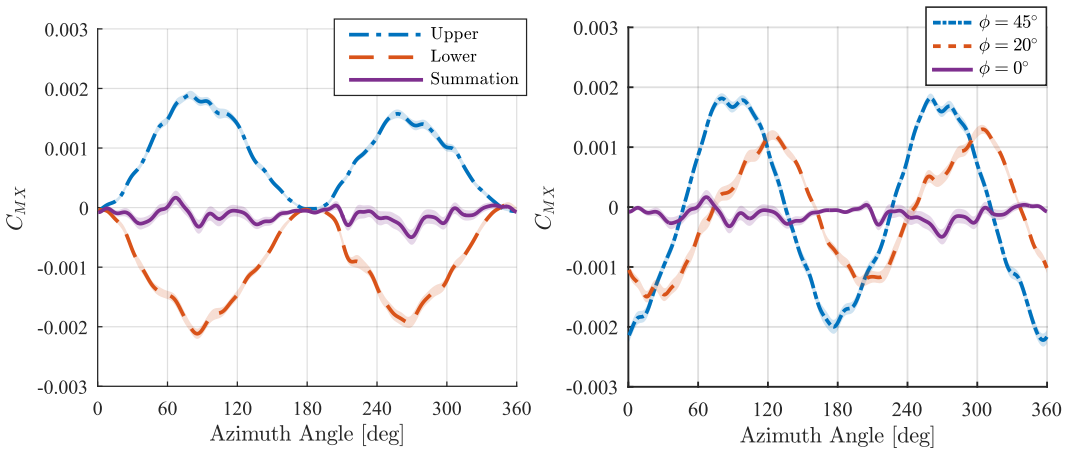

(a) (b)

Figure 6.26: C_{MX} azimuthal variation ($LO = 20\%$, $\theta_0 = 6°$, $\mu = 0.32$) (a)Summation of upper and lower rotor C_{MX} ($\phi = 0°$), (b) Coaxial system summed C_{MX} vs. index angle ϕ

index angle to reduce the vibratory C_{MY} and C_{FX} results in a corresponding increase in C_{MX} and C_{FY}.

The effect of phasing on the variation of the main vibratory hub loads with lift offset is explored further in figures 6.28 to 6.31. The two-per revolution in-plane forces in figures 6.28a and 6.28b are dominated by the side force C_X which increases with increasing lift offset. Increasing the inter-rotor index angle from 0 to 45 degrees results in total cancellation of the two-per-revolution side force. The four-per-revolution in-plane forces, shown in figures 6.29a and 6.29b, are smaller in amplitude and tend to decrease with increasing lift offset. Here $\phi = 45°$ increases vibratory C_X at zero lift offset, while $\phi = 20°$ increases C_Y. Figure 6.30 shows the two-per-revolution vibratory thrust C_T^2 decreasing

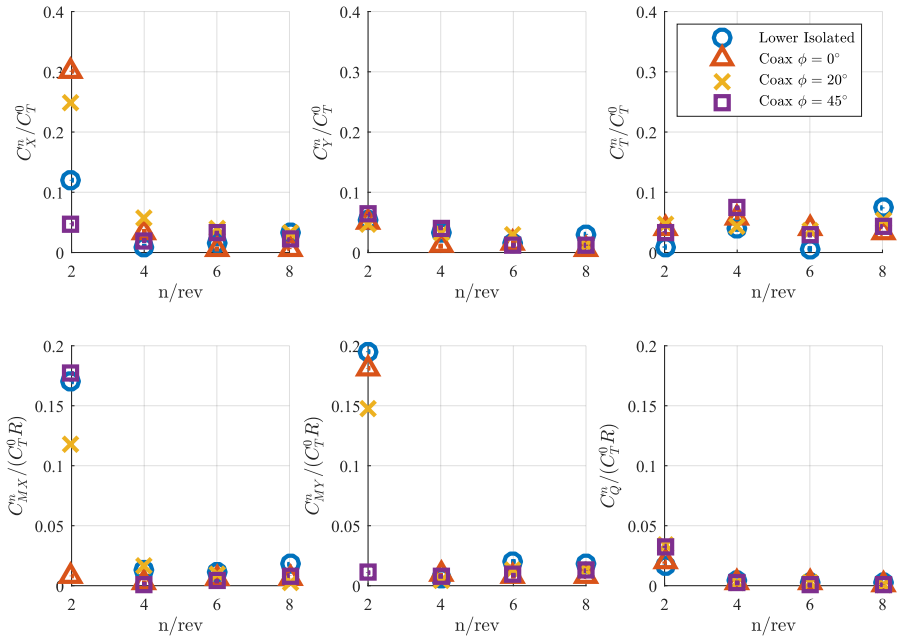

Figure 6.27: Rotor system vibratory hub load amplitudes vs. inter-rotor index angle ($\mu = 0.31$, $\theta_0 = 6°$, $LO = 20\%$)

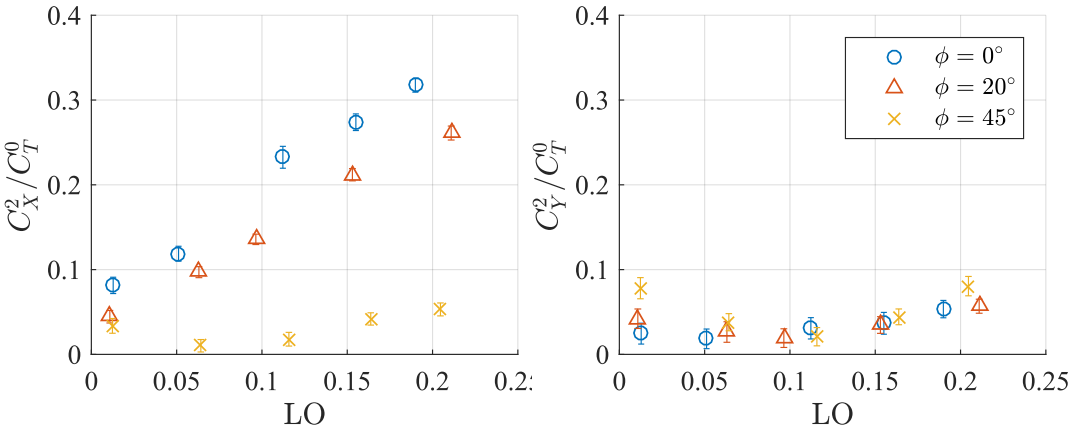

(a) (b)

Figure 6.28: Variation of two-per-revolution in-plane forces (normalized by C_T^0) with lift offset and index angle ($\mu = 0.31$, $\theta_0 = 6°$), (a) C_X^4, (b) C_Y^4

with increasing lift offset. Increasing the index angle to 20 degrees results in a small reduction in C_T^2 at lower lift offset, while there is complete cancellation of the two-per-revolution thrust at $\phi = 45°$. The two-per-revolution rolling and pitching moments C_{MX}^2 and C_{MY}^2 are shown in figures 6.31a and 6.31b. At $\phi = 0°$, C_{MY}^2 increases linearly with lift offset and C_{MX}^2 remains constant, while at $\phi = 45°$, C_{MX}^2 increases with lift offset and C_{MY}^2 remains near zero. The rolling and pitching moments are of similar magnitude when the index angle is 20 degrees, remaining lower than the peak loads in the $\phi = 0°$ and $\phi = 45°$ cases.

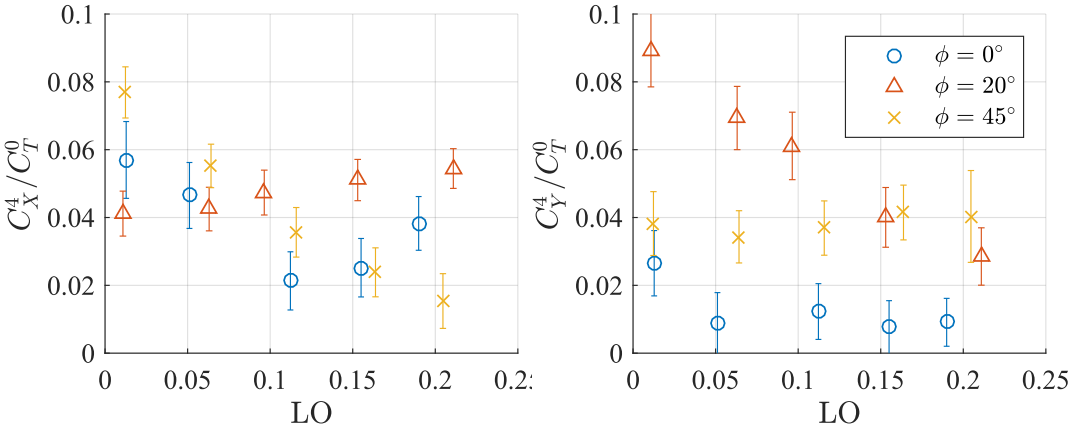

(a) (b)

Figure 6.29: Variation of four-per-revolution in-plane forces (normalized by C_T^0) with lift offset and index angle ($\mu = 0.31$, $\theta_0 = 6°$), (a) C_X^4, (b) C_Y^4

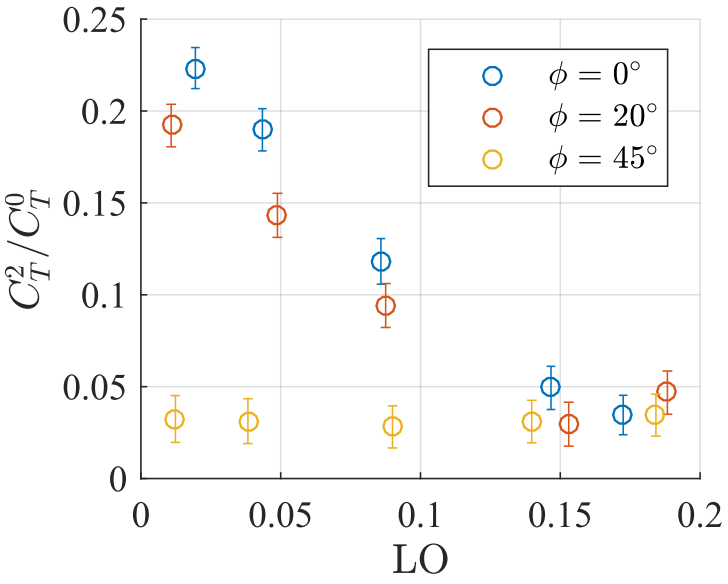

Figure 6.30: Variation of two-per-revolution thrust force (normalized by C_T^0) with lift offset and index angle ($\mu = 0.31$, $\theta_0 = 6°$)

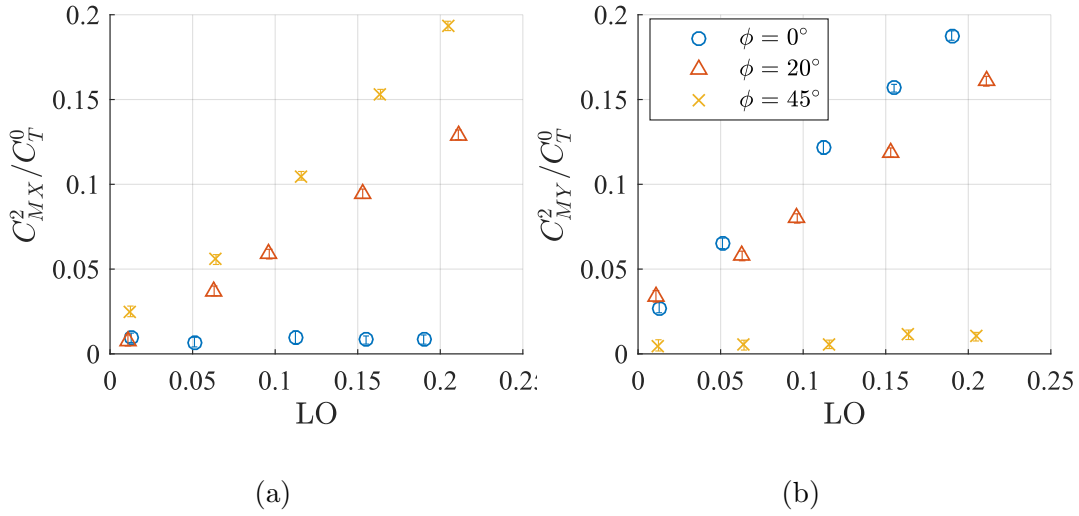

Figure 6.31: Variation of two-per-revolution in plane moments (normalized by $C_T^0 R$) with lift offset and index angle ($\mu = 0.31$, $\theta_0 = 6°$), (a) C^2_{MX}, (b) C^2_{MY}

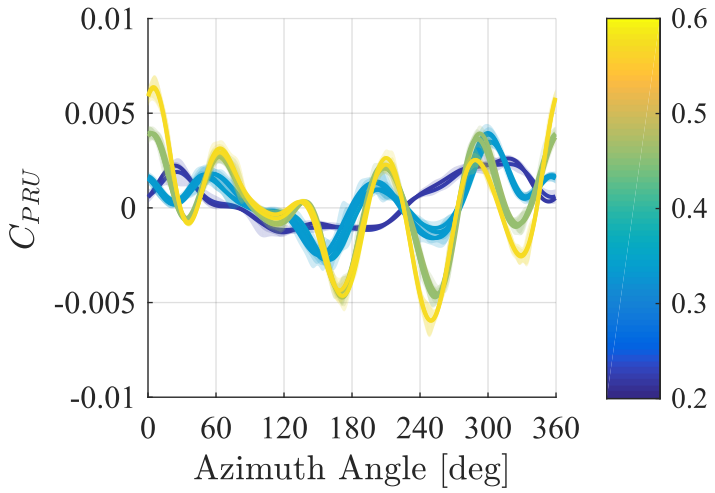

Figure 6.32: Azimuthal variation of upper rotor pushrod force colored by advance ratio, μ

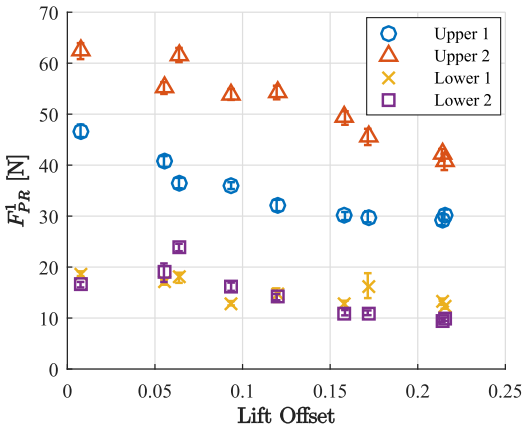

Figure 6.33: 1st harmonic pitch link load amplitude variation with lift offset ($\mu = 0.53$, $\theta_0 = 8°$)

6.3.3 Pushrod Loads

Pushrod loads provide insight into the rotor blade pitching moment dynamics and were measured for all four blades. They were also an important consideration during testing for safety reasons as the observed loads were significantly higher than those predicted by initial design studies. Figure 6.32 shows the azimuthal variation of upper rotor pushrod force colored by advance ratio. As with the pitch angles, higher harmonic components become large at high speeds. Figure 6.33 shows the variation of the first pitch link load harmonic with lift offset for all four rotor blades. All four loads tend to decrease with increasing lift offset, attributable due to the decreased swashplate inclination. The difference in pitch horn geometry is evident in the large difference between upper and lower rotor pitch link forces. The shorter upper rotor pitch horn moment arm, necessitated by space constraints, results in

larger pitch link loads for a given pitching moment. Additionally there is a significant difference between the first and second upper rotor-blade one-per-revolution loads. A numerical study of the pitch link loads by Schmaus and Chopra [98] revealed that a large portion of the one-per-revolution loading is attributable to viscous damping in the hub roller bearings. Thus the observed difference between upper rotor pitch link 1st harmonic forces is most likely due to a difference in bearing assembly and lubrication. Figure 6.34 shows the variation of the higher harmonic pushrod forces with lift offset. As with the first harmonic the higher harmonics tend to decrease with increasing lift offset. The most striking feature of the higher harmonics is the large five-per-revolution component, present in all four pushrod loads, because there is no obvious source of excitation for this mode. This corresponds with the pitch harmonic observed in the blade root pitch angle sensors shown in figure 6.18. It is possible that the backlash present in the rotor system results in broadband excitation that includes the observed five-per-revolution component.

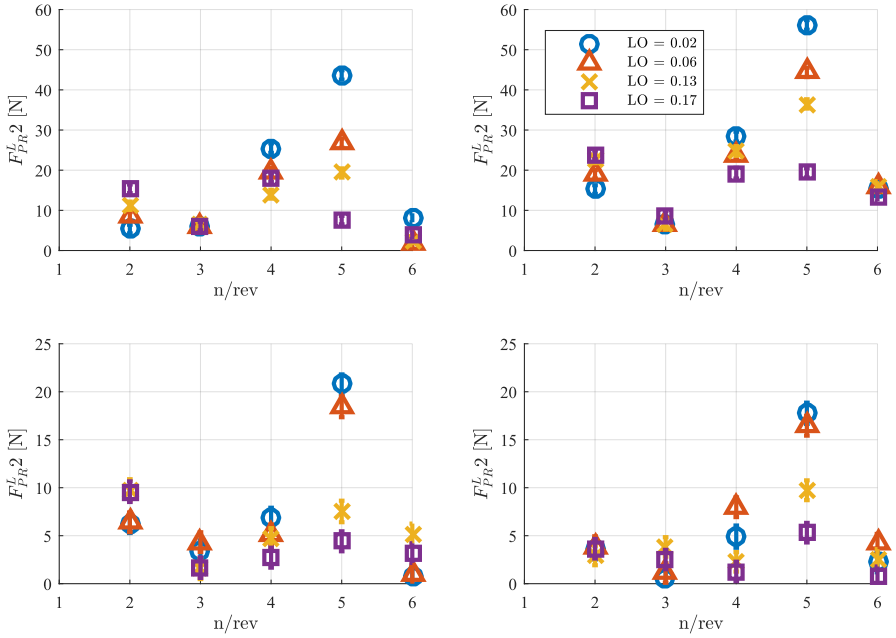

Figure 6.34: Higher harmonic pitch link load variation with lift offset ($\mu = 0.53$, $\theta_0 = 8°$)

Chapter 7

Summary and Future Work

7.1 Summary

A model-scale, rigid, counter-rotating coaxial rotor system was designed and fabricated. Toothed belts and pulleys maintain consistent phasing and angular velocity between upper and lower rotors. Modular, rigid rotor hubs, with roller bearing assemblies for reacting centrifugal and flap and lag bending modes were fabricated. A pitch control system, with two separate three degree of freedom swashplate assemblies for upper and lower rotors was designed and built. Custom linear servos, with high force output and high precision were designed for actuating the swashplate assemblies. Hub loads were measured by two custom 6 component load cells mounted below each rotor. Blade root pitch angles were measured using a compact arrangement of Hall effect sensors and magnets along with cubic calibration curves. Strain gauge instrumented hoop load cells with custom instrumentation amplifiers monitor pushrod loads. Finally a custom optical blade tip clearance sensor, embedded in the lower surface of the upper rotor blade, was designed and calibrated. Two sets of rotor blades were fabricated using a two-cell foam core construction with carbon-fiber prepregs. The first, reference blades featured a uniform VR-12 cross section, while the second set of blades utilized additional prepreg laminates

and a root reinforcement cuff to achieve high flap-bending stiffness, and Lock number targets for forward flight with lift offset. The layup and cuff were designed with the aid of linear rotating beam finite element model. Blade stiffness properties were measured for both reference and reinforced blades. Uniform beam assumptions and tip slope responses to applied tip loads were used to characterize the reference blades. Stereoscopic digital image correlation (DIC) was used to measure the full-field displacements of the reinforced rotor blades in response to tip loading. The distributed displacement measurements were then used to update the spanwise varying stiffness properties of the linear beam model by minimizing an error objective function between measured and predicted displacements.

High speed stereoscopic DIC was used along with a white noise, electromechanical shaker forcing to measure the dynamic response of the reinforced rotor blades. The response was then analyzed using the Natural Excitation Technique and Eigensystem Realization Algorithm operational modal analysis (OMA) techniques. The results of the analyses included blade natural frequencies and associated mode shapes. These results were compared to the outputs from a nonlinear beam model of the blade. Excellent agreement, both between natural frequencies and mode shapes was observed, validating high-speed DIC plus OMA techniques for measuring rotor blade dynamic properties. Additional dynamic characterization was performed on rotating rotor blades, excited by a transient gust disturbance. Deformations were measured using high-speed DIC, phase locked with the rotor system. The resulting deforma-

tions were then processed using a modified Ibrahim Time Domain analysis. The first flapping frequency and mode shape were successfully extracted and, while noisy, found to agree with the nonlinear beam model. Additionally the damping ratio for the first flap mode was successfully extracted and agreed with a theoretical calculation based on linear aerodynamics to within measurement uncertainty. The validation of accurate damping ratio extraction allows for the DIC and ITD technique to be used to characterize rotor systems with marginal stability, such as extremely flexible bladed micro-aerial vehicles.

7.1.1 Hover Results

Three distinct rounds of hover testing were performed. The first two tests concentrated on rotor system performance and steady loads with comparison to blade element momentum theory (BEMT) and free vortex method (FVM) codes. Performance measurements for both the isolated and the coaxial rotor systems showed good agreement with the FVM analysis without any modification of the CFD computed airfoil tables, while the BEMT underpredicted the coaxial rotor induced power. A momentum theory model was fit to the experimental data in order to compare profile and induced powers between rotor configurations. Comparisons between the four-bladed isolated and two-bladed coaxial rotors revealed a statistically significant difference (with 95% confidence) in induced power with the coaxial rotor consuming 6% less power than the isolated rotor. This result is in agreement with theoretical performance limits from momentum theory, as well as with FVM predictions. The

coaxial rotor system outperforms the equivalent solidity single rotor system without taking into account additional realizable efficiency gains such as the lack of necessity of a tail rotor.

By measuring independent upper and lower rotor hub loads, the wake interactions between rotors was investigated. The analytical model fits revealed 18% and 49% increases in induced power for the upper and lower coaxial rotors when compared to an equivalent isolated two-bladed rotor. Thrust sharing between upper and lower rotor coaxial rotors with the system torque balanced was found to be nearly constant with the upper rotor providing 54% of the total thrust at all collectives. The FVM analysis accurately captured this steady interaction, while the BEMT predictions were accurate for the lower rotor only. Examining the radial variation of inflow and thrust for upper and lower rotors as computed by the FVM and BEMT analyses reveals that the BEMT does not capture the influence of the lower rotor on the upper. Additionally the lack of diffusion the in the BEMT wake leads to unrealistically large gradients in spanwise rotor inflow and thrust when compared to the FVM analysis. A full FVM analysis is therefore recommended as the minimum resolution necessary for predicting individual upper and lower coaxial rotor performance with no empirical correction factors.

In addition to steady performance data, vibratory loads were also measured and analyzed during the third round of hover testing. In comparison to isolated rotors, the lower coaxial rotor demonstrated a statistically significant increase in four-per-revolution thrust variation. This variation corresponded

to the four upper-lower rotor blade crossings each revolution. Each thrust peak exhibited a board primary peak followed by a narrow secondary peak, indicating multiple excitation mechanisms between rotors. The broad peak is likely associated with bound-vortex interaction between rotor blades, while the secondary peak due to blade thickness effects. Full CFD analysis is necessary to capture this secondary effect, as the lifting line or panel methods employed by comprehensive codes will not account for blade thickness.

7.1.2 Forward Flight Results

Wind tunnel testing was performed to investigate the effects of lift offset in forward flight on performance and vibratory loads at several advance ratios and collectives. Lift offset was found to increase rotor system efficiency as measured by rotor effective lift-to-drag ratio, especially at high advance ratio. This increased efficiency is largely due to increased rotor thrust from the advancing rotor blade. This manifests itself as an increase in rotor thrust collective sensitivity with lift offset, counteracting the decrease that occurs with forward flight speed. Rotor torque is largely unaffected by lift offset while rotor drag increases with lift offset at low advance ratios, and remains constant at high advance ratios. Peak lift-to-drag ratio gains of 30% were measured when operating with lift offset for the coaxial rotor system at 8 degrees collective. Comparison of steady loads at 900 and 1200 RPM revealed no measurable Reynolds or Mach number effects on performance. The lower rotor in the coaxial configuration was found to operate at higher lift-to-drag ratios

than the upper rotor, primarily due to a, previously unmeasured, reversal of the upper-lower rotor thrust ratio from hover to forward flight. The thrust ratio decreases from a maximum of 1.17 in hover to a minimum near 0.85 at $\mu = 0.21$, before increasing back to between 0.9 and 1 at higher advance ratios. Increasing lift offset was found to decrease the difference in upper and lower rotor thrusts at all advance ratios. This is in contrast to a previous computational study which noted this thrust reversal effect.

Blade tip clearance decreased with lift offset, collective and tip speed but showed no appreciable variation with advance ratio. Tip clearance decrease with lift offset were accompanied by a corresponding rise in rotor side force due to blade flap-bending and normal force asymmetry. Pitch link loads were measured with dominant first harmonic loads, determined to be caused by viscous damping in the rotor hub bearings. Additional four-per-revolution forces were observed, associated with the blade passage frequency. Large five-per-revolution forces were observed in both upper and lower pitch links. With no source of five-per-revolution excitation these loads are likely due to the control system free-play generating a non-linear interaction between the large one and four-per-revolution forces.

Isolated, zero-lift offset rotor vibratory loads were found to increase with advance ratio with large four-per-revolution in-plane forces accompanied by two-per-revolution thrust variation. This two-per-revolution thrust was attributed to thrust concentration at the front and back of the rotor disk by using the response phase lag from the measured flap damping and natural frequency.

Additionally two-per-revolution vibratory pitching moment and torque increased with increasing advance ratio. Increasing lift offset decreased two and four-per-revolution vibratory forces, both in and out of plane, while increasing two-per-revolution pitching and rolling moment vibratory loads. The coaxial configuration was found to significantly decrease many vibratory loads, most notably the four-per-revolution in plane forces, and the two-per-revolution torque. Varying the inter-rotor index angle modified two-per-revolution loads with rolling moment and side-force increasing as pitching moment and drag force decrease and vice versa. The two-per-revolution thrust force was completely canceled at an inter-rotor phase angle of 45°. The changes in loads with index angle are a powerful design parameter for selective cancellation of vibratory hub loads.

7.2 Future Work

The results of the current work have implications for the design and study of closely spaced CCR rotorcraft in general. The interference effects on performance in hover and forward flight suggest that dissimilar upper and lower rotor designs may provide an opportunity for increasing system efficiency. The challenge in the dissimilar design comes from the observed reversal in interference effect between hover and forward flight. This reversal forces a choice between optimizing the relative rotor geometry for hover or for forward flight. Additionally, while lift offset was shown to greatly increase rotor efficiency, the rigid blade construction necessary for supporting lift offset transmits large

vibratory loads to the rotorcraft. While varying the rotor index angle was shown to provide selective cancellation of vibratory loads, additional technologies, such as higher harmonic or on-blade vibration control, would be valuable in any high speed CCR design.

The hardware developed for the current study provides a platform for future experimental exploration of coaxial rotorcraft aeromechanics. The following list includes suggestions for improving the experimental design, as well as recommendations for additional avenues research.

- A load cell calibration specifically tailored to the expected rotor loads could reduce bias uncertainty, which was the dominant source of measurement uncertainty during low RPM testing, especially for in-plane forces
- A full, six-degree-of-freedom dynamic calibration is recommended to verify and extend the measurement frequency ranges calculated from the reported load cell stiffness properties
- Additional high-speed cameras to capture the blade deformations over the entire disk would enable the use of NExT ERA for rotating modal extraction, allowing for higher spatial resolution, and more accurate modal properties
- Tests with co-rotating upper and lower rotors would provide insight into the effect of wake swirl recovery on coaxial rotor performance in hover

- Particle image velocimetry flow-field measurements of the rotor system in hover and forward flight is necessary to characterize the rotor wake geometry. Capturing the flow-field between crossing upper and lower rotor blades in hover would enhance the understanding of the apparent multi-modal interactions.

- The upper-lower rotor thrust reversal observed during wind tunnel testing may be investigated further. Low speed ($\mu < 0.2$) forward flight testing, as well as flow-field measurements are necessary to fully characterize the mechanisms causing the reversal

- Rotor blades with a more realistic geometry, including varying airfoil profiles, chord, and four-bladed rotors could allow for the investigation of realizable efficiency gains with rotor optimization.

Appendix

Appendix 1

Circuit Design

1.1 Load Cell Amplifier

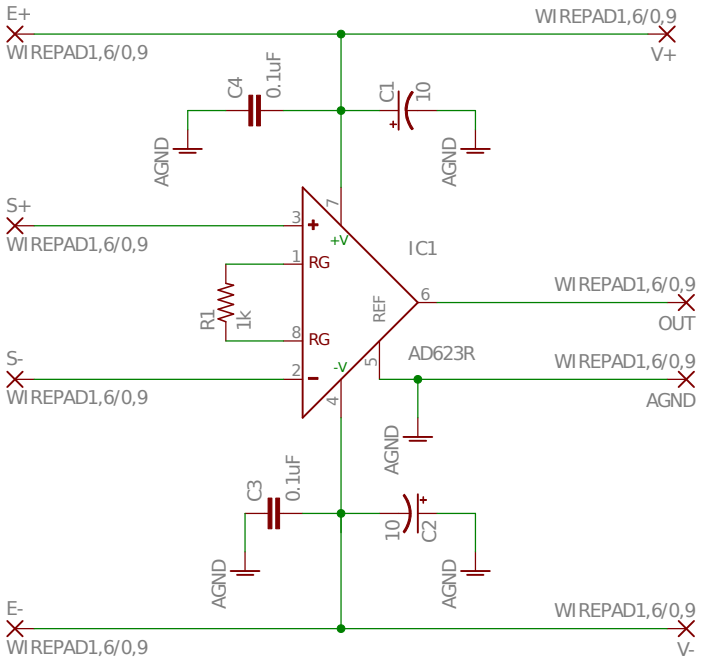

Figure A.1: Load cell amplifier circuit diagram

1.2 Digital Tip Clearance Sensor

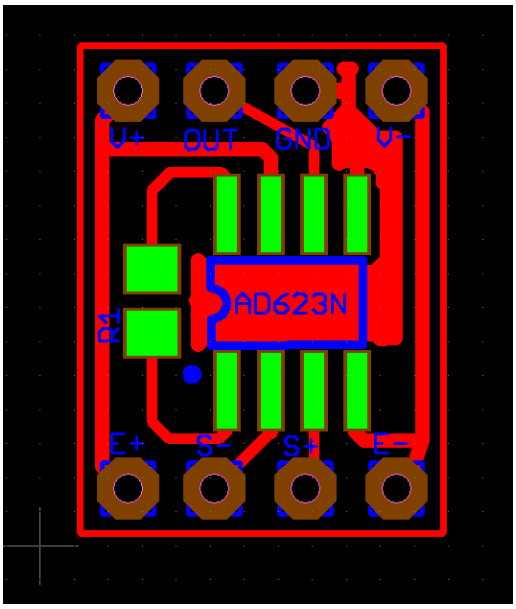

(a)

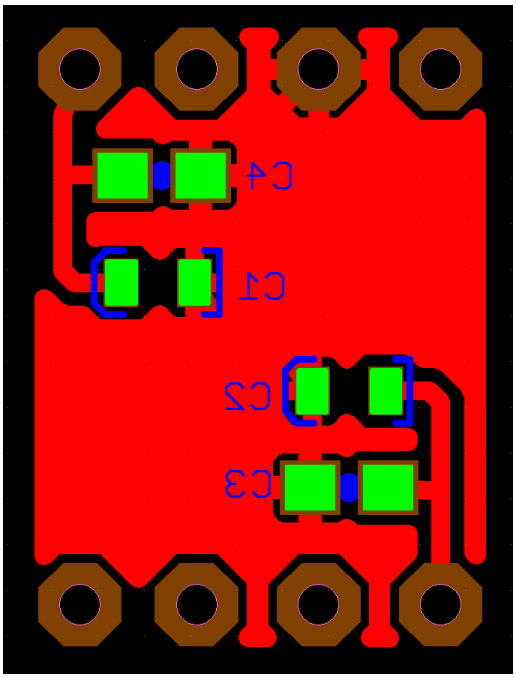

(b)

Figure A.2: Load cell amplifier board layout, (a) Upper, (b) Lower

Table A.1: Load cell amplifier bill of materials

Component ID	Part #	Description	Package
IC1	AD623ARZ-R7	Single Supply Instrumentation Amplifier	SOIC_N
C1,C2	TACL106K010XTA	10 uF Tantalum Capacitor	0603
C3,C4	06035C104JAT2A	0.1 uF ceramic capacitor	0603
R1	TNPW08051K00BEEA	Thin Film Resistor	0805

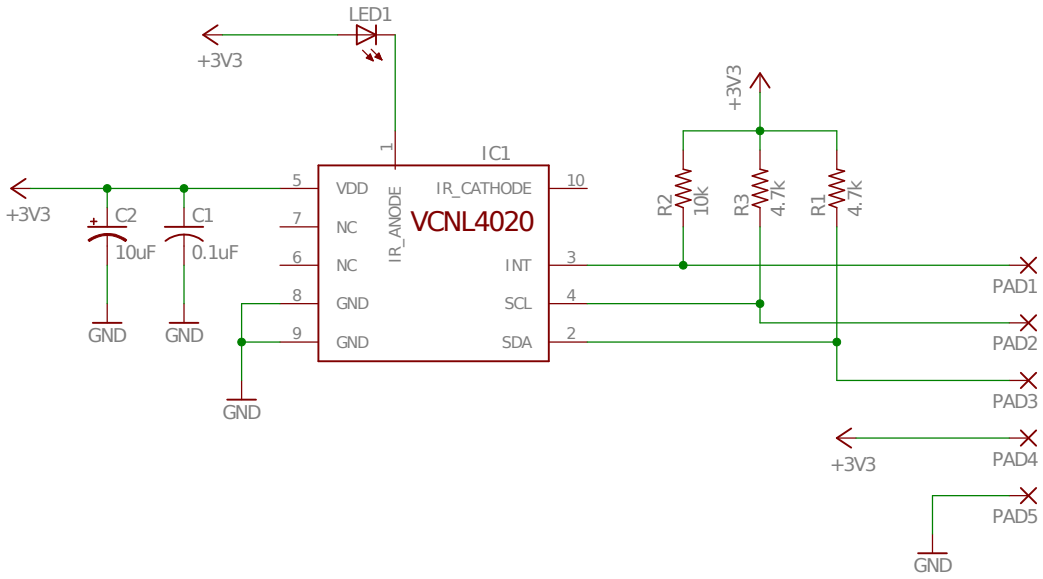

Figure A.3: Digital tip clearance sensor circuit diagram

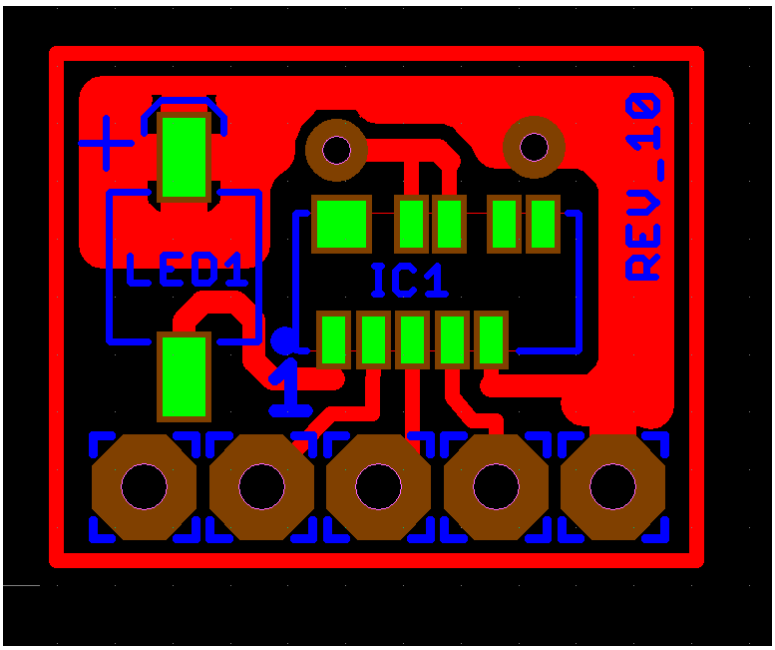

(a)

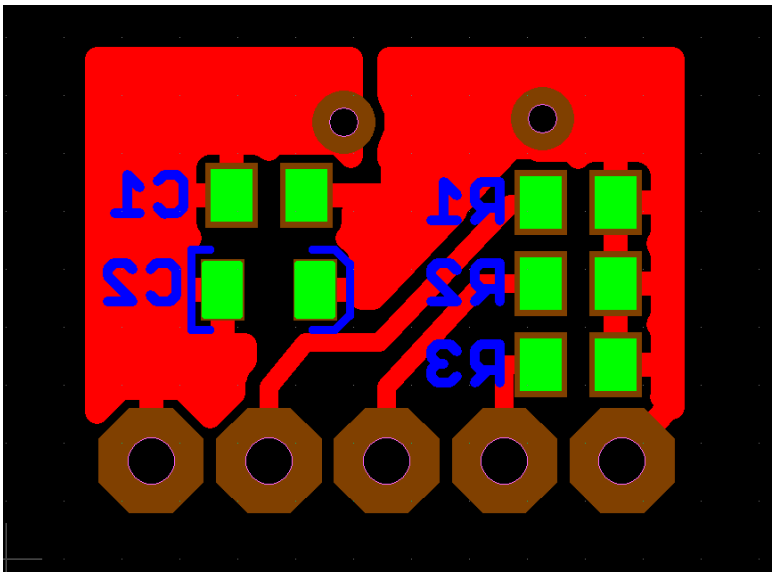

(b)

Figure A.4: Digital tip clearance sensor board layout, (a) Upper, (b) Lower

Table A.2: Tip clearance sensor bill of materials

Ref Des	Part #	Description	Package
IC1	VCNL4020-GS08	Single Supply Instrumentation Amplifier	SOIC_N
LED1	VSMF2893GX01	IR LED	
C2	F981A106MMA	10 uF Tantalum Capacitor	0603
C1	CL05B104KO5NNNC	0.1 uF ceramic capacitor	0402
R1,R3	ERJ-2RKF4701X	Thick Film Resistor	0402
R2	ERJ-2RKF1002X	Thick Film Resistor	0402

Bibliography

[1] *La Vision 2016 DaVIs StrainMaster 3-D, Software Package Version 8.1.* La Vision, Goettingen, Germany.

[2] Composite materials handbook, vol. 2. Handbook MIL-HDBK-17-2F, Department of Defense, 2002.

[3] Nist/sematech e-handbook of statistical methods, October 2013.

[4] A. I. Abrego, L. E. Olson, E. A. Romander, D. A. Barrows, and A. W. Burner. Blade displacement measurement technique applied to a full-scale rotor test. In *American Helicopter Society 68th Annual Forum Procedings (Fort Worth, TX, 1-3 May)*, 2012.

[5] D. N. Arents. An assessment of the hover performance of the XH-59A advancing blade concept demonstration helicopter. Technical Report USAAMRDL-TN-25, U. S. Army Air Mobility Research and Development Laboratory, May 1977.

[6] K. O. Arras. An introduction to error propagation: Derivation, meaning and examples of equation $c_y = f_x c_x f_x^t$. Technical Report EPFL-ASL-TR-98-01 R3, EPFL, September 1998.

[7] ATI Industrial Automation. *Six Axis Force/Torque Sensor System Installation and Operation Manual*, April 2012.

[8] A. Bagai. Aerodynamic design of the x2 technology demonstrator^{TM} main rotor blade. In *Proceedings of the American Helicopter Society 64th Annual Forum, Montréal, Québec*, April 29 - May 4 2008.

[9] A. Bagai and J. G. Leishman. Rotor free-wake modeling using a pseudo-implicit technique-including comparisons with experimental data. *Journal of the American Helicopter Society*, 40(3):29–41, 1995.

[10] A. Bagai and J. G. Leishman. Free-wake analysis of tandem, tilt-rotor and coaxial rotor configurations. *Journal of the American Helicopter Society*, 41(3):196–207, 1996.

[11] J. Bao. *Development of Mach Scale Rotor With Composite Tailored Couplings for Vibration Reduction.* PhD thesis, The University of Maryland, College Park, 2004.

[12] J. B. Barlow, W. H. Rae, and A. Pope. *Low Speed Wind Tunnel Testing.* Wiley-Interscience, Hoboken, NJ, 3rd edition, 1999.

[13] B. Berry and I. Chopra. *Wind Tunnel Testing of an Instrumented Rotor at High Advance Ratio.* American Institute of Aeronautics and Astronautics, 2016/08/25 2015.

[14] M. J. Bhagwat and J. G. Leishman. Stability, consistency and convergence of time-marching free-vortex rotor wake algorithms. *Journal of the American Helicopter Society*, 46(1):59–71, 2001.

[15] M. J. Bhagwat and J. G. Leishman. Generalized viscous vortex core models for application to free-vortex wake and aeroacoustic calculations. In *Proceedings of the 58th Annual Forum of the American Helicopter Society, Montréal Québec*, 2002.

[16] M. J. Bhagwat and J. G. Leishman. Rotor aerodynamics during maneuvering flight using a time-accurate free-vortex wake. *Journal of the American Helicopter Society*, 48(3):143–158, 2003.

[17] R. Blackwell and T. Millott. Dynamics design characteristics of the sikorsky x2 technology demonstrator^{TM} aircraft. In *Proceedings of the American Helicopter Society 64th Annual Forum, Montréal, Québec*, April 29 - May 4 2008.

[18] R. E. Brown and A. J. Line. Efficient high-resolution wake modeling using the vorticity transport equation. *AIAA Journal*, 43(7):1434–1443, July 2005.

[19] B. N. Burtsev. The coaxial helicopter vibration reduction. In *Proceedings of the 18th European Rotorcraft Forum, September, 1992*, 1992.

[20] C. Cameron, A. Karpatne, and J. Sirohi. Performance and vibratory hub loads of a mach-scale coaxial rotor in hover. In *Proceedings of the American Helicopter Society 70th Annual Forum, Montréal, Québec*, May 20 - 22 2014.

[21] C. Cameron, D. Uehara, and J. Sirohi. Transient hub loads and blade deformation of a mach-scale coaxial rotor in hover. In *56th AIAA/ASCE/AHS/ASC Structures, Structural Dynamics, and Materials Conference*. American Institute of Aeronautics and Astronautics Inc., January 5-9 2015.

[22] C. G. Cameron, A. Karpatne, and J. Sirohi. Performance of a mach-scale coaxial counter-rotating rotor in hover. *Journal of Aircraft*, 53(3):746–755, 2016/08/11 2016.

[23] T. G. Carne and G. H. J. III. The inception of {OMA} in the development of modal testing technology for wind turbines. *Mechanical Systems and Signal Processing*, 24(5):1213 – 1226, 2010. Special Issue: Operational Modal Analysis.

[24] M. Cheney. The abc helicopter. *Journal of the American Helicopter Society*, 14(4):10–19, 1969.

[25] C. P. Coleman. A survey of theoretical and experimental coaxial rotor aerodynamic research. *NASA TP 3675*, 1997.

[26] Cytec Industries Inc. *FM 300 Epoxy Film Adhesive*, October 2013.

[27] L. U. Dadone. Design and analytical study of a rotor airfoil. Contractor Report 2988, NASA Langley Research Center, 1980.

[28] I. M. Daniel and O. Ishai. *Engineering Mechanics of Composite Materials*. Oxford University Press, New York, NY, 2006.

[29] J. D'Errico. Adaptive robust numerical differentiaion, December 2014.

[30] R. C. Dingeldein. Wind-tunnel studies of the performance of multirotor configurations. Technical Report TN-3236, NACA, August 1954.

[31] M. Drela and H. Youngren. *XFOIL 6.9 User Primer*. Massachesetts Institute of Technology, Cambridge, MA, 2001.

[32] Evonik Resource Efficiency GmbH. *Rohacell IG/IG-F*, March 2016.

[33] F. F. Felker. Performance and loads data from a wind tunnel test of a full-scale, coaxial, hingeless rotor helicopter. Technical Report TM-81329, NASA, October 1981.

[34] G. A. Fleming and S. A. Gorton. Measurement of rotorcraft blade deformation using projection moiré interferometry. *Shock and Vibration*, 7(3):149–165, 2000.

[35] G. A. Fleming, H. L. Soto, and B. W. South. Projection moiré interferometry for rotorcraft applications: deformation measurement of active twist rotor blades. In *American Helicopter Society 58th Annual Forum Preceedings (Montréal, Quebec 11-13 June)*, 2002.

[36] R. D. Harrington. Full-scale-tunnel investigation of the static-thrust performance of a coaxial helicopter rotor. *NASA TN 2318*, 1951.

[37] L. Hermans and H. V. D. Auweraer. Modal testing and analysis of structures under operational conditions: Industrial applications. *Mechanical Systems and Signal Processing*, 13(2):193 – 216, 1999.

[38] Hexcel. *3501-6 Epoxy Matrix Product Data*, 1998.

[39] Hexcel. *8552 Epoxy Matrix Product Data*, February 2013.

[40] J. Ho, H. Yoo, and M. Bhagwat. Validation of rotorcraft comprehensive analysis performance predictions for coaxial rotors in hover. In *Proceedings of the American Helicopter Society 71st Annual Forum, Virginia Beach, Virgina, May 5-7*, 2015.

[41] D. H. Hodges and E. H. Dowell. Nonlinear equations of motion for the elastic bending and torsion of twisted nonuniform rotor blades. Technical Report NASA-TN-D-7818, NASA Ames Research Center, 1974.

[42] S. R. Ibrahim. Random decrement technique for modal identification of structures. *Journal of Spacecraft*, 14(11):696–700, 1977.

[43] S. R. Ibrahim. Doulbe least squares approach for use in structural modal identification. *AIAA Journal*, 24(3), 1986.

[44] S. R. Ibrahim and E. C. Milkulcik. The experimental deterimination of vibration test parameters from time responses. *The Shock and Vibration Bulletin*, 46(5):187–196, 1976.

[45] G. H. J. III, T. G. Carne, and P. S. Veers. Damping measurements using operational data. *Journal of Solar Energy Engineering*, 118(3):190 – 193, 1996.

[46] G. H. James, T. G. Carne, and J. P. Lauffer. The natural excitation technique (next) for modal parameter extraction from operating structures. *The International Journal of Analytical and Experimental Modal Analysis*, 10(4):260–277, October 1995.

[47] W. Johnson. *Helicopter Theory*. Priceton University Press, 1980.

[48] W. Johnson. Technology drivers in the development of camrad ii. In *Proceedings of the American Helicopter Society Aeromechanics Specialists Conference, San Francisco, California, January 19-21*, 1994.

[49] W. Johnson. Influence of lift offset on rotorcraft performance. Technical Report TP-2009-215404, NASA, Nov 2009.

[50] W. Johnson, A. M. Moodie, and H. Yeo. Design and performance of lift-offset rotorcraft for short-haul missions. In *Proceedings of the American Helicopter Society Future Vertical Lift Aircraft Design Conference, San Francisco, California, January 18-20*, 2012.

[51] F. J. B. Jr. A simplified theoretical method of determining the characteristics of a lifting rotor in forward flight. Technical Report 716, NACA, 1941.

[52] J.-N. Juang and R. S. Pappa. An eigensystem realizaiton algorithm for modal parameter identification and modal reduction. *Journal of Guidance, Control and Dynamics*, 8(5):620–627, 1985.

[53] A. Karpatne. *Study of Compressible Flow Through a Rotating Duct*. PhD thesis, The University of Texas at Austin, 2015.

[54] H. W. Kim and R. E. Brown. A comparison of coaxial and conventional rotor performance. *Journal of the American Helicopter Society*, 55, 2010.

[55] H. W. Kim and R. E. Brown. A rational approach to comparing the performance of coaxial and conventional rotors. *Journal of the American Helicopter Society*, 55(1):12003–1 – 12003–9, 2010.

[56] H. W. Kim, K. Duraisamy, and R. Brown. Aeroacoustics of a coaxial rotor in level flight. In *Proceedings of the American Helicopter Society 64th Annual Forum, Montréal, Québec*, April 29 - May 4 2008.

[57] R. Kimmel and A. M. Bruckstein. Shape offsets via level sets. *Computer-Aided Design*, 25(3):154–162, March 1993.

[58] R. Kube, W. Splettstoesser, W. Wagner, U. Seelhorst, Y. Yu, C. Tung, P. Beaumier, J. Prieur, G. Rahier, P. Spiegel, A. Boutier, T. Brooks, C. Burley, D. Boyd, E. Mercker, and K. Pengel. Hhc aeroacoustic rotor tests in the german-dutch wind tunnel: Improving physical understanding and prediction codes. *Aerospace Science and Technology*, 2(3):177 – 190, 1998.

[59] R. Kufeld, D. L. Balough, J. L. Cross, K. F. Studebaker, C. D. Jennison, and W. G. Bousman. Flight testing of the uh-60a airloads aircraft. In

American Helicopter Society 50th Annual Forum Proceedings, (Alexandria, VA May), 1994.

[60] V. K. Lakshminarayan and J. D. Baeder. High-resolution computational investigation of trimmed coaxial rotor aerodynamics in hover. *Journal of the American Helicopter Society*, 54:042008 (21 pages), 2009.

[61] H.-J. Langer, R. L. Peterson, and T. H. Maier. An experimental evaluation of wind tunnel wall correction methods for helicopter performance. In *Proceedings of the American Helicopter Society 52nd Annual Forum, Washington, D.C.*, June 4-6 1996.

[62] J. G. Leishman. *Principles of Helicopter Aerodynamics*. Cambridge University Press, New York, NY, 2nd edition, 2006.

[63] J. G. Leishman. Aerodynamic performance considerations in the design of a coaxial proprotor. *Journal of the American Helicopter Society*, 54(1), 2009.

[64] J. G. Leishman and S. Ananthan. An optimum coaxial rotor system for axial flight. *Journal of the American Helicopter Society*, 53(4):366–381, 2008.

[65] J. G. Leishman and M. Syal. Figure of merit definition for coaxial rotors. *Journal of the American Helicopter Society*, 53(3):290–300, 2008.

[66] J. M. Leuridan, D. L. Brown, and R. J. Allemang. Time domain parameter identification methods for linear modal analysis: A unifying

approach. *Journal of Vibration, Acoustics, Stress, and Reliability in Design*, 108(1):1–8, 1986.

[67] J. W. Lim, K. W. McAlister, and W. Johnson. Hover performance correlation for full-scale and model-scale coaxial rotors. *Journal of the American Helicopter Society*, 54(3):32005, 2009.

[68] T. Lundstrom, J. Baqersad, and C. Niezrecki. *Using High-Speed Stereophotogrammetry to Collect Operating Data on a Robinson R44 Helicopter*, pages 401–410. Springer New York, New York, NY, 2013.

[69] K. Marlett. Hexcel 8552 im7 unidirectional prepreg 190 gsm 35material property data report. Contractor Report CAM-RP-2009-015 Rev A, FAA,NCAMP, 2011.

[70] K. Marlett. Hexcel 8552s as4 plain weave fabric prepreg 193 gsm 38qualification material property data report. Contractor Report CAM-RP-2010-006 N/C, FAA,NCAMP, 2011.

[71] K. W. McAlister and C. Tung. Experimental study of a hovering coaxial rotor with highly twisted blades. In *Proceedings of the American Helicopter Society 64th Annual Forum, Montréal, Québec*, April 29 - May 4 2008.

[72] L. Meirovitch. *Principles of Helicopter Aerodynamics*. Waveland Press Inc., Chicago, IL, 1st edition, 2001.

[73] L. Molnár, K. Váradi, G. Bódai, P. Zweirczyk, and L. Oroszváry. Simplified modeling for needle roller bearings to analyze engineering structures by fem. *Periodica Polytechnica Mechanical Engineering*, 54(1):27–33, 2010.

[74] T. Nagashima and K. Nakanishi. Optimum performance and wake geometry of a coaxial rotor in hover. *Vertica*, 7(225-239), 1983.

[75] T. Nagashima, H. Ouchu, and F. Sasaki. Optimum performance and load sharing of coaxial rotor in hover. *Journal of Japan Society for Aeronautics and Space Sciences*, 26(293):325–333, June 1978.

[76] L. E. Olson, A. I. Abrego, D. A. Barrows, and A. W. Burner. Blade deflection measurement of a full-scale uh-60a rotor system. In *American Helicopter Society Aeromechanics Specialists' Conference Proceedings (San Francisco, CA, 20-22 Jan.)*, 2012.

[77] M. Ozbek, F. Meng, and D. J. Rixen. Challenges in testing and monitoring the in-operation vibration characteristics of wind turbines. *Mechanical Systems and Signal Processing*, 41(1–2):649 – 666, 2013.

[78] M. Ozbek and D. J. Rixen. Operational modal analysis of a 2.5mw wind turbine using optical measurement techniques and strain gauges. *Wind Energy*, 16(3):367–381, 2013.

[79] M. Ozbek and D. J. Rixen. A new analysis methodology for estimating the eigenfrequencies of systems with high modal damping. *Journal of*

Sound and Vibration, 361:290 – 306, 2016.

[80] V. M. Paglino. Forward flight performance of a coaxial rigid rotor. In *Proceedings of the 27th American Helicopter Society Forum, Washington, D.C.*, May 1971.

[81] R. S. Pappa and S. R. Ibrahim. A parametric study of the ibrahim time domain modal identification algorithm. Technical report, NASA Langley Research Center, 1985.

[82] B. Peeters and G. De Roeck. Stochastic system identification for operational modal analysis: A review. *Journal of Dynamic Systems, Measurement, and Control*, 123(4):659–667, 2001.

[83] B. PEETERS and C. VENTURA. Comparative study off modal analysis techniques for bridge dynamic characteristics. *Mechanical Systems and Signal Processing*, 17(5):965 – 988, 2003.

[84] D. A. Peters, C.-J. He, and D. Boyd. A finite-state induced-flow model for rotors in hover and forward flight. *Journal of the American Helicopter Society*, 34(4), 1989.

[85] A. E. Phelps and R. E. Mineck. Aerodynamic characteristics of a counter-rotating, coaxial, hingeless rotor helicopter model with auxiliary propulsion. Technical Report TM-78705, NASA, May 1978.

[86] L. Pirodda. Shadow and projection moire techniques for absolute or relative mapping of surface shapes. *Optical Engineering*, 21(4):214640–214640–, 1982.

[87] N. Rajmohan, J. Zhao, and C. He. A couple vortex particle/cfd methodology for studying coaxial rotor configurations. In *American Helicopter Society Aeromechanics Specialists' Conference Proceedings (San Francisco, CA, 22-24 Jan.)*, 2014.

[88] M. Ramasamy. Measurements comparing hover performance of single, coaxial, tandem, and tilt-rotor configurations. In *Proceedings of the American Helicopter Society 69th Annual Forum, Phoenix, Arizona, May 21-23*, 2013.

[89] M. Ramasamy. Hover performance measurements toward understanding aerodynamic interference in coaxial, tandem, and tilt rotors. *Journal of the American Helicopter Society*, 60:032005 (17 pages), 2015.

[90] M. Ramasamy and J. G. Leishman. The interdependence of straining and viscous diffusion effects on vorticity in rotor flow fields. In *Proceedings of the American Helicopter Society 59th Annual Forum, Phoenix, Arizona, May 6-8*, 2003.

[91] R. C. Rice, J. L. Jackson, J. Bakuckas, and S. Thompson. Metallic materials properties development and standardization (mmpds). Technical Report DOT/FAA/AR-MMPDS-01, Federal Aviation Administration, 2003.

[92] L. F. Richardson and J. A. Gaunt. The deferred approach to the limit. part i. single lattice. part ii. interpenetrating lattices. *Philosophical Transactions of the Royal Society of London A: Mathematical, Physical and Engineering Sciences*, 226(636-646):299–361, 1927.

[93] S. S. Rizo-Patron and J. Sirohi. Operational modal analysis of a rotating cantilever beam using high-speed digital image correlation. In *57th AIAA/ASCE/AHS/ASC Structures, Structural Dynamics, and Materials Conference*. American Institute of Aeronautics and Astronautics, 2016.

[94] T. P. Ryan. *Modern Regression Methods*. Wiley, 2nd edition, 2009.

[95] J. Schmaus and I. Chopra. Aeromechanics for a high advance ration coaxial helicopter. In *Proceedings of the American Helicopter Society 71st Annual Forum, Virginia Beach, VA*, May 5-7 2015.

[96] J. Schmaus and I. Chopra. Performance and loads prediciton for a high advance ratio coaxial helicopter. In *AIAA SciTech 2015, Kissimmee, FL*, 2015.

[97] J. Schmaus and I. Chopra. Performance and loads of a model coaxial rotor part ii: Prediction validations with measurements. In *Proceedings of the American Helicopter Society 73rd Annual Forum, West Palm Beach, Florida, May 17-19*, 2016.

[98] J. Schmaus and I. Chopra. Performance and loads of a model coaxial rotor part ii: Prediction validations with measurements. *Journal of the American Helicopter Society*, Submitted for Review October 2016.

[99] O. Schneider. Analysis of spr measurements from hart ii. *Aerospace Science and Technology*, 9(5):409 – 420, 2005.

[100] M. Sekula. The development and hover test application of a projection moiré interferometry blade displacement measurement system. In *American Helicopter Society 68th Annual Forum Procedings (Fort Worth, TX, 1-3 May)*, 2012.

[101] P. J. Sevenhuijsen. The photonical, pure grid method. *Optics and Lasers in Engineering*, 18(3):173 – 194, 1993.

[102] K. Shinohara. *Optimum aerodynamic character of the coaxial counter rotating rotor system.* PhD thesis, National Defense Academy, February 1977.

[103] J. Sicard. *Development of an Extremely Flexible, Variable-Diameter Rotor for a Micro-Helicopter.* PhD thesis, The University of Texas at Austin, 2014.

[104] J. Sicard and J. Sirohi. Measurement of the deformation of an extremely flexible rotor blade using digital image correlation. *Measurement Science and Technology*, 24(6):065203, 2013.

[105] J. Sicard and J. Sirohi. Modeling of the large torsional deformation of an extremely flexible rotor in hover. *AIAA Journal*, 52(8):1604–1615, August 2014.

[106] R. Singh, H. Kang, C. Cameron, and J. Sirohi. Computational and experimental investigations of coaxial rotor unsteady loads. In *54th AIAA Aerospace Sciences Meeting*, page 1787, 2016.

[107] J. Sirohi and M. S. Lawson. Measurement of helicopter rotor blade deformation using digital image correlation. *Optical Engineering*, 51(4):04603, April 2012.

[108] H. Xin, J. Goss, and C. Parkes. Development of a three-state rotor interference model and application to coaxial rotor inflow modeling. In *American Helicopter Society Aeromechanics Specialists' Conference Proceedings (San Francisco, CA, 22-24 Jan.)*, 2014.

[109] H. Yeo and W. Johnson. Investigation of maximum blade loading capability of lift-offset rotors. In *Proceedings of the American Helicopter Society 69th Annual Forum, Phoenix, Arizona, May 21-23*, 2013.

[110] L. A. Young. Vortex core size in the rotor near-wake. Technical report, NASA Technical Report TM-2003-212275, 2003.

[111] Y. Yu, B. Gmelin, H. Heller, J. J. Philippe, E. Mercker, and J. S. Preisser. Hhc aeroacoustic rotor test at the dnw - the joint german/french/us. In

Proceedings of the Twentieth European Rotorcraft Forum, Amsterdam, October 4-7 1994.

[112] L. Zhang, Y. Yao, and M. Lu. An improved time domain polyreference method for modal identification. *Mechanical Systems and Signal Processing*, 1(4):399 – 413, 1987.